APPLIED COMPUTATIONAL ELECTROMAGNETICS SOCIETY JOURNAL

April 2021
Vol. 36 No. 4
ISSN 1054-4887

The ACES Journal is abstracted in INSPEC, in Engineering Index, DTIC, Science Citation Index Expanded, the Research Alert, and to Current Contents/Engineering, Computing & Technology.

The illustrations on the front cover have been obtained from the research groups at the Department of Electrical Engineering, The University of Mississippi.

APRIL 2021 REVIEWERS

Hamza Ahmad
Saad Alhossin
Hristos Anastassiu
Toni Björninen
Guan-Yu Chen
Brinta Chowdhury
Fei Dai
Vinh Dang
Osama Dardeer
Chonghua Fang
Bernhard Hoenders
Ali Hosseini-Fahraji
Amjad Iqbal
Amir Jafargholi
Irum Jafri
Kyung-Young Jung
Wang-Sang Lee
Yan Li
Azzeddin Naghar
Xiao-Min Pan
Javad Pourahmadazar
Mohammd Pourbagher
Dudla Prabhakar
Syedakbar S.
Sivaprakash S.C.
Kensuke Sasaki
Stefano Selleri
Yasuhiro Tsunemitsu
Sapna Verma
Hengfeng Wang
Zhihong Ye
Yang Yu
Gang Zhang
Naming Zhang
Wenshen Zhou

THE APPLIED COMPUTATIONAL ELECTROMAGNETICS SOCIETY JOURNAL

Vol. 36 No. 4 April 2021

TABLE OF CONTENTS

A Numerically Efficient Technique for the Analysis of Metamaterial- and Metasurface-based Antennas

Abdelkhalek Nasri [1], Raj Mittra [1,2], Asim Ghalib [2], Bandar Hakim [1], and Hatem Rmili [1]

[1] Electrical and Computer Engineering Department, Faculty of Engineering
King Abdulaziz University, P.O. Box 80204, Jeddah 21589, Saudi Arabia

[2] Electrical and Computer Engineering, University of Central Florida, Orlando, FL 32816, USA
hmrmili@kau.edu.sa

Abstract ─ Metasurface-based antennas have received considerable recent attention in recent years because they are not only useful for designing new antennas, but for improving the performance of legacy designs as well. However, systematically designing these antennas is challenging because the antennas are usually multiscale in nature and they typically require a long time when simulated by using commercial solvers. In this work, we present a new approach for analyzing antennas that utilize Metasurfaces (MTSs) and Metamaterial (MTMs). The proposed method departs from the widely used technique based on an anisotropic impedance representation of the surface and relies on an equivalent medium approach instead. The principal advantage of the proposed approach is that such an equivalent medium representation can be conveniently inserted directly in commercial EM solvers, circumventing the need to develop special numerical EM simulation codes to handle metasurfaces. Several illustrative examples are presented in the paper to demonstrate the efficacy of the present approach when simulating MTS- and MTM-based antennas.

Index Terms ─ Equivalent medium, metamaterials, metasurfaces, multiscale problems, numerical simulation.

I. INTRODUCTION

Antennas based on Metasurface (MTS) and Metamaterial (MTM) antennas have received considerable recent attention in recent years, since they are not only useful for designing new antennas, but for improving the performance of legacy designs as well. This is often true for antennas designed for satellite communications, as well as 5G applications, where innovative designs are called for to replace the legacy designs.

Some recent works based on MTS-based design include Minatti [1], in which an MTS antenna was described for the enhancement of bandwidth and gain. Figure 1 shows some novel MTS antenna designs proposed by Maci in [2] for a variety of applications. A different strategy for designing high-gain antennas has been presented in [3]. It utilizes a lens-like superstrate to achieve a large gain-bandwidth product.

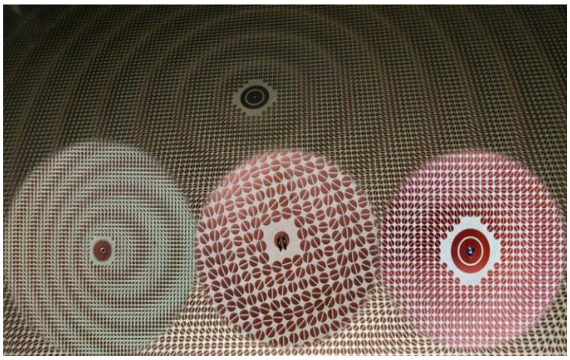

Fig. 1. Examples of metasurface-based antennas [2].

Lens antennas including flat lenses [4], Luneburg lenses [5], and others mentioned in [3], are typically fabricated by using artificially synthesized dielectrics that are also multiscale in nature; hence, in common with the MTS- and MTM-based antennas, they too are computer-intensive to simulate. Recently, some interesting methods for analyzing these metasurfaces have been reported in the literature to reduce the computational cost. Caminita in [6] have proposed a fast method for analyzing MTS antennas using the Method of Moments. In [7], Xiao has described a method utilizing surface impedance and equivalent circuit models for modulated metasurface antennas. Additionally, a literature search reveals a number of other papers which deal with the topic of MTS modeling. These include: Method of Moments using orthogonal entire domain basis Functions in [8], generalized sheet transition conditions (GSTCs) in [9], integral equation formulations based on impedance boundary condition in [10], Fourier-Bessel basis functions

Submitted On: October 16, 2020
Accepted On: March 1, 2021

https://doi.org/10.47037/2020.ACES.J.360401

in [11], dyadic Green's functions in[12] and Gaussian Ring basis functions in [13]. Additionally, the authors in [14] have used a combination method to characterize the metasurface, which utilizes the generalized sheet transition conditions (GSTCs), combined with the bi-anisotropic surface susceptibility functions.

In this work, we present a novel approach, which is altogether different in concept than the methods mentioned above. Our goal is to develop a general-purpose numerical modeling approach, for different types of multiscale antennas containing MTS and MTMs, which achieves numerical efficiency without sacrificing the accuracy. The new method we propose is referred to herein as the Equivalent Medium (ED) approach, which can be conveniently integrated with existing commercial software modules, rather than having the user to develop a new code for handling the simulation problems at hand---an important feature which is not readily available in other approaches, mentioned above. Furthermore, the proposed paradigm is useful for both electric and magnetic type elements, e.g., dipoles or loops, with little or no modification, as long as the operating frequencies are below the resonance range, which is indeed the case for most practical MTS applications, to circumvent the problem with lossy and highly dispersive nature of the MTM and MTS when operating near or above resonance. We should point out however, that the method itself works even after we go past the resonance range, though we strongly recommend that the metasurface-based antennas be used below the resonance range to avoid issues with dispersion and losses.

In general, the equivalent medium is comprised of both ε and μ that are both tensors, and they can be extracted by using inversion algorithms available in the literature [15]-[17]. However, in this work we choose an ε-only representation, which simplifies the numerical computation significantly, without compromising the accuracy of the results, as we will demonstrate below. The epsilon-only representation is referred to herein as the Equivalent Dielectric approach, which is detailed below in the next section.

The paper is organized as follows. Section II, describes the proposed approach which is applicable to a wide variety of metasurfaces; Section III demonstrates the accuracy and efficacy of the proposed method, which has previously been described in [18],[19], by presenting several examples and a comparison in terms of performance, simulation time and required memory for these examples. Finally, some conclusions are presented in Section IV.

II. PRINCIPLE OF THE EQUIVALENT DIELECTRIC APPROACH

In this section we present the basic principles of the Equivalent dielectric (ED) approach for modeling antennas with metasurfaces or metamaterials that are inherently multiscale in nature. Our core strategy for handling the problem of simulating structures containing metasurfaces or metamaterials is to replace them with an "equivalent dielectric" material slab, to be inserted later into a legacy EM simulation program, together with the antenna structure we are modeling. This strategy enables us to circumvent the need to use a fine mesh to model the multiscale geometry, which in turn requires a large number of unknowns and, hence, is both memory- and time-consuming. The principle of our proposed approach is summarized in the following.

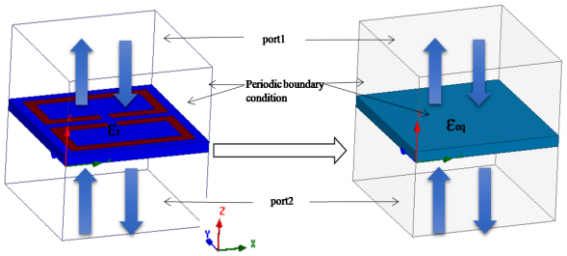

(a) (b)

Fig. 2. (a) Original unit cell of MTS with periodic boundary conditions; (b) equivalent dielectric slab.

Our first step is to determine the equivalent epsilon parameters for the original metamaterial slab. We do this by placing the unit cell of the metamaterial slab in a commercial EM simulation program and imposing the periodic boundary conditions, as shown in Fig. 2 (a). Next, we match the phase of S_{12} of the equivalent dielectric slab (see Fig. 2 (b)) is the same as with that of the original MTS medium shown in Fig. 2 (a). The thickness of the equivalent slab is typically chosen to be the same as that of the original MTM or MTS. It is worthwhile to point out that we only use an equivalent dielectric and not a combination of equivalent ε and μ, as is the usual practice. We will demonstrate below, by using several examples, that we are able to get accurate results using this approach which assumes that μ is equal to μ_0 or an appropriate constant value that we may choose. Note also that the equivalent epsilon that we derive by using the procedure described above is a function of frequency and, hence, the medium is dispersive, as the physics of the problem dictates that it would be. However, this does not create any problem when we simulate the antenna plus metasurface combination using a commercial solver, which can handle a dispersive medium in a routine manner.

In principle, for the general case, we need a 3*3 matrix to characterize the epsilon tensor of the ED in Fig. 2 (b), and it can be described by:

$$\varepsilon = \begin{pmatrix} \varepsilon_{xx} & \varepsilon_{xy} & \varepsilon_{xz} \\ \varepsilon_{yx} & \varepsilon_{yy} & \varepsilon_{yz} \\ \varepsilon_{zx} & \varepsilon_{zy} & \varepsilon_{zz} \end{pmatrix}, \quad (1)$$

where x,y and z are the three directions shown in Fig. 2.

However, in our experience it is sufficient to use either a scalar epsilon or a uniaxial one for most of the MTSs we deal with in practice. Much of the discussion presented below is limited only to those cases and it excludes the case of full tensor representation of the equivalent dielectric. The exception is the case of a chiral medium which is briefly described below by using one example in Section III.

For an isotropic material, the ε-tensor is the same in all directions, *i.e.*, $\varepsilon = \varepsilon_{xx} = \varepsilon_{yy} = \varepsilon_{zz}$. For the uniaxial case, the material is characterized by a diagonal matrix, whose diagonal elements are no longer the same:

$$\varepsilon = \begin{pmatrix} \varepsilon_{xx} & 0 & 0 \\ 0 & \varepsilon_{yy} & 0 \\ 0 & 0 & \varepsilon_{zz} \end{pmatrix}. \quad (2)$$

Finally, for MTSs that provide TE/TM and TM/TE mode conversion, we need to add off-diagonal terms in the ε-tensor to characterize them.

Figure 3 shows a metasurface comprising of square patches printed on a dielectric substrate. The geometry is x-y symmetric, and its equivalent epsilon is identical in both x- and y-directions. The extracted ε_{xx} and ε_{yy} -- they are identical for this geometry -- of the ED, derived by matching the phase of S_{12} of the unit cell of the MTS, is shown in Fig. 4 below. The phase match itself is shown in Fig. 5, which also serves to validate the equivalent dielectric concept for this example.

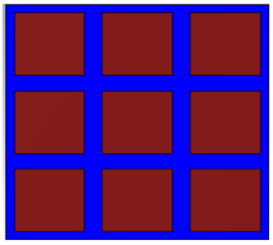

Fig. 3. Metasurface consisting of square-shaped patches.

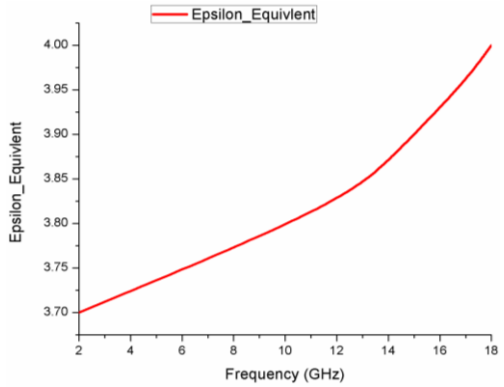

Fig. 4. Equivalent epsilon as a function of frequency for the MTS in Fig. 3.

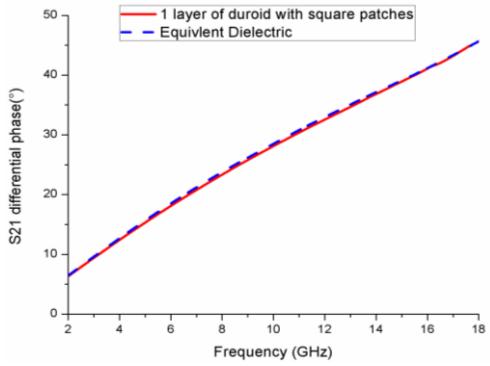

Fig. 5. Phase of S_{12} of the MTS in Fig. 3 and that of the equivalent dielectric.

A. Uniaxial metasurface

Figure 6 shows the example of a uniaxial metasurface, whose unit cell consists of two split ring patches printed on a dielectric substrate. Figure 6 highlights the extracted permittivity; ε_{xx} for the TM mode and ε_{yy} for the TE mode. For this example, it is evident from Fig. 7 that there are frequency ranges in which the permittivities are negative.

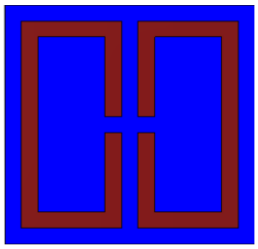

Fig. 6. Metasurface consisting of double split-rings.

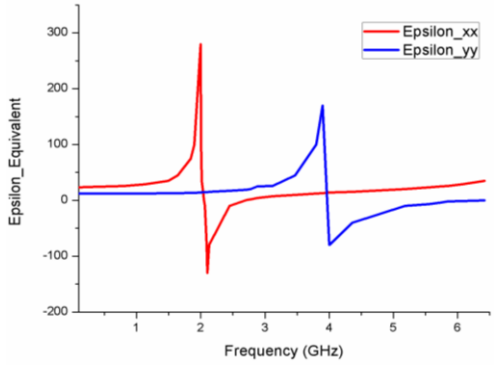

Fig. 7. Permittivities as functions of frequency for a double split-ring type of artificial medium.

Figures 8 and 9 show that both the magnitude and phase behaviors of the S-parameters of the equivalent dielectric and the original metamaterial surface agree well with each other, for both the TM and TE mode incidences. Furthermore, it is evident that the frequency

range exceeds well above the resonances of the split rings. Nonetheless, the agreement between the frequency response of the original metasurface and the equivalent dielectric representation of the same is maintained over the entire frequency range investigated, which goes well above the resonant frequencies for both ε_{xx} and ε_{yy}. This, in turn, indicates that the proposed approach is not limited to frequencies below resonance, at least for this type of MTS.

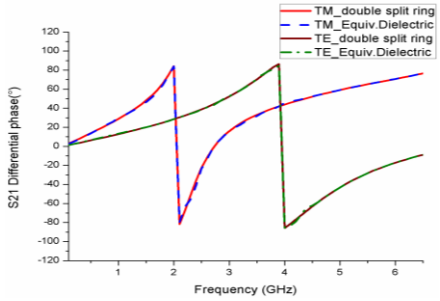

Fig. 8. Differential phase variations of the double split-ring and the Equivalent dielectric---TM and TE modes.

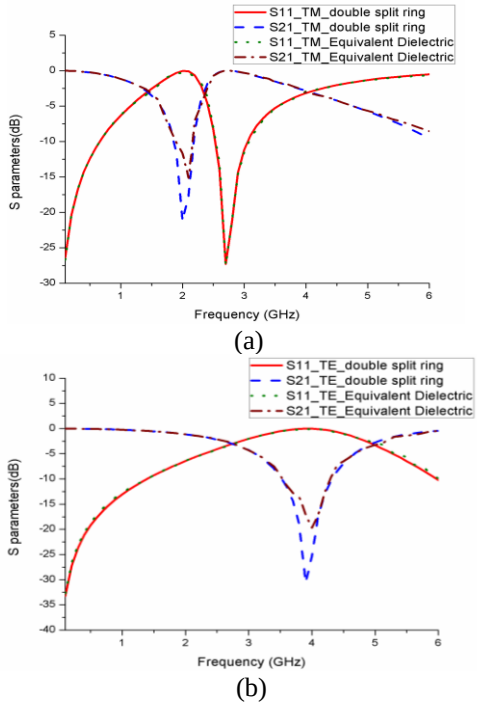

Fig. 9. Simulated S-parameter of the double split-ring and its equivalent dielectric representation: (a) TM mode and (b) TE mode.

B. Equivalent dielctric representation of Chiral metasurfaces

For the final example presented in this work, we consider a chiral type of dielectric MTS, which has been discussed in [19]. The authors in [19] have proposed a new design of an all- dielectric chiral metasurface based on elliptic dielectric resonators, which realizes circular dichroism proprieties over the frequency band of 10-20GHz.

For this type of MTS, neither the scalar nor the uniaxial representation of the epsilon tensor is adequate, and we must include off-diagonal terms in the epsilon tensor to accurately represent the TE/TM and TM/TE conversion properties of the surface. Figure 10 shows the layout of the chiral unit cell of the MTS. Figures 11 (a) and (b) present the extracted equivalent permittivity of the tensor representation. The ε_{xx} and ε_{yy} extracted parameters characterize the TM and TE modes, respectively, while the ε_{xy} and ε_{yx} parameters are associated with the TM/TE and TE/TM mode conversions, respectively.

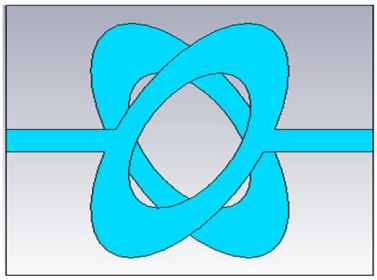

Fig. 10. Dielectric Chiral metasurface [19].

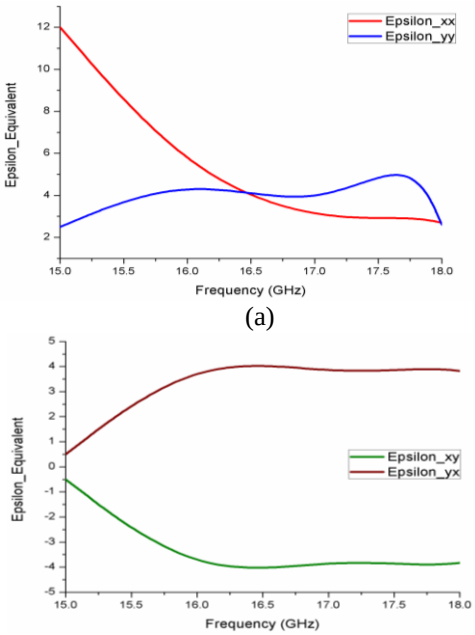

Fig. 11. Permittivities as functions of frequency for the dielectric Chiral medium shown in Fig. 10: (a) ε_{xx} and ε_{yy}; (b) ε_{xy} and ε_{yx}.

Figure 12 shows that the results for the differential phases of the TM and TE modes exhibit good agreement between the original and equivalent dielectric media. In addition, Fig. 13 demonstrates that the magnitude plots also agree with each other quite well over the entire frequency range investigated.

III. APPLICATIONS: CASE EXAMPLES

In this section we present several case examples of antennas with metasurfaces and metamaterial mediums, with a view to demonstrating the efficiency and accuracy of the proposed ED technique for modeling the metasurface type of multiscale problems.

A. Metasurfaces based antenna

For the first example, we consider a microstrip patch antenna with an MTS superstrate, as shown in Fig. 14. The unit cell of the MTS is a metallic cross printed on a dielectric substrate. Comparisons between the S-parameters and gain values of the original and equivalent configurations are shown in Figs. 15 and 16, respectively. We note that the two results are in good agreement over the entire frequency range of 1 to 5 GHz.

Table 1 compares the times needed to simulate the original design and its equivalent counterpart and shows that a 66% improvement is achieved.

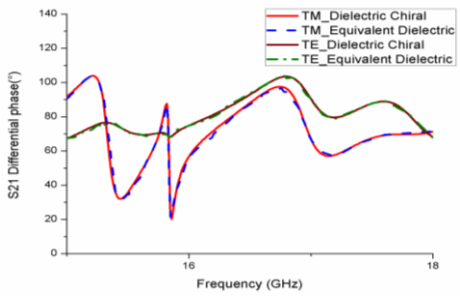

Fig. 12. Differential phase variations of S_{21} of the unit cell in Fig. 10 and that of the ED, for the TM and TE modes.

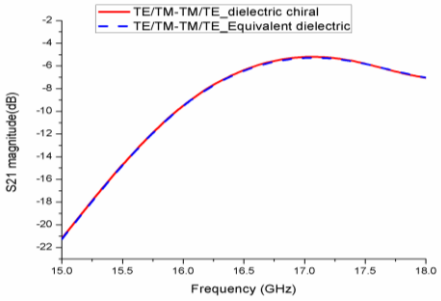

Fig. 13. Simulated magnitudes of the unit cell in Fig. 10 and the ED for TE/TM and TM/TE modes.

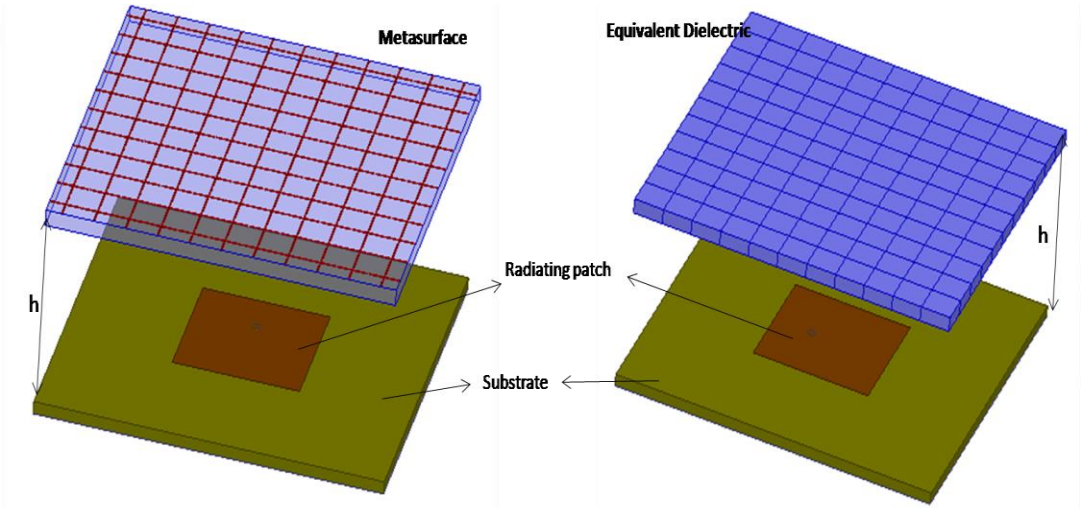

(a) (b)

Fig. 14. Patch antenna with different superstrate: (a) metasurface and (b) equivalent dielectric.

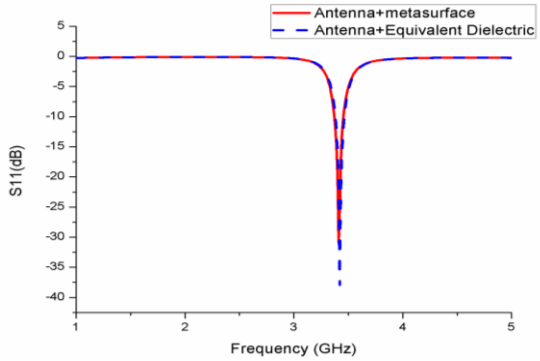

Fig.15. Simulated S parameters of the patch antenna with different superstrate.

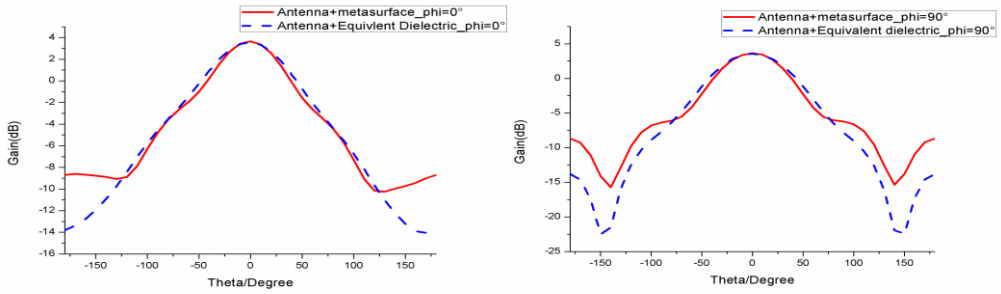

(a) (b)

Fig. 16. Simulated gain of the patch antenna with different superstrate at 3.36 GHz: (a) E plane and (b) H plane.

Table 1: Comparison of simulation times between the equivalent dielectric approach and the original design of patch antennas

	Antenna Only	**Antenna+Metasurface**	**Antenna+Equivalent Dielectric**
Frequency range (GHz)	1-5	1-5	1-5
Resonant frequency (GHz)	3.36	3.42	3.42
Gain (dB)	2.89	3.65	3.56
Simulation Time (hh:mm:ss)	00:03:37	00:25:02	00:07:47

For the second example, we consider a horn antenna with a metasurface panel placed just in front of its aperture. The original design and its equivalent dielectric counterpart are shown in Figs. 17 (a) and (b), respectively. Figures 18 and 19 plot the S-parameters and radiation patterns of the two antenna systems and demonstrate that they compare well with each other.

Next, Table 2 compares the simulation times for the two configurations, and demonstrates that the equivalent dielectric approach is faster by a factor of 23 in terms of the simulation time for a single layer of metasurface, and that this factor jumps to 162 for a double-layer metasurface.

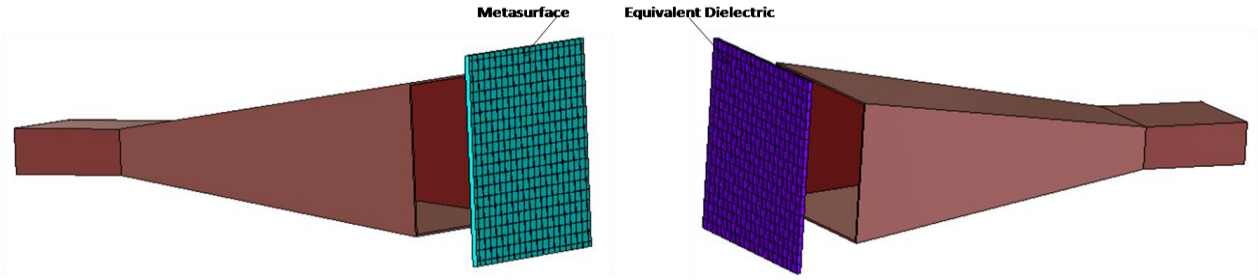

(a) (b)

Fig. 17. Horn antenna with different superstrates: (a) metasurface and (b) equivalent dielectric.

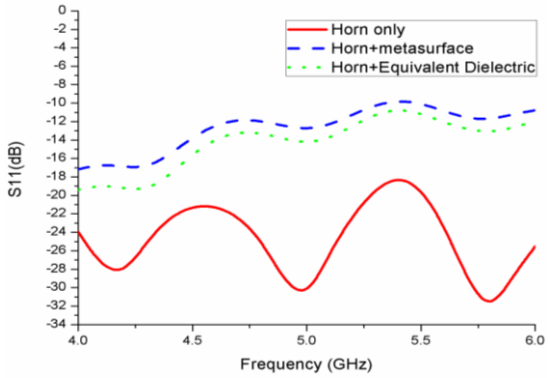

Fig. 18. Simulated S parameters of the horn antennas with different superstrate.

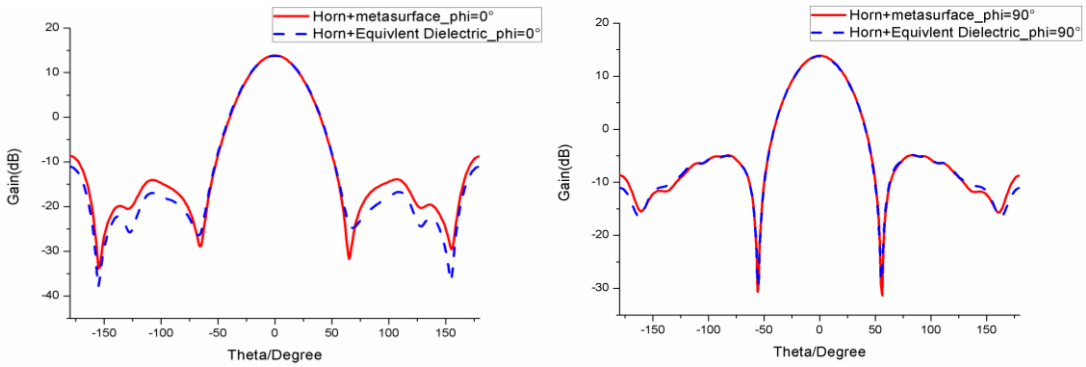

(a) (b)

Fig. 19. Simulated gain of the horn antennas with different superstrates at 5 GHz: (a) E-plane and (b) H-plane.

Table 2: Comparison of simulation times between the equivalent dielectric approach and the original design of horn antennas

	Antenna Only	**Horn+Metasurface**	**Horn+Equivalent Eielectric**	**Horn+2 Layers of Metasurface**	**Horn+2 Layers of Equivalent Dielectric**
Frequency range (GHz)	4-6	4-6	4-6	4-6	4-6
Gain (dB)	13.1	13.9	13.8	14.04	14.1
Simulation Time (hh:mm:ss)	00:03:30	02:20:00	00:06:00	16:17:00	00:12:00

Next, we turn to a geometry which is even more complex than the ones we have considered thus far. Figure 20 shows a 3x3 microstrip patch antenna array (MPA) covered by a metasurface superstrate comprising of 8*12 unit cell elements. Once again, we replace the superstrate with an equivalent dielectric slab, simulate the two configurations and compare the accuracies as well as relative numerical efficacies of the two approaches. Figures 21 and 22 show good agreement in both the results for the reflection coefficient as well as the radiations patterns, in both E-and H-planes, of the two antenna configurations depicted in Fig. 20. Table 3 compares the CPU time and RAM requirements of the original metasurface-based antenna array and its Equivalent Dielectric counterpart. We observe that the simulation time using the proposed approach decreases almost by a factor of 5, down to 15 hours from 73, and the max RAM required is also reduced to 24.4 GB from the original 91.3 GB.

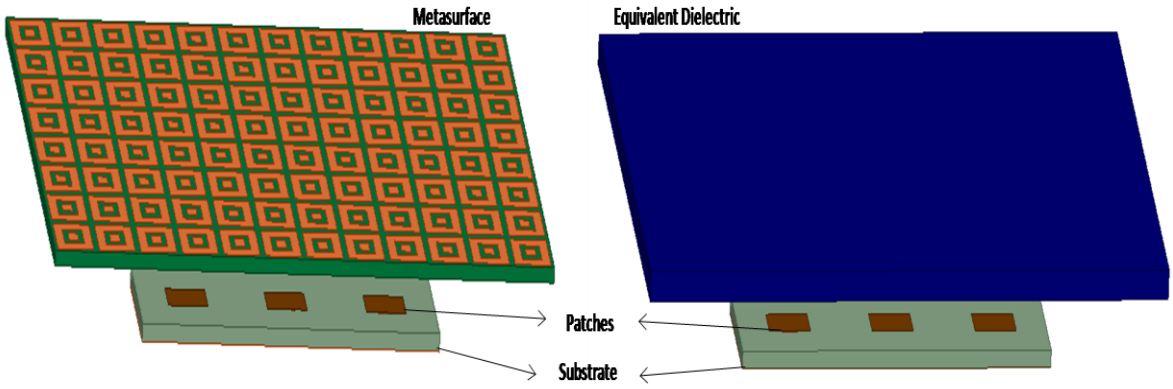

(a) (b)

Fig. 20. Three-element MPA with different superstrates: (a) metasurface and (b) equivalent dielectric (ED).

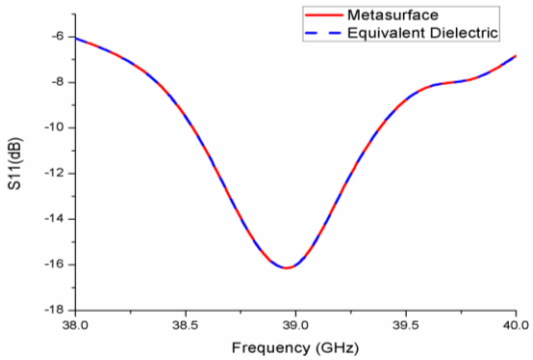

Fig. 21. Simulated S parameters of the three-element patch array with different superstrates.

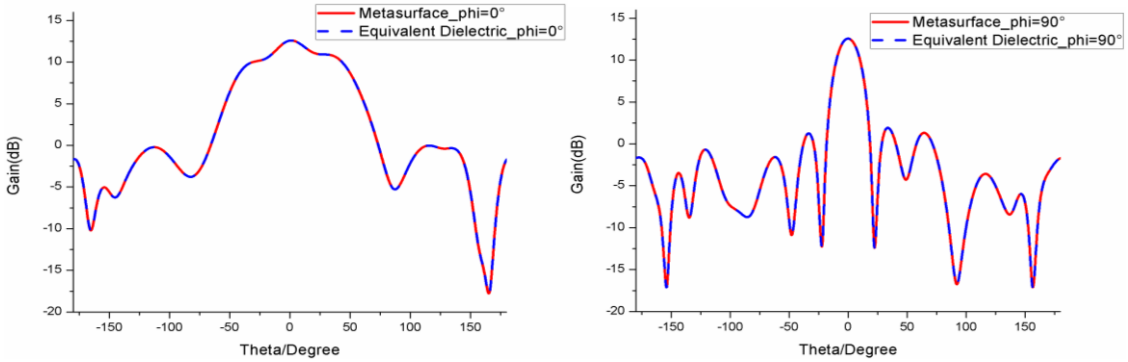

(a) (b)

Fig. 22. Simulated gain of the three-element patch with MTS and ED superstrates at 39 GHz: (a) E-plane and (b) H-plane.

Table 3: Comparison of CPU times and required RAM between the equivalent dielectric approach and the original design of metasurface superstrates antenna array

	Max RAM (GB)	**Real Time**	**CPU Time**
Three-element patch	1.04	0:14:04	0:13:59
Three element patch+Metasurface	91.3	72:55:04	95:51:09
Three element patch+Equivalent Dielectric	24.4	14:56:47	16:57:22

B. Flat lens application

For the final example, we consider a metamaterial-based flat lens, designed to replace the conventional convex dielectric lens to reduce the fabrication cost. The building block of the lens is shown in Fig. 24, which is a hollowed-out dielectric cuboid, and its Equivalent Dielectric model is shown in Fig. 23. So, our study displays that while the performances in terms of S_{11} of the horn and its gain enhancement with lens, shown in Figs. 25 and 26, respectively, are in good agreement over a broad frequency range of 12-18 GHz. However, the simulation time and memory requirement for the equivalent dielectric model are less by factors of 13x and 7x, respectively, than that for the original lens with air holes.

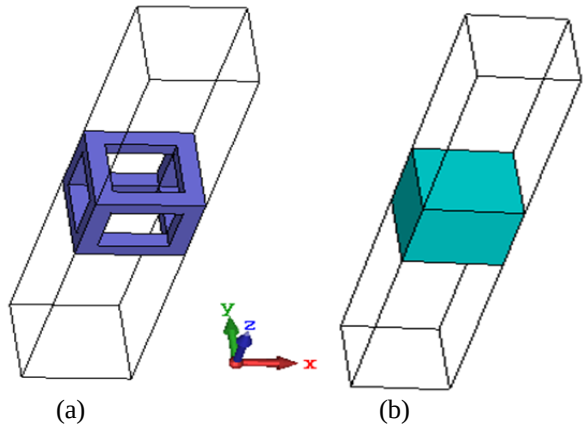

Fig. 23. Unit cell design: (a) dielectric with air hole, and (b) equivalent dielectric.

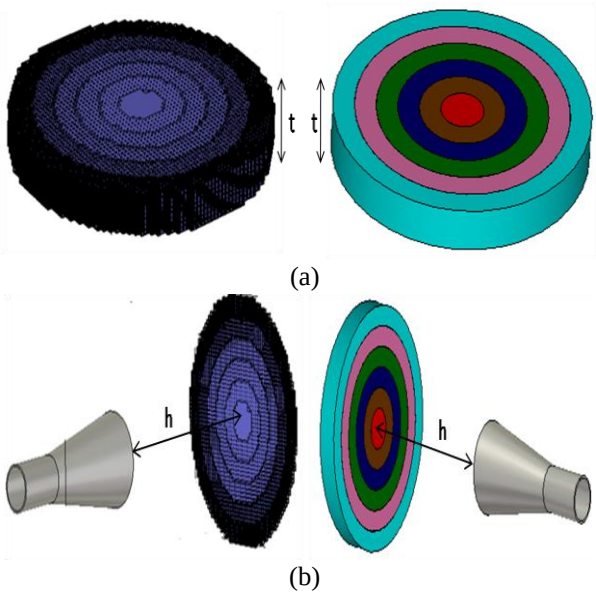

Fig. 24. Lenses with horn feed: (a) isometric view of flat lenses, and (b) lenses in front of the feed horn.

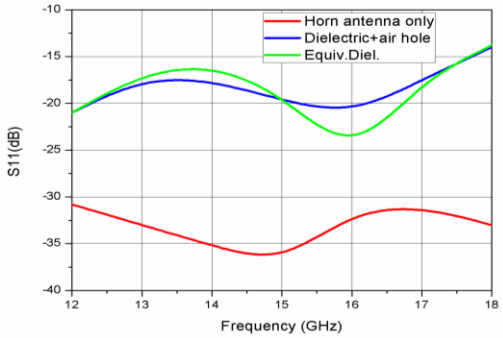

Fig. 25. S-parameters for horn and horn+lens combinations.

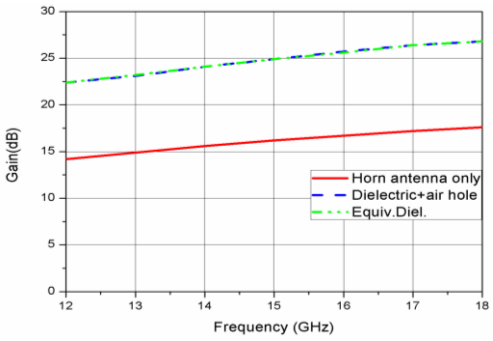

Fig. 26. Gain comparison of horn alone and horn+lenses.

IV. CONCLUSION

A novel approach for numerically efficient simulation of metamaterial- and metasurface-based antennas has been presented in this work. It relies on the use of an equivalent dielectric representation to characterize antennas with metasurfaces and metamaterials that are often multiscale in nature and, hence, are time-consuming and memory-intensive to simulate. Not only does the proposed approach offer a significant advantage over conventional brute-force type of techniques for multi-scale problems, it also assures that the accuracy of the results is not sacrificed in the process. The efficiency of the proposed ED method was tested for several different problems and it was found to yield accurate results while reducing the computational resources significantly. The reduction was 66% and 83%, respectively, for the single patch antenna and the 3x1 array, both with an MTS superstrate included for performance enhancement. For the horn antenna with single- and double-layer MTS covers, the computational resource requirement was reduced by factors of 23 and 162, respectively. Yet another significant advantage of the proposed technique is that the equivalent dielectric model can be directly inserted in commercial solvers; hence, no new special-purpose EM simulation code needs to be developed to handle multiscale problems when using the proposed approach.

ACKNOWLEDGEMENT

This project was funded in part by the Deanship of Scientific Research (DSR), King Abdulaziz University, Jeddah, Saudi Arabia, under Grant No. **RG-2-135-38**. The authors are pleased to acknowledge the technical and financial support from the DSR.

REFERENCES

[1] G. Minatti, M. Faenzi, M. Sabbadini, and S. Maci, "Bandwidth of gain in metasurface antennas," *IEEE Transactions on Antennas and Propagation*, vol. 65, no. 6, pp. 2836-2842, June 2017.

[2] M. Faenzi, G. Minatti, D. G.-Ovejero, F. Caminita, E. Martini, C. D. Giovampaola, and S. Maci, "Metasurface antennas: New models, applications and realizations," *A Nature Research Journal*, vol. 9, pp. 1-14, July 2019.

[3] A. A. Baba, R. M. Hashmi, and K. P. Esselle, "Achieving a large gain-bandwidth product from a compact antenna," *IEEE Transactions on Antennas and Propagation*, vol. 65, no. 7, pp. 3437-3446, July 2017.

[4] M. Imbert, J. Romeu, M. B.-Escudero, M.-T. Martinez-Ingles, J.-M. M. Garcia-Pardo, and L. Jofre, "Assessment of LTCC-based dielectric flat lens antennas and switched-beam arrays for future 5G millimeter-wave communication systems," *IEEE Transactions on Antennas And Propagation*, vol. 65, no. 12, pp. 6453-6473, Dec. 2017.

[5] A. Sayanskiy, S. Glybovski, V. Akimov, D. Filonov, P. Belov, and I. Meshkovskiy, "Broadband 3D Luneburg lenses based on metamaterials of radially diverging dielectric rods," *IEEE Antennas and Wireless Propagation Letters*, vol. 16, pp. 1520-1523, Jan. 2017.

[6] F. Caminita, E. Martini, G. Minatti, and S. Maci, "Fast integral equation method for metasurface antennas," *2016 URSI International Symposium on Electromagnetic Theory (EMTS)*, Sep. 2016.

[7] X. Liu, F. Yang, S. Xu, and M. Li, "Design method for modulated metasurface antennas composed of anisotropic elements based on generalized boundary conditions," *Antennas and Wireless Propagation Letters*, vol. 18, no. 9, pp. 1848-1852, July 2019.

[8] M. Bodehou, D. González-Ovejero, C. Craeye, and I. Huynen, "Method of moments simulation of modulated metasurface antennas with a set of orthogonal entire-domain basis functions," *IEEE Transactions on Antennas and Propagation*, vol. 1, no. 1, pp. 1-12, Jan. 2018.

[9] S. Sandeep and S. Y. Huang, "Simulation of circular cylindrical metasurfaces using GSTC-MoM," *IEEE Journal on Multiscale and Multi-physics Computational Techniques*, vol 3, pp. 185-192, Nov. 2018.

[10] M. A. Francavilla, E. Martini, S. Maci, and G. Vecchi, "On the numerical simulation of metasurfaces with impedance boundary condition integral equations," *IEEE Transactions on Antennas and Propagation*, vol. 63, no. 5, pp. 2153-2161, May 2015.

[11] M. Bodehou, C. Craeye, H.-B. Van, and I. Huynen, "Fourier-Bessel basis functions for the analysis of elliptical domain metasurface antennas," *IEEE Antennas and Wireless Propagation Letters*, vol. 1, pp. 1-4, 2018.

[12] F. Liang, G. W. Hanson, A. B. Yakovlev, G. Lovat, P. Burghignoli, R. Araneo, and S. A. H. Gangaraj, "Dyadic Green's functions for dipole excitation of homogenized metasurfaces," *IEEE Transactions on Antennas And Propagation*, vol. 64, no. 1, pp. 167-178, Jan. 2016.

[13] D. G.-Ovejero and S. Maci, "Gaussian ring basis functions for the analysis of modulated meta-surface antennas," *IEEE Transactions on Antennas and Propagation*, vol. 63, no. 9, pp. 3982-3993, 2018.

[14] Y. Vahabzadeh , N. Chamanara, K. Achouri, and C. Caloz, "Computational analysis of meta-surfaces," *IEEE Journal on Multiscale and Multiphysics Computational Techniques*, vol 3, pp. 37-49, Apr. 2018.

[15] D. R. Smith, S. Schultz, P. Markos, and C. M. Soukoulis, "Determination of effective permittivity and permeability of metamaterials from reflection and transmission coefficients," *Physical Review B*, vol. 65, Apr. 2002.

[16] X. Chen, T. M. Grzegorczyk, B.-I. Wu, J. Pacheco, Jr., and J. A. Kong, "Robust method to retrieve the constitutive effective parameters of metamaterials," *Physical Review E*, vol. 70, 016608, 2004.

[17] D. R. Smith, D. C. Vier, T. Koschny, and C. M. Soukoulis, "Electromagnetic parameter retrieval from inhomogeneous metamaterials," *Physical Review E*, vol. 71, 036617, 2005.

[18] A. Nasri, R. Mittra, H. Rmili, "Categorizing metamaterials by using equivalent dielectric approach," *2019 IEEE International Symposium on Antennas and Propagation and USNC-URSI Radio Science Meeting*, Oct. 31, 2019.

[19] A. Nasri and R. Mittra, "A numerically efficient technique for the analysis of metamaterial- and metasurface-based antennas," *2020 14th European Conference on Antennas and Propagation (EuCAP)*, July 8, 2020.

[20] A. Yahyaoui and H. Rmili, "Chiral all-dielectric metasurface based on elliptic resonators with circular dichroism behavior," *International Journal of Antennas and Propagation*, vol. 2018, pp. 1-7, 2018.

Focusing Technique for Holographic Subsurface Radar Based on Image Entropy

Haewon Jung*, Dal-Jae Yun, and Hoon Kang

Advanced Instrumentation Institute
Korea Research Institute of Standards and Science, Daejeon, 34113, Republic of Korea
*haewon.jung@kriss.re.kr, daljae.yun@kriss.re.kr, hkang@kriss.re.kr

Abstract ─ An image focusing method for holographic subsurface radar (HSR) is proposed herein. HSR is increasingly being utilized to survey objects buried at shallow depths and the acquired signals are converted into an image by a reconstruction algorithm. However, that algorithm requires actual depth and material information or depends on human decisions. In this paper, an entropy-based image focusing technique is proposed and validated by numerical simulation software package based on finite-difference time-domain method and experiment. The resulting images show good agreement with the actual positions and shapes of the targets.

Index Terms ─ Autofocusing, entropy, holographic subsurface radar, image reconstruction.

I. INTRODUCTION

Subsurface radar techniques are being widely used to image and identify concealed structures and objects. Typically for these tasks, two types of subsurface radar techniques are used: ground penetrating radar (GPR) and holographic subsurface radar (HSR) [1, 2].

The GPR technique is commonly utilized to investigate subsurface regions using impulse or ultra-wideband signals, because these signals can effectively penetrate subsurface materials. However, in a shallow region, reconstructed GPR images suffer from ghost images caused by multiple reflections. For these reasons, the HSR technique is increasingly being applied for subsurface imaging in shallow regions. This is due to its features of high resolution and freedom from multiple reflections between radiator and target, or from the target itself [3, 4].

Recently, the HSR technique has been actively researched for detection and imaging of subsurface objects such as defects in insulation forms, landmines, building structures, and weapons [5–9]. With HSR, the radar image is gathered at a plane located above the plane of the object of interest. Due to the gap between the measuring and object plane, which is filled with air or dielectric material, a raw image resulting from the survey on the measuring plane can be reconstructed using the proper algorithms [3, 5].

For proper algorithm processing, the depth of the object plane and relative permittivity (RP) of the subsurface materials are required to obtain a clear image. However, the RP may not be known exactly in a survey environment, so whether the radar image is clear and well-focused is judged by the operator. In this paper, we apply an entropy-based image focusing method to reconstruct automatically an HSR image when subsurface materials and depth of the target are unknown.

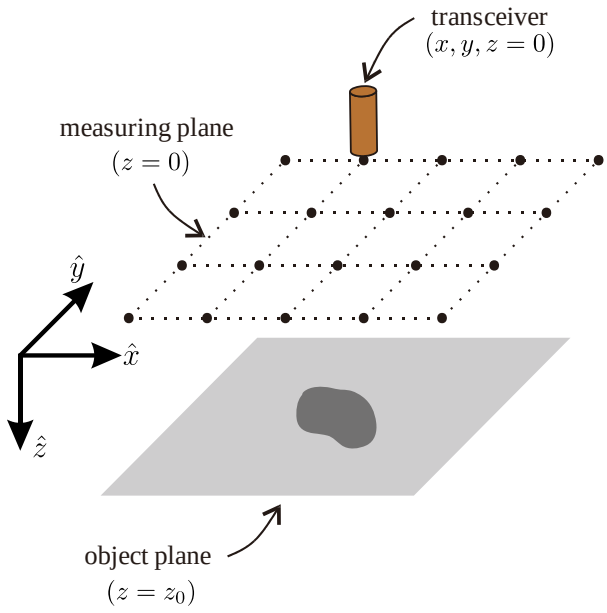

Fig. 1. Geometry for HSR image data acquisition model.

II. HOLOGRAPHIC SUBSURFACE RADAR IMAGING

The HSR technique configures a subsurface region as a plan-view image, which originated as an optical holography technique proposed by Gabor [10]. Details of the HSR principles and equations are described in recent research [1–8].

Submitted On: October 26, 2020
Accepted On: March 14, 2021
https://doi.org/10.47037/2020.ACES.J.360402

The method calls for acquisition of raw data in a two-dimensional (2D) geometry that can be modelled as shown in Fig. 1. The transceiver, typically an open-end waveguide with rectangular or circular shape, surveys the measuring plane in uniform sweeps in the *x* and *y* directions.

The raw image produced directly from the raw data has a look similar to that of the actual objects because the electromagnetic wave propagating through the open-end waveguide is highly attenuated outside of the waveguide [3]. Nevertheless, the raw data can be focused to provide a clear image using the reconstruction algorithms.

The raw data is composed of complex amplitudes depending on the *x* and *y* position; and they should be obtained at single or multiple frequency points. Then the raw data can be represented as $u(x, y, z = 0)$ and $u(x, y, z = 0, \omega)$ at a single and multiple frequency points respectively, where $x = x_1, x_2, \dots, x_m$ and $y = y_1, y_2, \dots, y_n$ positions, and $\omega = \omega_1, \omega_2, \dots, \omega_p$. The spatial sampling intervals Δx and Δy must be less than quarter wavelength to satisfy the Nyquist criterion [2]. Then the spectral sampling intervals can be defined by the spatial ones.

In the case of a single frequency, the raw data can be reconstructed as image $p(x, y, z = z_0)$ using equation (1), as follows:

$$p(x, y, z = z_0) = \mathrm{FFT}_{2D}^{-1}\begin{bmatrix}\mathrm{FFT}_{2D}[u(x, y, z = 0)] \\ \times\, e^{jk_z z_0}\end{bmatrix}. \quad (1)$$

In the multiple frequency case, the raw data $u(x, y, z = 0, \omega)$ can be reconstructed as image $p(x, y, z)$ using equation (2), as follows:

$$p(x, y, z) = \mathrm{FFT}_{3D}^{-1}\begin{bmatrix}\mathrm{FFT}_{2D}[u(x, y, z = 0, \omega)] \\ \times\, e^{jk_z z}\end{bmatrix}, \quad (2)$$

where k_z is defined from dispersion relations taking into account backward wave propagation, as shown in equation (3) [3, 8]:

$$k_z = \sqrt{4k^2 - k_x^2 - k_y^2} = \sqrt{4\left(\omega\sqrt{\varepsilon}/c\right)^2 - k_x^2 - k_y^2}. \quad (3)$$

Note that, in the multiple frequency reconstruction, the k_z vector should be interpolated to the uniform space to use the fast Fourier transform technique [6].

In equations (1–3), the variables affecting the focused image quality are the depth and material RP. Typically, to find the best focused image, a reconstruction algorithm is iteratively applied while a person checks the image quality while varying the depth and RP.

III. ENTROPY BASED HSR IMAGE FOCUSING METHOD

Autofocus is an essential technique for image-based systems. In particular, a passive autofocus system assessing an image by itself employs many kinds of image evaluation metrics. Among them, entropy is a commonly used metric that includes optical imaging, synthetic aperture radar imaging, and microscopy imaging [11–16]. When an image is represented in 2D space as $u(x_i, y_j)$, where, i = 1, 2, ..., m and j = 1, 2, ..., n, the image entropy can be obtained as follows:

$$\mathrm{E} = -\sum_{i=1}^{m}\sum_{j=1}^{n}\alpha(x_i, y_j)\ln\left[\alpha(x_i, y_j)\right], \quad (4)$$

where $\alpha(x_i, y_j) = \frac{|u(x_i, y_j)|^2}{\sum_{i=1}^{m}\sum_{j=1}^{n}|u(x_i, y_j)|}$.

Entropy based HSR reconstruction algorithm:

for all points (ω, z) {
  compute $\mathrm{E}(\omega, z)$ *using* (1) *and* (4)
}
for all ω {
  compute $\mathrm{E}_{\mathrm{diff}}(\omega)$
}
find optimum angular frequency ω_o *from* $\mathrm{E}_{\mathrm{diff}}(\omega)$
find optimum depth z_o *from* $\mathrm{E}(\omega = \omega_o, z)$

image reconstruction using ω_o, z_o, *and* (1) *or* (2)

Fig. 2. Summary of the entropy based HSR reconstruction algorithm.

In this paper, we iteratively applied an entropy metric to the HSR reconstruction algorithm. When we assumed the RP was a free space, we could adjust the image using only the depth values. For single frequency data, entropy values were evaluated as $\mathrm{E}(z)$ within $z = 0, \Delta z, 2\Delta z, \dots, N\Delta z$. Then, the depth value representing maximum entropy was selected as the optimum value. Note that the entirely evaluated entropy values were stored in the $\mathrm{E}(z)$ along the depth increments. Therefore, the optimum value can be selected from whole values regardless of the local optimums may exist.

Compared with single frequency data, multiple frequency data have the advantage of a greater amount of information. In this case, the same process used with the single frequency data was repeated for all the angular frequencies. The resulting entropy values form a 2D matrix $\mathrm{E}(\omega, z)$. In this matrix, the optimal frequency and depth can be obtained by the following procedures. Firstly, differences between the maximum and minimum entropy were calculated for all the angular frequency values, and represented as $\mathrm{E}_{\mathrm{diff}}(\omega)$. Then, the angular frequency value ω_c of the maximum difference among all the differences calculated for each frequency could be chosen and the remainder of the process was identical to that for single frequency data. The entropy-based HSR reconstruction algorithm can be summarized as in Fig. 2.

Since the penetrating depth of the HSR is typically one to two wavelength, the proposed method also can be applied in the range [2, 8]. Moreover, computational complexity of the proposed method may be represented as $O(kMN\log(MN))$ when assuming image pixels as $N \times M$ and depth intervals as k.

IV. NUMERICAL AND EXPERIMENTAL VALIDATIONS

A. Numerical validation

The proposed method was validated by numerically surveyed data. The data was produced using a gprMax software package that is based on the finite difference time domain (FDTD) method [17]. Because of the gprMax offers CUDA based graphical processing unit operation, that is proper to gather 2D geometrical data in an efficient manner [18].

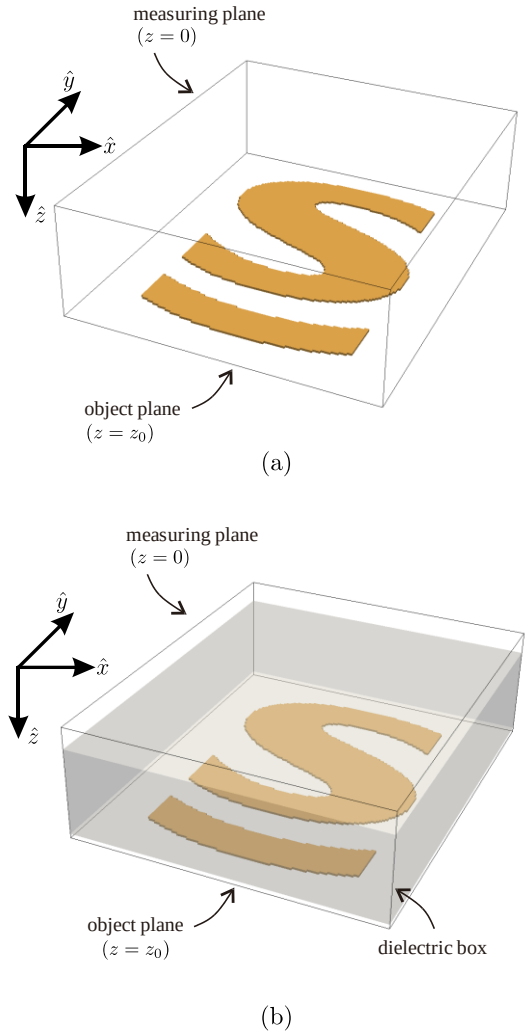

Fig. 3. Geometries for numerical validation: (a) only copper sheet target placed below the array, and (b) dielectric box placed above the copper sheet target.

In the validation, two geometries were surveyed using a copper sheet target with a special shape of letter 'S' as illustrated in Fig. 3. One is only target placing 5 cm below the surveyed array and another is dielectric box was covered with the target, where the box was composed by four RP material with 4 cm thickness. The surveyed array covers from -9 cm to +9 cm with 0.2 cm increment both in *x* and *y* directions configuring 91 × 91 array. The numerical geometry was modeled as 400 × 400 × 140 cells with 5 mm steps in *x*, *y*, and *z* directions. In the model, 1040 iterations were performed with 0.963 ns time step. And a differentiated Gaussian source with 20 GHz peak frequency was used as a point source for each acquisition of the array.

The numerically obtained data can be represented as raw images at an acquisition plane as represented in Figs. 4 (a) and (c), and reconstructed images at an object plane using the proposed method as represented in Figs. 4 (b) and (d). In the reconstruction process, the depth increments were arranged from 0 to 10 cm with 0.01 cm steps.

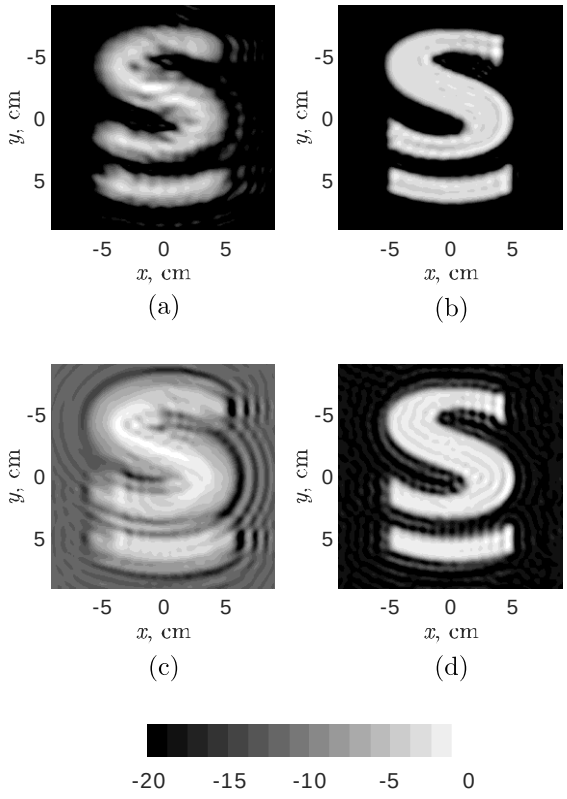

Fig. 4. Raw and reconstructed images using the proposed method via numerically obtained data: (a) raw image of target only geometry at 19.76 GHz, (b) reconstructed image of target only geometry, (c) raw image of target with dielectric box geometry at 20.49, and (d) reconstructed image of target with dielectric box geometry.

Table 1: Calculated optimal frequency and depth values of numerical validation

Target	f_o (GHz)	z_o (cm)
Free space	19.76	5.03
With dielectric box	20.49	2.59

Calculated results of optimal frequency and depth values are represented in Table 1. Compared to the raw and reconstructed images, the focused images are matched with the actual shape and position. Note that the second geometry case, optimal depth is decreased by effect of the dielectric box between surveying array and target.

B. Experimental validation

The proposed method was validated experimentally. A monostatic HSR system was made that included a vector network analyzer, three-dimensional position scanner, and a rectangular waveguide with open-end shape. The survey frequency range was from 18.5 to 19.5 GHz with 10 MHz steps. Two experiments were conducted by scanning letters with 'S' and 'ST' shapes made of silicon 2 cm thick, as shown in Fig. 5.

In the first experiment, the letter 'S' was placed 1.5 cm below the open-end of the waveguide. The scanning range was from -15 to +15 cm with steps of 0.5 cm in both the x and y directions. In the second, experiment, 'S' and 'T' were placed 6.5 and 3.5 cm below the waveguide, respectively. The scanning ranges were -35 to +35 cm and -20 to +20 cm, with 0.5 cm steps in the x and y directions, respectively.

The raw images and images reconstructed using the proposed focus method, are shown in Figs. 6 and 7. In the reconstruction process, the depth increments were arranged from 0 to 8 cm with 0.01 cm steps. The calculated entropies according to the depth increment are represented in Fig. 8. In Figs. 6 (a), 7 (a), and 7 (c), the raw images are illustrated at a single frequency calculated in the reconstruction process. In the first experiment, the optimal depth and frequency for a single target was obtained and the images were reconstructed using the depth value at single and multiple frequencies. In the second experiment, the letters were placed at different depths. Thus, the focus process was applied twice for each letter 'S' and 'T'. The results from calculation of the optimal frequency and depth values are represented in Table 2. In the table, the depth values are matched to the actual depth of the target. Compared to the raw images, each reconstructed image of a letter shows fewer layers in the shape. This reduction of the layering leads to better focused images with increased sharpness. This shows that the proposed method works well for automated focusing of HSR images.

Table 2: Calculated optimal frequency and depth values of experimental validation

Target	f_o (GHz)	z_o (cm)
'S' only	18.81	1.53
'S' of 'ST'	19.29	6.89
'T' of 'ST'	18.56	3.58

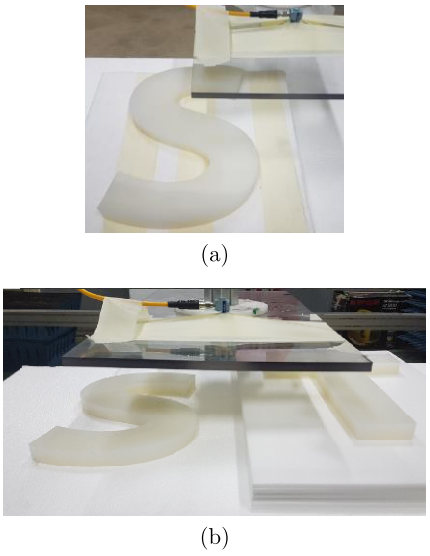

Fig. 5. Experimental setup for measuring letter 'S' and letters 'ST'.

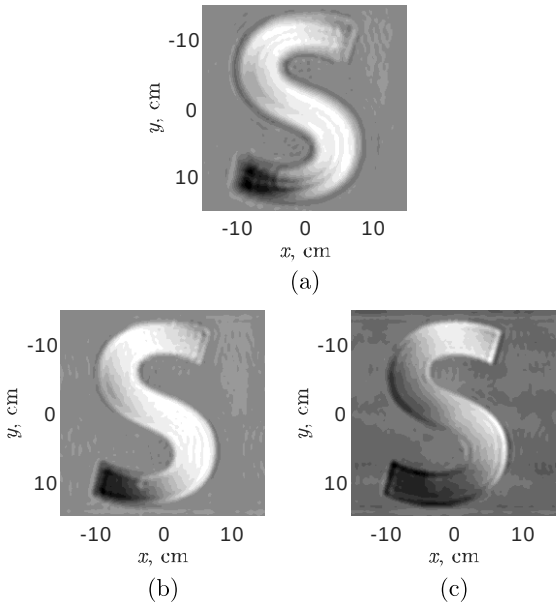

Fig. 6. Raw and reconstructed images using the proposed method: (a) raw image of letter 'S' at 18.81 GHz, (b) reconstructed image of 'S' at 18.81 GHz, and (c) reconstructed image of letter 'S' at multiple frequencies.

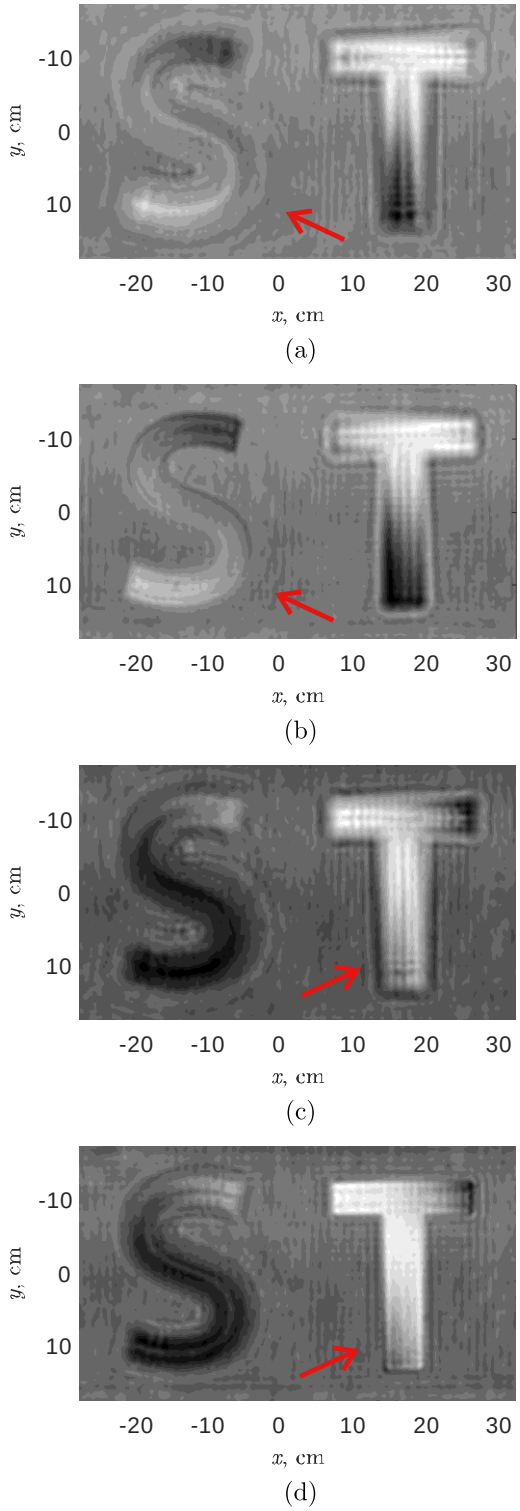

Fig. 7. Raw and reconstructed images using the proposed method: (a) raw image of letters 'ST' at 19.29 GHz, (b) reconstructed image of letter 'ST' focused on 'S' at 19.29 GHz, (c) raw image of letters 'ST' at 18.56 GHz, and (d) reconstructed image of letter 'ST' focused on 'T' at 18.56 GHz.

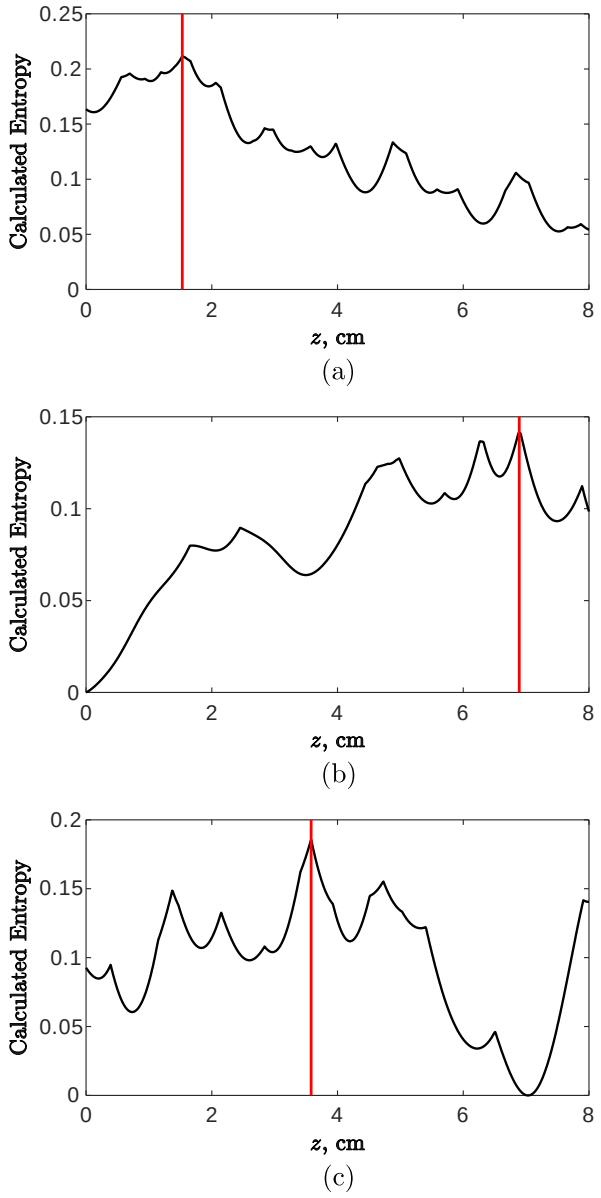

Fig. 8. Calculated entropies according to depth increment: (a) target placed 1.5 cm below, (b) target placed 6.5 cm below, and (c) target placed 3.5 cm below.

V. CONCLUSION

In this paper, an HSR image focusing method was proposed for evaluating images based on an entropy metric. The proposed method iteratively finds the optimal frequency and depth of target objects by assuming the subsurface materials to be free space. For each iteration, the reconstructed image was obtained varying frequency and depth value, and the optimum values were determined through the image evaluation results. The method was validated numerically and experimentally. The numerical validation was used a FDTD based gprMax software package and experimental

validation was used an HSR system configured at a laboratory level. The reconstructed images similarly illustrated the actual shapes of the targets. Thus, the proposed method appears helpful for automated focusing of HSR images.

ACKNOWLEDGMENT

This research was supported by Development of Core Technologies for Advanced Measuring Instruments funded by Korea Research Institute of Standards and Science (KRISS – 2021 – GP2021-0009).

REFERENCES

[1] J. D. Taylor, *Ultrawideband Radar Applications and Design*. CRC Press, Boca Raton, FL, 2012.

[2] J. D. Taylor, *Advanced Ultrawideband Radar Signals, Targets, and Applications*. CRC Press, Boca Raton, FL, 2017.

[3] S. Ivashov, V. Razevig, I. Vasiliev, T. Bechtel, and L. Capineri, "Holographic subsurface radar for diagnostics of cryogenic fuel tank thermal insulation of space vehicles," *NDT & E International*, vol. 69, pp. 48-54, 2015.

[4] S. I. Ivashov, I. A. Vasiliev, T. D. Bechtel, and C. Snapp, "Comparison between impulse and holographic subsurface radar for NDT of space vehicle structural material," *PIERS Online*, vol. 3, no. 5, pp. 658-661, 2007.

[5] A. Zhuravlev, S. Ivashov, I. Vasiliev, and V. Razevig, "Processing of holographic subsurface radar data," in *Proc. 14th Int. Conf. Ground Penetrat. Radar (GPR)*, Shanghai, China, June 4-8, 2012.

[6] J. T. Case, F. L. Hepbum, and R. Zoughi, "Inspection of spray on foam insulation (SOFI) using microwave and millimeter wave synthetic aperture focusing and holography," in *Proc. IEEE Instrum. Meas. Technol. Conf. (I2MTC)*, Sorrento, Italy, Apr. 24-27, 2006.

[7] S. Ivashov, A. Zhuravlev, M. Chizh, and V. Razevig, "High resolution MW holographic system for NDT of dielectric materials and details," in *Proc. 16th Int. Conf. Ground Penetrat. Radar (GPR)*, Hong Kong, June 13-16, 2016.

[8] S. I. Ivashov, V. V. Razevig, I. A. Vasiliev, A. V. Zhuravlev, T. D. Bechtel, and L. Capineri, "Holographic subsurface radar of RASCAN type: Development and applications," *IEEE J. Sel. Topics Appl. Earth Observ. Remote Sens.*, vol. 4, no. 4, pp. 763-778, 2011.

[9] D. M. Sheen, D. L. McMakin, and T. E. Hall, "Three-dimensional millimeter-wave imaging for concealed weapon detection," *IEEE Trans. Microw. Theory Techn.*, vol 49, no. 9, pp. 1581-1592, 2001.

[10] D. Gabor D, "A new microscopic principle," *Nature*, vol. 161, no. 4098, pp. 777-778, 1948.

[11] X. Wei and Y. Zhang, "Autofocusing techniques for GPR data from RC bridge decks," *IEEE J. Sel. Topics Appl. Earth Observ. Remote Sens.*, vol. 7, no. 12, pp. 4860-4868, 2014.

[12] R. L. Morrison, M. N. Do, and D. C. Munson, "SAR image autofocus by sharpness optimization: A theoretical study," *IEEE Trans. Image Process.*, vol. 16, no. 9, pp. 2309-2321, Sep. 2007.

[13] F. Ahmad, M. G. Amin, and G. Mandapati, "Autofocusing of through the-wall radar imagery under unknown wall characteristics," *IEEE Trans. Image Process.*, vol. 16, no. 7, pp. 1785-1795, July 2007.

[14] L. Xi, L. Guosui, and J. Ni, "Autofocusing of ISAR images based on entropy minimization," *IEEE Trans. Aerosp. Electron. Syst.*, vol. 35, no. 4, pp. 1240-1252, Oct. 1999.

[15] S. Podlech S, "Autofocus by Bayes spectral entropy applied to optical microscopy," *Microscopy and Microanalysis*, vol. 22, no. 1, pp. 199-207, 2016.

[16] S. Yazdanfar, K. B. Kenny, K. Tasimi, A. D. Corwin, E. L. Dixon, and R. J. Filkins, "Simple and robust image-based autofocusing for digital microscopy," *Optics Express*, vol. 16, no. 12, pp. 8670-8677, 2008.

[17] C. Warren, A. Giannopoulos, and I. Giannakis, "gprMax: Open source software to simulate electromagnetic wave propagation for ground penetrating padar," *Computer Physics Communications*, vol. 209, pp. 163-170, 2016.

[18] C. Warren, A. Giannopoulos, A. Gray, I. Giannakis, A. Patterson, L. Wetter, and A. Hamrah, "A CUDA-based GPU engine for gprMax: Open source FDTD electromagnetic simulation software," *Computer Physics Communications*, vol. 237, pp. 208-218, 2018.

New Approach of Efficiency Improvement in 10 dB Doherty Power Amplifier for 4G LTE and 5G Wireless Applications

Suganthi Santhanam [1] and Palavesam Thiruvalar Selvan [2]

[1] Department of Electronics and Communication Engineering
K. Ramakrishnan College of Technology, Trichy, Tamilnadu-621 112, India
tvssugi@gmail.com, suganthis.ece@krct.ac.in

[2] Department of Electronics and Communication Engineering
SRM TRP Engineering College, Trichy, Tamilnadu, India
thriuvalar@gmail.com

Abstract ─ In this research article, the design procedure and comparative analysis of the 10 dB Doherty power amplifier (DPA) with single and double auxiliary amplifier for maximum efficiency has been presented. A new Doherty amplifier structure with parallel two auxiliary amplifiers based on conventional design having optimum value of load resistance of 3.162 ohm has been proposed with higher efficiency of 85.803% and analyzed with n-tone sinusoidal signal. The proposed Doherty power amplifier can achieve drain efficiency of 83.299% & with single and 85.803% with dual auxiliary amplifier at the output power back, off of 10 dB from the saturated power point. The simulated outputs are matched with mathematically derived design values. The simulated n-tone time response shows that the proposed design of DPA can able to handle different modulation standards at different frequencies with compatible structure.

Index Terms ─ Auxiliary amplifier, Doherty power amplifier, efficiency, peak to average power ratio, transceiver, wireless communication.

I. INTRODUCTION

Present wireless industry moving towards 5G communication placed RF transceiver in the proximity of each antenna in MIMO (Multiple Input Multiple Output) system of high data rate and connectivity [1]. To achieve linear performance from power amplifier [2], it should be operated at far back-off level for high data rate enhancement. The modulation envelope in such mobile communication method can be measured by Peak – to – Average Power Ratio (PAPR) [3]. For higher PAPR, the power amplifiers (PAs) should be operated at a larger back off power level from saturation and in wideband [1]. 5G evaluation in modern wireless communication requires multi band [4] operable power amplifier (PAs) with high efficiency. Due to mature implementation and simple in structure [5-6], Doherty Power Amplifier (DPA) is widely used at GHz frequencies than other amplifier configuration such as envelope tracking and out phasing power amplifier [7].

DPA invented in [5] has been popular for the design of power amplifier [8] due to simple topology, self sufficient (no need of external circuit fro efficiency control), efficient amplification with linearity and large PAPR [9] to reduce the energy consumption in 5G communication. The conventional DPA consists of main and auxiliary amplifiers connected by common load with quarter wave transformer. Generally power amplifier is operated at saturation for higher efficiency at which the small increase in input power can push the amplifier from the linear mode to the saturated mode. To ensure the amplifier to operate in linear region we lower the power level from maximum efficiency point. This power level lower is called as power back – off (PBO). The PBO of symmetric DPA is 6 dB while the PAPR of 4G LTE [10] signal is 6 dB to 12 dB. Hence, to fulfill the requirement of 4G and 5G [11], [12] communication, various techniques like linearity and power added efficiency [13], power control technology [14], asymmetric structure [15] and harmonic injection [16] have been introduced to replace symmetric DPA's with extended PBO region. Among these, alternative asymmetric structure is mostly preferred due to its simple design process and structure.

Asymmetric Doherty power amplifier (ADPA) consists of main and auxiliary amplifier in two classes with power divider and power combiner. Generally, class B PA for main amplifier and class C PA biasing for auxiliary amplifiers are mostly preferred and theoretically discussed in [17]. This conventional ADPA can be operated at average output transmitted power in 9 - 12 dB range below the maximum power. It is possible to combine the output power of many PAs to increase the linearity, larger the PBO and to maintain the efficiency

Submitted On: November 4, 2020
Accepted On: March 4, 2021
https://doi.org/10.47037/2020.ACES.J.360403

[18] throw out the back off region. This configuration is called as "multistage DPA". In this paper, we have proposed a comprehensive discussion on efficiency enhancement for DPA and for thorough understanding of high efficiency DPA design for 5G wireless transmitters. This paper proposed the comparison of 10 dB back off power DPA with single and double auxiliary amplifier for efficiency improvement as compared to [19]. The proposed DPA with two auxiliary amplifiers delivers power added efficiency (PAE) of 85.803% with output power of 25.04 dB under n-tone test. Design equation for calculating efficiency has been elaborated and mapped with simulation parameters to give insight from theory to practical implementation.

II. THEORY AND DESIGN OF DPA

Power amplifier gains more attention now a day for wideband [19], low cost and high integration applications [20]. It is common in mobile communication to operate the power levels of 10 – 40 dB back off from peek power.

A. Structure of 10 dB DPA

In DPA, the drain current in main amplifier increases linearly from initial value since biased in class B mode. But in auxiliary amplifier drain current does not flow after certain value of input voltage since biased in class C mode. The auxiliary amplifier current starts to increase beyond threshold value (X) with respect to input voltage. In this design, the auxiliary class C amplifier is biased such that no current flows below X=0.3. The output of main amplifier is connected to input of auxiliary amplifier through quarter wave transformer [19] QWT to compensate for a 90° in main amplifier. Both transistors are operated as dependent current source with main amplifier saturate at high power at which auxiliary amplifier is in off state. Hence, the linearity of overall amplifier is improved for high efficiency at high input power level. The block diagram and the equivalent circuit of basic DPA are shown in Figs. 1 (a) & (b) respectively. In Fig. 1 (a), the quarter-wave transformer which connects the output of the main power amplifier and the input of the auxiliary amplifier is used to compensate for a 90c phase shift introduced by the transformer in the main amplifier.

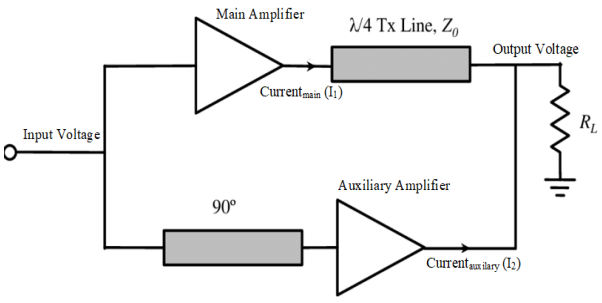

(a)

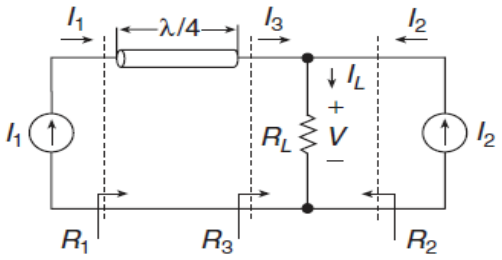

(b)

Fig. 1. Doherty power amplifier: (a) block diagram and (b) equivalent circuit.

In Fig. 1 (b), both amplifiers are represented as current source I_1 & I_2 with load resistance r1 and r3 as the load resistance seen by the drain and source with and without quarter-wave transmission line transformer as an impedance inverter. In Fig. 1 (b), the load resistance is to be increased to maintain the fundamental output voltage as constant. This is achieved by QWT as impedance inverter which is connected between the load R_L and the current source I_1. The relationship between R_1 and R_3 is given by:

$$R_1 = \frac{Z_0^2}{R_3}, \tag{1}$$

where Z_0 is the characteristics impedance of QWT, R_1 is the load resistance of current source I_1 (Main amplifier). The load resistance of current source I_2 (auxiliary amplifier) is given by:

$$R_2 = R_L\left(1+\frac{I_3}{I_2}\right). \tag{2}$$

B. Calculation of efficiency

In order to analyze the combined effect of main and auxiliary amplifiers and to analyze the efficiency, the two amplifiers current sources equivalent circuit model has been used. The simplified equivalent model of main and auxiliary current sources (I_1 and $-jI_2$) has been drawn in Fig. 2.

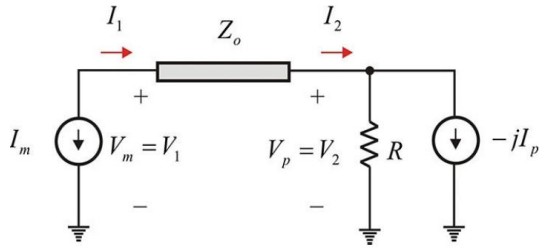

Fig. 2. Doherty amplifier output simplified model.

The drain current from main and auxiliary amplifiers are with 90° phase delay introduced by QWT represented by –j. The ABCD parameter of QWT is given by:

$$\begin{pmatrix} V_1 \\ I_1 \end{pmatrix} = \begin{pmatrix} 0 & jZ_0 \\ jZ_0 & 0 \end{pmatrix} \begin{pmatrix} V_2 \\ I_2 \end{pmatrix}. \quad (3)$$

V_1 can be expressed as:

$$\begin{aligned} V_1 &= jZ_0 I_2 = jZ_0 \left(\frac{V_2}{R} - jI_2 \right) \\ &= -I_1 \frac{Z_0^2}{R} + Z_0 I_2. \end{aligned} \quad (4)$$

Let X is the normalized input voltage at which the main and auxiliary amplifier switches between active and saturation for contributing efficiency. The value of Z_o^2/R is selected in such that X = 0.3 V, the efficiency of DPA becomes the efficiency of main amplifier alone since the auxiliary amplifier is in off state for below X = 0.3. For the above the value of X = 0.3, the auxiliary amplifier turns on for current I_2 to flow and main amplifier is in saturation state. Hence, the efficiency of DPA is:

$$\eta_{DPA/10dB} = \begin{Bmatrix} \eta_1 & X < 0.3 \\ \eta_2 & X > 0.3 \end{Bmatrix}, \quad (5)$$

where η_1 and η_2 depends on I_1 and I_2 in the normalized input voltage X range (0 < X < 1). I_1 and I_2 can be expressed as:

$$\begin{aligned} I_1 &= X \\ I_2 &= \begin{Bmatrix} 0 & X < 0.3 \\ 2(X - 0.3) & X > 0.3 \end{Bmatrix}. \end{aligned} \quad (6)$$

From the equation (4), we found that these two currents are opposite to each other and cancel out each other. This cancellation is done to make the two current terms that have the same slopes for X. But the slope of I_2 is 3.162 for X, and hence Z_o^2/R should be equal to 3.162 Z_o to cancel out each other, and hence Z_0 = 3.162xR. The efficiency of DPA can be calculated by Fourier series analysis of class B and class C PAs. Using Fourier series, the DC current component of main amplifier is expressed as:

$$I_0 = \frac{I_{RF}}{\pi} (\sin\theta - \theta\cos\theta) = I_{RF}\, \gamma_0, \quad (7)$$

$$\text{where} \quad \theta = \pm\cos^{-1}\left(\frac{I_q}{I_{RF}} \right). \quad (8)$$

Where Iq and I_{RF} are the DC quiescent in the absence of RF and fundamental drain current. The fundamental wave component of I_1 is given by:

$$I_1 = \frac{I_{RF}}{2\pi} (2\theta - \sin 2\theta) = I_{RF}\, \gamma_1. \quad (9)$$

The DC component of main and auxiliary amplifier are expressed as:

$$\begin{aligned} I_{10} &= \frac{2}{\pi} I_1 \\ I_{20} &= I_2 \frac{\gamma_0(\theta)}{\gamma_1(\theta)}, \end{aligned} \quad (10)$$

where conduction angle θ = $\cos^{-1}$ (0.3). From these two current components, we can get the DC power input expressed as:

$$P_{DC} = P_{in} = I_{10} + I_{20}. \quad (11)$$

This is the normalized DC power input to DPA by setting the DC supply to 1. The RF power output by two amplifiers due to this input power is given by:

$$P_{RF} = P_{out} = \frac{1}{2}(V_1 I_1 + V_2 I_2). \quad (12)$$

From equations (11) and (12), the efficiency of DPA is calculated as:

$$\%\eta = \frac{P_{RF}}{P_{DC}} x100. \quad (13)$$

III. SIMULATION STRUCTURE AND ITS PARAMETERS

The Advanced Design System (ADS) structure that used for simulation of Doherty Power Amplifier (DPA) for 10 dB PBO for high frequency is shown in Fig. 3.

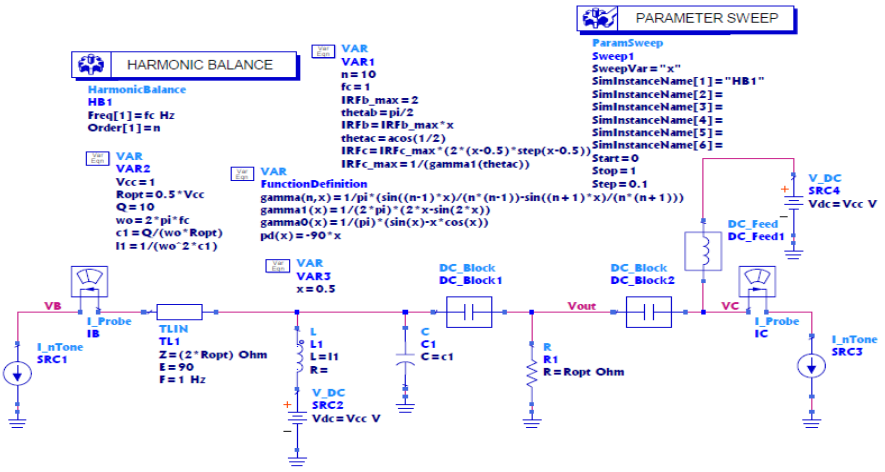

(a)

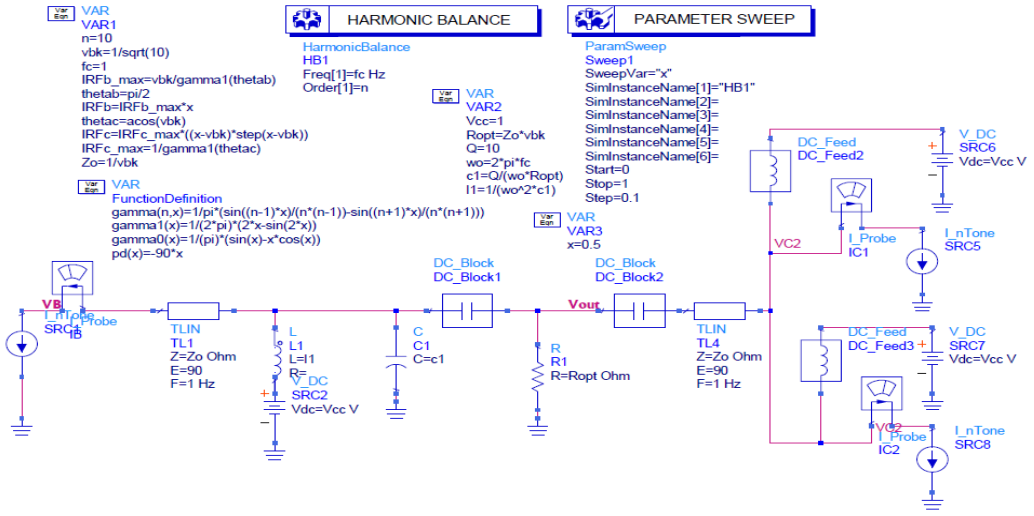

(b)

Fig. 3. Simulated structure of Doherty power amplifier: (a) with single auxiliary amplifier, and (b) with double auxiliary amplifier.

Figure 3 (a) represents the single stage n – tone 10 dB PBO DPA and Fig. 3 (b) represents the DPA that has two auxiliary amplifiers in parallel with same specification. The variable initialization used in simulation structure is defined in Table 1 with its name.

Table 1: Parameters used in ADS simulation

Variable Name	Description	Value
HB1	Nonlinear AC simulation for generation of sinusoidal source at fundamental frequency (freq) and n^{th} harmonic (order) frequency	
Sweep	Normalized input voltage (X) represented as VAR3 from 0 to 1 in 0.1 step along with HB1	
X	Normalized input voltage	0.3
IRFb	Peak value of the Main current source	IRFb_max * X
IRFc	Peak value of the auxiliary current source	IRFc_max*(2*(x–0.5)*step(x–0.5))
IRFb_max	Maximum peak value of the Main current source	Vbk/gamma1(thetab)
IRFc_max	Maximum peak value of the auxiliary current source	1/gamma1(thetac)
Pd(x)	Phase delay between main & auxiliary amplifier	$Cos^{-1}(X)$

IV. RESULTS AND DISCUSSION

The Doherty power amplifier with 10 dB power back off and n-tone sinusoidal inputs has been simulated with single auxiliary amplifier and double amplifier. Figure 4 represents the simulation results of single auxiliary 10 dB DPA characteristics. Figure 4 (a) shows the simulated output voltage of two amplifier current sources. Both the main and auxiliary current sources have the maximum value of 2 A.

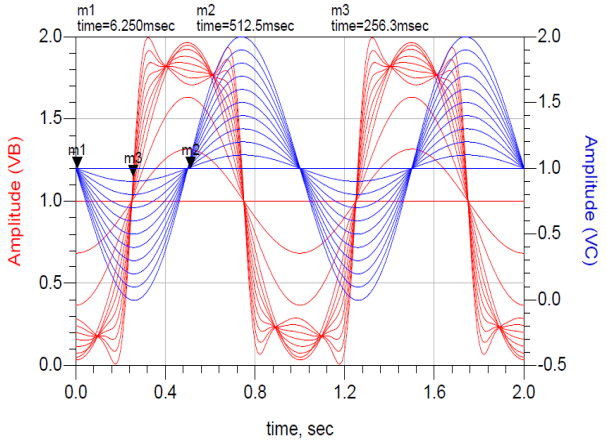

(a)

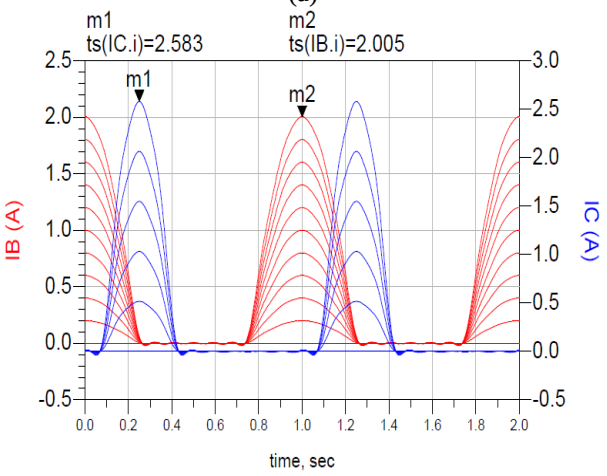

(b)

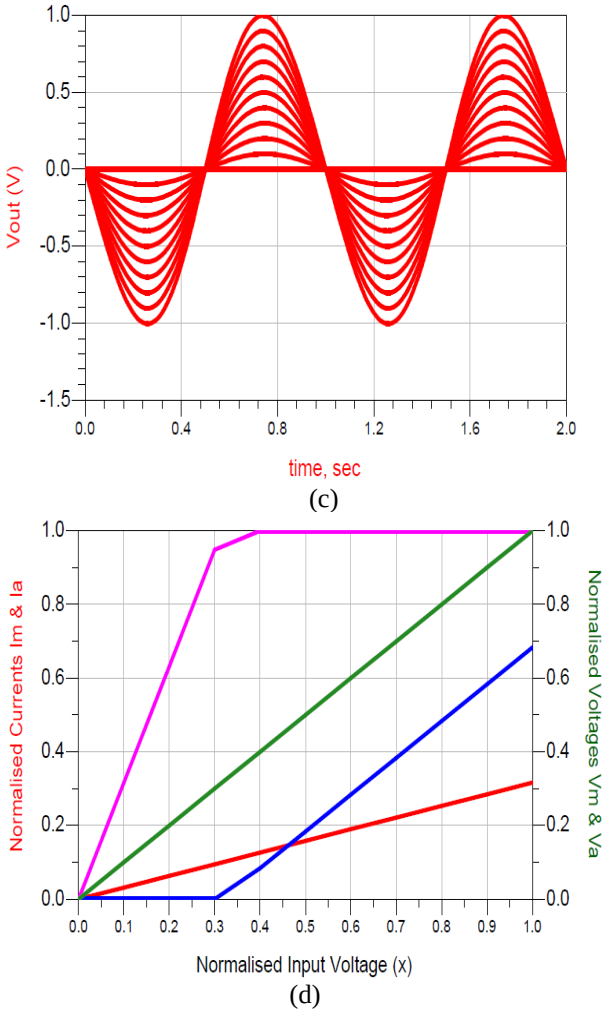

Fig. 4. Simulated response of Doherty power amplifier with single auxiliary current source. Main & auxiliary amplifier: (a) output voltage, (b) output current, (c) DPA output voltage, and (d) voltage and current in terms of input voltage.

The conduction angle can be found from the width sinusoidal tipped wave form of auxiliary source which is half of the main source (256.3 ms=512.5/2 ms). This validates the theoretical conduction angle of $\theta = \cos^{-1}(0.3)$. Figure 4 (b) shows the variation of two amplifiers output current in terms of input voltage with maximum current capacity of two transistors. It shows that the auxiliary amplifiers operating in class C, a maximum current capacity is 1.533 A while for main amplifier operating in class B, the maximum current capacity is 0.633 A. The parallel resonance L_1C_1 with quality factor 10 to calculate its value has been placed between the two amplifiers. This makes the output voltage close to sinusoidal waveform as shown in Fig. 4 (c). Figure 4 (d) shows the variation of main and auxiliary current sources output voltage and current in terms of input voltage. It shows that the auxiliary current begins to increase beyond threshold voltage (X=0.3). It shows the normalized voltages (V_1 and V_2) and normalized currents (I_1 and I_2) of main and auxiliary amplifiers with its maximum value of equal amplitude.

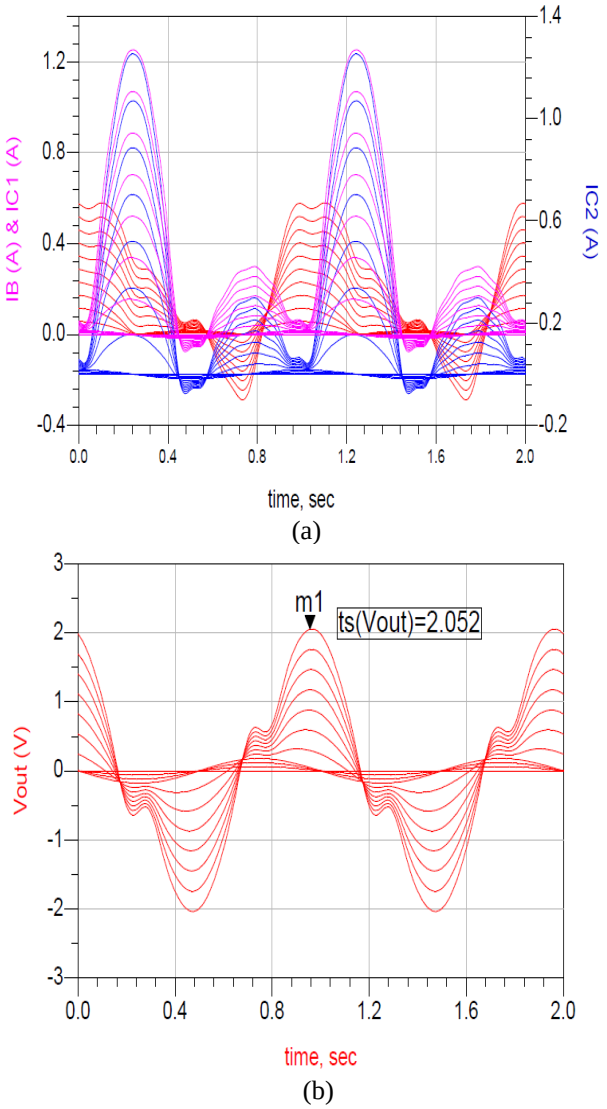

Fig. 5. Simulated output response of Doherty power amplifier with dual auxiliary current source: (a) currents and (b) voltage.

We have followed the similar procedure for DPA with two auxiliary amplifiers connected in parallel and the outputs derived are shown in Fig. 5. Table 2 shows the variation of efficiency for single auxiliary DPA having efficiency of 83.299% and for double auxiliary amplifiers with higher efficiency of 85.803%. Hence, it is proved that the Doherty power amplifier can be designed for high efficiency application by proper

design of main and auxiliary amplifiers in suitable configuration.

Table 2: Comparison of efficiency of DPA with single auxiliary amplifier (EFF) and for double auxiliary amplifier (EFF2b) with $R_{opt} = 1$ ohm and $Z_0 = 3.162$ ohm

X	EFF	EFF2b	X	EFF	EFF2b
0	0	0	0.6	62.86	22.63
0.1	24.84	0.17	0.7	67.16	35.96
0.2	49.67	0.68	0.8	72.19	51.19
0.3	74.51	**1.49**	0.9	77.62	67.91
0.4	61.82	4.36	1.0	83.29	85.80
0.5	**60.13**	11.81			

V. CONCLUSION

The method of designing 10 dB n-tone single and double auxiliary amplifiers Doherty power amplifier for high efficiency application is presented and reviewed. In this method it has been proved that the simplest way of providing a high efficiency at the output back – off region is Doherty power amplifier having load modulation and no additional circuit requirements. The simulated results show that 10 dB output power back off with higher efficiency of 85.803% has been achieved and matched with theoretical design values. The proposed DPA exhibits high efficiency over broad band which covers 5G bands for modern wireless communication standers. The attainment of above 85% efficiency shows that DPA can increase the power efficiency in comparison with class B amplifier operated at saturation level. Future work would be focused on fabrication of dual auxiliary amplifier DPA to validate the simulated results at mm wave spectrum.

REFERENCES

[1] S. Sakata, K. Kato, E. Teranishi, T. Sugitani, R. Ma, K. Chuang, Y.-C. Wu, K. Fukunaga, Y. Komatsuzaki, K. Horiguchi, K. Yamanaka, and S. Shinjo, "A fully-integrated GaN Doherty power amplifier module with a compact frequency-dependent compensation circuit for 5G massive MIMO base stations," *Mitsubishi Electric Research Laboratories, Inc*., 2020.

[2] A. M. Abdulkhaleq, M. A. Yahya, M. Sajedin, Y. Al-Yasir, N. Ojaroudi Parchin, A. Rayit, I. T. E. Elfergani, R. A. Abd-Alhameed, and J. Rodriguez, "Three-way Doherty power amplifier using class-F amplifier for more efficient mobile communications," *IMDC-SDSP*, June 28-30, 2020. DOI 10.4108/eai.28-6-2020.2297908.

[3] S. C. Cripps, *RF Power Amplifiers for Wireless Communications*. Artech House Microwave Library-Artech House, 2006.

[4] A. Barakat, M. Thian, V. Fusco, S. Bulja, and L. Guan, "Towards a more generalized Doherty power amplifier design for broadband operation," *IEEE Transactions on Microwave Theory and Techniques*, vol. 65, no. 3, pp. 846-859, 2017. https://doi.org/10.1109/TMTT.2016.2633261

[5] W. H. Doherty, "A new high efficiency power amplifier for modulated waves," *in Proc. IRE*, vol. 24, no. 9, pp. 1163-1182, Sep. 1936.

[6] K. Bathich, A. Z. Markos, and G. Boeck, "Frequency response analysis and bandwidth extension of the Doherty amplifier," *IEEE Transaction on Microwave Theory and Techniques*, vol. 59, no. 4, pp. 934-944, Apr. 2011.

[7] S. Rasheed, "Design and simulation of Ka/Q dual-band Doherty power amplifier using GaN pHEMT," *International Research Journal of Engineering and Technology (IRJET)*, e-ISSN: 2395-0056, vol. 7, no. 8, pp. 4339-4343, Aug. 2020.

[8] C. Liang, J. I. Martinez-Lopez, P. Roblin, Y. Hahn, D. Mikrut, and V. Chen, "Wideband two-way hybrid Doherty outphasing power amplifier," *IEEE Transactions on Microwave Theory and Techniques*, vol. 69, no. 2, pp. 1415-1428, 2021.

[9] V. Camarchia, M. Pirola, R. Quaglia, S. Jee, Y. Cho, and B. Kim, "The Doherty power amplifier: Review of recent solutions and trends," *IEEE Transaction on Microwave Theory and Techniques*, vol. 63, no. 2, pp. 559-271, 2015.

[10] A. M. Abdulkhaleq, M. A. Yahya, J. Brunning, Y. Al-Yasir, N. O. Parchin, A. Rayit, R. A. Abd-Alhameed, and J. Noras, "Load-modulation technique for next generation mobile," in *Proc. 2019 IEEE 2nd 5G World Forum (5GWF)*, 30 Sept.-2 Oct., 2019. DOI: 10.1109/5GWF.2019.8911689.

[11] A. M. Abdulkhaleq, Y. Al-Yasir, N. Ojaroudi Parchin, J. Brunning, N. McEwan, A. Rayit, R. A. Abd-Alhameed, J. Noras, and N. AbdulJabbar, "A 70-W asymmetrical Doherty power amplifier for 5G base stations," in *Proc. Broadband Communications, Networks, and Systems*, Cham, Faro, Portugal, pp. 446-454, 2019.

[12] A. M. Abdulkhaleq, M. A. Yahya, N. O. Parchin, Y. Al-Yasir, M. Sajedin, A. Rayit, I. T. E. Elfergani, R. A. Abd-Alhameed, and J. Rodriguez, "18-W three-way Doherty amplifiers for 5G applications," in *Proc. Antennas and Propagation Conference*, Birmingham, UK, 2019.

[13] H. Kim and C. Seo, "Improvement of power added efficiency and linearity in Doherty amplifier using dual bias control and photonic band-gap structure," in *Proc. Asia-Pacific Microwave Conference*, Bangkok, Thailand, pp. 1-7, 2007.

[14] A. M. Abdulkhaleq, M. A. Yahya, N. McEwan, A. Rayit, R. A. Abd-Alhameed, N. Ojaroudi Parchin, Y. A. Al-Yasir, and J. Noras, "Recent developments of dual-band Doherty power

amplifiers for upcoming mobile communications systems," *Electronics*, vol. 8, no. 6, pp. 1-19, 2019.

[15] A. Barakat, M. Thian, V. Fusco, S. Bulja, and L. Guan, "Toward a more generalized Doherty power amplifier design for broadband operation," *IEEE Transaction on Microwave Theory and Techniques*, vol. 65, no. 3, pp. 846-859, 2017.

[16] N. Kosaka, S. Fujiwara, A. Okamura, K. Chomei, Y. Sasaki, K. Horiguchi, and H. Katayama, "A high-efficiency and high-gain, plastic packaged GaN HEMT for 3.5-GHz-band LTE base stations," in *Proc IEEE International Symposium on Radio-Frequency Integration Technology (RFIT)*, Taipei, Taiwan, pp. 1-3, 2016.

[17] M. Sajedin, I. T. E. Elfergani, J. Rodriguez, R. Abd-Alhameed, and M. Fernandez Barciela, "A survey on RF and microwave Doherty power amplifier for mobile handset applications," *Electronics*, vol. 8, no. 717, pp. 1-31, 2019. DOI: 10.3390/electronics8060717.

[18] M. K. Kazimierczuk, *RF Power Amplifiers*. 1st edition, John Wiley & Sons, Ltd., 2008.

[19] M. Y. Abou-Shahine, Y. Nasser, and K. Y. Kabalan, "A high efficiency Doherty power amplifier for TV band applications," *Journal of Electromagnetic Analysis and Applications*, vol. 7, pp. 291-301, 2015.

[20] X. Fan, Z. Yu, J. Lu, and Z. Hua, "Design of a 0.7~1.5 GHz wideband power amplifier in 0.18-μm CMOS process," *Applied Computational Electromagnetics Society Journal*, vol. 31, no. 8, pp. 1003-1008, Aug. 2016.

Thermal Effects of 5G Frequency EM Waves on Ocular Tissue

Burak Aricioglu and Abdullah Ferikoglu

Department of Electrical and Electronics Engineering
Sakarya University of Applied Sciences, Sakarya, 54187, Turkey
baricioglu@subu.edu.tr, af@subu.edu.tr

Abstract ─ This research article aims to investigate the thermal effects on human eye due to exposure of EM (electromagnetic) field at 5G frequencies. A secondary purpose of the article is to show that SPICE, one of the most commonly used tools in circuit analysis, can be used to solve complex EM and bioheat transfer problems. Both electric field and temperature distributions in human eye are simulated with transmission line modelling (TLM) method. Also, finite element method (FEM) calculations are carried out for comparison. Temperature distributions are calculated for 30 minutes of EM radiation exposure. As a subject of the simulation, a human is chosen that the power density of incoming field at the human eye is assumed as the maximum of the ICNIRP general public exposure limits. A good consistency between TLM and FEM based simulations is found. A new transmission line model based on Debye parametric model is generated for simulation of EM field distribution in the tissues. With this generated transmission line, the results for the frequencies of interest can be obtained via single simulation. Also, a new transmission line model is developed for the temperature distribution simulation in which the effects of noncompressible fluid flow such as non-unidirectional blood flow in tissues and flow in aqueous humor are taken into consideration.

Index Terms ─ 5G, bioheat transfer, electromagnetic field, TLM.

I. INTRODUCTION

Wireless communication technologies have been advancing to meet constantly changing demands or to overcome the challenges such as capacity, quality of service, data rate, cost etc. [1]. To facilitate such increasing demands a new mobile cellular network architecture, 5G (fifth generation), is needed since, they cannot be provided sufficiently by the 4G (fourth generation) technologies [2].

However, these advances in wireless communication technologies cause some public concerns about possible hazardous health effects of mobile communication. In the recent decades, concerns on EM (electromagnetic) power absorption by the human eye have been raised since as the wireless communication advances, the chance of direct EM radiation exposure of the eye in a GHz frequency band increases [3]. Naturally, the public looks for reassurance that they are not in any way harmful or dangerous environment.

In the literature, numerous studies have been conducted to investigate the electromagnetic power absorption in the human eye with different models as well as for different frequencies. In Table 1, some of the related studies in the literature are given in terms of their eye model, frequency of interest and EM wave and bioheat transfer solution method.

Table 1: Some of the studies on EM power absorption by the human eye in the literature

Study	Eye Tissue Content	Freq. (GHz)	EM Solution Method	Bioheat Solution Method
[3]	ah, c, i, l, s, vh	0.9−10	FDTD	FDM
[4]	c, h, l, s	6, 18, 30	FDTD	FEM
[5]	ah, c, l, s, vh	0.6−6	FDTD	FDTD
[6]	ah, c, i, l, pc, s, vh	0.9	FEM	FEM
[7]	ah, c, i, l, s, vh	0.9−10	FDTD	FDM
[8]	ah, c, i, l, pc, s, vh	0.9, 1.8	FEM	FEM
[9]	ah, c, l, s	0.6−6	FDTD	-
[10]	ah, c, l, s	0.6−4	FDTD	-
[11]	ah, c, ch, i, l, r, s, vh	0.915	FDTD	-
[12]	ah, c, ch, i, l, m, r, s, vh	0.9, 2.6, 28	FIT	-

*ah: aqueous humor, c: cornea, ch: choroid, i: iris, l: lens, m: muscle, pc: posterior chamber, r: retina, s: sclera, vh: vitreous humor, FDTD: finite difference time domain, FDM: finite difference method, FEM: finite element method, FIT: finite integration theory.

Submitted On: January 23, 2019
Accepted On: March 14, 2021

https://doi.org/10.47037/2020.ACES.J.360404

In this study, thermal effects of EM waves at 5G frequencies on the human eye is investigated. Both EM field distribution and bioheat transfer in the eye is solved with transmission line modelling (TLM) method. Also, they are solved with FEM for comparison. The TLM based simulations are carried out in NGSpice environment while the FEM based simulations are carried out in COMSOL Multiphysics environment.

TLM is used in the literature as a numerical solving method for some types of partial differential equations. These equations are wave equation that can be used to define EM propagation in lossless media, diffusion equation that can be used to define bioheat transfer and an equation that is linear combination of wave and diffusion equations which can be used to define EM propagation in lossy media. The main advantages of TLM are unconditional stability and non-requirement of matrix inversion for time-domain solutions [13].

The model of the eye is taken as described in [14]. It consists of six tissues: aqueous humor, cornea, iris, lens, sclera and vitreous humor as shown in Fig. 1.

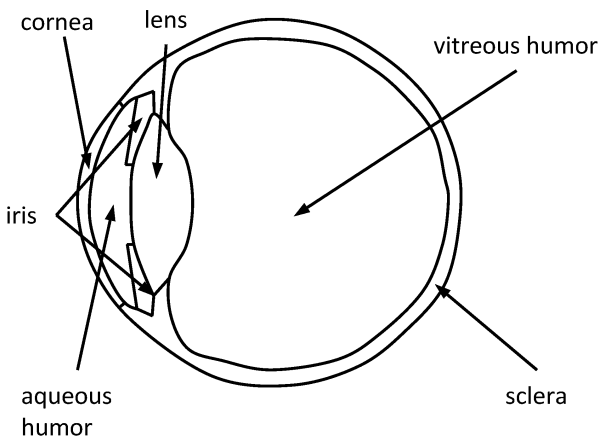

Fig. 1. 2D model of eye used in the study [14].

5G carrier frequencies considered in the study are 0.7GHz, 3.6GHz, 26GHz, 32GHz and 42GHz. According to European Conference of Postal and Telecommunications Administrations (CEPT) report:

- The Radio Spectrum Policy Group (RSPG) considers 0.7GHz band for indoor and nationwide 5G coverage.
- The RSPG considers 3.6GHz band to be the primary band for introducing 5G based services
- The RSPG recommends 26GHz band as a pioneer band.
- The RSPG considers 32GHz band as a promising band and 42GHz band as a viable option in the longer term [15].

The paper is so organized that, Section 2 provides materials and method, Section 3 contains simulations and results, and Section 4 offers the conclusion.

II. MATERIALS AND METHODS

Transmission line circuit theory can be applied to solve wave equations when $\lambda \gg l$ where λ is the wavelength and l is the spatial resolution [16]. Wavelength of an EM wave travelling through a lossy medium can be calculated as follows:

$$\lambda = \frac{c}{f\sqrt{\varepsilon_r \mu_r}}. \quad (1)$$

Here c is the speed of light in vacuum, ε_r is the relative permittivity of the medium, μ_r is the relative permeability of the medium and f is the frequency.

The wavelengths of EM waves travelling through the tissues for the frequencies of interest are given in Table 2.

Table 2: Wavelengths (mm) of EM waves travelling through ocular tissues with respect to frequency

Tissue	0.7GHz	3.6GHz	26GHz	32GHz	42GHz
a	51.52	10.38	2.11	1.87	1.61
c	57.12	11.81	2.39	2.11	1.80
i	57.48	11.63	2.27	2.00	1.71
l	71.13	14.55	3.02	2.66	2.27
s	57.32	11.67	2.35	2.08	1.78
v	51.63	10.16	2.07	1.88	1.68

*a: aqueous humor, c: cornea, i: iris, l: lens, s: sclera, v: vitreous humor.

In literature, thermal wave models of bioheat transfer (TWMBT) is proposed for solving bioheat transfer problems [17-19]. The wavelength of thermal waves can be calculated as:

$$\lambda = \frac{2\sqrt{2}\pi}{\sqrt{(c_T/\alpha)^2 + \sqrt{(c_T/\alpha)^4 + 4(\omega_b C_b / k_T)^2}}}. \quad (2)$$

Here c_T is the speed of thermal wave (m/s), α is the thermal diffusivity (m^2/s), ω_b is blood perfusion rate $(kg/m^3/s)$, C_b is specific heat capacity of blood $(Ws/kg/K)$ and k_T is thermal conductivity of tissue $(W/m/K)$. The speed of thermal wave and thermal diffusivity is defined as follow:

$$c_T = \sqrt{\frac{\alpha}{\tau}}, \alpha = \frac{k_T}{\rho_T C}. \quad (3)$$

Here ρ_T is density of tissue (kg/m^3), C is specific heat capacity of tissue $(Ws/kg/K)$, and τ is thermal relaxation time of tissues (s).

There are several studies conducting on finding thermal relaxation time of tissues [20-23] and its value varies between 0.426 and 50 seconds. By examining (2) and (3) the thermal wavelength and thermal relaxation time are proportional. Thermal relaxation time selected as its lowest value to determine spatial resolution for solving bioheat transfer problem with TLM. For this value thermal wavelength values in the ocular tissues are given in Table 3.

The wavelength values given in Tables 2 and 3 is used to determine the 2D-TLM mesh size to ensure the spatial

resolution is much smaller than wavelengths ($l \ll \lambda$). The mesh size will be given in Section III.

Table 3: Wavelength (mm) of thermal waves travelling in ocular tissues

Aqueous Humor	Cornea	Iris	Lens	Sclera	Vitreous Humor
1.64	1.61	1.57	1.53	1.57	1.63

A. TLM for electromagnetic wave solution

The field equations for a plane wave in a medium can be analogous to the circuit equations for a wave on a transmission line. This similarity can be favourably used for the analysis of a travelling EM wave in a medium based on transmission line analogy.

It is assumed that the incoming EM wave is characterized by TM (transverse magnetic) fields (TM-mode) to simplify the problem as in [6, 8, 24, 25]. Moreover, TM or TE (transvers electric) mode cavity resonators are usually employed in the current mobile base stations [26,27] and they will be still useful for 5G base stations [28].

It is very well established in the literature that TM or TE mode EM wave problems can be solved with 2D-TLM method [29]. Hence, 2D-TLM shown in Fig. 2 can be used to solve TM mode EM wave problems.

Consider a TM wave propagating along z direction in a lossy medium. The only none zero field components are H_x, H_y and E_z. Using Maxwell's Equations, the following equations are obtained:

$$\frac{\partial E_z}{\partial x} = \mu \frac{\partial H_y}{\partial t}, \tag{4}$$

$$\frac{\partial E_z}{\partial y} = -\mu \frac{\partial H_x}{\partial t}, \tag{5}$$

$$\frac{\partial H_y}{\partial x} - \frac{\partial H_x}{\partial y} = \sigma E_z + \varepsilon \frac{\partial E_z}{\partial t}. \tag{6}$$

By taking derivatives of (4) and (5) with respect to x and y respectively, combine the resultants with (6) yields to:

$$\frac{\partial^2 E_z}{\partial x^2} + \frac{\partial^2 E_z}{\partial y^2} = \mu\sigma \frac{\partial E_z}{\partial t} + \mu\varepsilon \frac{\partial^2 E_z}{\partial t^2}. \tag{7}$$

For solving (7), the transmission line shown in Fig. 2 can be used. In the figure V is voltage, R, L, C and G are resistance, inductance, capacitance and conductance per meter of the transmission line respectively and Δl is the unit length of the transmission line in the both x and y axis. If KVL (Kirchhoff's voltage law) is applied along x and y axis the followings are obtained, respectively:

$$-\frac{\partial V}{\partial x} = RI_x + L\frac{\partial I_x}{\partial t}, \tag{8}$$

$$-\frac{\partial V}{\partial y} = RI_y + L\frac{\partial I_y}{\partial t}. \tag{9}$$

Then, if KCL (Kirchhoff's current law) is applied to the node V shown in Fig. 2:

$$\frac{\partial I_x}{\partial x} + \frac{\partial I_y}{\partial y} = -2GV - 2C\frac{\partial V}{\partial t}, \tag{10}$$

is obtained. By taking derivatives of (8) and (9) with respect to x and y respectively and combine the resultants with (10) yields to:

$$\frac{\partial^2 V}{\partial x^2} + \frac{\partial^2 V}{\partial y^2} = 2RGV + 2RC\frac{\partial V}{\partial t} + 2LG\frac{\partial V}{\partial t} + 2LC\frac{\partial^2 V}{\partial t^2}. \tag{11}$$

If the value of R is taken as negligibly small or zero below equivalence can be established between (7) and (11):

$$\begin{aligned} &V \leftrightarrow E_z,\ I_x \leftrightarrow H_y,\ -I_y \leftrightarrow H_x, \\ &L \leftrightarrow \mu,\ 2C \leftrightarrow \varepsilon,\ 2G \leftrightarrow \sigma. \end{aligned} \tag{12}$$

The electrical parameters of the tissues are given in Table 4 with respect to frequency.

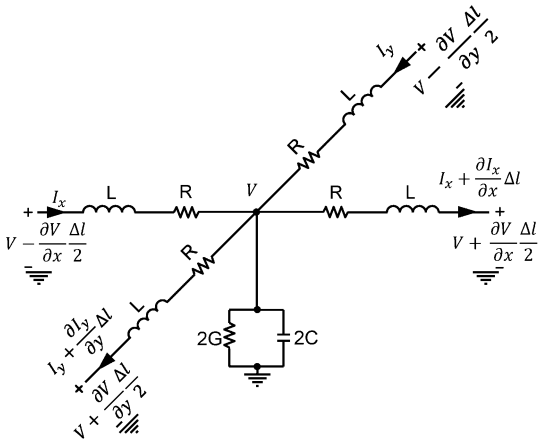

Fig. 2. 2D Lumped model of transmission line.

Table 4: Electrical parameters of ocular tissues with respect to frequency [30]

Tissue		0.7GHz	3.6GHz	26GHz	32GHz	42GHz
a	ε_r	69.20	64.40	30.0	25.1	19.7
	σ	2.34	4.69	41.4	48.0	56.3
c	ε_r	56.30	49.80	23.4	19.8	15.7
	σ	1.31	3.26	30.8	35.7	41.8
i	ε_r	55.60	51.30	25.8	22.0	17.5
	σ	0.88	2.65	31.6	37.2	44.4
l	ε_r	36.30	32.80	14.6	12.4	9.87
	σ	0.44	1.76	19.4	22.3	25.9
s	ε_r	55.9	51.0	24.1	20.4	16.1
	σ	1.1	3.0	31.4	36.5	42.9
v	ε_r	68.90	67.30	31.1	24.9	18.0
	σ	1.58	3.58	47.9	55.5	63.9

*a: aqueous humor, c: cornea, i: iris, l: lens, s: sclera, v: vitreous humor.

The value of μ_r (relative permeability) is selected as 1, since human tissues are a non-magnetic material that their magnetic permeability is same as or very close to that of vacuum [31,32].

In classical TLM method, it is not possible to solve a multi-frequency EM field distribution problem in a lossy media with a single simulation. Simulations must be carried as many as the number of the frequencies of interest. In this paper, a new transmission line model is design to make it possible to solve such multi-frequency EM field distribution problem with a single simulation.

In the literature, there are studies that employ parametric model of tissues' dielectric properties in order to solve a multi-frequency EM problem with a single simulation [33-35].

There are two parametric models of tissues commonly employed in the literature. These are Debye and Cole-Cole [36] parametric models. In both models, the dielectric properties of tissues can be expressed as a function of frequency over some frequency range. Debye parametric model is usually preferred because of its lower computational complexity and it can be easily expressed in time and frequency domain. On the other hand, Cole-Cole parametric model offers higher accuracy, and it can model the dielectric properties of tissues for a very large frequency range (typically from Hz to THz).

In this study, Debye parametric model is employed due to its lower computational complexity and it can be easily synthesized with an RC ladder network as it will be discussed in this section.

The Debye parametric model that describes the complex permittivity of a lossy medium is given in (13):

$$\varepsilon(\omega) = \varepsilon'(\omega) - j\varepsilon''(\omega) = \varepsilon_\infty + \frac{\sigma_s}{j\omega\varepsilon_0} + \sum_{i=1}^{n} \frac{\Delta\varepsilon_i}{1 + j\omega\tau_i}. \quad (13)$$

Here $\varepsilon'(\omega)$ and $\varepsilon''(\omega)$ relative permittivity and dielectric loss factor respectively, n is the total number of Debye poles, ε_∞ is relative permittivity at the highest frequency (usually in THz region), σ_s the static ionic conductivity, ε_0 is the permittivity of free space, $\Delta\varepsilon_i$ is the change in the relative permittivity and τ_i is the i^{th} relaxation constant at i^{th} dispersion.

The relation between conductivity of medium (σ) and dielectric loss factor $\varepsilon''(\omega)$ is given in (14):

$$\sigma = \omega\varepsilon_0\varepsilon''(\omega). \quad (14)$$

The parallel admittance per meter of the transmission line shown in Fig. 2 is given as:

$$Y(\omega) = 2(G + j\omega C). \quad (15)$$

Using (12) and (14), the parallel admittance can be described in terms of Debye parameters as given in (16):

$$\begin{aligned} &Y(\omega) = 2(G + j\omega C), \\ &2(G + j\omega C) \leftrightarrow \sigma + j\omega\varepsilon, \\ &\sigma + j\omega\varepsilon \leftrightarrow j\omega\varepsilon_0(\varepsilon'(\omega) - j\varepsilon''(\omega)), \\ &Y(\omega) \leftrightarrow j\omega\varepsilon_0(\varepsilon_\infty + \frac{\sigma_s}{j\omega\varepsilon_0} + \sum_{i=1}^{n} \frac{\Delta\varepsilon_i}{1 + j\omega\tau_i}). \end{aligned} \quad (16)$$

The parametric model of the parallel admittance $Y(\omega)$ given in (16) can be easily synthesized with Foster II circuit synthetization method as an RC ladder network. The method is given in (17):

$$\frac{Y(\omega)}{j\omega} = Y_\infty + \frac{Y_0}{j\omega} + \sum_{i=1}^{n} \frac{K_i}{j\omega + \alpha_i}. \quad (17)$$

Where Y_∞ is the parallel capacitance, Y_0 is the parallel conductance and $\frac{K_i}{j\omega+\alpha_i}$ term is the pole introduced by a parallel admittance of a series RC branch. Using the relation given in (17) transmission line model of the tissues based on Debye parametric model can be generated as in Fig. 3. Here the number of Debye poles is three. Moreover, the relation between the synthesized parallel admittance and Debye parameters are given in Table 5.

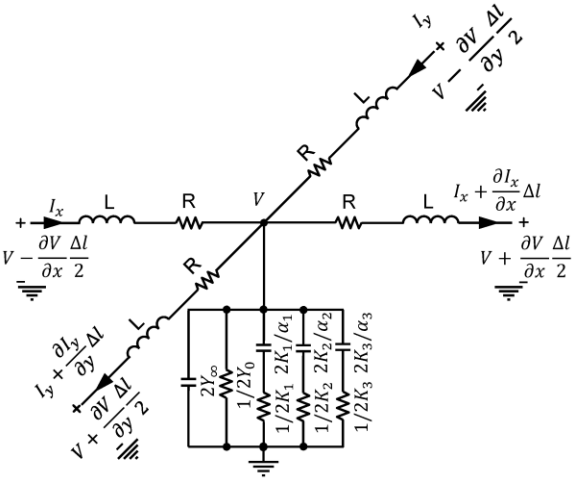

Fig. 3. 2D transmission line model based on Debye parametric model.

Table 5: Equivalence between parameters of transmission line in Fig. 3 versus Debye parameters

TLM Parameters		EM Field/Debye Parameters
L (H/m)	↔	μ (kgm/s^2/A^2)
$2Y_\infty$ (F/m)	↔	$\varepsilon_\infty\varepsilon_0$ (s^{4}A^2/kg/m^3)
$2Y_0$ (1/Ω/m)	↔	σ_s (1/Ω/m)
$2K_1$ (1/Ω/m)	↔	$\frac{\varepsilon_0\Delta\varepsilon_1}{\tau_1}$ (s^{3}A^2/kg/m^3)
$2K_2$ (1/Ω/m)	↔	$\frac{\varepsilon_0\Delta\varepsilon_2}{\tau_2}$ (s^{3}A^2/kg/m^3)
$2K_3$ (1/Ω/m)	↔	$\frac{\varepsilon_0\Delta\varepsilon_3}{\tau_3}$ (s^{3}A^2/kg/m^3)
α_1 (1/Ω/F)	↔	$\frac{1}{\tau_1}$ (1/s)
α_2 (1/Ω/F)	↔	$\frac{1}{\tau_2}$ (1/s)
α_3 (1/Ω/F)	↔	$\frac{1}{\tau_3}$ (1/s)

Although the computational complexity of Debye parametric model is lower, its biggest drawback is it cannot describe complex permittivity of a medium very accurately [36]. In their study, Salahuddin et al. [37], Debye parametric model is optimized for 500MHz and 20GHz frequency range to reduce the error introduced by the model.

Debye parameters given in [37] is used for analysing EM distribution in the human eye problem for 700MHz and 42GHz frequency range. However, some of the frequencies of interest in this study are out of the frequency range given in [37]. Maximum deviation error is for the conductivities of the tissues is about 7% and for the relative permittivity is about 3%. This will introduce a computational error. However, it can be said that the error is negligible since the electric field magnitude at these higher frequencies of interest, as it can be seen in Fig. 8, is almost zero. The Debye parameters for the ocular tissues are given in Table 6.

Table 6: Debye parameter values of the ocular tissues [37]

Tissue	ε_∞	σ_s	$\Delta\varepsilon_1$	$\Delta\varepsilon_2$	$\Delta\varepsilon_3$	τ_1 [ps]	τ_2 [ps]	τ_3 [ps]
a	8	1	100	48.4	11.2	674.8	7.111	20.94
c	8.3	0.8	39.2	62.1	6.5	8.066	1200	40.11
i	8.8	0.7	4.93	41	11.6	40.11	7.549	769.1
l	6.3	0.6	2.4	8.3	30.1	153.1	19.27	6.822
s	8	0.9	39.7	4	6.5	7.73	260.1	29.49
v	6.5	1	100	57.6	5.4	1259	7.362	21.71

*a: aqueous humor, c: cornea, i: iris, l: lens, s: sclera, v: vitreous humor.

B. TLM for bioheat transfer

Bioheat transfer in the human eye is calculated with Klinger's model, a continuum model of Pennes' model, in which the effect of non-unidirectional blood flow is taken into consideration [38]. It can also model noncompressible fluid flow in the tissues such as the flow in aqueous humor. Klinger's model can be described as:

$$\rho_T C_T \frac{\partial T}{\partial t} + (\rho_T C_T)\vec{u}.\nabla T = k_T \nabla^2 T + \omega_b C_b (T_b - T) + Q. \quad (18)$$

Where ρ_T is density of tissue (kg/m^3), C_T specific heat capacity of tissue ($Ws/kg/K$), T is temperature (K), t is time (s), $\vec{u}$ is the velocity vector (m/s), k_T is thermal conductivity of tissue ($W/m/K$), ω_b is blood perfusion rate ($kg/m^3/s$), C_b is specific heat capacity of blood ($Ws/kg/K$), T_b is the initial temperature value of blood (K) and Q is the sum of metabolic heat generation rate and the electromagnetic power density absorbed by the tissues (W/m^3). (18) can be rearranged as:

$$\nabla^2 T = \frac{\rho_T C_T}{k_T}\frac{\partial T}{\partial t} + \frac{(\rho_T C_T)}{k_T}\vec{u}\nabla T + \frac{\omega_b C_b}{k_T}(T - T_b) - \frac{Q}{k_T}. \quad (19)$$

Bioheat transfer problem can also be solved with TLM method [13, 39]. For this, transmission line model shown in Fig. 4 is used.

In the literature, the studies on solving bioheat transfer problems with TLM method often ignore the effects of noncompressible fluid flow in the tissues. In some cases, this may lead to small spatial errors on the distribution of temperature at tissues. To cope with this drawback, transmission line model for solving bioheat transfer problems is modified by adding dependent voltage sources as shown in Fig. 4. Hence, the modified transmission line model can reduce the spatial temperature distribution errors.

If the circuit analysis for the circuit shown Fig. 4 is performed as in the previous section, the following equation is obtained:

$$\nabla^2 V = 2LC\frac{\partial^2 V}{\partial t^2} + 2(LG + RC)\frac{\partial V}{\partial t} + 2RGV + \frac{2a_x}{\Delta l}\frac{\partial V}{\partial x} + \frac{2a_y}{\Delta l}\frac{\partial V}{\partial y} - \frac{L}{\Delta l}\frac{\partial I_s}{\partial t} - \frac{I_s R}{\Delta l}. \quad (20)$$

Here R, L, C and G are resistance, inductance, capacitance and conductance per meter of the transmission line respectively, Δl is the unit length of the transmission line in the both x and y axis, and the value a_x and a_y are the gain of the voltage controlled voltage sources. If the value of L is taken as 0 (or $\omega L \ll R$) the following is obtained:

$$\nabla^2 V = 2RC\frac{\partial V}{\partial t} + 2RGV + \frac{2a_x}{\Delta l}\frac{\partial V}{\partial x} + \frac{2a_y}{\Delta l}\frac{\partial V}{\partial y} - \frac{I_s R}{\Delta l}. \quad (21)$$

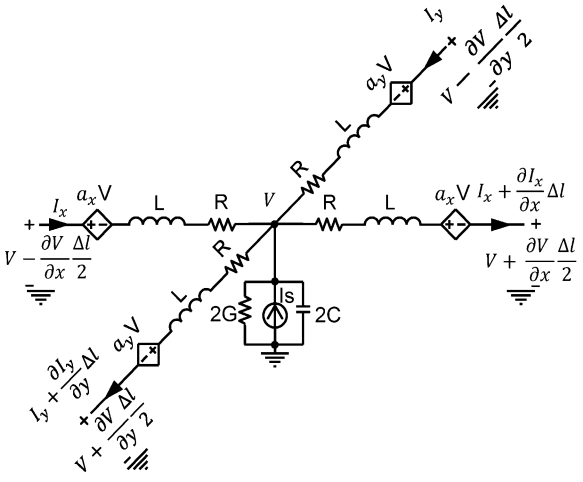

Fig. 4. Transmission line model for bioheat transfer.

As it can be seen in (19) and (21) that their solutions are mathematically equivalent with:

$$V \leftrightarrow T,\ 2RC \leftrightarrow \frac{\rho_T C_T}{k_T},\ 2RG \leftrightarrow \frac{\omega_b C_b}{k_T}, \quad \frac{2a_x}{\Delta l} \leftrightarrow \frac{\rho_T C_T}{k_T}u_x,\ \frac{2a_y}{\Delta l} \leftrightarrow \frac{\rho_T C_T}{k_T}u_y,\ \frac{I_s R}{\Delta l} \leftrightarrow \frac{\omega_b C_b T_b + Q}{k_T}. \quad (22)$$

The value of lumped elements and sources in Fig. 4 can be calculated as:

$$C \leftrightarrow \rho_T C_T \Delta l, a_x \leftrightarrow \frac{C_T}{4k_T}\omega_b \Delta l^2, a_y \leftrightarrow \frac{C_T}{4k_T}\omega_b \Delta l^2, \quad R \leftrightarrow \frac{1}{2k_T \Delta l}, G \leftrightarrow \omega_b C_b \Delta l, I_s \leftrightarrow 2(\omega_b C_b T_b + Q)\Delta l^2. \tag{23}$$

Thermal properties of the tissues are given in Table 7.

Table 7: Thermal properties of the tissues [30]

Tissue	ρ_T	C_T	k_T	Q_{met}	ω_b
a	993.8	3997	0.58	-	-
c	1062	3615	0.54	-	-
i	1091	3421	0.50	43899	32.3
l	1076	3133	0.43	-	-
s	1032	4200	0.58	6073	6.74
v	1005	4047	0.59	-	-

*a: aqueous humor, c: cornea, i: iris, l: lens, s: sclera, v: vitreous humor.

III. SIMULATION AND RESULTS

Simulations are performed for a far field radiation and the power density of the incoming electric field is assumed as the top of the general public exposure limit of ICNIRP (International Commission on Non-Ionizing Radiation Protection) guideline. The limits are given in Table 8 for the 5G frequencies used in the study.

Table 8: Reference level for general public exposure of EM field [40]

Frequency (GHz)	E Field RMS Strength (V/m)	Plane Wave Power Density (mW/cm^2)
0.7	36	0.35
3.6	61	1
26	61	1
32	61	1
42	61	1

In the TLM based simulation, the proposed transmission line model based on three-term Debye parameters is used. In the TLM simulation, all the electric field distribution results obtained with a single simulation run for the frequencies of interest. Moreover, the lumped element values of the proposed transmission line are calculated from Debye parameters given in Table 6 in accordance with the equivalence given in Table 5. On the other hand, FEM based simulations are carried out by the number the frequencies of interest, even though FEM based simulation supports the parametric model of the tissues. The reason for this is that the FEM based simulations are carried out for comparison and in these simulations dielectric properties of the tissues given in [30] are used.

The simulation setup is shown in Fig. 5. In both EM and bioheat transfer problems, a square TLM mesh is used. The size of the mesh is 0.3mm X 0.3mm. A 2D TLM consists of two transmission line in each direction. Hence, the spatial resolution in each direction is the half of the side length of the square mesh. Since a 2D TLM shunt node is used in the problems, the spatial resolution is 0.15mm and this resolution value is less than a tenth of wavelengths given in Tables 2 and 3, hence, it can be said that the spatial resolution is much lesser than wavelength in all EM and bioheat transfer problems.

In the simulation setup, cornea has a boundary with air medium while sclera has a boundary with head. The rest of the air and head medium in Fig. 5 are truncated with matched boundary condition as described in [29] for the electric field distribution calculation. The impedance connected at the matched boundary is chosen to be equal to the characteristic impedance of the medium. The region labelled as air in Fig. 5 is truncated with impedance that equals to the characteristic impedance of air and the region labelled as head in Fig. 5 is truncated with impedance that equals to the characteristic impedance of head tissue. The dielectric properties of the head tissue are taken as the average of that of white and gray matter as in [41].

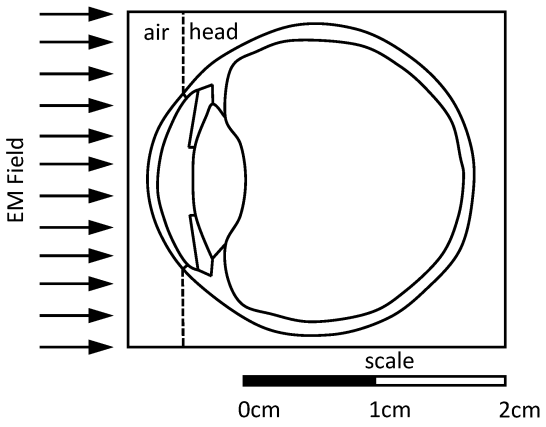

Fig. 5. Simulation setup.

Since the field considered to be come at right angles, the matched boundary condition will give good results with low computational complexity [29]. The circuit representation of matched boundary condition is given in Fig. 6.

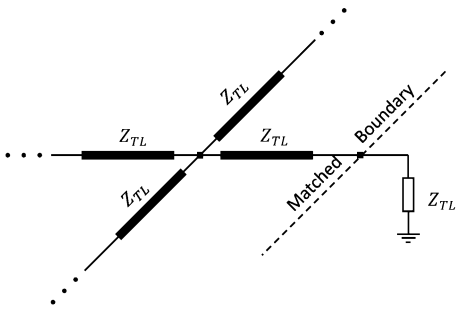

Fig. 6. Circuit representation of matched boundary condition.

The reflection coefficient at the boundary is calculated as follows:

$$\Gamma = \frac{Z_{Load} - Z_{TL}}{Z_{Load} + Z_{TL}} = \frac{Z_{TL} - Z_{TL}}{Z_{TL} + Z_{TL}} = 0. \quad (24)$$

For bioheat transfer problem convection boundary condition is used. The convection boundary condition is described as:

$$-k_T \frac{\partial T}{\partial l} = h(T - T_T). \quad (25)$$

Here h $(W/m^2/K)$ is the heat transfer coefficient between two region and T_T (K) is the temperature at the boundary. In Fig. 7, the resistance R is used to model the heat transfer coefficient and the voltage source V_T is used to model the temperature at the boundary and their relations can be found in [42] and are given in (26):

$$h \leftrightarrow \frac{1}{2R\Delta l}, T_{T\leftrightarrow} V_T. \quad (26)$$

Convection boundary is considered for two different boundaries. First one is the boundary between air and cornea and the second one is between sclera and head regions. The heat transfer coefficients for these boundaries are taken as in [43]. Also, the ambient temperature is taken as 25℃ and the body temperature is taken as 37℃. The convection boundary in TLM is used as described in [42] and shown in Fig. 7.

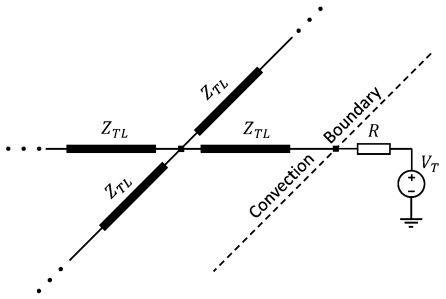

Fig. 7. Circuit representation of convection boundary condition.

The electric field distribution in the human eye is calculated with both TLM and FEM methods and their results are given in Fig. 8. As it can be seen in the figure, both results of TLM and FEM based electric field distribution calculation are close to each other.

As it can be seen in Fig. 8, at the lowest frequency, the electric field magnitude gradually decreasing as it travels inside the human eye, but it never reaches down to zero. For 3.6GHz frequency, the electric field magnitude inside human eye exceeds that of incoming field and the maxima occurs at a region between aqueous humour and lens tissues. Electric field distribution at the higher frequencies (26, 32 and 42GHz) can only be observed at near the cornea and at the other part of the eye electric field magnitude is almost zero.

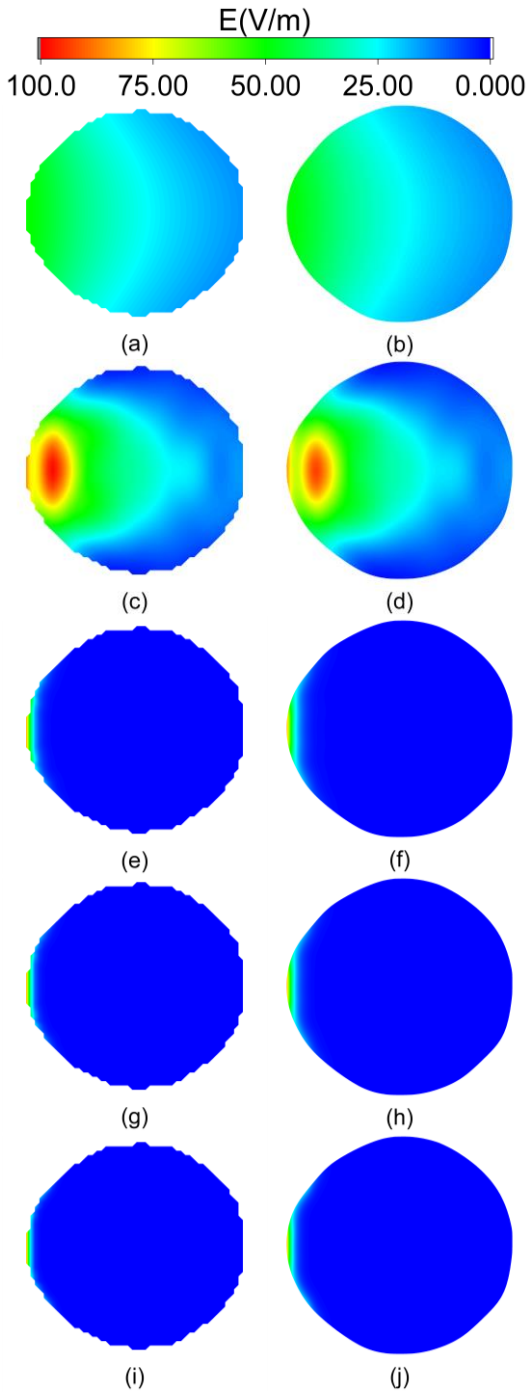

Fig. 8. Electric field distributions inside of the human eye at 700MHz ((a) TLM - (b) FEM), 3.6GHz ((c) TLM - (d) FEM), 26GHz ((e) TLM - (f) FEM), 32 GHz ((g) TLM - (h) FEM) and 42 GHz ((i) TLM - (j) FEM).

Specific absorption rate (SAR) values of the ocular tissues for the frequencies of interest are calculated before calculation of temperature distribution in the human eye. SAR calculated by using (27):

$$SAR = \frac{\sigma E_{rms}^2}{\rho}. \quad (27)$$

Here σ is the conductivity of tissue and ρ is the density of tissue. The SAR in the human eye is calculated by using electric field distributions obtained from TLM and FEM based calculations and given in Fig. 9 for both methods. At the lower frequencies (700MHz and 3.6GHz) maximum SAR value is observed at aqueous humor due to its higher conductivity. On the other hand, at the higher frequencies (26GHz, 32GHz and 42GHz) maximum SAR value observed at cornea for at these frequencies maximum of the electric field magnitudes are observed at the surface.

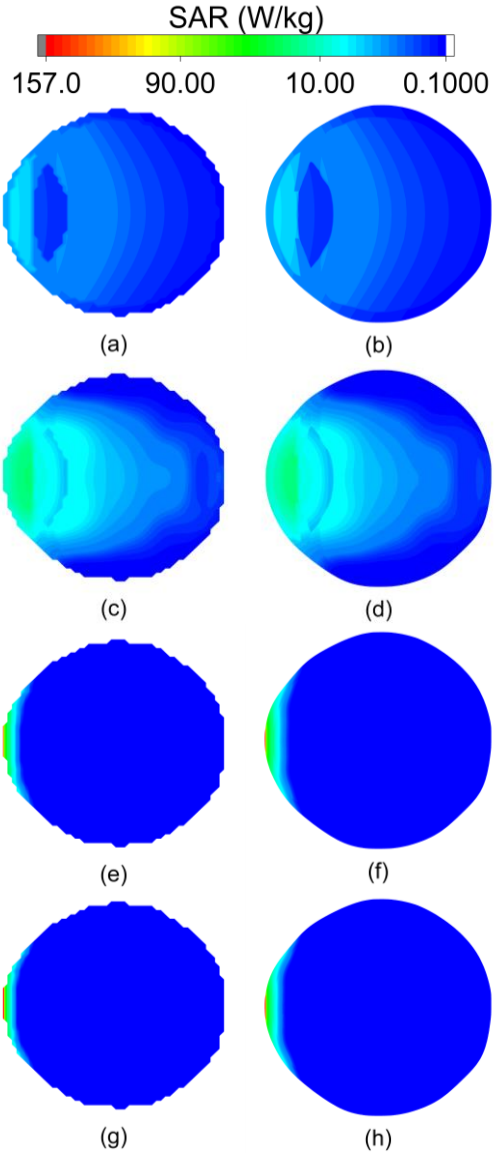

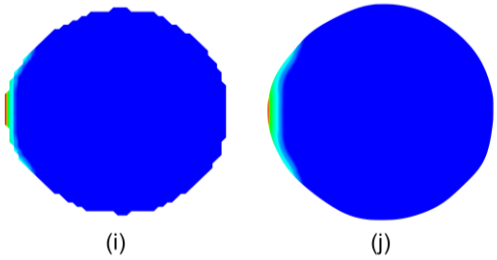

Fig. 9. SAR distributions inside of the human eye at 700MHz ((a) TLM - (b) FEM), 3.6GHz ((c) TLM - (d) FEM), 26GHz ((e) TLM - (f) FEM), 32 GHz ((g) TLM - (h) FEM) and 42 GHz ((i) TLM - (j) FEM).

The temperature distribution in the human eye is also calculated with TLM method for two different cases. In the first one, the effects of fluid dynamics in aqueous humor are not considered while in the second one these effects are considered. As in the electric field distribution calculation, FEM based calculation of the temperature distribution in the human eye is also carried out for comparison. In the simulation, exposure time is assumed as 30 minutes. Also, the subject of the experiment is considered as in standing position.

The temperature rise due to exposure to EM field at 5G frequencies are given in Fig. 10 for the case where fluid flow in aqueous humor is neglected. As it can be seen in the figure the results of TLM, and FEM based calculations are very close to each other.

For the second case where the effects of fluid flow in aqueous humor are considered, the temperature rise due to exposure to EM field at 5G frequencies are given in Fig. 11. As in the previous case, the results of TLM and FEM based calculations are very close to each other.

As seen in Figs. 10 and 11, the highest temperature rise occurs at 3.6GHz and the lowest one occurs at 700MHz. For the rest of the frequencies the temperature rise decreases as the frequency increases. There are two main reason for why the lowest temperature rise occurs at 700MHz. The first one is the power density is at 700MHz is lower than at other frequencies and the second one is at 700MHz tissue conductivities are the lowest. The highest rise is observed at 3.6GHz since the magnitude of electric field distribution is the highest at this frequency.

When both Figs. 10 and 11 are examined, there is a little difference between both figures in terms of temperature rise distributions. The difference can be easily observed at aqueous humor and its neighbour regions. However, the maximum temperature rises in both case at all frequencies is very close to each other.

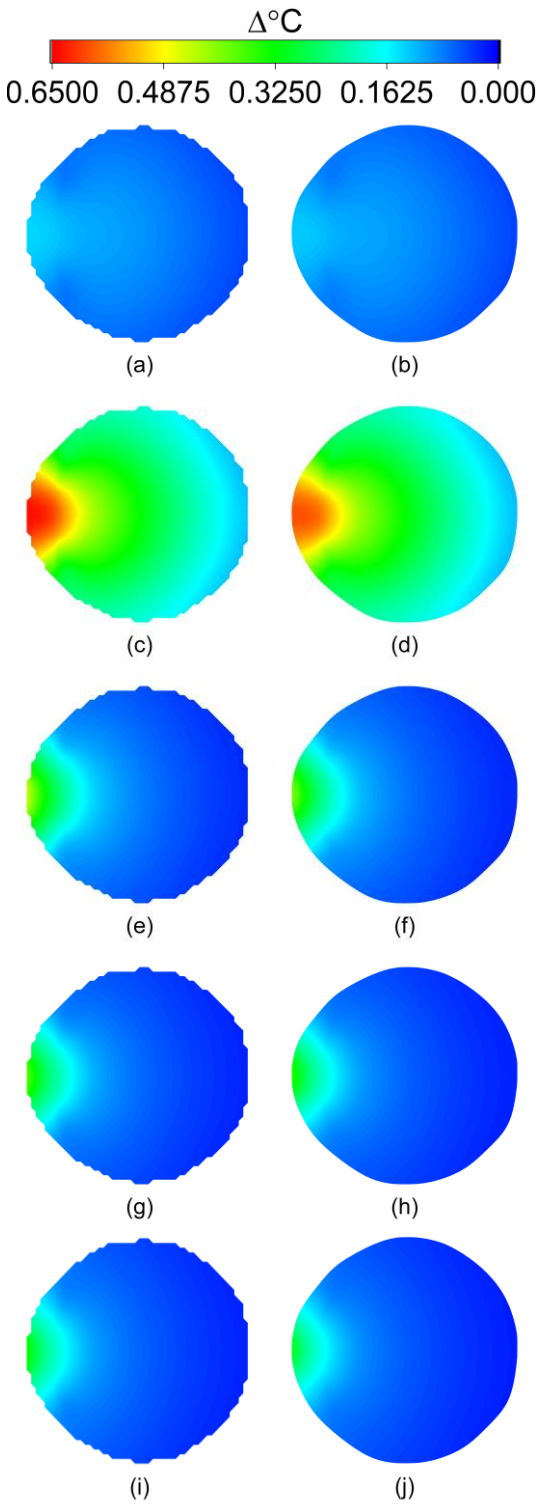

Fig. 10. Temperature rise distribution in the human eye when the aqueous humor flow dynamics are neglected, after 30 minutes exposure to EM fields at 700MHz ((a) TLM - (b) FEM), 3.6GHz ((c) TLM - (d) FEM), 26GHz ((e) TLM - (f) FEM), 32 GHz ((g) TLM - (h) FEM) and 42 GHz ((i) TLM - (j) FEM).

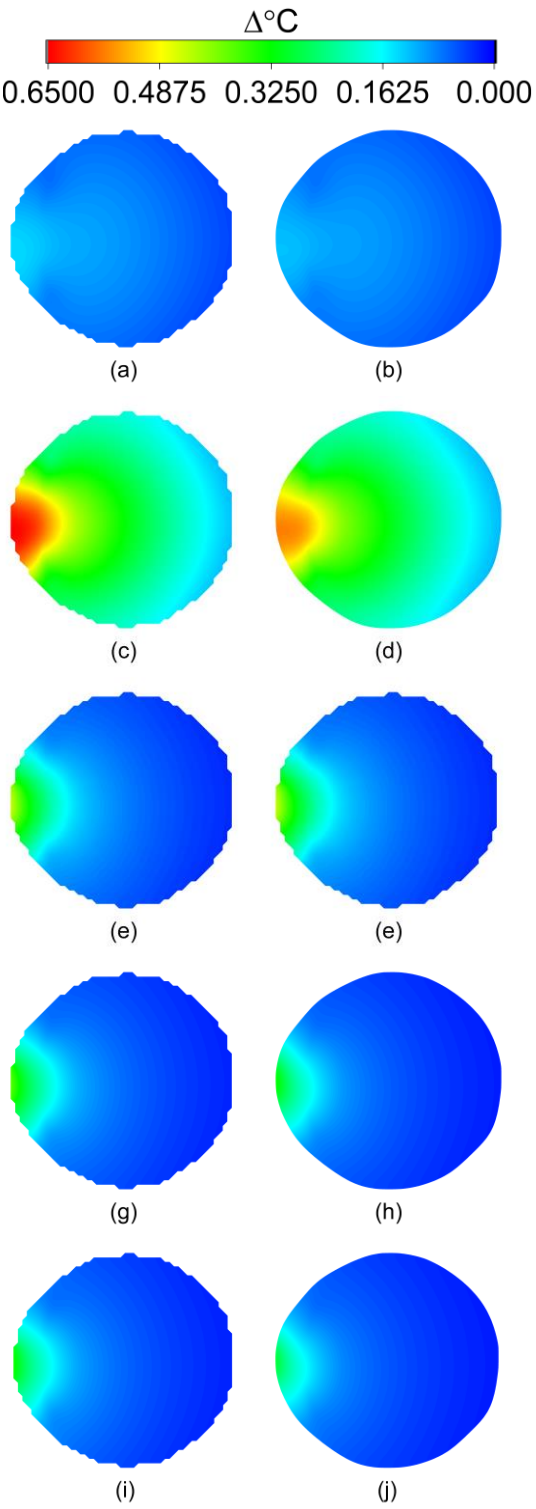

Fig. 11. Temperature rise distribution in the human eye when the aqueous humor flow dynamics are considered, after 30 minutes exposure to EM fields at 700MHz ((a) TLM - (b) FEM), 3.6GHz ((c) TLM - (d) FEM), 26GHz ((e) TLM - (f) FEM), 32 GHz ((g) TLM - (h) FEM) and 42 GHz ((i) TLM - (j) FEM).

Since the effect of the aqueous humor (AH) flow dynamics on temperature rise distribution is not very apparent from Figs. 10 and 11, temperature rise distributions in the neighbourhood of aqueous humor at 3.6 GHz for both FEM and TLM methods are given in Fig. 12.

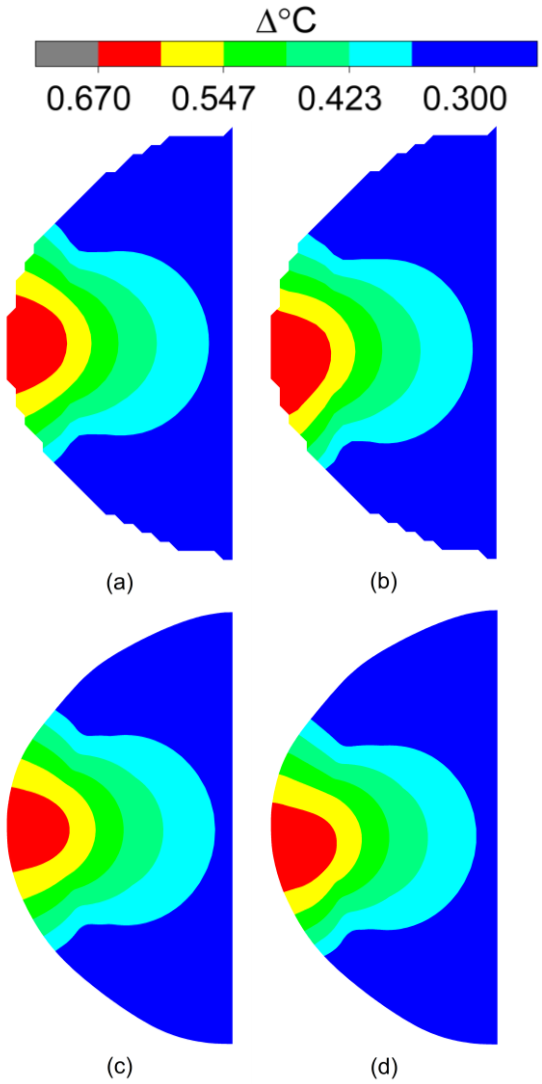

Fig. 12. Temperature rise distribution in the human eye after 30 minutes exposure to EM fields at 3.6 GHz (a) TLM without AH flow, (b) TLM with AH flow, (c) FEM without AH flow, and (d) FEM with AH flow.

IV. CONCLUSION

In this work, calculation of electric field distribution in human eye and temperature rise due to exposure to electric field is carried with TLM method. Temperature increase is calculated with Klinger's bioheat transfer equation for 30 minutes exposure for a standing person. Moreover, both electric field distribution and its resultant temperature increase in human eye is calculated with FEM method. The all results of TLM based calculations are consistent with that of FEM based calculations.

From temperature rise point of view, Bernardi et al. [4] defined the temperature rise limits as 0.3℃ for lens and 1℃ for cornea tissue. These temperature limits are a tenth of the temperatures at which thermal damage (cataract) to the eye can occur. For all the frequencies this limit is not exceeded in both cases except at 3.6GHz. At this frequency the maximum temperature rise on the cornea is 0.65℃, which is below the limit, while the maximum temperature rise at the lens is around 0.5℃ that its thermal effect may not be neglected and is needed to be investigated further.

REFERENCES

[1] A. Gupta and R. K. Jha, "A survey of 5G network: Architecture and emerging technologies," *IEEE Access*, vol. 3, pp. 1206-1232, July 2015.

[2] P. K. Agyapong, M. Iwamura, D. Staehle, W. Kiess, and A. Benjebbour, "Design considerations for a 5G network architecture," *IEEE Communications Magazine*, vol. 52, no. 11, pp. 65-75, Nov. 2014.

[3] Y. Diao, S. Leung, Y. He, W. Sun, K. Chan, Y. Siu, and R. Kong, "Detailed modelling of palpebral fissure and its influence on SAR and temperature rise in human eye under GHz exposures," *Bio-electromagnetics*, vol. 37, pp. 256-263, Apr. 2016.

[4] P. Bernardi, M. Cavagnaro, S. Pisa, and E. Piuzzi, "SAR distribution and temperature increase in an anatomical model of the human eye exposed to the field radiated by the user antenna in a wireless LAN," *IEEE Transactions on Microwave Theory and Techniques*, vol. 46, no. 12, pp. 2074-2082, Dec. 1998.

[5] A. Hirata, S. Matsuyama, and T. Shiozawa, "Temperature rises in the human eye exposed to EM waves in the frequency range 0.6-6 GHz," *IEEE Transactions on Electromagnetic Compatibility*, vol. 42, no. 4, pp. 386-393, Nov. 2000.

[6] T. Wessapan and P. Rattanadecho, "Specific absorption rate and temperature increase in human eye subjected to electromagnetic fields at 900 MHz," *ASME Journal of Heat Transfer*, vol. 134, no.9, pp. 091101-01-091101-11, July 2012.

[7] Y. Diao, S. Leung, K. H. Chan, W. Sun, Y.-M. Siu, and R. Kong, "The effect of gaze angle on the evaluations of SAR and temperature rise in human eye under plane-wave exposures from 0.9 to 10 GHz," *Radiation Protection Dosimetry*, vol. 172, no. 4, pp. 393-400, Dec. 2016.

[8] T. Wessapan, P. Rattanadecho, and P. Wongchadakul, "Effect of the body position on natural convection within the anterior chamber of the human eye during exposure to electromagnetic fields," *Numerical Heat Transfer, Part A:*

Applications, vol. 69, no. 9, pp. 1014-1028, Jan. 2016.

[9] S. Otsu, T. Michiyama, and S. Kuwano, "Body effect on SAR in the human eye close to metallic spectacles for plane-microwave exposure," *IEICE Communications Express*, vol. 6, no. 10, pp. 602-606, 2017.

[10] S. Kuwano, M. Kobayashi, and T. Michiyama, "SAR analysis in the eye of human whole-body model for plane-microwave exposure," *IEICE Communications Express*, vol. 6, no. 4 pp. 172-176, 2017.

[11] J. Lan, T. Hong, X. Liang, and G. Du, "Evaluation of microwave microdosimetry for human eyes with glasses exposed to wireless eyewear devices at phone call state," *Progress in Electromagnetics Research M*, vol. 63, pp. 71-81, 2018.

[12] N. Cvetković, D. Krstić, V. Stanković, and D. Jovanović, "Electric field distribution and SAR inside a human eye exposed to VR glasses," *IET Microwaves, Antennas & Propagation*, vol. 12, no. 14, pp. 2234-2240, Nov. 2018.

[13] H. F. Milan and K. G. Gebremedhin, "General node for transmission-line modeling (TLM) method applied to bio-heat transfer," *International Journal of Numerical Modelling: Electronic Networks, Devices and Fields*, vol. 31 no. 5, May 2018.

[14] A. Karampatzakis and S. Theodoros, "Numerical model of heat transfer in the human eye with consideration of fluid dynamics of the aqueous humour," *Physics in Medicine & Biology*, vol. 55, no. 19, pp. 5653-5665, Oct. 2010.

[15] Report B from CEPT to the European Commission in response to the Mandate "to develop harmonised technical conditions for spectrum use in support of the introduction of next-generation (5G) terrestrial wireless systems in the union," Harmonised technical conditions for the 24.25-27.5 GHz ('26 GHz') frequency band, 2018.

[16] P. P. Silvester and R. L. Ferrari, *Finite Elements for Electrical Engineers*, Cambridge University Press, Cambridge, UK, 1996.

[17] J. Liu, Z. Ren, and C. Wang, "Interpretations of living tissue's temperature oscillations by thermal wave theory," *China Science Bulletin*, vol. 40, pp. 1493-1495, 1995.

[18] J. Liu, X. Zhang, C. Wang, W.Q. Lu, and Z. Ren, "Generalized time delay bioheat equations and preliminary analysis on its wave nature," *China Science Bulletin*, vol. 42, pp. 289-292, Feb. 1997.

[19] S. Ozen, S. Helhel, and O. Cerezci, "Heat analysis of biological tissue exposed to microwave by using thermal wave model of bio-heat transfer (TWMBT)," *Burns: Journal of the International Society for Burn Injuries*, vol. 34, no. 1, pp. 45-49, Jan. 2008.

[20] W. Kaminski, "Hyperbolic heat conduction equation for materials with a nonhomogeneous inner structure," *ASME Journal of Heat Transfer-Transactions*, vol. 112, pp. 555-560, Aug. 1990.

[21] K. Mitra, S. Kumar, A. Vedavarz, and M. K. Moallemin, "Experimental evidence of hyperbolic heat conduction in processed meat," *ASME Journal of Heat Transfer-Transactions*, vol. 117, pp. 568-573, Aug. 1995.

[22] W. Roetzel, N. Putra, and S. K. Das, "Experiment and analysis for non-Fourier conduction in materials with non-homogeneous inner structure," *International Journal of Thermal Sciences*, vol. 42, pp. 541-552, Oct. 2003.

[23] Y. Zhang, "Generalized dual-phase lag bioheat equations based on non-equilibrium heat transfer in living biological tissues," *International Journal of Heat Mass Transfer*, vol. 52, pp. 4829-4834, Feb. 2009.

[24] S. C. DeMarco, G. Lazzi, W. Liu, J. D. Weil, and M. S. Humayun, "Computed SAR and thermal elevation in a 0.25-mm 2-D model of the human eye and head in response to an implanted retinal stimulator-Part I: Models and methods," *IEEE Transactions on Antennas and Propagation*, vol. 51, no. 9, pp. 2274-2285, Sep. 2003.

[25] T. Wessapan and P. Rattanadecho, "Aqueous humor natural convection of the human eye induced by electromagnetic fields: In the supine position," *Journal of Medical and Bioengineering*, vol. 3, no. 4, Dec. 2014.

[26] K. Wakino, T. Nishikawa, and Y. Ishikawa, "Miniaturization technologies of dielectric resonator filters for mobile communications," *IEEE Transactions on Microwave Theory and Techniques*, vol. 42, no. 7, pp. 1295-1300, July 1994.

[27] M. Höft and M. Thore, "Compact base-station filters using TM-mode dielectric resonators," *German Microwave Conference GeMIC, Karlsrhue*, Mar. 2006.

[28] M. Mantash, A. Kesavan, and T. A. Denidni, "Beam-tilting endfire antenna using a single-layer FSS for 5G communication networks," *IEEE Antennas and Wireless Propagation Letters*, vol. 17, no. 1, pp. 29-33, Nov. 2018.

[29] C. Christopoulos and C. Christopoulos, *The Transmission-line Modeling Method: TLM*, IEEE Press, New York, USA, 1995.

[30] IT'IS Foundation tissue properties database, https://itis.swiss/virtual-population/tissue-properties/database/database-summary/, Accessed on Jan. 21, 2019.

[31] H. P. Schwan and K. R. Foster, "RF-field interactions with biological systems: Electrical properties and biophysical mechanisms," *Proceedings of the IEEE*, vol. 68, no. 1, pp. 104-113, Jan. 1980.

[32] M. A. Stuchly, "Biological effects of electromagnetic

fields," *International Journal of Bioelectromagnetism*, vol. 4 no. 2, pp. 157-160, 2002.
[33] M. A. Eleiwa and A. Z. Elsherbeni, "Debye constants for biological tissues from 30 Hz to 20 GHz," *Applied Computational Electromagnetics Society Journal*, vol. 18, no. 3, pp. 202-213, Nov. 2001
[34] F. Kaburcuk and A. Z. Elsherbeni, "Temperature rise and SAR distribution at wide range of frequencies in a human head due to an antenna radiation," *Applied Computational Electromagnetics Society Journal*, vol. 33, no. 4, pp. 367-372, Apr. 2018.
[35] F. Kaburcuk and A. Z. Elsherbeni, "Efficient computation of SAR and temperature rise distributions in a human head at wide range of frequencies due to 5G RF field exposure," *Applied Computational Electromagnetics Society Journal*, vol. 33, no. 11, pp. 367-372, Nov. 2018.
[36] K. S. Cole and R. H. Cole, "Dispersion and absorption in dielectrics I. Alternating current characteristics," *The Journal of Chemical Physics*, vol. 9, no. 4, pp. 341-351, 1941.
[37] S. Salahuddin, E. Porter, F. Krewer, and M. O'Halloran, "Optimised analytical models of the dielectric properties of biological tissue," *Medical Engineering &Pphysics*, vol. 43, pp. 103-111, Mar. 2017.
[38] H. G. Klinger, "Heat transfer in perfused biological tissue—I: General theory," *Bulletin of Mathematical Biology*, vol. 36, no. 4, pp. 403-415, June 1974.
[39] A. A. Ijjeh and M. Ney, "Local time-step TLM unstructured block meshing for electromagnetic and bio-thermal applications," *IEEE Journal on Multiscale and Multiphysics Computational Techniques*, vol. 2, pp. 174-182, Nov. 2017.
[40] A. Ahlbom, U. Bergqvist, J. H. Bernhardt, J. P. Cesarini, M. Grandolfo, M. Hietanen, A. F. Mckinlay, M. H. Repacholi, D. H. Sliney, J. A. Stolwijk, and M. L. Swicord, "Guidelines for limiting exposure to time-varying electric, magnetic, and electromagnetic fields (up to 300 GHz)," *Health Physics*, vol. 74, no. 4, pp. 494-521, 1998.
[41] M. Cvetkovič, S. Lallechere, K. E. Khamlichi Drissi, P. Bonnet, and D. Poljak, "Stochastic sensitivity in homogeneous electromagnetic-thermal dosimetry model of human brain," *Applied Computational Electromagnetics Society*, vol. 31, no. 6, June 2016.
[42] H. F. Milan and K. G. Gebremedhin, *Journal of Thermal Biology*, vol. 62, pp. 116-122, Feb. 2016.
[43] E. H. Ooi and W. T. Ang, "A boundary element model of the human eye undergoing laser thermokeratoplasty," *Computers in Biology and Medicine*, vol. 38, no. 6, pp. 727-737, July 2008.

Burak Aricioglu was born in 1989. He received B.Sc. and M.Sc. degrees in Electrical and Electronics Engineering from Bogazici University in 2011 and 2014, respectively and Ph.D. degree in Electrical & Electronics Engineering from Sakarya University in 2019. He is, currently, a Research Assistant at Sakarya University of Applied Sciences. His main research interests are nonlinear systems analysis, and bioelectromagnetic interactions.

Abdullah Ferikoglu was born in 1953, received his B.Sc. in Electronics and Communications Engineering from Istanbul Technical University in 1982, his M.S. degree in Electronics and Computer Education from Marmara University in 1992 and Ph.D. degree in Electronics and Communications Engineering department from Istanbul Technical University in 1996. He is now with Sakarya University of Applied Sciences, Electrical and Electronics Engineering Department. His research areas include circuit analysis and design, modeling and simulation, and biomedical engineering.

Dual-Band Bandpass Filter Optimized for High Q-Factor

Walid M. Fahmy [1], Asmaa E. Farahat [1], Khalid F. A. Hussein [1], and Abd-El-Hadi A. Ammar [2]

[1] Microwave Engineering Department
Electronics Research Institute, Cairo, Egypt
walidfahmy48@yahoo.com, asmaa@eri.sci.eg, khalid_elgabaly@yahoo.com

[2] Electronics and Electrical Communications Department, Faculty of Engineering, El-Azhar University, Cairo, Egypt
hady42amar@gmail.com

Abstract ─ High quality factor bandpass filters based on a number of cascaded resonators of dual-resonance mechanism are proposed in the present paper. Each resonator is constructed as two overlapped coplanar waveguide (CPW) resonant structures. The cascaded resonators mediate microwave coupling between two isolated corner-shaped CPW feeders only at the resonant frequencies leading to a bandpass filter of high quality factor. The two resonant frequencies and the separation between them can be fine-tuned by the dimensions of the structure. The effects of the dimensional parameters of the resonator and the feeding CPW regions on the resonant frequencies and the performance of the bandpass filter are investigated. The effect of the loss tangent of the dielectric substrate material on the quality factors at the two resonant frequencies is studied. Three prototypes of the proposed filter are fabricated and experimentally studied for more understanding of the underlying physical principles of operation and for verifying some of the simulation results. The experimental results show good agreement when compared with the corresponding simulation results. It is shown that, at low enough absolute temperature, the proposed structure can operate as superconducting microwave resonator when made from the appropriate materials. Also, it is shown that an optimized design of the proposed bandpass filter, based on superconducting CPWR structure, can achieve quality factors high enough to form a quantum data bus for hybrid architecture of quantum information systems.

Index Terms ─ Band-pass filter, dual-band filter, high-Q filter.

I. INTRODUCTION

A coplanar waveguide (CPW) has the principal advantage that the signal line and the signal grounds are placed on the same substrate surface. This eliminates the need for via holes and, thereby, simplifies the circuit fabrication. Moreover, this allows simple connection of series as well as shunt components [1]. Another main advantage of the CPW is that it exhibits lower conductor loss than microstrip lines [2], [3]. CPW parameters are not sensitive to the substrate thickness, and a wide range of impedance is achievable on reasonably thick substrates. Also, circuits can be built using both the odd and the even CPW modes [4]. Moreover, CPWs are open structures, and do not require metallic enclosures [4].

CPW resonators have their distributed element construction avoiding uncontrolled stray inductances and capacitances, and, thereby, have better microwave properties than lumped element resonators [5]. Another advantage of CPW structures practically arises when performing microwave measurements; that is a series of CPW resonators with different frequencies can be measured using a single feed line, which greatly simplifies the measurement process [6].

The end-coupled and edge-coupled CPW resonator structures are commonly used for microwave and millimeter-wave filter design [7]. In end-coupled resonators, the interchange of energy with the coupling gap may be insufficient, even when very narrow gaps are employed. Due to this reason parallel- or edge-coupled CPWRs are more commonly used than end-coupled CPWRs [7]. Planar structures based on the edge-coupled CPW have been developed as circuit elements for monolithic microwave integrated circuits (MMIC's) [8].

Due to their practical importance, microwave and millimeter-wave bandpass filter design based on CPWRs has attracted the attention of many research works. In [1], the design of high-quality bandpass filter employing shunt inductively coupled CPW resonators is introduced and shown to exhibit low radiation loss due to the removal of the capacitively coupled gaps encountered in bandpass filter employing end or edge coupled CPW resonators. In [9], a cross-coupled CPW structure design is proposed for bandpass filter, which is constructed by cascading several sections of quarter wavelength open-end series stubs. In [10] and [11], compact edge-coupled

Submitted On: December 17, 2019
Accepted On: January 28, 2021

https://doi.org/10.47037/2020.ACES.J.360405

CPW bandpass filter designs are proposed for operation at microwave and millimeter-wave frequencies.

Superconducting CPWRs with large internal quality factors of typically several hundred thousand can be routinely realized [5]. Such resonators find a wide range of applications as radiation detectors in the optical, ultraviolet, and x-ray frequency range, in parametric amplifiers, for magnetic field tunable resonators and to act as quantum data bus for superconducting qubits [6], [5].

The present work proposes a design of a bandpass filter of high quality factor. The proposed filter is constructed as two feeding CPW regions which are parallel-coupled (or edge-coupled) to a CPW resonating structure. As long as the operating frequency is far from the resonant frequencies of the CPW resonating structure, the feeding CPW regions are isolated from each other preventing any possible power transfer from one port of the filter to the other. Only at the resonant frequencies the feeding CPW regions are coupled to each other via the CPW resonating structure and, thereby, allowing power transfer between the filter ports. Some prototypes of the proposed filter are fabricated and experimentally studied for more understanding of the underlying physical principles of operation and for verifying some of the simulation results. The experimental results show good agreement when compared with the corresponding simulation results. Near zero-Kelvin absolute temperature, the proposed structure can operate as superconducting microwave resonator when made from the appropriate materials, where a quality factor high enough to form a quantum data bus for hybrid architecture of quantum information systems can be achieved.

II. PROPOSED BANDPASS FILTER DESIGNS

The proposed bandpass filter has the sketch of its geometry shown in Fig. 1 with the indicated symbolic dimensional parameters. This filter is constructed as two feeding (normally isolated) corner-shaped CPW regions which are (capacitively) parallel-coupled (at resonance) to the dual-resonant CPW structure. The design of higher-order BPF for each pass-band can be based on using cascaded resonators to mediate coupling between the isolated CPW feeding regions as shown in Fig. 1 (a).

For the design shown in Fig. 2, the dual-resonator structure can be considered as composed of two overlapped resonators. One of them is a half-wavelength CPWR, which is short-circuited at its both ends and forms the perimeter of U-shape. The other resonator is a straight CPWR of relatively wide central conductor formed by the area subtended between the arms of the U-shape. This CPWR is open-circuited at the base of the U-shape and short-circuited at the other end (top of the U-shape) and, thus forms a quarter-wavelength resonator. As long as the operating frequency is far from the resonant frequencies of the dual CPWR structure, the corner-shaped CPW feeding regions are isolated from each other leading to zero power transfer between the filter ports (1) and (2). Only at the resonant frequencies, the CPW feeders are parallel-coupled to the dual-resonant CPW structure and, hence, the power transfer can occur only at these frequencies leading to high-quality factor bandpass filter response.

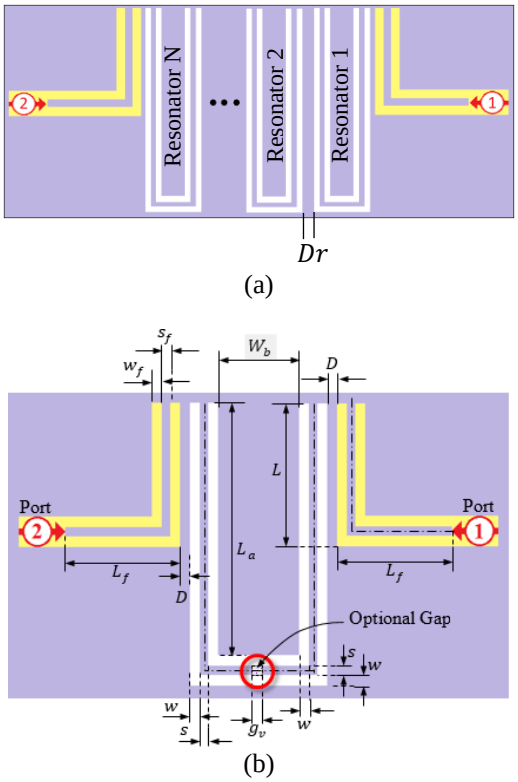

Fig. 1. Schematic of the proposed design for high quality-factor dual-band BPF: (a) Higher-order BPF based on cascaded CPW resonators, and (b) dimensional parameters.

A dual-bandpass filter design is shown in Fig. 3, which can be considered as a modification of the filter design shown in Fig. 2. The difference is a gap made in the central conductor of the short-ended CPW region forming the perimeter of the U-shape. The gap divides the U-shaped CPW region into two symmetric CPW regions of mirrored-L shape; each of them is short-circuited at one end and open-circuited at the other end and, thus, forming two identical quarter-wavelength resonators.

A single-bandpass filter design is shown in Fig. 4. This design can be considered as a modification of the design shown in Fig. 3 by making two other gaps; each gap is cut in one of the central conductors of the two quarter-wavelength resonators forming the mirrored-L shape. The purpose of these gaps is to diminish or damp

the resonance of the two quarter-wavelength CPW resonators forming the mirrored-L so as to get the new design working as a high-quality-factor single-bandpass filter.

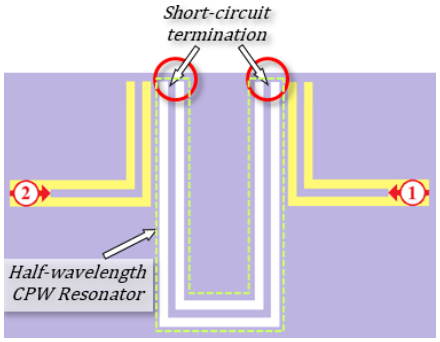

(a) The first resonant mechanism (Lower pass band)

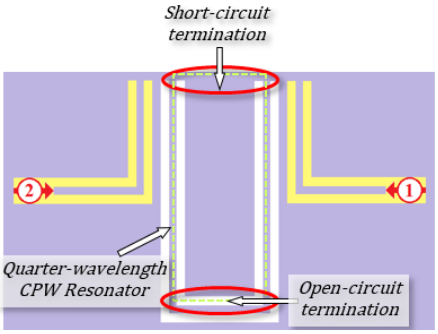

(b) The second resonant mechanism (Upper pass band)

Fig. 2. Mechanisms of resonance in the proposed bandpass filter based on dual-CPWR structure.

III. THEORETICAL BASIS OF OPERATION

For simplified analysis of the proposed bandpass filter designs, simple configurations of end-coupled CPWRs are considered. The simplest method to create a CPWR is to make a gap in the central conductor as shown in Fig. 5 (a) or to short the central conductor to the side (ground) conductors as shown in Fig. 5 (b). The gap can be considered as a series capacitance C_g between the central conductor of the feeder waveguide region and the central conductor of the resonator. The short constitutes a shunt inductance L_s between the central conductor and the side ground conductors. Both configurations result in half-wavelength resonator over which the standing wave has the current and voltage distributions as those shown in Fig. 5 (a) and 5 (b). A third configuration of transmission line resonators is to terminate a CPW region by a series gap at one of its ends and to terminate the other end by a shunt short as shown in Fig. 5 (c). This creates a quarter-wavelength resonator in which a standing wave exists with the voltage and current distributions presented in the same figure. The CPW region between the two shorts, the two gaps, or the gap and short has a length l_R and constitutes a CPWR which is end-coupled to the main feeder through the terminating gaps or shorts. The gap terminations create capacitive coupling between the CPW feeder and the CPWR, whereas the short terminations create inductive coupling.

For half-wavelength transmission line resonators, the resonant frequencies can be expressed as follows [12]:

$$f_n^{(1/2)} = ,n\,c\ /2l_R\sqrt{\varepsilon_{r_{eff}}}\ n = 1,2,\ldots \qquad \text{(1-a)}$$

where c is the velocity of light in free space, n is the mode order, and $\varepsilon_{r_{eff}}$ is the effective dielectric constant of the quasi-TEM mode of the CPW. For the quarter-wavelength transmission line resonators, the resonant frequencies can be expressed as follows:

$$f_n^{(1/4)} = (2n-1)\,c/l_R\sqrt{\varepsilon_{r_{eff}}},\ n = 1,2,\ldots \qquad \text{(1-b)}$$

The effective dielectric constant of the quasi-TEM mode of the CPW can be expressed as follows [13]:

$$\varepsilon_{r_{eff}} = 1 + \varepsilon_r - 1/2\ K(\acute{k}_0)/K(k_0)\ K(k_1)/K(\acute{k}_1), \qquad (2)$$

where ε_r is the dielectric constant of the substrate material and K denotes the complete elliptic integral of the first kind, which is defined as follows:

$$K(k) = \int_0^{\frac{\pi}{2}} d\theta/\sqrt{1-k\,sin^2\,\theta} \qquad (3)$$

The arguments, k_0, $\acute{k}_0$, k_1, and $\acute{k}_1$, of K are defined as follows:

$$k_0 = s/s+2w,\ \ \acute{k}_0 = \sqrt{1-k_0^2},\ \ k_1 = \sinh(\pi s/4h)/\sinh[\pi(s+2w)/4h],\ \ \acute{k}_1 = \sqrt{1-k_1^2}, \qquad (4)$$

where s is the width of the central conductor, w is the width of each slot, and h is the height of the dielectric substrate. The characteristic impedance of the quasi-TEM mode of the CPW is expressed as follows [13]:

$$Z_0 = 30\pi/\sqrt{\varepsilon_{r_{eff}}}\ K(\acute{k}_0)/K(k_0). \qquad (5)$$

A. Estimation of the quality factor of the bandpass filter

Two types of U-shaped CPWR which are parallel edge-coupled to the L-shaped CPW feeder are shown in Fig. 3. Definitely, the edge coupling between the resonator and the feeding CPW regions has the capacitive coupling effect as regards the external loading

on the resonator. As a consequence, the resonance frequency can be shifted due to the reactive coupling as part of the energy is stored in the electric field of the coupling capacitance. Besides, due to such capacitive coupling, the resultant (loaded) quality factor (Q_l) is decreased as the edge coupling to the feeding transmission lines can be considered as a loss channel. The coupling (external) quality factor Q_e, which is related to the edge (capacitive) coupling between the resonator and the feeder, dominates the resultant (loaded) quality factor. Thus, the total quality factor can be evaluated through the following relation:

$$1/Q_l = 1/Q_u + 1/Q_e, \quad (6)$$

where, Q_u is the self or internal (unloaded) quality factor of the CPWR without being coupled to the feeding transmission line.

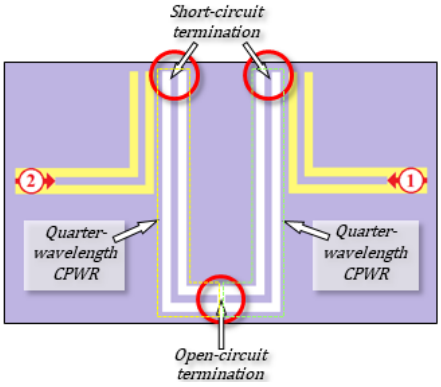

Fig. 3. Dual-bandpass filter based on two mirrored-L-shaped quarter-wavelength resonators subtending and overlapping with a third straight quarter-wavelength resonator.

B. Unloaded quality factor of the half-wavelength CPWR on the perimeter of the U-shape

For the bandpass filter design shown in Fig. 2, the CPW region forming the perimeter of the U-Shape can be considered a short-circuited half-wavelength transmission line resonator. As shown in [14], the unloaded quality factor of both short-circuited and open-circuited half-wavelength CPWR, the quality factor can be expressed as follows:

$$Q_u = \pi/2\alpha l_{R\frac{1}{2}} = \beta_0\sqrt{\varepsilon_{r_{eff}}}/2\alpha = \omega_0\sqrt{\varepsilon_{r_{eff}}}/2c\alpha, \quad (7)$$

where, $l_{R_{1/2}}$ is the length of the half-wavelength resonator, β_0 is the free space wave number, ω_0 is the resonant angular frequency, α is the attenuation constant of the CPW, and $\varepsilon_{r_{eff}}$ is given by (2).

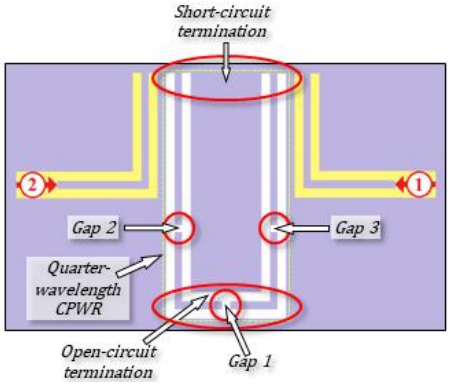

Fig. 4. Single-bandpass filter based on a single quarter-wavelength resonator.

C. Unloaded quality factor of the quarter-wavelength CPWR subtended between the arms of the U-shape

As mentioned in Section II, the CPW region whose center conductor is subtended between the arms of the U-Shape shown in Fig. 2 is open-circuited at one end and short-circuited at the other end and, hence, it can be considered as quarter-wavelength resonator. As shown in [14], a short-circuited quarter-wavelength transmission line has the same expression as (7) for the unloaded quality factor. For open-circuited quarter-wavelength transmission line, the input impedance can be calculated as follows:

$$Z_{in} = Z_0 \tanh \alpha l - j \cot \beta l / 1 - j \tanh \alpha l \cot \beta l. \quad (8)$$

Let $\omega = \omega_0 + \Delta\omega$, and assume $l = l_{R_{1/4}} = \lambda/4$ at ω_0, hence, near the resonance for a TEM line:

$$\beta l \approx \beta l_{R_{1/4}} = \pi/2 + \pi/2\,\Delta\omega/\omega_0. \quad (9)$$

Thus,

$$\cot \beta l_{R_{1/4}} = -\tan \pi/2\,\Delta\omega/\omega_0\,. \quad (10)$$

For low-loss quarter-wavelength transmission line resonator near resonance, $\alpha l_{R_{1/4}} \ll 1$, and $\Delta\omega/\omega_0 \ll 1$, hence,

$$\cot \beta l_{R_{1/4}} \approx -\pi/2\,\Delta\omega/\omega_0\,,\ \tanh \alpha l_{R\frac{1}{4}} \approx \alpha l_{R\frac{1}{4}}. \quad (11)$$

Substituting from (11) into (8), the expression of Z_{in} is reduced to:

$$Z_{in}Z_0\ \alpha l + J\,\pi/2\,\Delta\omega/\omega_0/1 + J\alpha l\,\pi/2\,\Delta\omega/\omega_0. \quad (12)$$

For low loss CPWR in a narrow frequency band around the resonance, one has $\alpha l\Delta\omega/\omega_0 \ll 1$ and, hence the expression (12) can be reduced to take the following form:

$$Z_{in} \approx Z_0(\alpha l + J\,\pi/2\,\Delta\omega/\omega_0). \quad (13)$$

For a resonant series RLC circuit, $\omega_0 = 1/\sqrt{LC}$ and, in a narrow frequency band around the resonance, the circuit impedance can be expressed as follows [14]:

$$Z = R + j2L\,\Delta\omega. \quad (14)$$

By comparison between (13) and (14) one finds,

$$R = Z_0\alpha l, \quad L = Z_0\pi/4\omega_0\,, \quad C = 1/\omega_0^2 L = 4/\pi Z_0\omega_0. \quad (15)$$

Also, for series RLC resonant circuit, the quality factor can be expressed as follows [14]:

$$Q_{RLC} = \omega_0 L/R = 1/\omega_0 RC. \quad (16)$$

Making use of (15) and (16), the unloaded quality factor of an open-circuited quarter-wavelength CPWR can be expressed as follows:

$$Q_u = \pi/4\alpha l_{R_{1/4}} = \beta/2\alpha = \beta_0\sqrt{\varepsilon_{r_{eff}}}/2\alpha = \omega_0\sqrt{\varepsilon_{r_{eff}}}/2c\alpha, \quad (17)$$

where, β_0 is the wavenumber of free space. In general, for low loss transmission line:

$$Z_0 \approx \sqrt{L_T/C_T}\,, \quad \alpha \approx 1/2\,(R_T/Z_0 + G_T Z_0), \quad \beta \approx \sqrt{L_T C_T}\,, \quad (18)$$

where, R_T, L_T, C_T, and G_T are, respectively, the resistance, inductance, capacitance and conductance per unit length of the lumped-element circuit model of the transmission line.

IV. RESULTS AND DISCUSSIONS

In the present section, both the numerical results obtained by simulation and the experimental results obtained by microwave measurements of the fabricated bandpass filter prototypes are presented, discussed and compared for the purpose of arriving at accurate performance assessment and understanding of the resonance mechanisms underlying the filter operation.

It should be noted that the following presentations and discussions of numerical and experimental results are concerned with a dual bandpass filter as that shown in Fig. 2 designed with the following dimensional parameters, unless otherwise stated: $s = s_f = 0.1$ mm, $w = w_f = 0.2$ mm, $W_b = 2.4$ mm, $L_a = 26$ mm, $L_f = 10.3$ mm, $D = 0.35$ mm, and $L = 10.4$ mm. The substrate material has dielectric constant $\varepsilon_r = 3.38$, and height $h = 0.2$ mm. The metal strips and ground are made of copper and have conductivity $\sigma = 5.6 \times 10^7$ S/m. It should be noted that other materials are assumed when presenting the results concerned with filters designs based on superconducting CPWR which is indicated during the discussions.

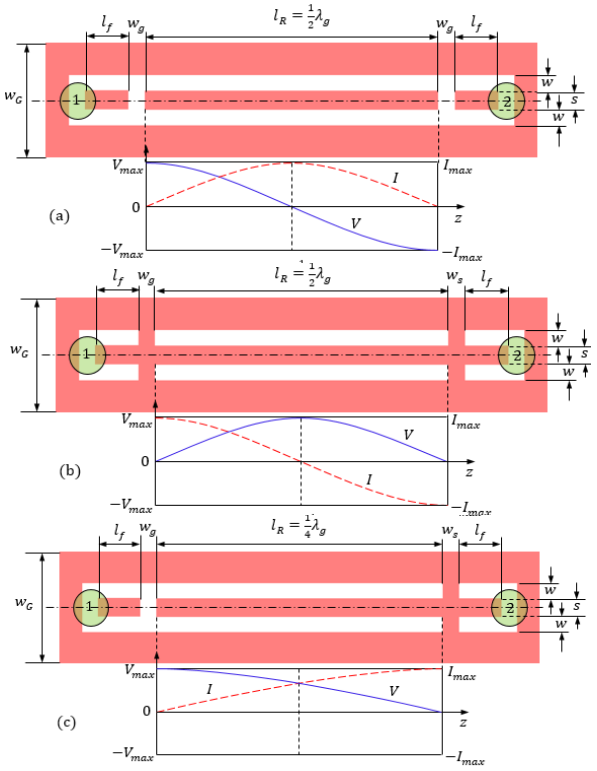

Fig. 5. Different regimes of CPW resonators: (a) open-ended, half-wavelength CPWR, (b) short-ended half-wavelength CPWR, and (c) open/short-ended quarter-wavelength CPWR.

A. Performance comparison of multi-resonator BPF

This section is dedicated for the performance comparison of cascaded dual-band BPF employing single, double, and triple resonators arranged as shown in Fig. 1 (a). The design dimensions are $w = 0.4$ mm, $L_a = 15.3$ mm, $L = 14$ mm, $L_f = 4.4$ mm, $s_f = 0.5$ mm, $w_f = 0.4$ mm, $W_b = 1$mm, $D = 0.2$ mm, $Dr = 0.1$mm. The frequency response of the transmission coefficient of the first band centered at 2.02 GHz for the BPF composed of one, two, and three resonators is plotted in Fig. 6. It is clear in the figure that the design of the BPF constructed from single dual-band resonator has a sharp behavior and narrower bandwidth than the designs employing double and triple resonators. The quality factor is also higher for a BPF with single resonator. For this reason, the next discussions will deal with the results of performance assessment of BPF composed of only single resonator.

B. Frequency response of bandpass filter based on half-wavelength CPWR of U-shape

The frequency response of the transmission

coefficients $|S_{21}|$ of the proposed dual bandpass filter having the same design as that shown in Fig. 2, under the assumption of perfect conductor and lossless dielectric substrate, is presented in Fig. 7. The frequency response exhibits two sharp peaks: the first peak is at $f = 1.9405$ GHz , with quality factor $Q = 6130$, whereas the second peak is at $f = 2.169$ GHz, with quality factor $Q = 1000$. The mechanisms of resonance leading to these values of the resonant frequencies and the corresponding quality factors are explained in the following subsection.

The two corner-shaped CPW regions of the main feeder are coupled to each other only at the resonances of each of the two CPW resonators formed by the U-shape as mentioned above. The frequency response of the filter transfer function has two sharp peaks as shown in Fig. 7. The first peak corresponds to the first resonance of the half-wavelength CPW resonator on the perimeter of the U-shape which is short-circuited terminated at its both ends. The second peak corresponds to the first resonance of the quarter-wavelength CPW resonator whose central conductor is the area subtended between the arms of the U-shape. The side (ground) conductors for this CPW are actually the central conductor of the CPW on the perimeter of the U-shape mentioned above. As shown in the sketch of the geometry presented in Fig. 2, these side conductors have much narrower width in comparison to the width of the central conductor. This resonator is open circuit terminated at the base of the U-shape and is short-circuit terminated at the other end. This is more elaborated showing illustrations of the current and field distributions on the resonator in the following two subsections.

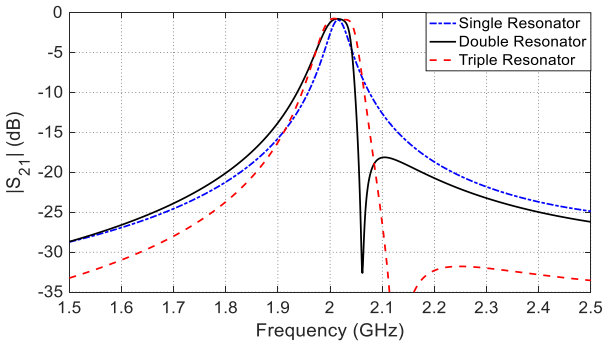

Fig. 6. $|S_{21}|$ for the first band of cascaded dual-band BPF designed with one, two, and three resonators.

B.1. Mechanism of resonance in the lower pass Band

At the lower resonant frequency (1.9405 GHz) of the short-circuit-terminated CPWR formed by the perimeter of the U-shape, the surface current distribution is presented in Fig. 8. It is shown that, like a short-ended half-wavelength resonator, as explained in Section III and illustrated in Fig. 5 (b), the current has its maximum magnitude at the short-circuited terminals of the resonator whereas the current node of the standing wave is at the middle of the resonator length. The electric field distribution in the slots of this CPW is presented in Fig. 8 which exhibits the behaviour of the (even) quasi-TEM mode of the CPW formed by the arms of the U-shape. As this CPW region is a half-wavelength resonator whose total length is 55.2 mm, the resonant frequency can be calculated using (1-a), which gives $f_0^{(1/2)} = 1.914$ GHz. The slight deviation of the resonant frequency obtained by simulation from the theoretical value given by (1-a) can be attributed to the reactive load resulting from coupling the CPW feeder to the CPWR as part of the energy is stored in the electric field of the coupling capacitance and, thereby causing a shift of the resonant frequency . Moreover, a part of the frequency shift can be attributed to the error of the approximate analytic formula for $\varepsilon_{r_{eff}}$ given by (2).

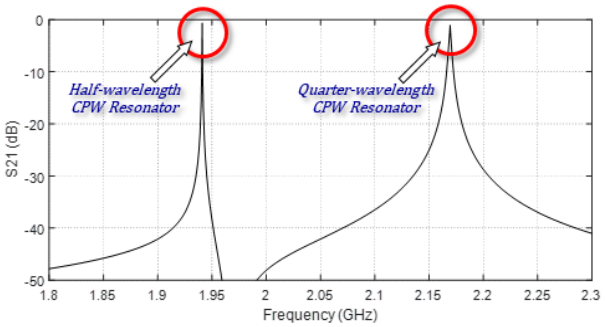

Fig. 7. Frequency response of the bandpass filter (with the design shown in Fig. 2) based on half-wave length CPWR with U shape subtending another quarter-wavelength CPWR.

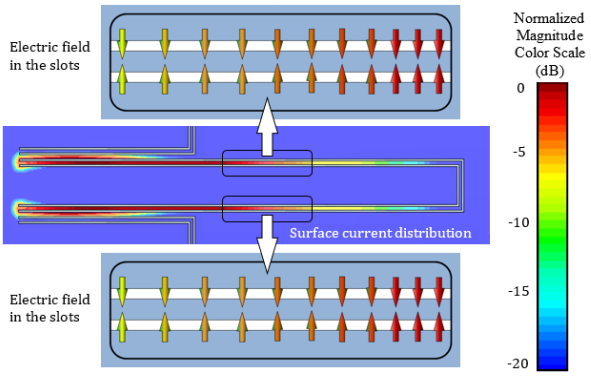

Fig. 8. Surface current on the conductors and electric field distribution in the slots at the resonant frequency corresponding to the short-circuit terminated half-wavelength CPW resonator, $f = 1.9405$ GHz.

B.2. Mechanism of resonance in the upper pass band

At the higher resonant frequency (2.169 GHz) of the CPWR whose central conductor is the region subtended between the arms of the U-shape, the surface current distribution is presented in Fig. 9. This CPW region is open-circuit terminated at the base of the U-shape and is short-circuit terminated at its other end. It is shown that, like a quarter-wavelength resonator, as explained in Section II and illustrated in Fig. 5 (c), the current has its maximum magnitude at the short-circuit terminal whereas the current node is at its open-circuit terminal. As this CPW region is a quarter-wavelength resonator whose length is 26.0 mm, the resonant frequency can be calculated using (1-b), which gives $f_0^{(1/4)} = 2.311$ GHz. In addition to the approximation error of the analytical formula given by (2) for $\varepsilon_{r_{eff}}$, the slight deviation of the resonant frequency obtained by simulation from the theoretical value given by (1-b) can be attributed to the reactive load resulting from coupling the CPW feeder to the CPWR as part of the energy is stored in the electric field of the coupling capacitance and, thereby causing a shift of the resonant frequency.

C. Frequency response of BPF based on quarter-wavelength CPWR with mirrored-L shape

For the bandpass filter design shown in Fig. 3, which is based on two identical quarter-wavelength CPWRs forming a Mirrored-L shape, the corresponding frequency response of the transmission coefficient, $|S_{21}|$, of a lossless filter is shown in Fig. 10. By comparison to the bandpass filter of the design shown in Fig. 2, whose frequency response is presented in Fig. 7, it is shown that their frequency responses of the transmission coefficients seem to be identical. However, this is not actually true as the quality factor at the lower frequency band for the filter design based on two quarter-wavelength resonators concerned in this section is $Q = 14{,}300$, which is much higher than that obtained by the filter design shown in Fig. 2 whose quality factor is $Q = 6{,}130$ as presented in Section IV.A. Also, the quality factor for the upper pass band is improved from $Q = 1{,}000$ for the old design to $Q = 1{,}100$ for the new design. The results for comparison between the two designs are presented in Table 1. Thus, the main advantage of the gap made in the central conductor at the middle of the base of the U-shape is the considerable improvement of the quality factor especially for the lower pass band.

D. Effect of dielectric losses on the performance of the bandpass filter based on CPWR

It is well-known that the quality factor of a resonant structure is reduced with increasing the losses. The purpose of the present section is the quantitative assessment of dependence of the quality factor of the proposed bandpass filter on the dielectric losses of the substrate material.

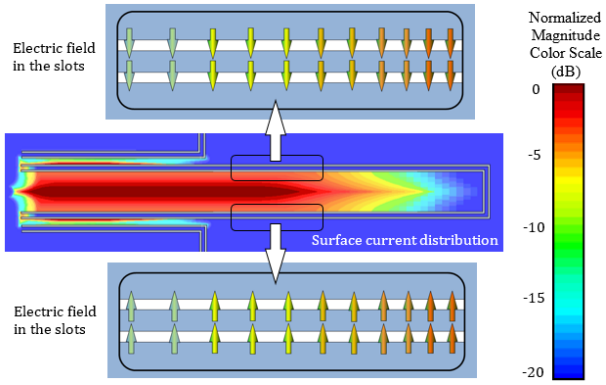

Fig. 9. Surface current on the conductors and electric field distribution in the slots of the CPWR at the resonant frequency corresponding the quarter-wavelength CPWR subtended between the arms of the U-shape, $f = 2.169$ GHz.

Table 1: Comparison between the resonant frequencies and quality factors of the bandpass filter designs shown in Fig. 2 and Fig. 3

Base of U-shape	Lower Pass Band			Upper Pass Band		
	Resonance Regime	f_0 (GHz)	Q	Resonance Regime	f_0 (GHz)	Q
Solid	1/2-Wavelength	1.9405	6130	1/4-Wavelength	1.1695	1000
Slotted	1/4-Wavelength	1.9404	14300	1/4-Wavelength	1.1697	1100

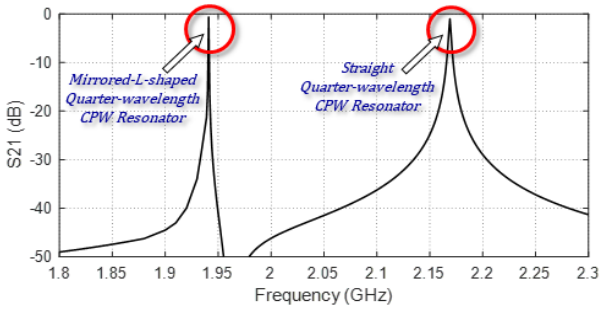

Fig. 10. Frequency response of the bandpass filter (with the design shown in Fig. 3 based on two identical quarter-wavelength CPWRs forming a mirrored-L shape.

D.1. Effect of dielectric loss on the quality factor of the half-wavelength CPWR with U-shape

The effects of the losses of the dielectric substrate on the filter response at the lower and higher frequency pass bands are presented in Fig. 11. It is shown that, for the lower and upper bands, the peak of $|S_{21}|$ is decreased, the bandwidth is increased and, consequently, the quality factor is significantly decreased with increasing the loss tangent ($\tan\delta \approx \delta$) of the substrate material. Generally,

the bandpass performance is considerably degraded with increasing the dielectric losses. Due to its higher quality factor, the lower frequency pass band is considerably more affected by the dielectric loss than the higher frequency pass band.

D.2. Effect of dielectric loss on the quality factor of the quarter-wavelength CPWR with mirrored-L shape

The higher the quality-factor of a resonator, the worse the effect of losses on the frequency response of its transfer function. As discussed in Section IV-C, the bandpass filter employing a quarter-wavelength CPWR with mirrored-L shape has a considerably higher quality factor than that of the bandpass filter employing half-wavelength U-shaped CPWR. As a consequence, the quality factor of the former bandpass filter is more badly affected by the dielectric losses. This may be more clear when investigating the frequency response of the of the transmission coefficients $|S_{21}|$ for this filter which is presented in Fig. 12.

D.3. Comparison between the effects of dielectric loss on the quality factors of single half-wavelength and double quarter-wavelength resonators

The dependence of the quality factor on the dielectric loss tangent of the substrate material for the bandpass filter employing U-shaped half-wavelength CPWR subtending another quarter-wavelength CPWR, in comparison to that employing two quarter-wavelength CPWRs of mirrored-L shape subtending a third quarter wavelength CPWR, is presented in Fig. 13. In the lower pass band the quality factor obtained in the case of double quarter-wavelength resonator is much larger than that obtained by employing single half-wavelength resonator over the indicated range of δ as shown in Fig. 13 (a). By comparing the Q-δ relation in the lower pass band, presented in Fig. 13 (a) to the Q-δ relation in the upper pass band, presented in Fig. 13 (b), it becomes clear that the quality factor rapidly decays with increasing the loss tangent in a manner such that the higher the quality-factor the higher the slope of decay. Also, by comparing the slopes of the Q-δ curves for the two pass bands it becomes clear that the decay of Q with increasing δ for the lower pass band is considerably steeper than that of the upper pass band due to the considerable larger value of Q in the lower pass band for both filter designs.

E. Experimental assessment of dual-bandpass filters based on Dual-CPWR

The purpose of the experimental work is to study the underlying physical principles of operation and to investigate the performance of the proposed high quality factor bandpass filter based on dual-resonance mechanism.

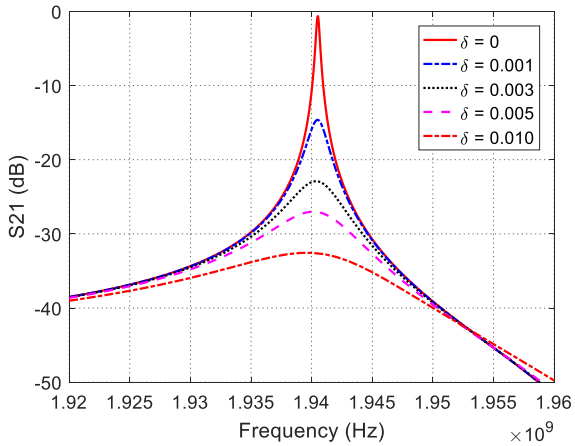

(a) Filter response in the lower pass band

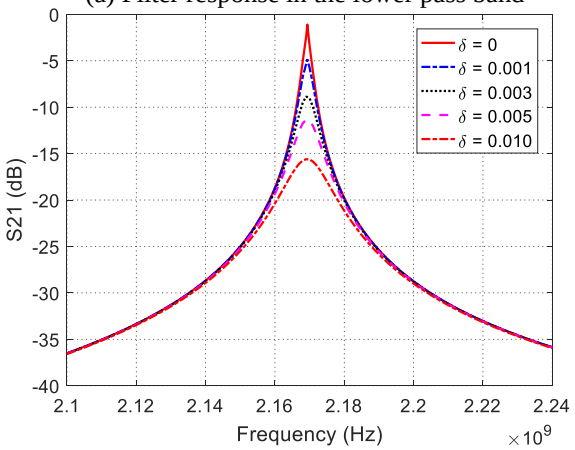

(b) Fiter response in the higher pass band

Fig. 11. Effect of dielectric substarte loss on the frequency response of the transmission coefficients $|S_{21}|$ for the BPF based on half-waevlength CPWR with U-shape.

E.1. Fabrication of prototypes for the proposed bandpass filter

Three prototypes of the proposed bandpass filter are fabricated for experimental studying of the underlying physical principles of operation. The substrate used for fabrication is RO4003C™, with substrate height $h = 0.2$ mm, dielectric constant $\varepsilon_r = 3.38$ and dielectric loss tangent $\delta = 0.0021$ at 2.5 GHz. The same design dimensions given at the beginning of section IV are used for fabrication. A photograph of the fabricated prototypes is presented in Fig. 14.

Prototype '1' is fabricated for the bandpass filter design shown in Fig. 2 with the dimensional parameters given at the beginning of Section IV. This filter is composed of a U-shaped half-wavelength CPWR overlapping with another quarter-wavelength CPWR of wide central conductor which is sandwiched between the arms of the U-shape.

The prototype '2' is fabricated for the bandpass filter design shown in Fig. 3. Its shape similar to that of prototype '1' with a basic difference is that the single half-wavelength U-shaped CPWR is replaced by two identical quarter-wavelength resonators forming a shape of mirrored-L as shown in Fig. 3. This is simply achieved by modifying prototype '1' by cutting a gap in the central conductor at the middle point of the base of the U-shaped CPWR. Thus, the resulting prototype '2' can be considered as bandpass filter composed of three quarter-wavelength CPW resonators which are parallel and overlapped.

Prototype '3' is fabricated for the bandpass filter design shown in Fig. 4. It is made by modifying prototype '2' by etching two other gaps each gap is cut in one of the two quarter-wavelength resonators forming the mirrored-L of prototype '2'. The purpose of these gaps is to damp or reduce the resonance of the two quarter-wavelength CPW resonators forming the mirrored-L so as to get prototype '3' working as a high-quality-factor single-bandpass filter.

E.2. Experimental setup

The vector network analyzed (VNA) of the Keysight (Agilent) FieldFox N9928A is used to measure the transmission and reflection coefficients $|S_{21}|$ and $|S_{11}|$, respectively, of the bandpass filter prototype under test. For this purpose the filter prototype is mounted on the substrate test fixture as shown in Fig. 15 (a). After performing the required settings and calibration procedure, the test fixture holding the prototype under test is connected to the VNA as shown in Fig. 15 (b).

E.3. Experimental results

It should be noted that, for the three fabricated prototypes shown in Fig. 14, the bandpass filters have the designs shown in Figs. 2, 3, and 4, respectively, with the values of the design parameters given at the beginning of Section IV, in addition to the following dimensions for the gaps cut in the central conductors as modifications of the original filter design: $g_v = g_h = 0.2$ mm, $d_v = 1.25$ mm, and $d_h = 5.1$ mm.

The frequency response of the transmission coefficient of the prototype '1' for the proposed bandpass filter as measured by the VNA is presented in Fig. 16 and compared to that obtained by simulation using the commercially available CST® software package. Both the experimental and simulation results show that the peak of $|S_{21}|$ in the lower pass band is considerably more decreased due to the dielectric losses than that of the upper pass band. The experimental measurements and simulation results show good agreement except for a little shift of the resonant frequency of the lower band, which is, most probably, attributed to the losses encountered in the measurement process.

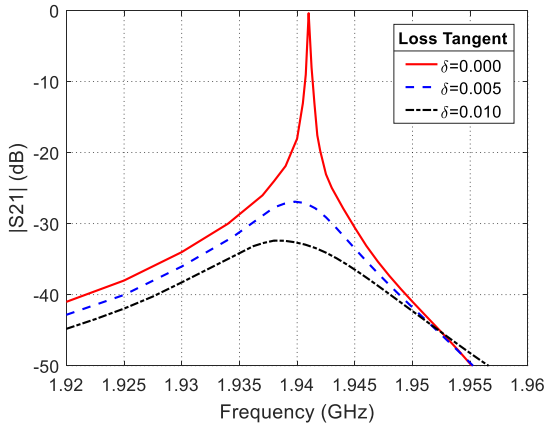

(a) Filter response in the lower pass band

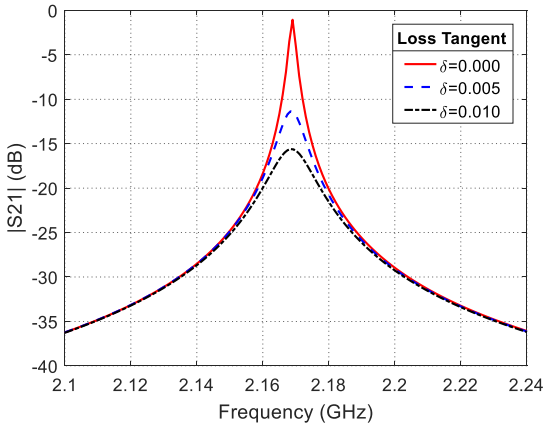

(b) Filter response in the higher pass band

Fig. 12. Effect of dielectric substarte loss on the frequency response of the transmission coefficients $|S_{21}|$ for the bandpass filter based on quarter-wavelength CPWR with mirrored L-shape.

The frequency response of the transmission coefficient of prototype '2' which is fabricated for a bandpass filter employing double quarter-wavelength CPWR subtending a third quarter-wavelength CPWR as measured by the VNA is presented in Fig. 17 and compared to that obtained by simulation using the CST® software package. Both the experimental and simulation results show that the peak of $|S_{21}|$ in the lower pass band is considerably more decreased due to the dielectric losses than that obtained for the bandpass filter prototype '1' due to the considerably higher quality factor of the former bandpass filter. This comes in agreement with the simulation results presented in both Figs. 11 and 12 where the quality factor of the lower frequency pass band is shown to be more degraded due to the dielectric loss than that of the upper pass band. Thus, both the simulation and experimental results leads us to arrive at the same conclusion: the higher the quality factor the worse the effect of the dielectric loss on the bandpass

filter response. Also, the experimental measurements and simulation results show good agreement except for a little shift of the resonant frequency of the lower band, which is, most probably, attributed to the losses encountered in the measurement process.

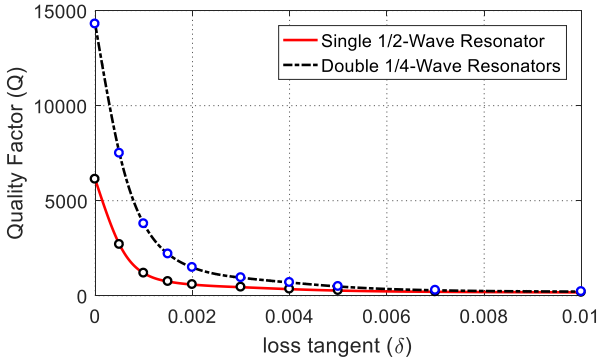

(a) Q versus δ for the lower pass band

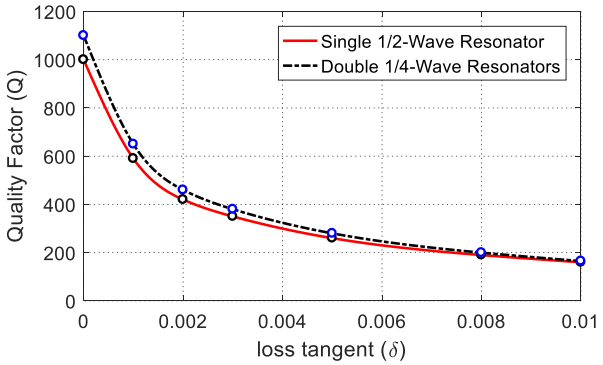

(b) Q versus δ for the higher pass band

Fig. 13. Comparing the dependence of the quality factor, Q, on the dielectric loss tangent, δ, for the bandpass filter with half-wavelength CPWR of U shape to that of the bandpass filter with two quarter-wavelength CPWRs forming a mirrored-L shape.

The prototype '3' is fabricated for a single-bandpass filter that employs a single quarter-wavelength CPWR and, hence, exhibits a single resonance. The frequency responses of the transmission and reflection coefficients $|S_{21}|$ and $|S_{11}|$, respectively, of this filter are presented in Fig. 18. The measurements are achieved by the VNA and compared to that obtained by simulation using the CST® software package. The experimental measurements and simulation results show good agreement. The quality factor obtained for the fabricated prototype '3' of the proposed single-bandpass filter is $Q = 102$, whereas that calculated through simulation is $Q = 167$. The deviation of the measured quality factor than that calculated by simulation is most probably attributed to the losses encountered in the measurement process.

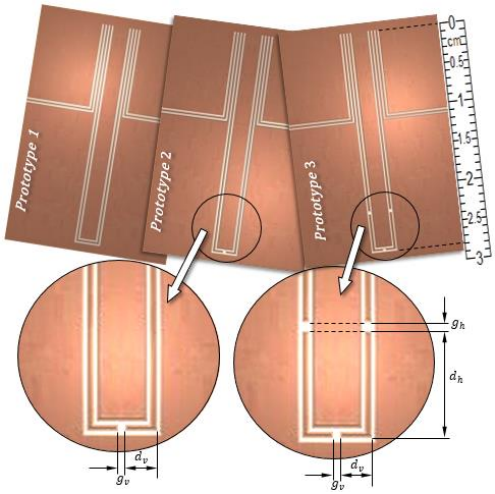

Fig. 14. Three fabricated prototypes for the proposed high quality bandpass filter.

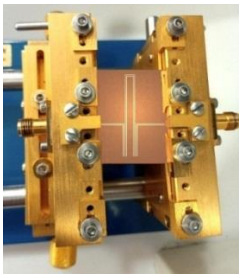

(a) The fabricated BPF mounted on the VNA test fixture

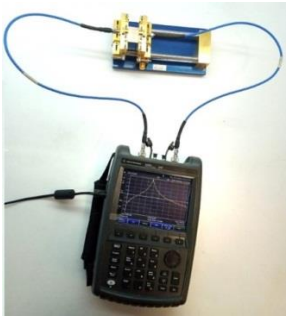

(b) The test fixture connected to the VNA

Fig. 15. Measurement of the frequency response of the fabricated prototypes.

F. Improvement of the quality factor of the bandpass filter

As mentioned in the introduction of the present paper, the high quality-factor superconducting CPWR is required in many applications such as a quantum data bus for hybrid quantum information systems. In this section, some modifications of the proposed BPF design are suggested to increase the quality factor so as to be

valid for applications like that mentioned above when it is fabricated form a metal that exhibits superconductivity at achievable low Kelvin temperature and printed on a substrate of a lossless dielectric material. Thus the dual-resonant structure is constructed as superconductor CPWR printed on a lossless dielectric substrate.

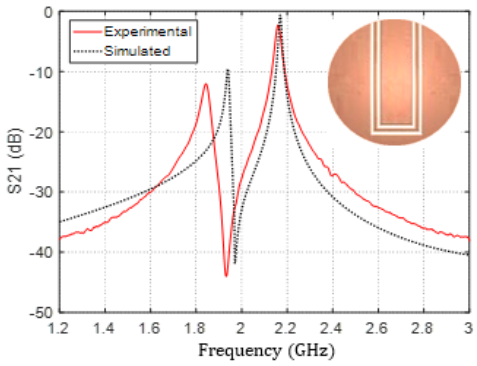

Fig. 16. Frequency response of the transmission coefficient $|S_{21}|$ of the BPF prototype '1' of the original (No-gap) filter design.

F.1. Dual-band BPF based on open-circuited U-shaped CPWR

It may be interesting to investigate the bandpass filter response when the short-circuit terminations at the ends of the CPWR formed by the perimeter of the U-shape, presented in Fig. 2, are replaced by open-circuit terminations. It is expected that such a replacement may lead to a significant change of the filter response at its lower pass band due the major change of the current distribution along the arms of the U-shape at its resonant frequency. As the quarter-wavelength CPWR whose central strip is the area subtended between the arms of the U-shape is geometrically unaffected by the termination replacement, it is expected that the filter response at its upper pass band will not be significantly different from the response of the previous design in this band of the frequency.

F.2. Comparison between short-circuited and open-circuited U-shaped CPWR bandpass filter

A comparison between the frequency responses of the transmission coefficients, $|S_{21}|$, for bandpass filters employing short-ended and open-ended half-wavelength CPW resonator of U shape is presented in Fig. 19. It is clear that the open-circuit termination of the U-shaped resonator results in a considerably higher quality factor as listed in Table 2. A quality factor of 3.71×10^4 is obtained by the open-ended superconducting CPWR printed on a lossless dielectric substrate in the lower pass band (about 6 times that obtained with the short-ended CPWR). On the other hand, by comparing the frequency responses of the filters with open-ended and short-ended U-shaped resonators in the upper pass band, Fig. 19 (b), it seems that the design modification results in a slight shift of the resonant frequency associated with a slight reduction of the quality factor as given in Table 2.

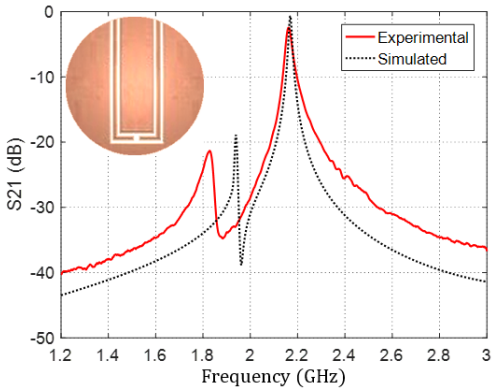

Fig. 17. Frequency response of the transmission coefficient $|S_{21}|$ of the bandpass filter prototype '2' of the 'one-gap' design.

Table 2: Resonant frequency and quality factor of the bandpass filter for the possible termination types of the U-shaped CPWR

Termination of CPW Resonator	Lower Pass Band		Upper Pass Band	
	f_0(GHz)	Q	f_0(GHz)	Q
Short	1.9405	6.13×10^3	1.1695	1070
Open	1.9450	3.71×10^4	1.1605	905

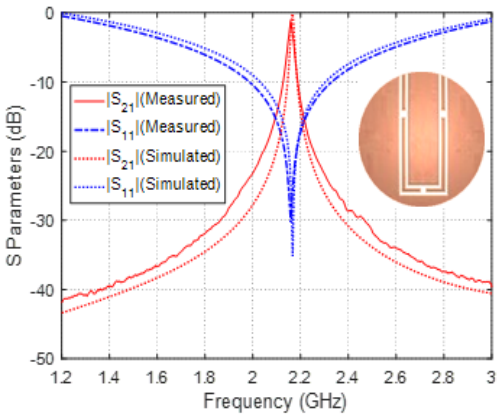

Fig. 18. Frequency response of the transmission and reflection coefficients $|S_{21}|$ and $|S_{11}|$, respectively, of the BPF prototype '3'.

F.3. Mechanism of resonance in the lower frequency band for open-circuit termination

At the lower resonant frequency (1.9451 GHz) of the open-circuit terminated CPWR on the perimeter of the U-shape, the surface current distribution is presented in Fig. 20. It is shown that, like an open-ended half-

wavelength resonator as explained in Section II and illustrated in Fig. 5 (a), the current has its maximum magnitude at the middle of the resonator length whereas the current nodes of the standing wave are at the open-end of the CPWR.

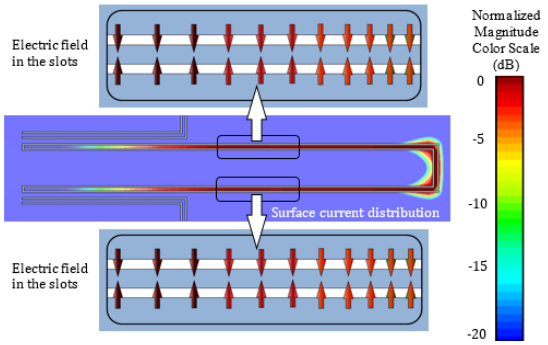

Fig. 19 Surface current on the conductors and electric field distribution in the slots at the resonant frequency corresponding the open-circuit terminated half-wavelength CPW resonator, $f = 1.9451$ GHz.

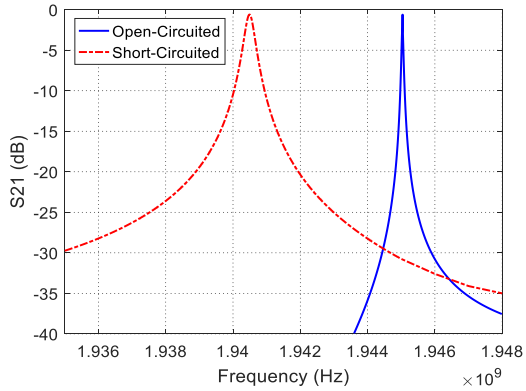

(a) Frequency response in the lower pass band

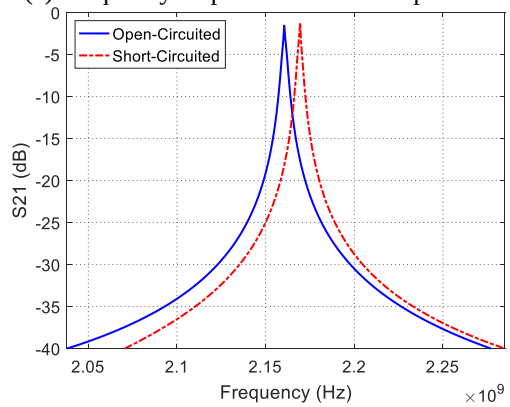

(b) Frequency response in the upper pass band

Fig. 20. Comparison between the frequency response of the transmission coefficients $|S_{21}|$ for the bandpass filters with open-circuit and short-circuit terminated U-shaped half-wavelength CPWRs.

A comparison of the proposed BPF with BPFs found in literature is presented in Table 3.

Table 3: Comparison with similar works

	Size ($\lambda_g \times \lambda_g$)	S_{21}(dB)	S_{11}(dB)
Proposed BPF	0.3 × 0.21	0.33	-27
[15]	0.25 × 0.25	1.3	-25
[16]	0.5 × 0.5	0.1	-25
[17]	0.75 × 0.6	0.04	-23

VI. CONCLUSION

High quality factor bandpass filter based on a number of cascaded dual-resonance CPW resonators is proposed. Each resonant structure is constructed as two overlapped CPWRs. The cascaded resonators mediate microwave coupling between two isolated CPW feeders only at the resonant frequencies leading to a bandpass filter of high quality factor. Each resonator has its two resonances first-order, where the resonant frequencies and the separation between them can be fine-tuned by the dimensions of the structure. The current distribution on the conducting strips and the electric field distributions in the slots are presented to demonstrate the mechanism of operation of the proposed bandpass filter designs. The effects of the loss tangent of the dielectric substrate material on the quality factors at the two resonant frequencies are presented and discussed. Some experimental results concerned with the frequency response of three fabricated prototypes for three different designs are presented showing good agreement when compared with the corresponding simulation results. It is shown that, at low enough temperature, the proposed structure can operate as superconducting microwave resonator when made from the appropriate materials. An optimized design of the proposed bandpass filter, based on superconducting CPWR structure, is shown to achieve quality factors high enough to form a quantum data bus for hybrid architecture of quantum information systems.

REFERENCES

[1] J. K. A. Everard and K. K. M. Cheng, "High performance direct coupled bandpass filters on coplanar waveguide," *IEEE Transactions on Microwave Theory and Techniques*, vol. 41, no. 9, pp. 1568-1573, 1993.

[2] K. C. Gupta, R. Garg, and I. Bahl, *Microstrip Lines and Slotlines*, Dedham, MA Artech, 1979.

[3] A. Gopinath, "Losses in coplanar waveguides," *IEEE Transactions on Microwave Theory and Techniques*, vol. 30, no. 7, pp. 1101-1104, 1982.

[4] F. D. Williams and S. E. Schwarz, "Design and performance of coplanar waveguide bandpass filters," *IEEE Transactions on Microwave Theory and Techniques*, vol. 31, no. 7, pp. 558-566, 1983.

[5] M. Göppl, A. Fragner, M. Baur, R. Bianchetti, S. Filipp, J. M. Fink, P. J. Leek, G. Puebla, L. Steffen, and A. Wallraff, "Coplanar waveguide resonators for circuit quantum electrodynamics," *Journal of Applied Physics*, vol. 104, no. 11, p. 113904, 2008.

[6] H.-J. Li, Y.-W. Wang, L.-F. Wei, P.-J. Zhou, Q. Wei, C.-H. Cao, Y.-R. Fang, Y. Yu, and P.-H. Wu, "Experimental demonstrations of high-Q superconducting coplanar waveguide resonators," *Chinese Science Bulletin*, vol. 58, no. 20, pp. 2413-2417, 2013.

[7] M. Kumar and R. Gowri, "Review on various issues and design topologies of edge coupled coplanar waveguide filters," *Journal of Graphic Era University*, vol. 5, no. 2, pp. 91-96, 2017.

[8] M. Kumar and R. Gowri, "Analysis and characterization of edge coupled coplanar waveguide discontinuities for filter applications," *Proceedings of the Sixth International Conference on Computer and Communication Technology, ACM*, pp. 309-312, Sep. 2015.

[9] R. El Haffar, A. Farkhsi, O. Mahboub, and N. A. Touhami, "Compact size coplanar waveguide bandpass filter design and modeling," *Proceedings of the 2nd International Conference on Computing and Wireless Communication Systems, ACM*, p. 49, Nov. 2017.

[10] M. Kumar and R. Gowri, "Design of compact and high performance edge coupled coplanar waveguide band pass filter," *IEEE 1st International Conference on Power Electronics, Intelligent Control and Energy Systems (ICPEICES)*, pp. 1-3, July 2016.

[11] T. M. Weller, "Edge-coupled coplanar waveguide bandpass filter design," *IEEE Transactions on Microwave Theory and Techniques*, vol. 48, no. 12, pp. 2453-2458, 2000.

[12] D. Bothner, M. Knufinke, H. Hattermann, R. Wölbing, B. Ferdinand, P. Weiss, R. Kleiner, P. Weiss, S. Bernon, J. Fortagh, D. Koelle, and R. Kleiner, "Inductively coupled superconducting half wavelength resonators as persistent current traps for ultracold atoms," *New Journal of Physics*, vol. 15, no. 9, p. 093024, 2013.

[13] R. N. Simons, *Coplanar Waveguide Circuits, Components, and Systems*, John Wiley & Sons, vol. 165, 2004.

[14] D. M. Pozar, *Microwave Engineering*, John Wiley & Sons, Inc., 2012.

[15] B. George, N. S. Bhuvana, and S. K. Menon, "Compact band pass filter using triangular open loop resonator," *Progress in Electromagnetics Research Symposium*, Nov. 19-22, 2017.

[16] M. S. S. Subramanian, K. V. Siddharth, S. N. Abhinav, V. V. Arthi, K. S. Praveen, R. Jayavarshini, and G. A. S. Sundaram, "Design of dual log-spiral metamaterial resonator for X-band applications," *2012 International Conference on Computing, Communication and Applications (ICCCA)*, 2012.

[17] A. Boutejdar, A. Darwish, and A. Omar, "Design and improvement of compact half-wavelength band pass filter employing overlapped slotted ground structure (SGS) and multilayer technique," *Applied Computational Electromagnetics Society (ACES) Journal*, vol. 28, no. 8, Aug. 2013.

Millimeter Wave Fuze Radome Design Based Bandpass Frequency Selective Surface

Min Zhao [1], Junjian Bi [2], Juan Xu [1,3*], and Jianping Zhao [1]

[1] School of Cyber Science and Engineering, Qufu Normal University, Qufu,273165, People's Republic of China
zhaomin219@163.com, xujuan125@163.com, zjp-wlx@163.com

[2] Key Laboratory of Electromagnetic Environmental Effects, Army University of Engineering
Shijiazhuang, 050003, People's Republic of China
13303315178@189.cn

[3] State Key Laboratory of Millimeter Waves, Southeast University, Nanjing, 211189, People's Republic of China
*xujuan125@163.com

Abstract ─ This paper studies a fuze radome system applied to millimeter waves. The system consists of feed antenna, radome, planar FSS array or curve conformal array. Microstrip antenna is used as the feed antenna. Based on the principle of equispaced and equal period respectively, cross units loading single layer dielectric form planar and curve FSS array. The FSS radome system can improve the permeability of hood to electromagnetic waves (EM) of passband, and reduce the interference of complex EM in the external environment to the system. The FSS radome will not deteriorate radiation characteristics of the feed antenna. The planar FSS radome has a passband of 98.2 GHz to 101.55 GHz with -10dB relative bandwidth of 3.35%. The curve FSS radome has a passband of 96.3 GHz to 101.8 GHz with -10dB relative bandwidth of 5.5%. In addition, the radiation characteristics of the proposed system are analyzed. It is found that the radiation pattern of the antenna is basically consistency before and after loading the radome.

Index Terms ─ Bandpass, frequency selective surfaces, millimeter waves, radiation, radome, transmission.

I. INTRODUCTION

Millimeter waves [1,2] are favored by researchers because of rich frequency resources, small electromagnetic interference in the same frequency band, and narrow beam. FSS radome has a wide application prospect in the fields of electromagnetic protection and reflective surface antennas. Therefore, this paper designs a FSS radome working in the millimeter wave band. The FSS [3-10] is a metal patch or slot unit periodically arranged on the medium, which realizes bandpass or bandstop characteristics by effectively controlling the reflection and transmission characteristics of EM. The FSS is a spatial filter essentially. The FSS radome not only protects the antenna from the external environment, but also acts as an electromagnetic window to receive and transmit electromagnetic waves of a specific frequency.

In recent years, a large number of studies on frequency selective surfaces have emerged. In [5], the authors proposed an equivalent circuit model of tunable square FSS, which uses discrete capacitive components to achieve tuning, and then approximates the cell size of FSS by circuit model. In [7], a three-dimensional (3D) FSS based on split square coaxial waveguide (SSCW) is proposed, which introduces two transmission zeros on both sides of the passband to achieve high selectivity. In [11], it applies two layers of FSS made of cross element on the radome's dielectric slab. By setting the radome slab thickness as an odd multiple of a quarter-wavelength, the two layers form a phase cancellation structure and suppress electromagnetic wave return. In [12], a filter-antenna consisting of a monopole antenna and a conical FSS radome was designed and investigated. It can keep the input reflection coefficient, radiation pattern of the monopole antenna within the designed passband, and reflects out-of-band signals. The radome [13-18] loaded with bandpass FSS has attracted the attention of many experts and scholars.

The dielectric radome designed in this paper adopts a cone structure. A cross slot unit operating at 100 GHz is used as FSS. A microstrip antenna is used as the feed antenna, because it has stable performance and is easy to integrate with radome. Using the transmission line theory to analyze the influence of different thickness of radome wall on the transmittance, and the influence of various dielectric constant of radome on the radiation performance. It provides reliable theoretical support for improving the radiation performance of FSS radome

Submitted On: August 31, 2020
Accepted On: March 17, 2021

https://doi.org/10.47037/2020.ACES.J.360406

system. A planar FSS radome and a curve conformal FSS radome are designed respectively in this paper. The author studied the influence of FSS radome on antenna's S parameters and radiation performance. The numerical results in this article use electromagnetic simulation software HFSS to calculate and solve.

II. TRANSMISSION LINE THEORY AND FULL WAVE ANALYSIS

The equivalent transmission line theory of the radome is used to calculate the transmission coefficient of the radome. The four-terminal equivalent transmission line theory, which is characterized by matrix form, can be applied to radomes of flat structure. For a radome with an N-layer ($N \geq 1$) structure, the transmission characteristics can be represented by a series of N+1 matrices. The radome of the N layers structure is shown in Fig. 1. The relative permittivity and magnetic permeability of air are represented by ε_0 and μ_0, respectively. Similarly, ε_i and μ_i show relative permittivity and magnetic permeability of the layer i, and the thickness substrate is represented by d_i.

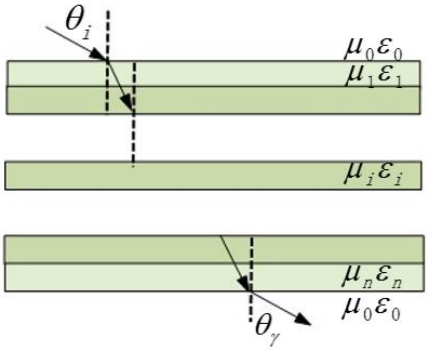

Fig. 1. Schematic of N layers plate electromagnetic wave propagation.

For the structure of the N layers medium, it can be equivalent to an N+1 four-terminal network, and the total cascading matrix T_{all} is expressed as formula (1),

$$T_{all} = \begin{pmatrix} A & B \\ C & D \end{pmatrix}\begin{pmatrix} A_1 & B_1 \\ C_1 & D_1 \end{pmatrix}\begin{pmatrix} A_2 & B_2 \\ C_2 & D_2 \end{pmatrix}\cdots\begin{pmatrix} A_n & B_n \\ C_n & D_n \end{pmatrix}, \quad (1)$$

$$\begin{pmatrix} A_i & B_i \\ C_i & D_i \end{pmatrix} = \begin{pmatrix} ch(j\gamma_i d_i) & Z_i sh(j\gamma_i d_i) \\ \dfrac{sh(j\gamma_i d_i)}{Z_i} & ch(j\gamma_i d_i) \end{pmatrix}, \quad (2)$$

where $\gamma_i = \sqrt{\mu_i\varepsilon_i - \sin^2\theta_i} \times 2\pi/\lambda_0$, $sh()$ and $ch()$ represent hyperbolic sine and hyperbolic cosine functions respectively. The characteristic impedance of the layer i relative to the free space can be normalized to Z_i. The $Z_i^{\parallel}$ represents horizontally polarized normalized characteristic impedance, expressed as formula (3). The $Z_i^{\perp}$ represents vertical polarization normalized characteristic impedance, expressed as formula (4):

$$Z_i^{\parallel} = Z_0 \frac{\mu_i}{\varepsilon_i}\sqrt{\mu_i\varepsilon_i - \sin^2\theta_i}, \quad (3)$$

$$Z_i^{\perp} = \frac{Z_0\mu_i}{\sqrt{\mu_i\varepsilon_i - \sin^2\theta_i}}, \quad (4)$$

Z_0 in the above equation is the free-space characteristic impedance, $Z_0 = 377\Omega$. For horizontally polarized waves, its characteristic impedance is $Z_0^{\parallel} = Z_0\cos\theta_0$. For vertically polarized waves, the characteristic impedance is $Z_0^{\perp} = Z_0/\cos\theta_0$. After solving the total cascading matrix T_{all} of the N four-terminal network, the transmission coefficient can be calculated by the formula (5):

$$Trans = \frac{2}{(A_{all} + B_{all}/Z_0) + (Z_0 C_{all} + D_{all})}. \quad (5)$$

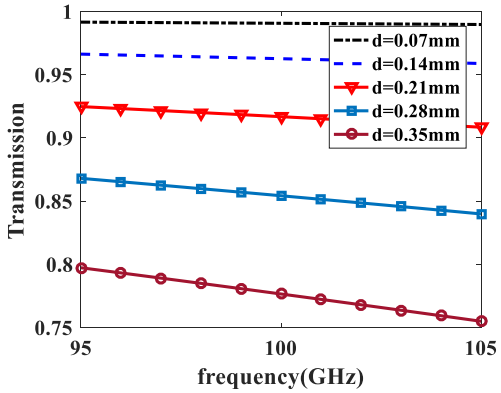

Fig. 2. Effect of radome wall thickness on transmittance.

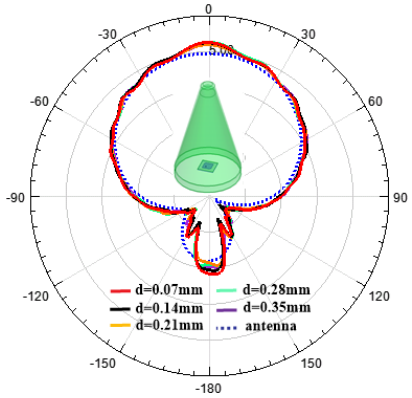

Fig. 3. Effect of radome wall thickness on radiation performances.

Assume that the relative permittivity of radome is 1.08, the transmission rate is decreasing as the thickness increases from 0.07mm to 0.35mm, as shown in Fig. 2.

Table 1 shows the transmission rate at different wall thicknesses at 100 GHz. When the wall thickness is less than or equal to 0.21 mm, the transmission rate is more than 90%. The radiation characteristics of the radome are analyzed in combination with full-wave simulation. Figure 3 shows the effect of the thickness of the radome wall on the radiation performance. In the range of 0.07mm~0.21mm, the radiation curves of different radome wall thicknesses are basically coincident, which is in good agreement with the radiation pattern of the antenna. Combined with the data in Table 1, after loading dielectric radome the gain of antenna is approximately equal to 6dB. In order to ensure the overall strength of the radome, the thickness of the radome is increased as much as possible under the condition that the electrical performance index is satisfied. Therefore, the overall thickness of the radome wall is determined to be 0.21 mm.

Table 1: Comparison of transmission and gain at 100 GHz for different wall thicknesses

d (mm)	0.07	0.14	0.21	0.28	0.35
Trans. (%)	99.06	96.26	91.67	85.42	77.65
Gain (dB)	6.29	6.25	5.99	6.26	6.03

Assume that the thickness of the radome wall is 0.21 mm, the transmission rate decreases with the increase of the relative permittivity of the radome wall, as shown in Fig. 4.

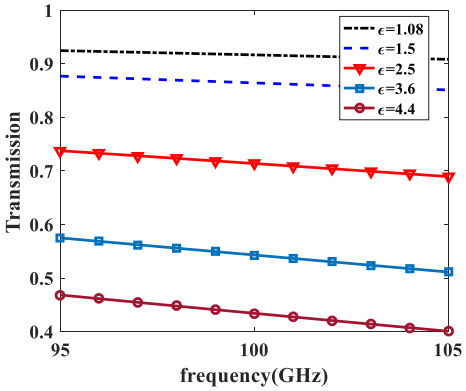

Fig. 4. Effect of permittivity of radome wall on the transmission rate.

Figure 5 shows the effect of relative permittivity of radome wall on the radiation performance. It can be obtained that the radiation pattern is gradually distorted with the increase of the relative permittivity. Table 2 shows the transmission of the different relative permittivity radome at 100 GHz. When the relative permittivity of radome wall is 1.08, the transmittance is more than 90%. Considering the radiation gain of different wall materials, honeycomb materials with the relative permittivity of 1.08 are selected.

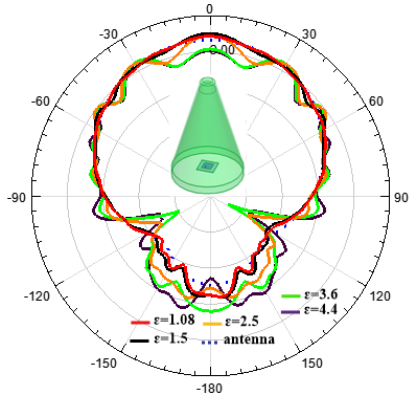

Fig. 5. Effect of relative permittivity of radome wall on radiation performance.

Table 2: Comparison of transmission and gain at 100 GHz for different wall materials

ε_r	1.08	1.5	2.5	3.6	4.4
Trans (%)	91.67	86.44	71.39	54.31	43.42
Gain (dB)	5.99	6.52	6.12	5.97	5.44

III. RADOME SYSTEM DESIGN

A. FSS design and simulation

The frequency of FSS depends on the total length of the gap, and resonance occurs when the length is equal to half the wavelength. In this paper, cross slot units are designed for planar and curve FSS radome, as shown in Fig. 6. The planar unit is loaded with Rogers 5880 with dielectric constant of 2.2, and the curve unit is loaded with material with dielectric of 1.08. The size parameters are shown in Table 3.

Table 3: Size parameter of plane and curve cross FSS

Variables	a	D	h	L	w
Plane (mm)	0.07	1.06	0.12	0.37	0.044
Curve (mm)	0.089	1.34	0.152	0.465	0.054

The resonant frequency of the planar and curve unit are 100 GHz, as shown in Fig. 7. When the EM is incident on the radome wall at a large angle, the FSS unit is required to have excellent angle stability. Both units can maintain stable resonance when incidence angle is 0 degrees and 45 degrees by analyzing reflection coefficient and transmission coefficient. It confirms that planar and curve FSS unit have good angle stability.

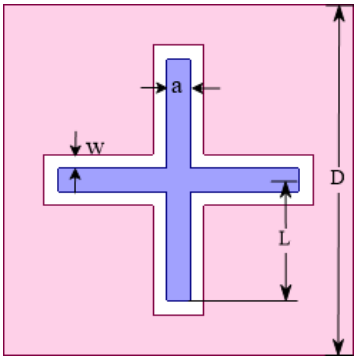

Fig. 6. Classic cross gap type FSS unit.

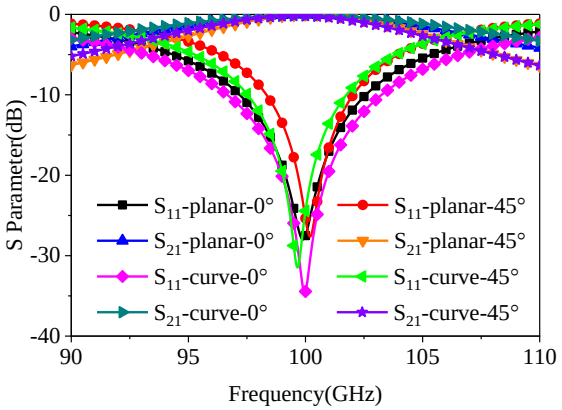

Fig. 7. S parameter of plane and curve FSS unit.

Table 4 analyzes the influence of arm length L on center frequency. As L increases, the center frequency of planar and curve FSS unit both shows downward trend. This further illustrates the inverse relationship between the gap length and center frequency.

Table 4: Effect of the value of w on center frequency

f_0 (GHz)	L (mm)		
	0.32	0.37	0.42
Plane	112.8	99.88	86.75
f_0 (GHz)	L (mm)		
	0.45	0.465	0.48
Curve	101	99.97	94.68

B. Planar FSS radome design and analysis

Based on requirements for aircraft stability and aerodynamic performance, this paper designs a cone radome. The radome wall adopts a single-layer thin wall to improve the transmission rate. In order to obtain a wider operating frequency band, it is required that the relative permittivity of the material is as low as possible. Meanwhile, the loss of wall material should be as small as possible to improve the transmission efficiency of radome. Figure 8 shows a schematic diagram of the dielectric radome. Table 5 shows the size parameters of cone radome.

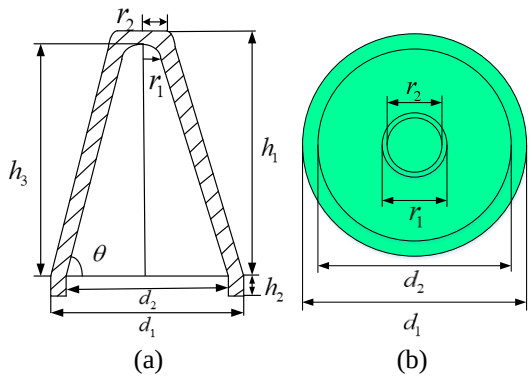

Fig. 8. Schematic diagram of dielectric radome: (a) cross-sectional view and (b) top view.

Table 5: Size parameters of cone radome

Variables	r1	r2	h1	h2
Value (mm)	2.5	3.365	28.64	2.26
Variables	h3	d1	d2	--
Value (mm)	28.14	23.22	20.64	--

The model of planar FSS radome is established through joint programming of HFSS and MATLAB. The author writes programs to call HFSS for automatic modelling using MATLAB's application programming interface (API). Compared with the traditional manual modeling method, this method greatly improves the modeling efficiency and saves time.

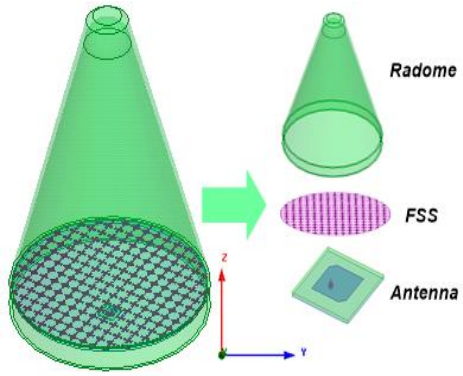

Fig. 9. Planar FSS radome system model.

According to the equidistant principle, the two-dimensional FSS array are arranged along the plane edge of the cylindrical dielectric substrate. Then the planar FSS array are loaded to the bottom of radome. Similarly, the microstrip antenna is placed below the FSS array, and

the planar FSS radome model is shown in Fig. 9. Figure 10 shows the comparison of S_{11} between planar FSS radome system and antenna. The S_{11} curves of the antenna are in good agreement before and after loading planar FSS radome. The absolute bandwidth of the system is 98.2GHz~101.55GHz, and the relative bandwidth is 3.35%. Figure 11 shows the comparison of the E-plane and H-plane radiation characteristics. After loading planar FSS radome, the radiation pattern is shaken slightly. The main lobe gain is basically stable. The beam pointing error is within the allowable range. Figure 12 shows the 3D radiation pattern of dielectric radome, and the gain is approximately 6dB. Figure 13 shows the 3D radiation pattern of planar FSS radome, and the gain is about 6.4dB, which is an increase of 0.4dB compared with loading dielectric radome. It shows that loading the planar FSS radome can increase the radiation gain of the radome system.

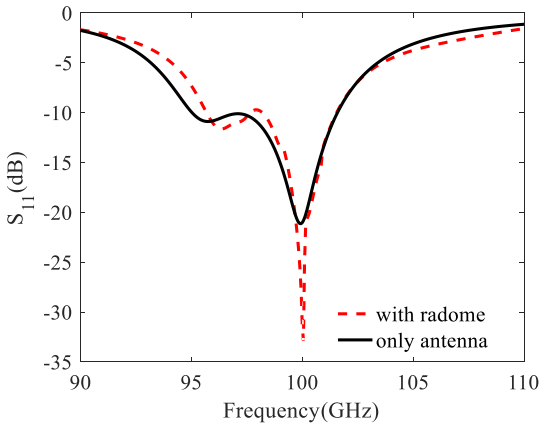

Fig. 10. Comparison of S_{11} between planar FSS radome system and antenna.

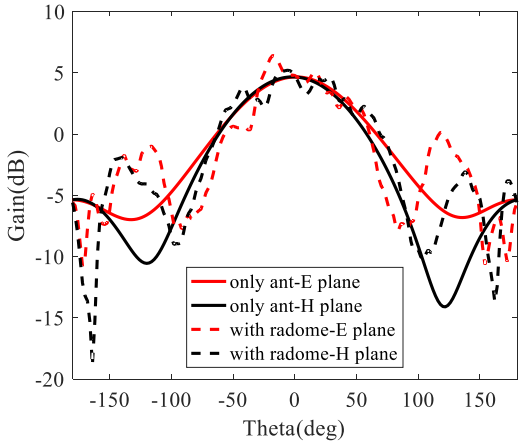

Fig. 11. Comparison of E- and H-plane patterns between planar FSS radome and antenna.

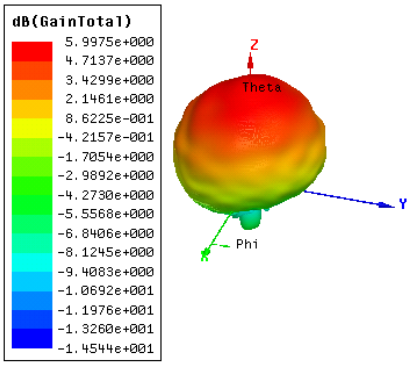

Fig. 12. 3D radiation pattern of substrate radome.

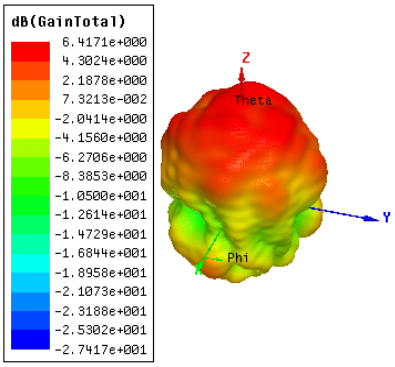

Fig. 13. 3D radiation pattern of planar FSS radome system.

C. Surface conformal FSS design and simulation

Different from planar FSS radome, the FSS array of curve FSS radome is conformal to the surface of cover wall. The modeling method still uses API by calling HFSS automatic modeling in MATLAB programming. According to the principle of quasi-period arrangement, the curve FSS array is composed of classical cross FSS unit. The three-dimensional model of the curve FSS radome system is shown in Fig. 14.

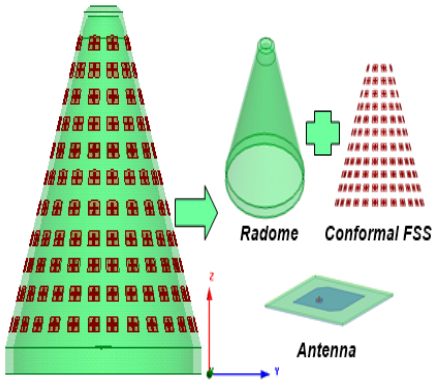

Fig. 14. Curve FSS radome system model.

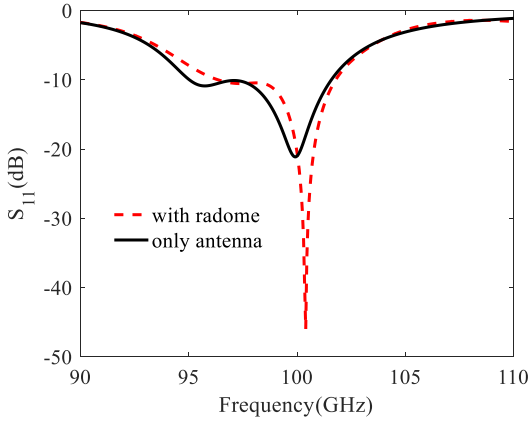

Fig. 15. Comparison of S_{11} between conformal FSS radome and antenna.

The feed antenna uses a microstrip patch antenna, and the center frequency of the radiation is 100 GHz. Figure 15 shows the comparison of S_{11} between curve FSS radome system and antenna. The S_{11} curves of the antenna are in good agreement before and after loading curve FSS radome. The absolute bandwidth of the system is 96.3 GHz to 101.8 GHz. The relative bandwidth is 5.5%. Figure 16 and Fig. 17 show the comparison of the E-plane and H-plane radiation characteristics. Figure 18 shows the 3D radiation pattern of curve FSS radome system. After loading the curve FSS radome, the radiation pattern is dithered slightly compared to the antenna. The main lobe gain is reduced by 1.3 dB, and the beam pointing error is within the allowable range. The backward gain becomes larger and the sidelobe level is raised by 8.17 dB.

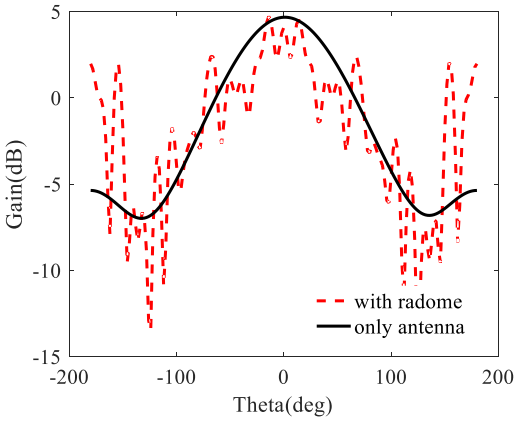

Fig. 16. Comparison of E-plane pattern between curve FSS radome and antenna.

Table 6 has compared the radome structure, frequency band and performance between this paper and literature [12-15]. The FSS radome designed in this paper is a dome-shaped cone. It works in the millimeter wave band. It has a -10dB bandwidth greater than 3GHz, and the bandwidth in other literatures is less than 2GHz.

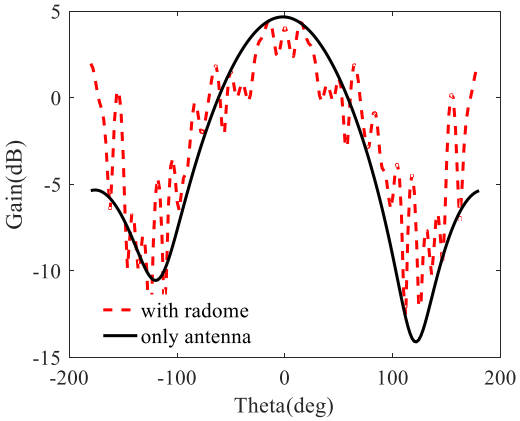

Fig. 17. Comparison of H-plane pattern between curve FSS radome and antenna.

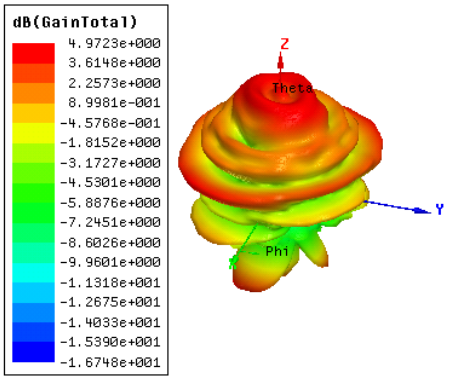

Fig. 18. 3D radiation pattern of curve FSS radome system.

The radome system designed in this paper works in the millimeter wave and the center frequency is 100 GHz. This is extremely demanding for machining accuracy and testing environment. No actual tests have been conducted yet. In the following work, the author will carry out the actual processing based on the data and conclusions obtained in this paper, and then give the comparison results of simulation and actual measurement in the subsequent articles.

IV. CONCLUSION

In this paper, based on the classical cross FSS unit, a planar FSS radome and a curve FSS radome are designed. They can be applied to the front end of the aircraft to prevent electromagnetic interference and improve the permeable performance of radome. The results show that both planar and curve FSS radome

can improve the transmission rate without affecting the radiation characteristics of the antenna. They can suppress interference from out-of-band signals to the system. The two radome systems designed in this paper have broad application prospects in fuze radomes.

Table 6: Comparison of the proposed structure to the existing structure

Refs.	Frequency (GHz)	Cover Shape	Core Dielectric	FSS Loading	10dB BW (GHz)
[12]	6.1	Conical	2.33	Curved	0.418
[13]	5.3	Flat type	2.55	Planar	0.18
[14]	9.8	Flat type	2.65	Planar	1.5
[15]	12.4	Conical	3	Curved	—
This work	100	Dome cone	1.08	Planar	3.35
		Dome cone	1.08	Curved	5.5

ACKNOWLEDGMENT

This work is founded by Natural Science Foundation of 61701278 and State Key Laboratory of Millimeter Waves Foundation of K201929.

REFERENCES

[1] D. M. Syahkal and D. Wake, "Bow-tie antennas on high dielectric substrates for MMIC and OEIC applications at millimetre wave frequencies," *Electronics Letters*, vol. 31, no. 24, pp. 2060-2061, Nov. 23, 1995.

[2] P. Hallbjorner, M. Bergstrom, M. Boman, P. Lindberg, E. Ojefors, and A. Rydberg, "Millimetre-wave switched beam antenna using multiple travelling-wave patch arrays," *IEE Proceedings - Microwaves, Antennas and Propagation*, vol. 152, no. 6, pp. 551-555, Dec. 9, 2005.

[3] B. Wu, Y.-J. Yang, H.-L. Li, Y.-T. Zhao, C. Fan, and W.-B. Lu, "Low-loss dual-polarized frequency-selective rasorber with graphene-based planar resistor," *IEEE Transactions on Antennas and Propagation*, vol. 68, no. 11, pp. 7439-7446, Nov. 2020.

[4] H. B. Wang, Y. J. Cheng, and Z. N. Chen, "Wideband and wide-angle FSS using loop slotted hybrid quarter-mode substrate integrated cavity with two independently controllable poles," *IEEE Transactions on Antennas and Propagation*, vol. 68, no. 12, pp. 8221-8226, Dec. 2020.

[5] D. Ferreira, R. F. da Silva Caldeirinha, I. Cuiñas, and T. R. Fernandes, "Tunable square slot FSS EC modelling and optimisation," *IET Microwaves, Antennas & Propagation*, vol. 11, no. 5, pp. 737-742, Apr. 15, 2017.

[6] F. Costa, A. Monorchio, and G. Manara, "An overview of equivalent circuit modeling techniques of frequency selective surfaces and metasurfaces," *Applied Computational Electromagnetics Society Journal*, vol. 29, no. 12, pp. 960-976, Dec. 2014.

[7] Z. Yu, X. Yang, W. Tang, Y. Shi, J. Zhu, and C. Wang, "Compact three-dimensional bandpass FSS with high selectivity based on split square coaxial waveguide," *Electronics Letters*, vol. 55, no. 21, pp. 1135-1137, 2019.

[8] B. Lin, S. Du, H. Zhang, and X. Ye, "Design and simulation of frequency-selective radome together with a monopole antenna," *Applied Computational Electromagnetics Society Journal*, vol. 25, no. 7, pp. 620-625, July 2010.

[9] A. A. Omar and Z. Shen, "Thin 3-D bandpass frequency-selective structure based on folded substrate for conformal radome applications," *IEEE Transactions on Antennas and Propagation*, vol. 67, no. 1, pp. 282-290, Jan. 2019.

[10] K. K. Varikuntla and R. Singara Velu, "Design and development of angularly stable and polarisation rotating FSS radome based on substrate-integrated waveguide technology," *IET Microwaves, Antennas & Propagation*, vol. 13, no. 4, pp. 478-484, 2019.

[11] W.-J. Liao, W.-Y. Zhang, Y.-C. Hou, S.-T. Chen, C. Y. Kuo, and M. Chou, "An FSS-integrated low-RCS radome design," *IEEE Antennas and Wireless Propagation Letters*, vol. 18, no. 10, pp. 2076-2080, Oct. 2019.

[12] H. Zhou, S. Qu, B. Lin, J. Wang, H. Ma, Z. Xu, W. Peng, and P. Bai, "Filter-antenna consisting of conical FSS radome and monopole antenna," *IEEE Transactions on Antennas and Propagation*, vol. 60, no. 6, pp. 3040-3045, June 2012.

[13] W. Pan, C. Huang, P. Chen, M. Pu, X. Ma, and X. Luo, "A beam steering horn antenna using active frequency selective curface," *IEEE Transactions on Antennas and Propagation*, vol. 61, no. 12, pp. 6218-6223, Dec. 2013.

[14] G. Q. Luo, W. Hong, H. J. Tang, J. X. Chen, X. X. Yin, Z. Q. Kuai, and K. Wu, "Filtenna consisting of horn antenna and substrate integrated waveguide cavity FSS," *IEEE Transactions on Antennas and Propagation*, vol. 55, no. 1, pp. 92-98, Jan. 2007.

[15] Y. W. Chia (Michael), "Radiation from curved (conical) frequency selective surfaces," *Department of Electronic and Electrical Engineering Loughborough University of Technology*, United Kingdom, 1993.

[16] Y. E. Erdemli, K. Sertel, R. A. Gilbert, D. E. Wright, and J. L. Volakis, "Frequency-selective

surfaces to enhance performance of broad-band reconfigurable arrays," *IEEE Transactions on Antennas and Propagation*, vol. 50, no. 12, pp. 1716-1724, Dec. 2002.

[17] B. Munk, *Frequency Selective Surfaces: Theory and Design*. John Wiley & Sons, Inc., 2000.

[18] H.-Y. Chen and S.-H. Wen, "An empirical formula for resonant frequency shift due to Jerusalem-cross FSS with substrate on one side," *Applied Computational Electromagnetics Society Journal*, vol. 33, no. 7, pp. 730-740, July 2018.

Min Zhao was born in Dezhou, Shandong Province, China in 1996. She received the B.S. degree in Communication Engineering from QuFu Normal University, Qufu, China, in 2018 and is currently working toward the M.S. degree in Communication and Information Systems at QuFu Normal University. Her research interests include frequency selective surfaces, metamaterials and millimeter wave fields.

Junjian Bi was born in Shijiazhuang, Hebei Province, China, in 1972. He received the Ph.D. degrees in Weapon System and Application Engineering from Beijing University of Technology, Beijing, China, in 2005. At present, he is mainly engaged in the research of electro-magnetic environment effect technology of equipment.

Juan Xu was born in Jining, Shandong Province, China, in 1982. She received the Ph.D. degrees in Electronic Science and Technology from Nanjing University of Science and Technology, Nanjing, China, in 2016. Since 2016, she has worked at QuFu Normal University. She has been an associate professor since 2019.

Her esearch interests include simulation, design and experimental measurement of new high performance RF, microwave and millimeter wave passive devices, antennas and antenna arrays.

Jianping Zhao was born in Heze, Shandong Province, China, in 1964. He received the B.S. degree in Physics from QuFu Normal University, Qufu, China, in 1985. In 1988, he studied in Wuhan University for master's degree in Radio and Information Engineering.

Since 1985, he has worked at QuFu Normal University. He was promoted to Associate Professor in 1997, Professor in 2002. Since 1992, he has been the Director of the Radio Teaching and Research Section. He has been engaged in application of electronic technology and scientific research in communication and information system of electronic information engineering and communication engineering.

Performance Evaluation of SDR Blade RF using Wide-band Monopole Antenna for Spectrum Sensing Applications

Ahmed A. Ibrahim [1], Wael A. E. Ali [2], and Hassan Aboushady [3]

[1] Electrical Engineering Department
Faculty of Engineering, Minia University, Minia, Egypt
ahmedabdel_monem@mu.edu.eg

[2] Dept. of Electronics & Communications Engineering, College of Engineering and Technology
Arab Academy for Science, Technology and Maritime Transport (AASTMT), Alexandria, Egypt
wael.ali@aast.edu

[3] Sorbonne University, LIP6 Laboratory, CNRS, France
hassan.aboushady@lip6.fr

Abstract ─ A spectrum-sensing algorithm is used to detect the available and the occupied frequency bands. The wideband antenna design approach is used for a microstrip fed monopole antenna that can be used for various wireless technologies such as GSM, UMTS, LTE, and WiFi operating at different frequencies from 1.25 to 3 GHz. The antenna is constructed from two copper layers of rectangular radiator and a partial ground plane. These layers are printed on an RO4003 substrate with dimensions 60 x 80 mm^2. The antenna is experimentally fabricated to verify the simulation predictions and good matching between simulated and measured results is achieved. The wide-band antenna is tested by connecting it to the receiver of the Blade-RF Software Defined Radio (SDR) platform. A matlab script is then used to control the SDR board and to perform Spectrum Sensing for Cognitive Radio Applications.

Index Terms ─ Partial ground plane, software defined radio, wide-band monopole antenna, wireless transceivers.

I. INTRODUCTION

The design of wide-band antenna for high speed fixed and mobile wireless communications is regarded as a challenging issue due to the fast development of nowadays technologies [1]. These technologies requires wideband antennas to support various wireless communications due to their advantage in providing higher data rate and lower power consumption as well as smaller system size [2-6]. These wireless communication systems covering different technologies such as GSM, UMTS, LTE and WiFi. The specific frequency bands defined for these standards are as follow: GSM1800 (1710–1880 MHz), GSM1900 (1850–1990 MHz), UMTS (1920–2170 MHz), LTE2300 (2305–2400 MHz), and LTE2500 (2500–2690 MHz). WiFi has different standards like the IEEE 802.11 b/g operating in the ISM-band from 2.4 GHz to 2.48 GHz [7-9]. Many efforts have been directed to widen the bandwidth of the antenna and many techniques have been addressed to meet the requirements of modern wireless technologies. Some of the addressed techniques used to realize wide-band antennas are: loading parasitic structure [10], etching round steps and stepped cuts from the patch [11, 12], hexagonal radiator [13], partial ground plane [14-16], distributed inductive strip [17] and loading stubs based on multi-mode resonance concept [18]. In this paper, we present Spectrum Sensing hardware measurements using a wide-band monopole antenna and a Blade-RF SDR-board [19]. The proposed system is used to detect RF signals in the frequency bands dedicated to GSM, UMTS, LTE and WiFi. The antenna is designed with rectangular microstrip antenna and partial ground plane in order to achieve the required bandwidth for the aforementioned wireless standards. The impedance and radiation characteristics of the monopole antenna are investigated using Computer Simulation Tool (CST) software which is based on the Finite Integration Technique (FIT). The suggested antenna is fabricated on a RO4003 substrate and then measured to validate the simulation outcomes.

II. WIDE-BAND ANTENNA DESIGN

The designed wide-band antenna is fed by a 50 ohm microstrip feed-line and is printed on a RO4003C substrate with dielectric constant of 3.38, loss tangent of 0.0027, and 0.813 mm thickness. The antenna is composed of rectangular microstrip antenna on the top layer of the substrate and partial ground plane on the bottom layer. This antenna is designed to achieve the desired performance to satisfy the requirements of

Submitted On: October 1, 2020
Accepted On: January 18, 2021

https://doi.org/10.47037/2020.ACES.J.360407

different wireless communication standards such as GSM, UMTS, LTE, and WiFi. The suggested antenna with the detailed dimensions is shown in Fig. 1. It can be noticed from the layout that the partial ground length is approximately the same that of the feed-line and the patch is designed with the size of 45 x 38 mm^2 to increase the antenna bandwidth for further operation in the desired band. The initial design of the antenna with full ground plane was resonating at 1.78 GHz with a very narrow bandwidth. Subsequently, a partial ground is utilized to achieve the desired band of operation and this is evident by the simulation results shown in Fig. 2. The simulation results of the proposed antenna are shown in Fig. 2 and it can be demonstrated that the return loss is less than –10 dB for about 1.75 GHz from 1.25 GHz to 3 GHz.

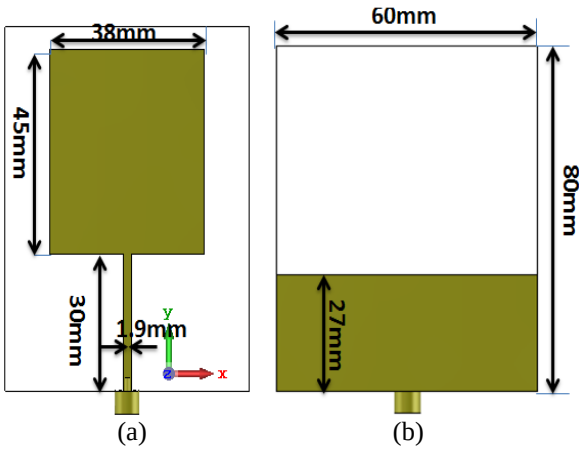

Fig. 1. The geometry of the proposed wide-band monopole antenna: (a) top view and (b) back view.

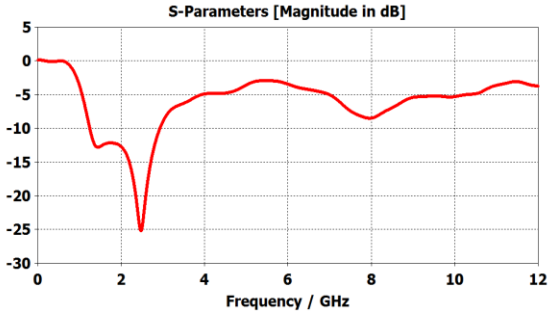

Fig. 2. The simulated S_{11} of the wide-band antenna.

III. RESULTS AND DISCUSSIONS

A. Wide band antenna results

A photograph of the fabricated wide-band antenna is depicted in Fig. 3. The antenna was tested for its impedance characteristics using Agilent N9918A vector network analyzer (VNA). The radiation pattern and gain were measured in an anechoic chamber. Figure 4 shows a comparison between the simulated and measured S_{11} results of the proposed wide-band monopole antenna, where the experimental results resemble the simulation results over the achieved bandwidth. It is seen from Fig. 4 that both the simulated and the measured S_{11} are both below –10 dB in the desired band. Nevertheless, the two curves are not identical since the simulation results show a minimum reflection of –25 dB at 2.5 GHz while the measurement results show a minimum reflection of –50dB at 2.2 GHz. This discrepancy is due the connector loss and the fabrication tolerance. In all cases, the proposed antenna can be considered as an adequate antenna for the various targeted wireless communications standards due to its good impedance matching performance.

Fig. 3. Photograph of the fabricated wide-band monopole antenna.

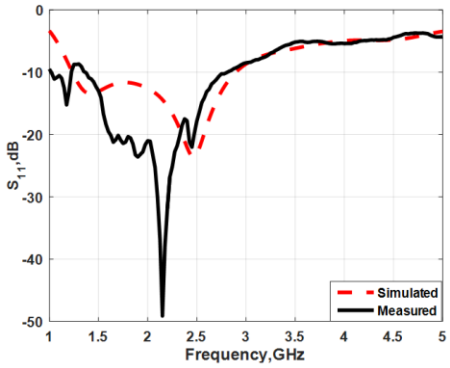

Fig. 4. Simulated and measured S_{11} of the proposed antenna against frequency.

The normalized simulated and measured radiation patterns in E- and H-planes of the proposed antenna are shown in Fig. 5(a) at f = 1.8 GHz and in Fig. 5 (b) at f = 2.4 GHz. It is obvious from Fig. 5 that the wide-band monopole antenna has a dipole-like radaiation pattern since it has a bi-directional pattern in the E-plane and omnidirectional pattern in H-plane for both frequencies. From the previous results, it is clear that the proposed antenna is convenient for different wireless communication standards in the 1.25-3.0GHz frequency range. A

comparison between simulation and measurement results realized gain of the proposed wide-band monopole is shown in Fig. 6. The simulated gain varries from 1.9 dB to 3.05 dB while the measured one varies from 1.6 dB to 3.1 dB. The average gain in simulation is 2.43 dB and the average gain in measurements is 2.38 dB. It is hence possible to conclude that simulation and measurement results are very similar.

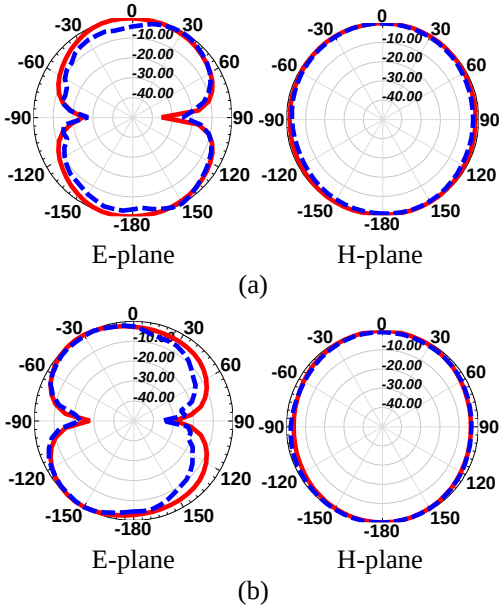

Fig. 5. The simulated (solid) and measured (dashed) normalized radiation patterns: (a) f = 1.8 GHz and (b) f = 2.4 GHz.

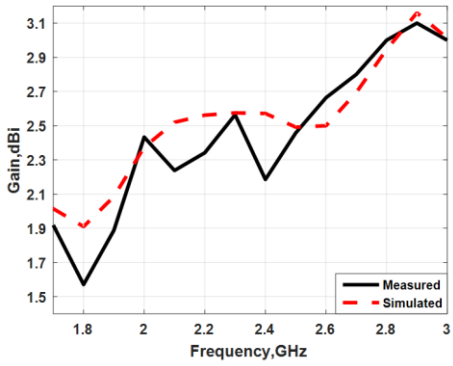

Fig. 6. The simulated and measured realized gain of the wide-band antenna.

B. Software defined radio with antenna

For the Spectrum Sensing operation, we use the SDR transceiver of the Blade RF board [19]. As shown in Fig. 7, the transceiver has one port for RF transmission and anotherport for RF reception. The Blade RF SDR can operate in a frequency band from 0.3 GHz to 3.8 GHz. The transmitter gain control range is 56 dB and the receiver gain control range is 61dB. The signal bandwidth can be selected from 1.5 MHz up to 28 MHz. The Analog Front End (AFE) of the Blade-RF board uses the LM6002 transceiver with several imperfections like DC offset and IQ imbalance. The effects of these imperfections are digitally compensated using the on-board FPGA in order to avoid any degradation in the overall system performance.

Spectrum sensing can be performed either in the time-domain or in the frequency domain. In this work, we used frequency domain Spectrum Sensing because of its higher resolution [20]. The spectrum is divided into many sub-bands. Spectrum sensing is carried out by dividing the total band of interest, B, into R_{sb} sub-bands each having a bandwidth of B/R_{sb}. After down-conversion, these sub-bands are converted to the digital domain. Finally, an N-points FFT is performed for each sub-band to calculate the Power Spectral Density (PSD):

$$PSD(f) = |F(x(nT))|^2, \quad (1)$$

where F(x(nT)) represents the Fourier Transform of the sampled signal in the time domain, x[nT], where T is the sampling period.

The $PSD_{sbi}(f)$ is the PSD of sub-band number (i), which has a range from 0 to R_{sb}-1. In order to achieve higher resolution, the number of FFT points, N, should be increased. However, larger N increases the time required for sensing. The parameters that are used in the spectrum sensing detection are as follows: the frequency range used for Spectrum Sensing is B = 2.7 GHz (0.3 - 3 GHz). This range is divided into R_{sb} = 135 sub-bands, each sub-band with a bandwidth of B/R_{sb} = 20 MHz. The number of FFT points N = 1024 and the sampling frequency is 40 MHz. The total sensing time in this case is 3.47 ms.

Before starting in detection, the blade RF should be calibrated to balance the transmitting and receiving output powers. The signal with constant power and operated at frequency band from 0.3 GHz to 3 GHz is used to configure the transmitting end. While the signal from RF generator with constant power and operated from 0.3 GHz to 3 GHz is used at the receiving port.

The wide-band antenna is attached at the receiving port as shown in Fig. 7 after finishing the calibration process. The wide-band antenna is used to detect the surrounding energy spectrum to be sensed. Then matlab digital signal processing (DSP) algorithm is utilized to analyze the detected energy as shown in Fig. 8. It is clear that the antenna detected (commercial signals from the air) GSM signal at 1.8 GHz, UMTS signal at 2.1 GHz and WiFi signal at 2.4 GHz as shown from the Power Spectral Density shown in Fig. 8.

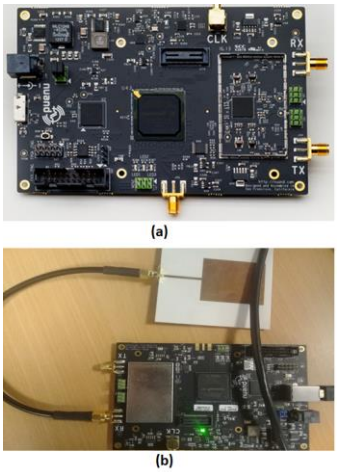

Fig. 7. (a) SDR blade RF [19], and (b) blade RF connected with wide band antenna.

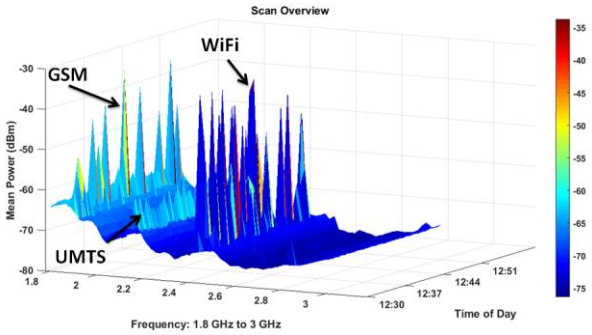

Fig. 8. The mean power density spectrums of blade RF at frequency range from 1.8 GHz up to 3 GHz.

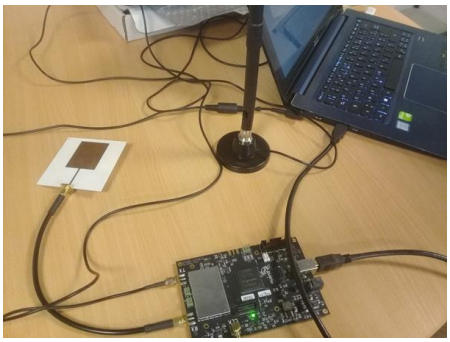

Fig. 9. The transmitting (using monopole) and receiving (using wide band antenna) setup of SDR blade RF.

In order to obtain a complete evaluation of the SDR Blade RF, The transmitting port is connected with conventional monopole as shown in Fig. 9. The monopole antenna is operated from 0.3 GHz up to 2.9 GHz. The DSP algorithm is used to produce power at the transmitting port; two frequency bands (2.44 GHz and 2.7 GHz) are used for transmission. The setup of this experiment is carried out inside isolated room to prevent the interference with other wireless signals. The receiving antenna is put at the far field. The receiving antenna is detected the energy of the two bands as shown in Fig. 10 and Fig. 11. It is seen that the spectral power densities are high at the two transmitting frequency bands 2.44 GHz and 2.7 GHz. Finally we can conclude that, the wide band antenna, spectrum sensing algorithm and SDR blade RF are used in spectrum sensing applications which enables our system can be used in cognitive radio applications.

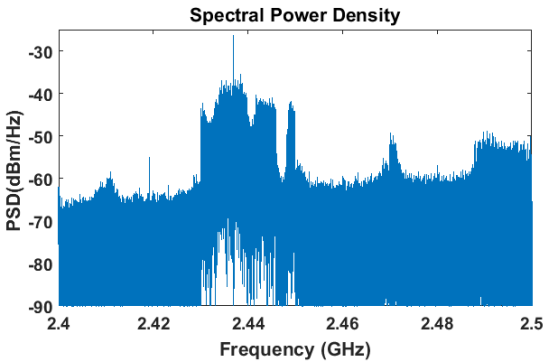

Fig. 10. The scanned spectral power density of SDR blade RF with wide band antenna at receiving end and conventional monopole at transmitting end.

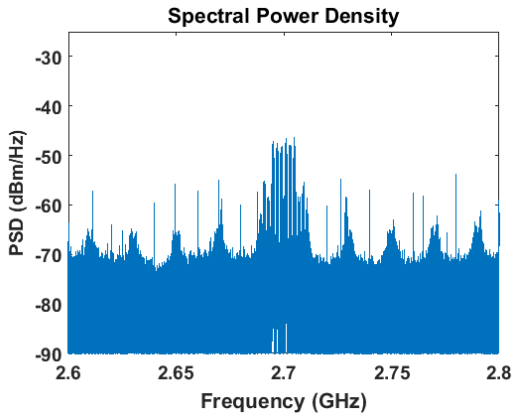

Fig. 11. The scanned spectral power density of SDR blade RF with wide band antenna at receiving end and conventional monopole at transmitting end.

IV. CONCLUSION

Hardware measurements using SDR blade RF platform has been used to detect the surrounding energy by using spectrum sensing algorithm. The wide-band monopole antenna has been designed, fabricated, measured and utilized at the receiving end of the blade RF to detect GSM/UMTS/LTE/WLAN applications. The antenna is operated at frequency band form 1.25

GHz up to 3 GHz. The blade RF first has been calibrated to balance the frequency gains between the transmissions and reception modes. The proposed wide band antenna has been utlized at receiving end to sense the spectrum energy from 1.25 GHz up to 3 GHz. Also the antenna has been received power from conventional monopole antenna added at the transmitting end of the balde RF. The blade RF sensing setup has been introduced with sensing time of 41.4 =*uS* for 20 MHz band and 3.47 *mS* for the whole 2.7 GHz band.

ACKNOWLEDGMENTS

This work was supported by the French and Egyptian governments through a co-financed fellowship granted by the French Embassy in Egypt (Institute Français d'Egypt), the Scientific and Technology Development Fund (STDF) (Project ID 30642) and the French Research Agency: TOLTECA project ANR-16-CE04-001301. We would also like to thank Tamer Badran, Alan Rodrigo Diaz Rizo and Alexandre Mendy from Sorbonne University for their help with the Blade-RF SDR board.

REFERENCES

[1] A. Kurniawan and S. Mukhlishin, "Wideband antenna design and fabrication for modern wireless communications systems," *Procedia Technology, 11 of International Conference on Electrical Engineering and Informatics*, Kualalumpur, Malaysia, pp. 335-340, June 2013.

[2] H. Liu, C. Yin, W. Gao, and Y. Sun, "Optimization and design of wideband antenna based on factor," *International Journal of Antennas and Propagation*, 2015.

[3] A. A. Ibrahim, J. Machac, and R. M. Shubair, "UWB MIMO antenna for high speed wireless applications," *Applied Computational Electromagnetics Society Journal*, vol. 34, no. 9, pp. 1294-1299, 2019.

[4] W. Hu, Z. Tang, L. Zhou, and Y. Yin, "Design of planar differential-fed antenna with dual band-notched characteristics for UWB applications," *Applied Computational Electromagnetics Society Journal*, vol. 32, no. 3, pp. 209-214, 2017.

[5] W. A. E. Ali and A. A. Ibrahim, "Tunable band-notched UWB antenna from WLAN to WiMAX with open loop resonators using lumped capacitors," *Applied Computational Electromagnetics Society Journal*, vol. 33, no. 6, pp. 603-609, 2018.

[6] A. Boutejdar, A. A. Ibrahim, and E. P. Burte, "Novel microstrip antenna aims at UWB applications," *Microwaves & RF Magazine*, vol. 7, no. 7, pp. 8-14, 2015.

[7] X. Wang, Y. Wu, W. Wang, and A. A. Kishk, "A simple multi-broadband planar antenna for LTE/GSM/UMTS and WLAN/WiMAX mobile handset applications," *IEEE Access*, vol. 6, pp. 74453-74461, 2018.

[8] Y. Hong, J. Tak, J. Baek, B. Myeong, and J. Choi, "Design of a multiband antenna for LTE/GSM/ UMTS band operation," *International Journal of Antennas and Propagation*, vol. 7, pp. 1187-1190, 2014.

[9] A. A. R. Saad, A. A. Ibrahim, O. M. Haraz, and A. Elboushi, "Tri-band compact ACS-fed meander-line antenna for wireless communications," *International Journal of Microwave and Wireless Technologies*, vol. 9, no. 9, pp. 1895-1903, 2017.

[10] M. Ojaroudi, S. Yazdanifard, N. Ojaroudi, and M. Naser-Moghaddasi, "Small square monopole antenna with enhanced bandwidth by using inverted T-shaped slot and conductor-backed plane," *IEEE Transactions on Antennas and Propagation*, vol. 59, no. 2, pp. 670-674, 2011.

[11] N. M. Awad and M. K. Abdelazeez, "Multislot microstrip antenna for ultra-wide band applications," *Journal of King Saud University-Engineering Sciences*, vol. 30, no. 1, pp. 38-45, 2018.

[12] A. Boutejdar and W. A. Ellatif, "A novel compact UWB monopole antenna with enhanced bandwidth using triangular defected microstrip structure and stepped cut technique," *Microwave and Optical Technology Letters*, vol. 58, no. 6, pp. 1514-1519, 2016.

[13] A. Joshi and R. Singhal, "Probe-fed hexagonal ultra wideband antenna using flangeless SMA connector," *Wireless Personal Communications*, vol. 110, no. 2, pp. 973-982, 2020.

[14] A. Bekasiewicz and S. Koziel, "Compact UWB monopole antenna for internet of things applications," *Electronics Letters*, vol. 52, no. 7, pp. 492-494, 2016.

[15] W. Ali, A. A. Ibrahim, and J. Machac, "Compact size UWB monopole antenna with triple band-notches," *Radioengineering*, vol. 26, no. 1, pp. 57-63, 2017.

[16] W. A. Ali, A. M. Mansour, and D. A. Mohamed, "Compact UWB wearable planar antenna mounted on different phantoms and human body," *Microwave and Optical Technology Letters*, vol. 58, no. 10, pp. 2531-2536, 2016.

[17] G.-H. Kim and T.-Y. Yun, "Small wideband monopole antenna with a distributed inductive strip for LTE/GSM/UMTS," *IEEE Antennas and Wireless Propagation Letters*, vol. 14, pp. 1677-1680, 2015.

[18] W.-J. Lu, L. Zhu, K. W. Tam, and H.-B. Zhu, "Wideband dipole antenna using multi-mode resonance concept," *International Journal of Microwave and Wireless Technologies*, vol. 9, no. 2, pp. 365-371, 2017.

[19] Nuand, "Blade-RF software defined radio." https://www.nuand.com/product/bladerf-x40/

[20] T. Badran, "Spectrum Sensing Using RF Software

Defined Radio Receivers," *Ph.D. Thesis*, Sorbonne University, Paris, France, June 2020.

Ahmed A. Ibrahim was born in 1986. He received the B.Sc., M.Sc., and Ph.D. degrees in Electrical Engineering from the Electronic and Communication Engineering Department, Minia University, Elminia, Egypt in 2007, 2011 and 2014 respectively. He is now an Associated Professor in Electrical Engineering Department in Faculty of Engineering Minia University. He has been a Visiting Professor in University Pierre and Marie Curie, Sorbonne University, Paris VI, France for 7 months and Otto-von-Guericke-Universität Magdeburg-Germany for 6 months. He has published more than 70 peer-reviewed journals and conference papers. His research has focused on miniaturized multiband antennas/ wideband, microwave/millimeter components. Also, his research includes MIMO antennas and energy harvesting systems. Ibrahim is senior member of the IEEE and senior member in URSI also member in the National Committee of Radio Science in Egypt.

Wael A. E. Ali was born in 1982. He received his B.Sc. and M.Sc. in Electronics and Communications Engineering from Arab Academy for Science, Technology and Maritime Transport (AASTMT), Alexandria, Egypt in 2004 & 2007, respectively. He obtained his Ph.D. in Electronics and Communications Engineering from Alexandria University, Alexandria, Egypt in 2012. He is currently an Associate Professor at Arab Academy for Science, Technology and Maritime Transport (AASTMT), Alexandria, Egypt. He has published more than 65 peer-reviewed journals and conference papers. His research interests include smart antennas, microstrip antennas, microwave filters, metamaterials, millimetric-wave antennas and MIMO antennas for various wireless communications applications.

Hassan Aboushady received the B.Sc. degree in Electrical Engineering from Cairo University, Egypt, in 1993, the M.Sc. and Ph.D. degrees in Electrical Engineering and Computer Science from Sorbonne University, Campus Pierre & Marie Curie, Paris, France, in 1996 and 2002 respectively. He also obtained his accreditation to supervise research (HDR) from the same University in 2010. Aboushady is currently an Associate Professor at Sorbonne University, Campus Pierre and Marie Curie, Paris, France. He worked on the design of high resolution audio Digital-to-Analog converters at Philips Research Laboratories (currently NXP), Eindhoven, The Netherlands. He also worked on the implementation of a baseband continuous-time Sigma-Delta modulator for RF receivers at STMicroelectronics, Crolles, France. Aboushady was a visiting professor for several months at the French University in Egypt, UFE, the Federal University of Rio Grande do Norte, UFRN, Brazil, and "Technologico de Monterrey", ITESM, Guadalajara, Mexico, in 2007, 2011 and 2013 respectively.

Analysis and Modeling of Film Capacitor Radiation Generic Radiating Model for the Rectangular Capacitors

Walid Labiedh, Bessem Zitouna, Mohamed Tlig, and Jaleleddine Ben Hadj Slama

LATIS, Laboratory of Advanced Technology and Intelligent Systems
ENISo, National Engineering School of Sousse - University of Sousse, Tunisia

Abstract ─ Capacitors are sources of EM field emissions whose characterization is crucial for electronic circuits EMC. This paper presents the modeling of equivalent radiating sources of rectangular film capacitors. It presents and analyses the magnetic near field measured above plastic and polyester capacitors. The measurements are then used by the inverse method to create a radiating source model for the capacitor. The results show a good agreement between the measured cartography and the one obtained when using radiating sources model. Finally, a generic radiating model is proposed for various types of rectangular film capacitors. The generic model is validated using the measurements on a rectangular capacitor. The suggested radiating model accelerates solving the inverse method. It can be used by circuit designers to optimize the placement of capacitors on the printed circuit board to reduce their coupling with other components of the studied system.

Index Terms ─ Electromagnetic compatibility, electromagnetic radiation, film capacitors, inverse problems, near field.

I. INTRODUCTION

In power electronics, the switching frequencies are increasingly high so as to reduce the weight, the volume and the cost of these systems. This rise in frequency is accompanied with an increase in conducted and radiated electromagnetic disturbances. It also has important effects on the behavior of these components at high frequencies. The characterization of the electromagnetic behavior of the various components of power electronics systems is an important step that will serve to better control the electromagnetic compatibility of these systems as early as the design phase [1-4].

There are many researches that have proposed radiating models for components or systems. In fact, concerning systems, [2] put forward a radiating model of a DC-DC converter, referenced as TEN 40-2412. The suggested model was composed of a network of four magnetic dipoles. The study [3] proposed two radiating models of a circuit based on a microcontroller. The first model was based on 53 magnetic dipoles while the second one was based on 517 electric dipoles. For components, [4] put forward a radiating model of the MOSFET. The obtained model was constituted by a magnetic dipole. Two radiating models of a toric self-inductance were suggested in [5]. The first developed model consisted of a large number of dipoles (676 dipoles). It was got by using a modeling approach based on the matrix inversion. The second model was composed of a network of 12 dipoles. Previous, researches have already put forward a radiating model for an inductor [6-7]. The proposed model by [6] consisted of a network of two simple magnetic dipoles. However, the one suggested by [7] was composed of a large number of magnetic and electric dipoles (520 dipoles). The measurements of the electromagnetic radiation were performed as described in [8].

On the other hand, several methods have been developed to model the radiated emissions of components and electrical systems. The study [3] suggested two methods. The first one was based on magnetic dipoles and the second one was based on electric dipoles. The two presented methods required both the amplitude and the phase of the field. The study [4] put forward an electromagnetic inverse method based on the Genetic Algorithms (GA). The method gave good results in the case where the number of searched parameters is not very important; otherwise the method was inefficient when considering calculation time and convergence. For this, the same authors developed in [2] a new approach based on image processing descriptor PZMI, which consisted in processing only a scan window of the measured magnetic field cartography. Another approach was developed by [6-7]. It was based on the matrix calculation.

In this paper, we are interested in radiation of film capacitors. The film capacitors are widely used in the power electronics domain and they are replacing electrolytic capacitors. They particularly permit the improvement of reliability and EMI suppression. Indeed, they are often used in new industrial applications, such as power converters for renewable energy and also for hybrid automotive systems. The film capacitors are mainly characterized by a high insulation resistance, large

Submitted On: October 15, 2020
Accepted On: March 6, 2021

https://doi.org/10.47037/2020.ACES.J.360408

conducted currents and a good stability of its capacitance. These components are generally cumbersome and their radiation certainly affects the overall radiation of the circuits. The electromagnetic field radiated by capacitors creates induced disturbances that may cause a dysfunction to the neighboring circuits. Therefore, the mastery of all the circuit's radiated field is a requirement for the proper functioning of the system. It will be worthwhile to dispose of the radiation model of capacitors.

The literature review of papers related to EMC analysis of discrete capacitors shows few studies dealing only with conducted disturbances across these components and their coupling effects on other neighboring components. Particularly, in [9-12] the authors first studied the electromagnetic coupling between the components of an EMC filter. The filter was composed of two capacitors and two coils. Second, they proposed an automatic method to determine the optimal placement of components and the associated tracks' design. However, these studies treat the coupling in a special single application which is an EMC filter. They were not interested in the capacitors radiation. [12] put forward methods for predicting the distribution of the magnetic field in capacitors. Although, the existence of a magnetic field may seem anecdotal in capacitors who's functioning depends on the electric field, this is not the case because the magnetic field is precisely the cause of imperfections of the capacitors: the equivalent series inductance, the resonant frequencies, the associated losses, and the currents induced in metallization [13].

The aim of the present paper is to propose a radiation model for film capacitors, which has never been proposed before. In the next section, we will present the experimental techniques used to characterize the near field around the capacitors. In the third section, we will analyze the magnetic near field above the capacitors. The modeling method will be explained in the section four. It will be then applied in the following section to develop the radiating models of the studied capacitors. Finally, we will put forward a generic model for all rectangular capacitors.

II. EXPERIMENTAL TECHNIQUES AND CHARACTERIZATION METHOD

A. Excitation circuit

To allow characterization over a wide frequency band, we excite the studied component with a current having a large frequency band similar to the one found in power electronics. Therefore, we propose to insert the component under test in a converter circuit supplied by a voltage equal to 30V and having a duty cycle equal to 0.5 (Fig. 1). The output current of the circuit is of 0.5 A. The switching frequency is 50 kHz.

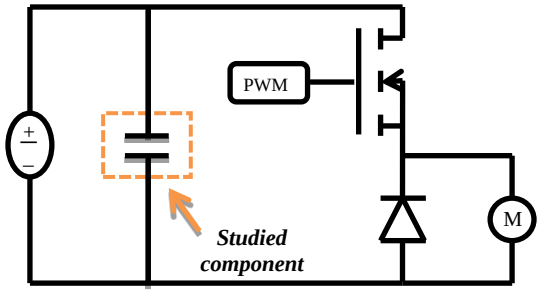

Fig. 1. Chopper circuit where studied component is characterized.

B. Measurements methods

In our study, we utilize only one component of the field radiated by the system under test. Indeed, the use of a single component in a large number of points is quite sufficient for identifying the equivalent source by guaranteeing the uniqueness of the solution [14-15].

Furthermore, the developed radiating model is capable of modeling the electric field as well as the magnetic field. Actually, based on [16-18], we can calculate from the magnetic field, the electric one and vice versa.

Since the method can be applied to any component of the magnetic or electric field, we have used the vertical component Hz. We may also utilize the other tangential components (Hx or Hy). For measuring the magnetic near field, we place a magnetic probe above the device under test. It is a manually made probe, which consists of a 1.6mm radius circular loop connected to the central conductor on one side and to the external shield of a coaxial cable on the other side. To capture the various components of the H field, it is necessary to place the normal of the collinear loop to the desired component.

In our study, we use two methods for measuring the magnetic field around the component. The first method performs the measurements of the near field in the frequency domain and the second one is performed in the time domain.

C. Probe calibration

It is worth noting that the used electronic probes are none other than small sensors or antennas as proposed and implemented in the IRSEEM NF test bench [7-8] [19]. In these studies, the authors suggested a method to validate the accuracy of their magnetic field probes. They measured the radiated magnetic field around a simple circuit which was a conductive wire above a ground plane. The values of the measured field were compared to those calculated theoretically. Thus, the results comparison enabled the validation of the used probes.

Similarly, in this work, to calibrate the magnetic probe, we have used a radiating circuit whose radiation is known theoretically. We compare the measured radiated magnetic field to that calculated by the numerical electromagnetic tool NEC [20] based on the moment's method. The radiating circuit is a rectangular loop of 5 cm length and 3 cm width excited by a sinusoidal voltage of 10V amplitude at a frequency of 5MHz (Fig. 2).

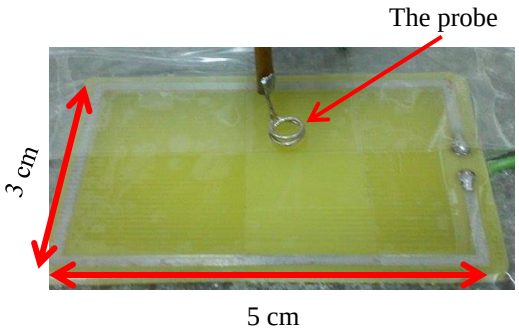

Fig. 2. Loop used for probe calibration.

The simulations and measurements are made at the points located in a horizontal plane at a height of 3 mm above the radiating loop and having dimensions of 5 cm X 3 cm. The calculation step is of 2.5 mm along the X axis and of 1.5 mm along the Y axis (441 measurement points).

Figures 3, 4 and 5 present the magnetic field components Hz, Hx and Hy along the X and Y axis respectively. It shows a good agreement between the measured and calculated curves of Hz component. In order to, have a good signal to noise ratio when measuring Hx and Hy components, we chose measurements lines located at the edge of the emitting loop. Consequently, in some positions of the measuring probe we notice a difference between measurements and simulations due to the edges effects and the coupling effects between the probe and the radiating loop. These phenomena are not significant on the Hz component and therefore do not affect the construction of the model.

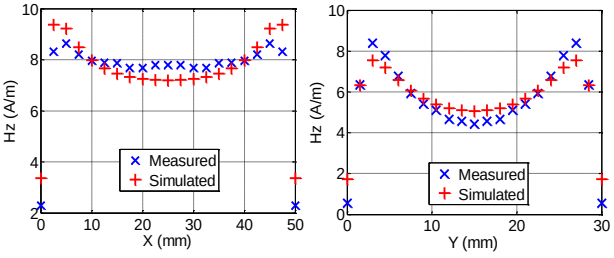

Fig. 3. Hz following X and Y axes respectively for Y = 4.5 mm and X = 25 mm.

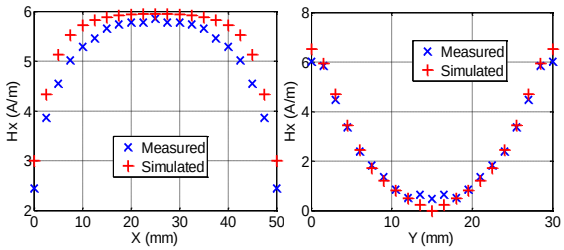

Fig. 4. Hx following X and Y axes respectively for Y = 1.5 mm and X = 25 mm.

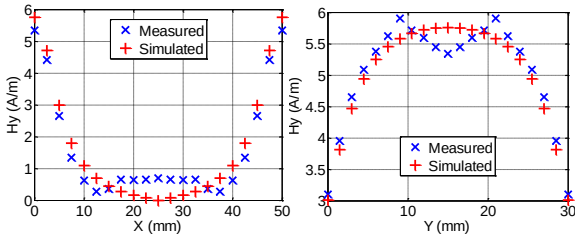

Fig. 5. Hy following X and Y axes respectively for Y = 1.5 mm and X = 25 mm.

In order to examine the electric field rejection capability of our magnetic probe, we have placed it over a transmitting electric antenna where the amplitude of the electric field is important. The observed voltage across the probe is so low that we cannot dissociate it from the noise. Hence, we deduce that our shielded probe rejects very well the electric field and measures the magnetic field with great accuracy.

III. MEASUREMENTS AND ANALYSIS OF POLYPROPYLENE CAPACITOR RADIATION

Measurements are performed in the time domain using a high bandwidth oscilloscope. We have measured the vertical component Hz of the magnetic near-field radiated above a plastic polypropylene capacitor of a 2.2uF capacitance and a maximum voltage of 100V (the capacitor size is15mm x 6mm x 26.5mm). To avoid the interferences caused by the capacitor legs, we have folded the legs of the latter. The probe is located at a distance of 2 mm above the capacitor in a plane whose dimensions are 4cm x 2cm. The displacements are done with a measuring step of 2 mm on the X axis and 1 mm on the Y axis. Thus, we have 400 measurement points. Figure 6 shows the measurement plane and the component under test. It gives a particular point (3,5) position in the measurement plane.

Figure 7 shows the temporal signal measured at the terminals of the magnetic probe once it is situated at the point (3,5): the third position along the X axis and

the fifth position along the Y axis. When analyzing the measured magnetic field signal, we notice the existence of switching transients during the turning on and the turning off of the power component utilized in the chopper.

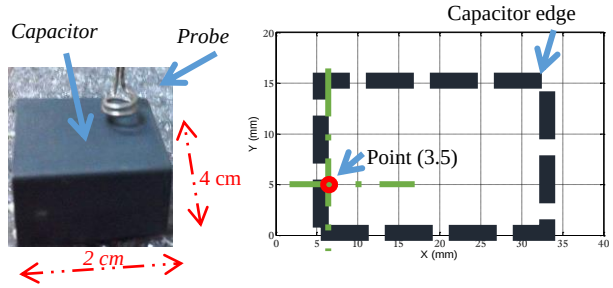

Fig. 6. Measurement plane over component under test.

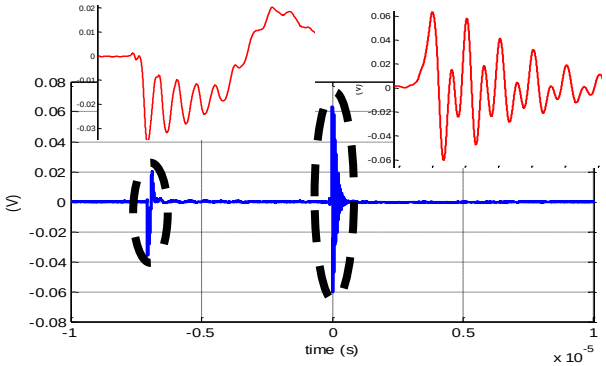

Fig. 7. Measured temporal signal at the terminals of the probe above capacitor under test.

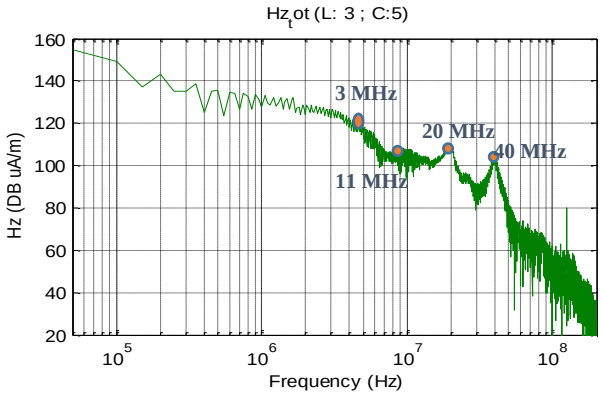

Fig. 8. Spectrum of radiated magnetic field Hz at the terminals of the probe above the studied capacitor at point (3.5).

Figure 8 shows the spectrum analysis of the full temporal signal with both switching phases (closing and opening of the MOSFET in the excitation circuit where our studied component is characterized). That measured above the capacitor at the point of the coordinates (3,5) presented in Fig. 7. By analyzing the spectrum of the measured temporal signal, we notice the appearance of four principal harmonics which have the following frequencies: 3 MHz, 11 MHz, 20 MHz, and 40 MHz. The resonances that appear above the capacitor are principally due to the operating current flowing into the chopper circuit.

We present in Fig. 9 the cartographies of the field above the capacitor at these different frequencies.

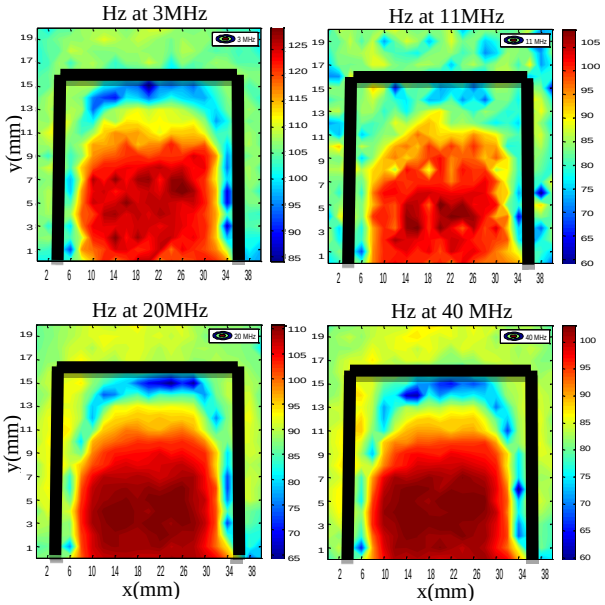

Fig. 9. Cartographies of near field for 3MHz, 11 MHz, 20 MHz, and 40 MHz frequencies.

According to the previous cartographies, it is noted that the distribution of the radiated magnetic field above the capacitor is located on the entire surface of the component as illustrated in Fig. 10.

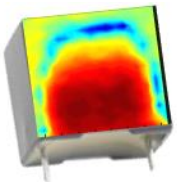

Fig. 10. Distribution of magnetic field above capacitor (frequency equal 20 MHz).

IV. MODELING METHODOLOGY

To develop a radiating model that enables producing a near field equal to that's radiated by the system under test. The modeling methodology given in Fig. 11 is based on a hybrid approach consisting in the coupling between

the electromagnetic inverse method and the Method of Moments (MoM) [21]. The optimization method used in this work is based on genetic algorithm that has been presented in [22-24]. To reduce the convergence time of the electromagnetic inverse method, we take into account the study presented in [22] to choose the optimum parameters of the genetic algorithms. These optimum parameters are given in Table 1.

The equation presented in Table 1 gives the fitness function which ensures the comparison between the estimated and the measured field. It is equal to the sum, on all points of the measured cartography of the relative errors between the measured magnetic near-field and the estimated one.

Table 1: Optimum parameters of genetic algorithms

Fitness Function	Population Size (Np)	Selection Function	Crossover Rate
$Error = \sum_{i=1}^{n} \frac{\lvert H\ measured - H\ estimated \rvert}{H\ measured} \times 100$	Np = 20 × number of parameters of dipoles	Roulette	0.8

These numerical modeling methods depend on the performance of the machines on which they are run and the complexity of the simulated structure. Therefore, very high precision is required; a more powerful PC in order to reduce the computing time is required.

After, the search is launched to find the parameters of the equivalent radiating structure by comparing the measured cartography to the one calculated numerically by the moment's method and using the obtained parameters.

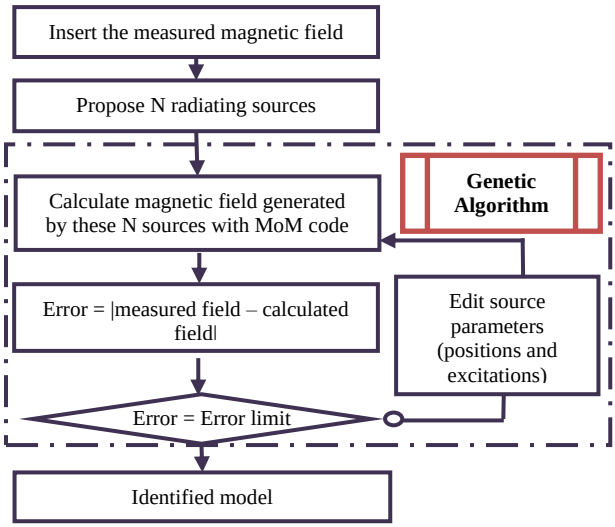

Fig. 11. Flow chart of the modeling approach.

The calculation of the magnetic field generated by the N sources is done through the NEC2D software core which is based on the MoM.

As the capacitor cartographies gather at the radiation of a rectangular loop, the search for models has been launched to find a rectangular current loop using the method based on the coupling between inverse method and the MoM. Each rectangular loop as given in Fig. 12 is characterized by the coordinates of its center (X0, Y0, Z0), its width (w), its length (L), its orientations (φ, θ), the radius (r) of the loop wire, and the current flowing through it.

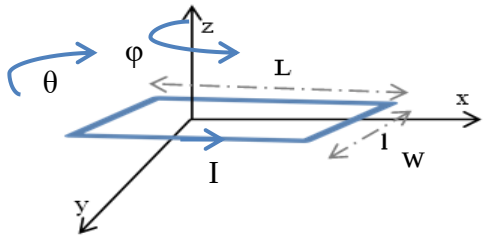

Fig. 12. Rectangular current loop parameters.

V. MODEL FOR THE POLYPROPYLENE CAPACITOR

A. Model research

After presenting the cartographies of the magnetic field radiated by the capacitor in section 3, we apply our approach to find a model that gives the same radiation as that measured over the capacitor. To do this, we used the cartography of the vertical component Hz of the magnetic field at a frequency of 20 MHz. We chose the cartography of 20 MHz because it was the clearest one. The modeling results are shown in Table 2.

Figure 13 shows the position of the identified loop on the capacitor cartography.

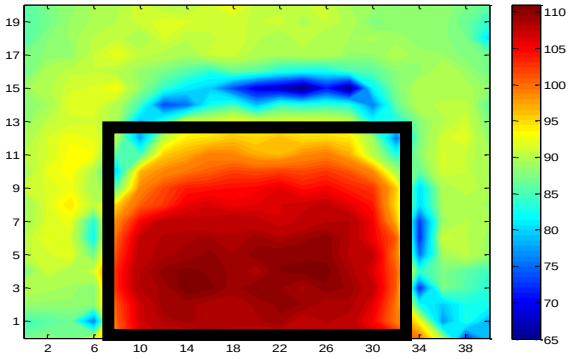

Fig. 13. Obtained loop position.

Table 2: Parameters of the obtained rectangular loop

Center Coordinates (X_0, Y_0, Z_0) (mm)	Loop Dimensions Width, Length (mm)	Orientations Φ, θ (rd)	Conductor Radius R (mm)	Voltage Excitation (V)
3.6; 19; -2.9	12; 23	0; 0	1	0.035

Figure 14 presents the measured and estimated cartographies of the magnetic field vertical component Hz. A reasonable agreement between the two cartographies is observed.

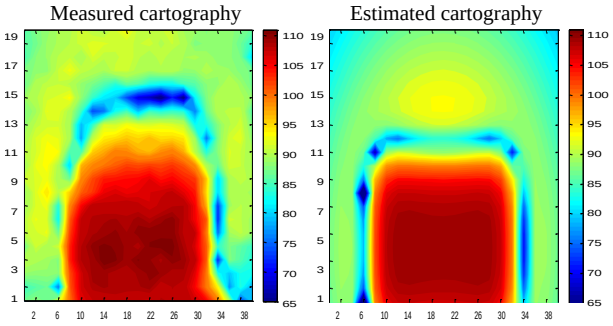

Fig. 14. Measured and estimated cartographies.

B. Model validation

To validate the reconstructed model, we propose to present a comparison between the estimated and measured cartographies for other faces of the capacitor or other components as proposed in [4], [25]. To do this, initially, we perform an experimental measurement of the cartography of the magnetic field on other face of the capacitor (Hx measured). For this, we placed the capacitor vertically and we measured the magnetic field radiated from this face. In the second step, we exploit the estimated parameters to calculate the cartography of the tangential component of the magnetic field (Hx estimated). Figure 15 depicts the layout of the measurements.

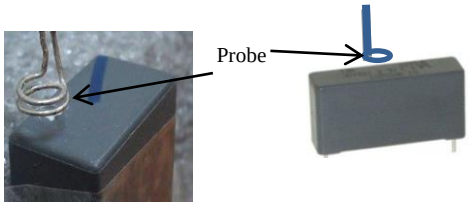

Fig. 15. Measurement of magnetic field over vertically placed capacitor.

The validation of the model is made for the frequency of 20 MHz and at a measurement height of 3 mm. We give in Fig. 16 the measured magnetic field cartography and that's calculated by the model above the vertically placed capacitor.

According to the previous results, the magnetic field reconstructed by the model shows a good accordance with the measured one. These results confirm the existence of an equivalent rectangular current loop in the capacitor. To explain the obtained results, we present in Fig. 17 the internal structure of the capacitor.

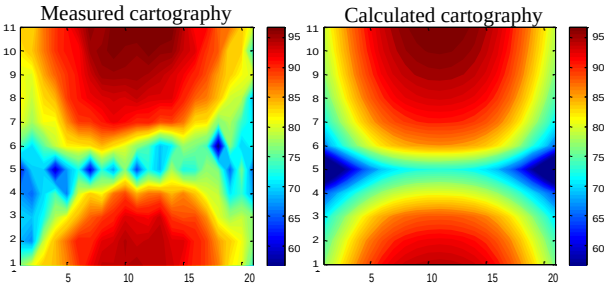

Fig. 16. Cartographies of measured and calculated field above vertically placed capacitor.

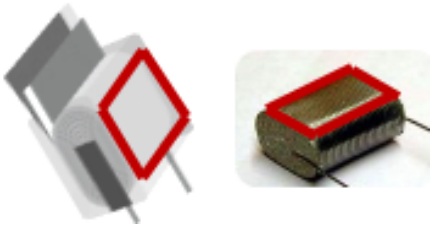

Fig. 17. Film capacitor's internal structure.

The analysis of the internal structure of the film capacitor confirms the obtained equivalent model. Indeed, the surface of the capacitor appears as a rectangular loop.

This current distribution at the capacitor contour is certainly caused by the internal coupling phenomena in the component. This current distribution in the capacitor film is consistent with that introduced in [12-13].

VI. MODEL FOR THE METALLIZED POLYESTER CAPACITOR

A. Measurement of magnetic near-field radiated by polyester capacitors

Based on the frequency measurement method, we measured the vertical component Hz of the magnetic field radiated above a metallized polyester capacitor of a 1μF capacitance and having a maximum voltage of 100V (the capacitor size 14mm x 7mm x 18mm). In order to have exactly only the magnetic field radiated by the capacitor, we bent the legs of the capacitor. The probe was located at a 3 mm distance from the capacitor. The measurements of the magnetic-field were performed in

a plane whose dimensions were 30mm x 20mm with a measuring step of 1.5 mm on the X axis and 1 mm on the Y axis. Figure 18 shows the measurement plane and the component under test.

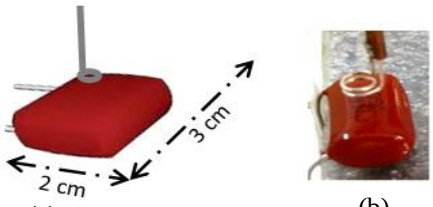

(a) (b)

Fig. 18. (a) Measurement plan and (b) device under test.

After making Fast Fourier transformation (FFT) of the measured signals above the capacitor, we notice that the frequency of 26 MHz has maximum amplitude. We present in Fig. 19 the cartographies of the Hz and Hy components measured at the frequency of 26 MHz.

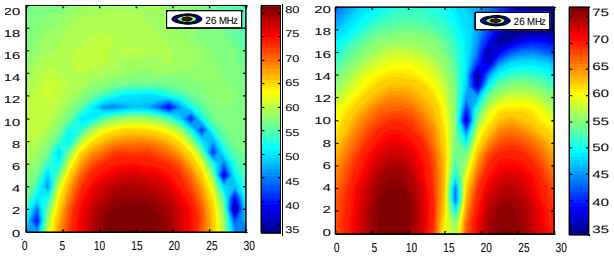

(a) (b)

Fig. 19. Cartographies of the field above the capacitor: (a) Hz and (b) Hy.

B. Radiated-field modelling

As for the polypropylene capacitor, the radiation of the polyester capacitor looks like that of a rectangular loop. We applied the same method exposed previously to the cartography of the measured magnetic field Hz at the frequency of 26 MHz. The modeling result is a rectangular current loop whose parameters are given in Table 3.

Table 3: Parameters of the obtained rectangular loop

Center Coordinates (X_0, Y_0, Z_0) (mm)	Loop Dimensions Width, Length (mm)	Orientations Φ, θ (rd)	Conductor Radius R (mm)	Voltage Excitation (V)
1; 15; -3.3	12; 16	0; -0.2	1	0.0017

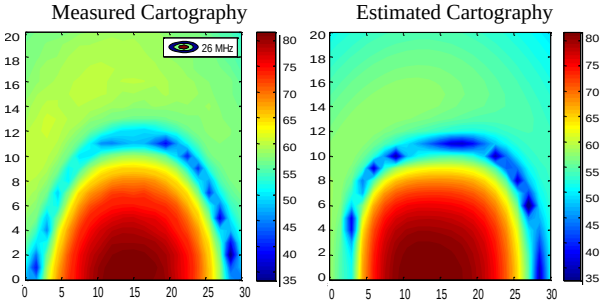

Fig. 20. Measured and estimated the vertical component Hz cartographies of polyester capacitor.

Figure 20 exposes the cartographies of the magnetic field Hz measured and estimated by the obtained model above the capacitor. A good agreement between the two cartographies is observed.

C. Model validation

To validate the obtained model in a better way, we examined the cartographies of the other components of the magnetic field above the capacitor. We specifically compared the measured component Hy of the magnetic field with that calculated using the obtained model.

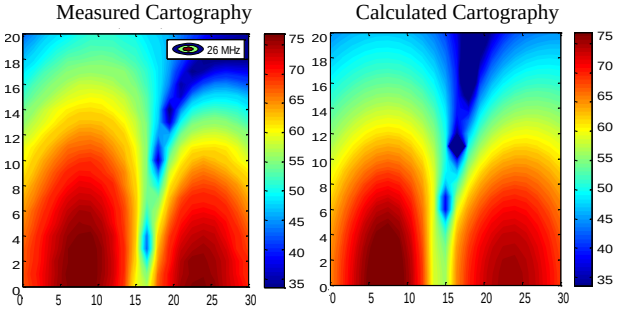

Fig. 21. Cartographies of measured and estimated Hy component of the magnetic field above the capacitor.

Figure 21 show that the magnetic field reconstructed by the model resembles to a great extent the measured magnetic field.

D. Generic model for capacitor

The examination of the results obtained previously allows us to conclude that the equivalent radiating model for the different types of the rectangular film capacitors is a rectangular loop whose parameters depend on the geometry of the capacitor as illustrated in Fig. 22 and explained in equations (1) to (4).

We suggest formulas to determine, using capacitor dimensions, and the size of the source rectangular loop of the generic model.

The center coordinates	= Gravity center of the capacitor
Loop dimensions	$Width_{Generic} \cong 0.8 \times Width_{capacitor}$, (1)
	$Length_{Generic} \cong 0.86 \times Length_{capacitor}$, (2)
Orientations	$\varphi = 0$ (rd) (3)
	θ depends on the position of the capacitor under test relative the x-axis $\cong 0$. (4)
Excitation Voltage	Dependence on the field amplitude

To validate the proposed generic model, we applied it on another rectangular capacitor. Therefore, we measured the magnetic field above a third rectangular capacitor having 2.2μF capacitance and a maximum voltage of 250V (the capacitor size is 25mm x 14mm x 41.5mm).

We performed measurements of the near field cartography above the studied capacitor and then we applied the method based on the coupling of the electromagnetic inverse method with the MoM to find the equivalent model that will be compared to the one obtained by the generic model formulas.

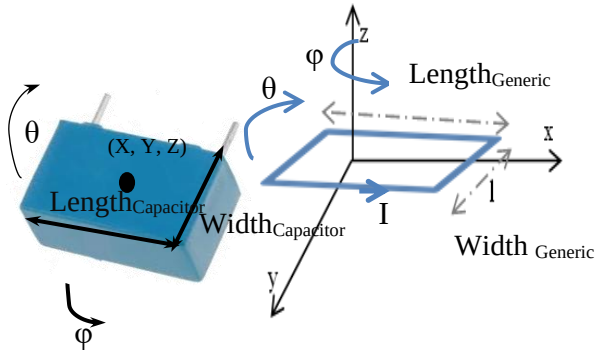

Fig. 22. Capacitor parameters and the analogy with the equivalent loop.

According to Table 4, we notice that the calculated parameters by the formulas of the generic model are very close to those obtained by the inverse electromagnetic method.

Table 4: Parameters of rectangular loop obtained by two methods

Obtained Parameters by Two Methods	Center Coordinates (X_0, Y_0, Z_0) (mm)	Loop Dimensions Width, Length (mm)	Orientations Φ, θ (rd)	Conductor Radius R (mm)	Voltage Excitation (V)	Modeling Time (min.)
Without generic model	2; 26; -7.3	21; 37	0; 0	1	0.0007	62
Generic model	2.3; 25; -7	20; 35.69	0; 0	1	0.00055	8

We observe from the previous table that searching model using the generic model is seven times faster than when being used without the generic model. Indeed, in the generic model we search only one parameter (the excitation voltage) whiles the others parameters are calculated using the formulas given in equations (1) to (4).

Figure 23 shows the components Hy and Hz of the magnetic near-field measured and estimated by the two obtained models above the capacitor under test at a frequency of 27 MHz.

According to the results presented in Fig. 23, the magnetic field reconstructed using the proposed generic model shows an agreement with the measured magnetic field. In fact, in our modeling approach, we are interested in the high amplitudes of the magnetic field (red parts in the cartographies) because they have the most important magnetic field radiated by the component under test. For these values we notice a good agreement between the measured field and the one calculated by the generic model.

Figure 24 presents a comparison between the two models for cuts of the components Hz and Hy along the x-axis. It shows a reasonable agreement between the measured magnetic field and the obtained one with the two models.

The examination of all the obtained results enables us to conclude that the suggested generic model is a slight model that permits, in a very short time, the calculation of the radiation of the different types of the rectangular capacitors.

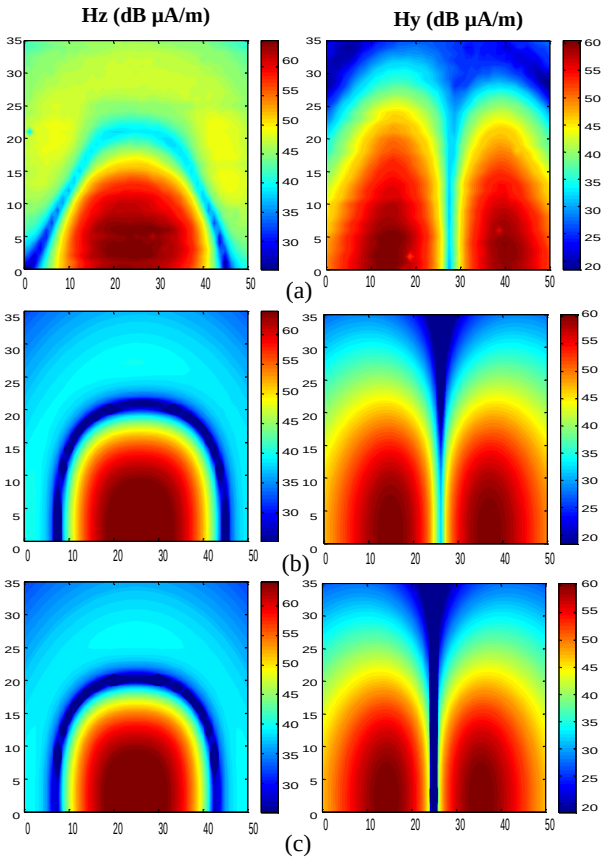

Fig. 23. Cartographies of magnetic field: (a) measured, (b) estimated using inverse method, and (c) using generic model (at frequency of 27 MHz).

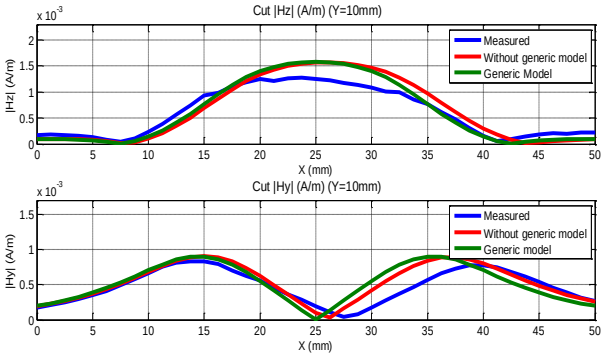

Fig. 24. Comparison of the two models for cuts of Hz and Hy components along the x-axis.

VII. CONCLUSION

Film capacitors are among the larger components on power electronics boards. Therefore, they cause a considerable radiation above all the circuit. In this paper, we have presented the characterization measurements of the magnetic field radiated by different film capacitors utilized in power electronics. We have then used the inverse electromagnetic method based on coupling between the Genetic algorithms and the moment's method to propose models of equivalent radiating sources of these capacitors. A generic radiating model for different types of rectangular film capacitors has been finally put forward and validated using measurements on another capacitor.

This equivalent model is special; hence, its radiation is much more complicated than the one that is usually used by the electromagnetic inverse problem (elementary magnetic and electric dipoles).

The proposed radiating model reduces the number of parameters to be determined by the GA method and consequently reduces the convergence time of the inverse method. It can be utilized by circuit designers to optimize the placement of capacitors on the printed circuit board to reduce their coupling with other components of the studied system.

REFERENCES

[1] J. Ben Hadj Slama and W. Labiedh, "Library of EMC models for passive components and printed circuit board," *Electrotechnical Conference (MELECON), 16th IEEE Mediterranean*, pp. 325-330, Mar. 25-28, 2012.

[2] S. Saidi and J. Ben Hadj Slama, "A near-field technique based on PZMI, GA, and ANN: Application to power electronics systems," *Electromagnetic Compatibility, IEEE Transactions on*, vol. 56, no. 4, pp. 784-791, Aug. 2014.

[3] Y. Vives-Gilabert, C. Arcambal, A. Louis, F. De Daran, P. Eudeline, and B. Mazari, "Modeling magnetic radiations of electronic circuits using near-field scanning method," *Electromagnetic Compatibility, IEEE Transactions on*, vol. 49, no. 2, pp. 391-400, May 2007.

[4] S. Saidi and J. Ben Hadj Slama, "Analysis and modeling of power mosfet radiation," *Progress in Electromagnetics Research M*, vol. 31, pp. 247-262, 2013.

[5] Y. Vives-Gilabert, C. Arcambal, A. Louis, P. Eudeline, and B. Mazari, "Modeling magnetic emissions combining image processing and an optimization algorithm" *IEEE Transactions on Electromagnetic Compatibility*, vol. 51, no. 4, pp. 909-918, Nov. 2009.

[6] P.-E. Levy, C. Gautier, F. Costa, B. Revol, and C. Labarre, "Accurate modeling of radiated electromagnetic field by a coil with a toroidal ferromagnetic core," *Electromagnetic Compatibility, IEEE Transactions on*, vol. 55, no. 5, pp. 825-833, Oct. 2013.

[7] H. Shall, Z. Riah, and M. Kadi, "A 3-D near-field modeling approach for electromagnetic interference prediction," *Electromagnetic Compatibility, IEEE Transactions on*, vol. 56, no. 1, pp. 102-112,

Feb. 2014.

[8] D. Baudry, C. Arcambal, A. Louis, B. Mazari, and P. Eudeline, "Applications of the near-field techniques in EMC investigations," *Electromagnetic Compatibility, IEEE Transactions on*, vol. 49, no. 3, pp. 485-493, Aug. 2007.

[9] T. De-Oliveira, J.-L. Schanen, J.-M. Guichon, and L. Gerbaud, "Optimal stray magnetic couplings for EMC filters," Industry Applications, *IEEE Transactions on*, vol. 49, no. 4, pp. 1619-1627, July-Aug. 2013.

[10] T. De Oliveira, J.-M. Guichon, J.-L. Schanen, and L. Gerbaud, "PEEC-models for EMC filter layout optimization," *Integrated Power Electronics Systems (CIPS), 2010 6th International Conference on*, pp. 1-6, Mar. 16-18, 2010.

[11] H. Chen and Z. Qian, "Modeling and characterization of parasitic inductive coupling effects on differential-mode EMI performance of a boost converter," *Electromagnetic Compatibility, IEEE Transactions on*, vol. 53, no. 4, pp. 1072-1080, Nov. 2011.

[12] E. L. Nativel, T. Talbert, T. Martire, C. Joubert, N. Daude, and P. Falgayrettes, "Near-field electromagnetic tomography applied to current density reconstruction in metallized capacitors," *in IEEE Transactions on Power Electronics*, vol. 20, no. 1, pp. 11-16, Jan. 2005.

[13] C. Joubert, A. Béroual, and G. Rojat, "Magnetic field and current distribution in metallized capacitors," *Journal of Applied Physics*, vol. 76, no. 9, pp. 5288-52931, Nov. 1994.

[14] J. Fan, "Near-field scanning for EM emission characterization," *in IEEE Electromagnetic Compatibility Magazine*, vol. 4, no. 3, pp. 67-73, 3rd Quarter 2015.

[15] X. Gao, J. Fan, Y. Zhang, H. Kajbaf, and D. Pommerenke, "Far-field prediction using only magnetic near-field scanning for EMI test," *in IEEE Transactions on Electromagnetic Compatibility*, vol. 56, no. 6, pp. 1335-1343, Dec. 2014.

[16] Y. Liu, B. Ravelo, and A. K. Jastrzebski, "Calculation of time-domain near field Ex,y,z(t) from Hx,y(t) with PWS and FFT transforms," *in Proc. Int. Symp. Electromagn. Compat*., Roma, Italy, pp. 1-6, Sep. 17-20, 2012.

[17] B. Ravelo, "E-field extraction from H-near-field in time-domain by using PWS method," *Progress Electromagn. Res. B*, vol. 25, pp. 171-189, 2010.

[18] Y. Liu, B. Ravelo, A. K. Jastrzebski, and J. B. Hadj Slama, "Calculation of the time domain z-component of the EM-near-field from the x- and y-components," in *Proc. 41st Eur. Microw. Conf.*, pp. 317-320, Oct. 10-13, 2011.

[19] Y. Vives-Gilabert, C. Arcambal, A. Louis, F. de Daran, P. Eudeline, and B. Mazari, "Modeling magnetic radiations of electronic circuits using near-field scanning method," *IEEE Transactions on Electromagnetic Compatibility*, vol. 49, no. 2, pp. 391-400, 2007.

[20] G. J. Burke and A. J. Poggio, "Numerical electromagnetics code (NEC) - Method of moments," *NOSC TD 116 Part I*, Jan. 1981.

[21] J. Ben Hadj Slama and S. Saidi, "Coupling the electromagnetic inverse problem based on genetic algorithms with moment's method for EMC of circuits," *15th IEEE Mediterranean Electrotechnical Conference MELECON'10*, Malta, pp. 709-714, Apr. 26-28, 2010.

[22] S. Saidi and J. Ben Hadj Slama, "Effect of genetic algorithm parameters on convergence of the electromagnetic inverse method," *8th International Multi-Conference on Systems, Signals & Devices*, pp. 1-5, Mar. 22-25, 2011.

[23] Z. Javad, Y. Cai, and N. Ojaroudi, "UWB slot antenna with band-notched property with time domain modeling based on genetic algorithm optimization," *Applied Computational Electromagnetics Society Journal*, vol. 31, no.8, pp. 926-932, Aug. 2016.

[24] Zitouna, B., Ben Hadj Slama, J. , "Enhancement of time-domain electromagnetic inverse method for modeling circuits radiations," *IEEE Trans. Electromagn. Compat., 58, (2), pp. 534–542, 2016.*

[25] B. Zitouna and J. Ben Hadj Slama, "Time domain inverse method based on the near field technique to solve electromagnetic interference problems: Application to an AC/DC flyback converter," *IET Power Electronics*, vol. 11, no. 13, pp. 2133-2139, June 2018.

Prediction and Suppression of Twisted-wire Pair Crosstalk Based on Beetle Swarm Optimization Algorithm

Jianming Zhou [1], Shijin Li [1*], Wu Zhang [1], Wei Yan [1], Yang Zhao [1], Yanxing Ji [1], and Xingfa Liu [2]

[1] School of Electrical & Automation Engineering
Nanjing Normal University, Nanjing 210046, China
zhoujianmingz@163.com, *lishijin@njnu.edu.cn, m13571872250@163.com, 61197@njnu.edu.cn, zhaoyang2@njnu.edu.cn, 397832514@qq.com

[2] State Key Laboratory of Power Grid Environmental Protection
Wuhan Branch of China Electric Power Research Institute Co., Ltd., Wuhan 430000, China
liuxingfa@epri.sgcc.com.cn

Abstract ─ Based on the theory of multi-conductor transmission lines (MTL), this paper proposes a new method for predicting and suppressing crosstalk of twisted-wire pair (TWP). The per unit length (p.u.l) RLCG parameters change caused by the inconsistent cross-sectional shape of TWP, changes in parameters make it difficult to solve the telegraph equation. In this paper, the method of transmission lines cascade is used. TWP is divided into several segments, and p.u.l parameters of each segment are predicted. Compared with before method, we propose a higher precision algorithm—beetle swarm optimization (BSO) to optimize the weights of back-propagation (BP) neural network, which predict p.u.l parameters at each segment. On this basis, it is divided into two steps: 1) Use MTL frequency domain method combined with lines' terminal conditions to solve crosstalk and compare with CST simulation results; 2) Use the singular value decomposition (SVD) method to add matrix modules at both ends of lines for suppressing crosstalk. The results show that proposed method in this paper is consistent with the simulation, and the accuracy is higher than before.

Index Terms ─ Beetle swarm optimization, crosstalk, multi-conductor transmission lines, singular value decomposition.

I. INTRODUCTION

As people's requirements for electronic equipment increase, the circuit system gradually becomes smaller and more compact. The increase of the operating frequency has caused various electromagnetic interference (EMI) problems. Today, the effects of crosstalk between TWP cannot be ignored [1-3], then influence the signal integrity (SI). Unintentional coupling of energy between electro-magnetic fields will cause crosstalk in the line, in other words, the energy in the signal line is coupled to other lines. This part of the energy is useless [4]. The traditional MTL usually refers to a group of *n*-parallel conductor transmission line structures that propagate electrical signals in two or more fixed points. The crosstalk value can be achieved by directly solving the telegraph equation. However, the cross-section position in TWP is random and unknown, which brings different p.u.l RLCG parameters, so it is difficult to predict crosstalk directly by the traditional method [5,6].

In the past thirty years of research on crosstalk, many scholars have proposed a variety of TWP crosstalk prediction methods. Cannas proposed to treat non-uniformly TWP as cascade of several uniformly cross sections, and use BP neural network to make prediction [7]. In [8], Dai proposed to use the random displacement spline interpolation [9] (RDSI) to generate a set of non-uniformly TWP to provide training samples, and then use the trained BP to predict the crosstalk, but ordinary BP neural network have large errors, and its prediction range is narrow. In [10], the ANSI parameter matrix was proposed to predict the near-end crosstalk of unshielded TWP.

Based on the theory of MTL [11], some novel methods for suppressing crosstalk have been proposed. The proper feeding and matching modules at the line ends method was proposed in [12]. Increasing the effects of the capacitive coupling to cancel that of the inductive coupling along two parallel lines for reducing far end crosstalk is reported in [13]. By adding coefficient matrices at both ends of line, the unitization of transmission matrix is realized to suppress crosstalk have also been discussed [14]. However, these suppression methods are mainly aimed at parallel transmission lines,

Submitted On: November 10, 2020
Accepted On: January 28, 2021
https://doi.org/10.47037/2020.ACES.J.360409

and there is little research on TWP.

In fact, when the TWP is segmented, each fixed section position will correspond to a defined p.u.l matrix. This paper uses the cascade method [15] with BSO-BP algorithm, which has strong nonlinear mapping ability and is suitable for crosstalk prediction and suppression.

This paper is organized as follows. In Section II, MTL's distributed parameter circuit diagram and chain parameter theory will be given, the transmission lines model will be established. Besides, the process of BSO algorithm is introduced, the prediction errors of BSO, beetle antennae search (BAS) [16] and BP are compared in Section III. In Section IV, MTL frequency domain method will be used to solve the telegraph equation and be compared with the CST simulation results; the SVD method will be used to suppress crosstalk, and comparison figure before and after crosstalk suppression is given with PSPICE software. Conclusions are eventually drawn in Section V.

II. EQUIVALENT CIRCUIT AND CHAIN PARAMETER

A. Equivalent circuit

In MTL theory, the telegraph equation regards the transmission lines as having a distributed parameter structure along the axis. The micro-element conduction model of per unit length MTL is shown in Fig. 1. r_{ij}, l_{ij}, c_{ij} and g_{ij} represent the elements in resistance **R**, inductance **L**, capacitance **C**, and conductance **G** parameter matrices, where: i, j=1,2,…,n.

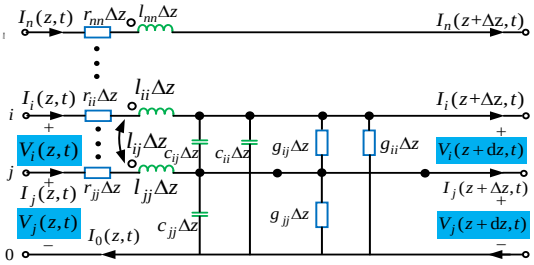

Fig. 1. The equivalent circuit model of micro-element.

The satisfied telegraph equations are expressed as:

$$\frac{\partial \mathbf{V}(z,t)}{\partial z}+\mathbf{R}(z)\mathbf{I}(z,t)+\mathbf{L}(z)\frac{\partial \mathbf{I}(z,t)}{\partial t}=0\,, \tag{1}$$

$$\frac{\partial \mathbf{I}(z,t)}{\partial z}+\mathbf{G}(z)\mathbf{V}(z,t)+\mathbf{C}(z)\frac{\partial \mathbf{V}(z,t)}{\partial t}=0\,, \tag{2}$$

where, $\mathbf{V}(z,t)$ and $\mathbf{I}(z,t)$ are voltage and current vectors at different positions and times on the transmission line. $\mathbf{R}(z)$, $\mathbf{L}(z)$, $\mathbf{C}(z)$, and $\mathbf{G}(z)$ are variables about the position z of transmission line, both of which are n-dimensional symmetric matrices.

B. Chain parameter

In this section, the transmission line will be regarded as a 2n port, and we generally care about the voltage and current at both ends of transmission line. First of all, convert equations (1) and (2) into frequency domain form:

$$\frac{d}{dz}\hat{\mathbf{V}}(z)=-\hat{\mathbf{Z}}\hat{\mathbf{I}}(z)\,, \tag{3}$$

$$\frac{d}{dz}\hat{\mathbf{I}}(z)=-\hat{\mathbf{Y}}\hat{\mathbf{V}}(z)\,, \tag{4}$$

where $\hat{\mathbf{Z}}=\mathbf{R}+j\omega\mathbf{L}$ and $\hat{\mathbf{Y}}=\mathbf{G}+j\omega\mathbf{C}$. Next the characteristic impedance matrix $\hat{\mathbf{Z}}_C$ of line is needed:

$$\hat{\mathbf{T}}_I^{-1}\hat{\mathbf{Y}}\hat{\mathbf{Z}}\hat{\mathbf{T}}_I=\hat{\boldsymbol{\gamma}}^2\,, \tag{5}$$

$$\hat{\mathbf{Z}}_C=\hat{\mathbf{Z}}\hat{\mathbf{T}}_I\boldsymbol{\gamma}^{-1}\hat{\mathbf{T}}_I^{-1}\,, \tag{6}$$

$$\hat{\mathbf{Y}}_C=\hat{\mathbf{Z}}_C^{-1}\,. \tag{7}$$

From [17], the relationship between the voltage and current at both ends of transmission line can be expressed by the chain parameter matrix:

$$\begin{bmatrix}\hat{\mathbf{V}}(\varphi)\\ \hat{\mathbf{I}}(\varphi)\end{bmatrix}=\hat{\Phi}(\varphi)\begin{bmatrix}\hat{\mathbf{V}}(0)\\ \hat{\mathbf{I}}(0)\end{bmatrix}=\begin{bmatrix}\hat{\Phi}_{11}(\varphi) & \hat{\Phi}_{12}(\varphi)\\ \hat{\Phi}_{21}(\varphi) & \hat{\Phi}_{22}(\varphi)\end{bmatrix}\begin{bmatrix}\hat{\mathbf{V}}(0)\\ \hat{\mathbf{I}}(0)\end{bmatrix}. \tag{8}$$

Where the sub-matrix can be defined as follows:

$$\hat{\Phi}_{11}(\varphi)=\cosh(\sqrt{\hat{\mathbf{Z}}\hat{\mathbf{Y}}}\varphi)\,, \tag{9}$$

$$\hat{\Phi}_{12}(\varphi)=-\hat{\mathbf{Z}}_C\sinh(\sqrt{\hat{\mathbf{Y}}\hat{\mathbf{Z}}}\varphi)\,, \tag{10}$$

$$\hat{\Phi}_{21}(\varphi)=-\hat{\mathbf{Y}}_C\sinh(\sqrt{\hat{\mathbf{Z}}\hat{\mathbf{Y}}}\varphi)\,, \tag{11}$$

$$\hat{\Phi}_{22}(\varphi)=\cosh(\sqrt{\hat{\mathbf{Y}}\hat{\mathbf{Z}}}\varphi)\,. \tag{12}$$

When the signal source amplitude is 1V, near-end crosstalk (NEXT) and far-end crosstalk (FEXT) are expressed as follows, i is the victim line number:

$$\mathrm{NEXT}_i=20*\log_{10}(V_i(0))\,, \tag{13}$$

$$\mathrm{FEXT}_i=20*\log_{10}(V_i(\varphi))\,. \tag{14}$$

III. BSO ALGORITHM

A. Modeling of TWP and single line

In this paper, the TWP and single line model in [18] are selected to verify the effectiveness of proposed method.

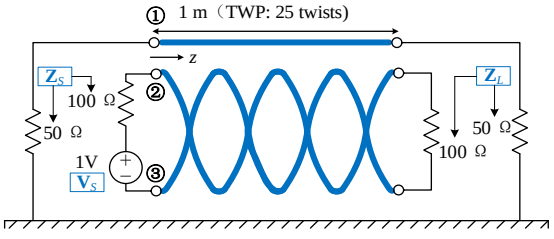

Fig. 2. Line configuration of a single line and TWP.

The model is shown in Fig. 2. Lines have a total

diameter d = 1.7 mm and a 0.11-mm thick PVC coating (relative permittivity of 2.7). The separation between the single line and the center of the TWP is s = 2.55 mm, so three lines are touching when they are lined up horizontally, and they lie at a height h = 5 cm above a perfect ground plane. Lines' length l= 1 m and TWP has N = 25 full twists (a lay length = 40 mm). Load at both ends of the transmission line: Z_S=Z_L=50Ω. The extracted p.u.l RLCG parameters and crosstalk are all based on this model.

B. BSO process introduction

Based on our previous research [19-21], we found that the optimization effect of BAS algorithm for high-dimensional data is not ideal, and its iterative results are greatly affected by initial position of the beetle. Therefore, inspired by the particle swarm algorithm, we have made improvements to the BAS algorithm based on expanded a single beetle into beetle group, which is the beetle swarm optimization (BSO) algorithm.

In this algorithm, each beetle represents a potential optimization solution. Similar to the particle swarm algorithm, beetles can share information with each other. However, the specific moving distance and direction of each beetle depends on the odor intensity it senses, which is the fitness function.

In this paper, we use BSO algorithm to optimize the weights of BP neural network. And on this basis, predict the p.u.l parameters at each segment position of TWP. The schematic diagram is shown in Fig. 3.

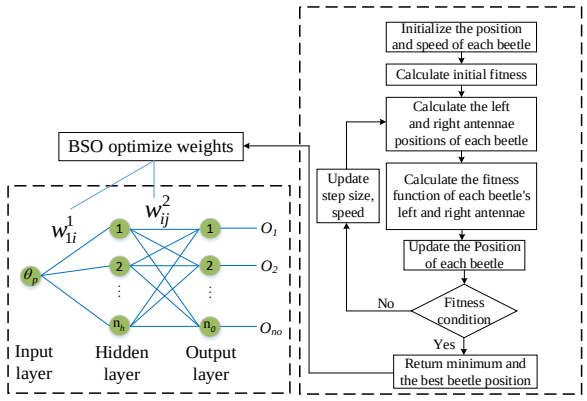

Fig. 3. BSO algorithm to optimize BP weights.

The number of hidden layers n_h is an empirical value determined by the number of input layers and output layers, which can be as follows:

$$n_h = \left(inputlayer + outputlayer\right)^{1/2} + a\,, \tag{15}$$

where a is the empirical constant between [1,10]. The hidden layer uses the sigmoid function $f(x)$, and output layer uses the linear function $g(x)$. They are as follows:

$$f\left(x\right) = \frac{1}{1+e^{-x}}\,, \tag{16}$$

$$g\left(x\right) = x\,. \tag{17}$$

Then, the output of neural network is:

$$y_j = \sum_{i=1}^{n_h} \frac{w_{ij}^2}{1+e^{-w_{1i}^1\theta_p}}\,. \tag{18}$$

For M sets of training samples, the mean square error E between the neural network output value y_j and the actual value $\hat{y}_j$ is:

$$E = \left(\frac{\sum_{j=1}^{M} (\hat{y}_j - y_j)^2}{M} \right)^{1/2}\,. \tag{19}$$

Next, the specific steps of BSO algorithm to optimize weights w_{1i}^1 and w_{ij}^2 will be introduced. Here, the position of each beetle is the BP weight, and the fitness function is the BP neural network error E.

Step 1: Generate a group of n beetles: $B = (B_1, B_2, \cdots B_n)$ in an S-dimensional search space, where the i th beetle represents a vector: $B_i = (b_{i1}, b_{i2}, \cdots b_{iS})$, this represents a potential solution to the optimization problem. The speed of the i th is expressed as: $V_i = (V_{i1}, V_{i2}, \cdots V_{iS})$. In order to improve the calculation speed, we have stipulated the threshold range for the individual and the whole beetle: $U_i = (U_{i1}, U_{i2}, \cdots U_{iS})$ and $U_g = (U_{g1}, U_{g2}, \cdots U_{gS})$.

Step 2: Give the iterative formula of beetle position B_{is}^{k+1} and speed V_{is}^{k+1}.

$$B_{is}^{k+1} = B_{is}^{k} + \lambda V_{is}^{k} + (1-\lambda)\delta_{is}^{k}\,, \tag{20}$$

where s=1,2,…S; i=1,2,…n; k is the current number of iterations. δ_{is} is increase in beetle position movement. λ is a constant.

$$V_{is}^{k+1} = \omega V_{is}^{k} + c_1 r_1 (U_{is}^{k} - B_{is}^{k}) + c_2 r_2 (U_{gs}^{k} - B_{gs}^{k})\,, \tag{21}$$

where ω is inertia weight, c_1, c_2 are constants, r_1 and r_2 are two random functions in the range [0,1].

Step 3: Give the distance and direction of the beetle.

$$\delta_{is}^{k+1} = \varepsilon^{k} * V_{is}^{k} * sign(f(B_{rs}^{k}) - f(B_{ls}^{k}))\,. \tag{22}$$

In this step, ε is step size. The search functions of the left and right antennae of beetle are respectively expressed as:

$$B_{rs}^{k+1} = B_{rs}^{k} + V_{is}^{k} * d/2\,, \tag{23}$$

$$B_{ls}^{k+1} = B_{ls}^{k} - V_{is}^{k} * d/2\,, \tag{24}$$

d represents the distance between two antennae. After the iterative loop is over, return a minimum error value, and the corresponding beetle position, that is, the weights.

C. Error comparison

In this section, we use ANSYS software to extract a set of p.u.l parameters at fixed rotation degrees (0: 5: 175 degrees) as training samples first. Secondly, rotation degrees θ_p are used as the neural network input, and p.u.l RLCG parameters is combined into one column as the output **O**.

$$\mathbf{O} = [tri(\mathbf{R}), tri(\mathbf{L}), tri(\mathbf{C}), tri(\mathbf{G})]^T . \quad (25)$$

Then use BP neural network optimized by BSO and BAS to predict p.u.l. RLCG parameters. In Fig. 4, iterative fitness (error) of BSO and BAS are compared.

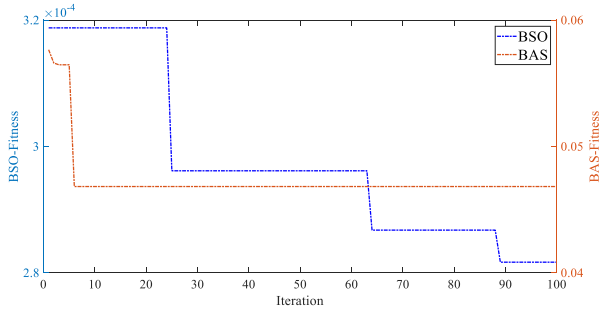

Fig. 4. BSO and BAS iteration error comparison.

It can be inferred from Fig. 4 that compared to BAS, the group optimization method used by BSO reduces the iteration error by 187.5 times, and it is almost unaffected by the initial position of beetle. We use trained neural network to predict the original training samples again and compare two samples' error. Taking **L** parameter matrix elements l_{ij} as example, the relative prediction error under three algorithms of BS0-BP, BAS-BP and BP are given.

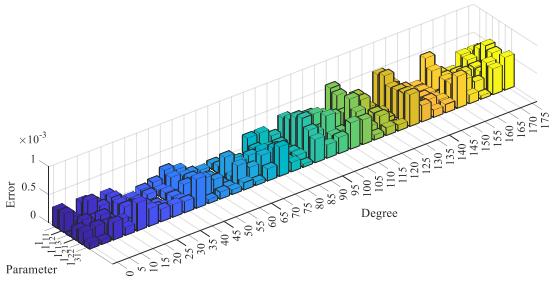

(a)

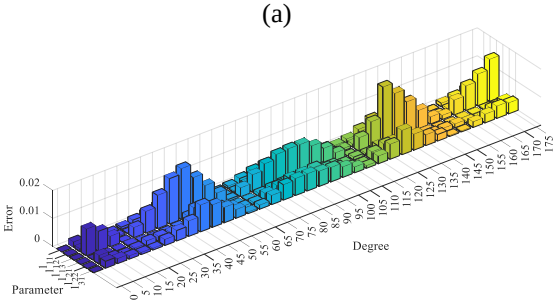

(b)

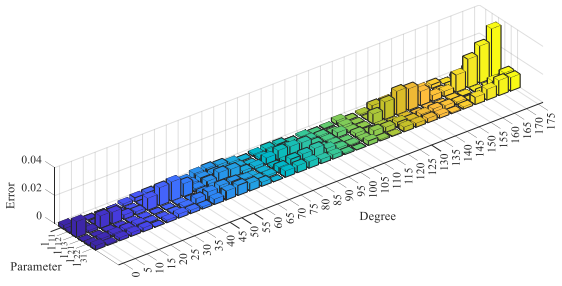

(c)

Fig. 5. BSO-BP, BAS-BP and BP prediction error comparison (a) BSO-BP, (b) BAS-BP, and (c) BP.

It can be seen from Fig. 5 that compared with the previous BAS and BP algorithms, the prediction accuracy of BSO for parameters has been improved by more than 20 times.

IV. CROSSTALK PREDICTION AND SUPPRESSION VERIFICATION

A. MTL frequency domain method to solve crosstalk

After the p.u.l parameters at each segment have been obtained, the MTL frequency domain method combined with terminal conditions is used to solve crosstalk. In the Section II, we have derived the chain parameter expression of transmission line. Then crosstalk solutions based on the terminal condition are given.

From equation (8):

$$[\hat{\Phi}_{12} - \hat{\Phi}_{11}\hat{\mathbf{Z}}_S - \hat{\mathbf{Z}}_L\hat{\Phi}_{22} + \hat{\mathbf{Z}}_L\hat{\Phi}_{21}\hat{\mathbf{Z}}_S]\hat{\mathbf{I}}(0) = [\hat{\mathbf{Z}}_L\hat{\Phi}_{21} - \hat{\Phi}_{11}]\hat{\mathbf{V}}_S , \quad (26)$$

$$\hat{\mathbf{I}}(\varphi) = \hat{\Phi}_{21}\hat{\mathbf{Z}}_S + [\hat{\Phi}_{22} - \hat{\Phi}_{21}\hat{\mathbf{Z}}_S]\hat{\mathbf{I}}(0), \quad (27)$$

where $\hat{\mathbf{Z}}_S$ and $\hat{\mathbf{Z}}_L$ are termination load matrix. $\hat{\mathbf{V}}_S$ is the power supply.

Combined with terminal conditions:

$$\hat{\mathbf{V}}(0) = \hat{\mathbf{V}}_S - \hat{\mathbf{Z}}_S\hat{\mathbf{I}}(0), \quad (28)$$

$$\hat{\mathbf{V}}(\varphi) = \hat{\mathbf{Z}}_L\hat{\mathbf{I}}(\varphi). \quad (29)$$

The 2*n* terminal voltages $\hat{\mathbf{V}}(0)$ and $\hat{\mathbf{V}}(\varphi)$ can be obtained from equations (26-29).

Next, compare crosstalk obtained based on the three parameter prediction methods with the CST simulation software results, as shown in Fig. 5. The frequency range of crosstalk result is 5MHz ~ 1GHz.

In Fig. 6, the optimized algorithm can maintain good consistency with the results in CST. And compared with BAS, it is obvious that BSO has better fit and high accuracy. Next, we provide the relative error of predicting crosstalk in three methods under sub-frequency band and sub-port in Table 1.

Among them, the highest error is BP, and the lowest is BSO-BP, which also reflects the necessity of optimization algorithm. The FEXT prediction accuracy

is better than NEXT. In the sub-frequency bands: prediction accuracy for low frequency band is the highest, and the accuracy is the lowest in the mid frequency band due to large number of resonance points.

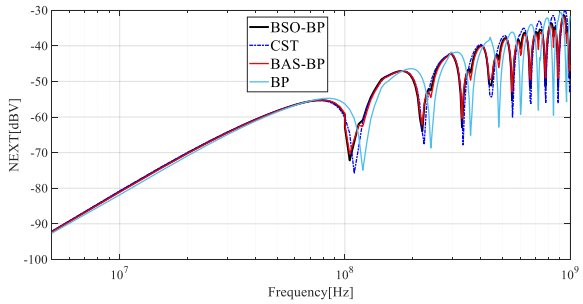

(a)

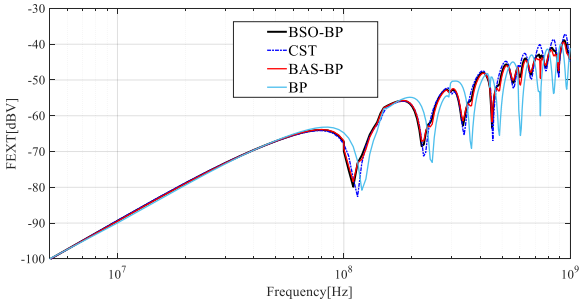

(b)

Fig. 6. Comparison of crosstalk under three parameter prediction algorithms (a) NEXT and (b) FEXT.

Table 1: Average error (%) of crosstalk prediction (N: NEXT; F: FEXT)

Frequency (MHz)	**5~100**		**100~500**		**500~1000**	
	N	F	N	F	N	F
BSO-BP	2.32	2.23	19.19	15.76	21.94	8.35
BAS-BP	5.71	5.47	40.00	35.65	43.45	21.44
BP	13.53	13.72	92.75	88.93	95.31	67.96

B. SVD method to suppress crosstalk

Based on equations (8-12), we can obtain the relationship between the far-end and near-end voltages of the transmission line, defined as **P**:

$$\begin{aligned}\hat{\mathbf{V}}(\varphi) &= \mathbf{P}\hat{\mathbf{V}}(0) \\ &= [\hat{\Phi}_{11}(\varphi)+\hat{\Phi}_{12}(\varphi)(\hat{\Phi}_{12}(\varphi)-\mathbf{Z}_L\hat{\Phi}_{22}(\varphi))^{-1} \\ &\quad \cdot(\hat{\Phi}_{11}(\varphi)-\mathbf{Z}_L\hat{\Phi}_{21}(\varphi))]\hat{\mathbf{V}}(0). \end{aligned} \quad (30)$$

The non-diagonal elements in the matrix **P** correspond to crosstalk. If the matrix **P** is transformed into a unit matrix, the crosstalk is suppressed. We can use singular value decomposition (SVD) in matrix theory to achieve this goal. For the P matrix, since it is a full rank ($n\times n$) matrix, there are unitary matrices **G** and **F** exist, such that:

$$\mathbf{G}^H\mathbf{P}\mathbf{F}=\mathbf{B}, \quad (31)$$

where **B** is the diagonal matrix, σ is the singular value of **P**, and then:

$$\mathbf{P}=\mathbf{G}\mathbf{B}\mathbf{F}^H, \quad (32)$$

$$\mathbf{G}^H\mathbf{P}\mathbf{F}\mathbf{B}^{-1}=\mathbf{E}_n. \quad (33)$$

From (32), it can be seen that the transmission matrix **P** become an identity matrix, which needs to undergo three signal transformations:

1) The first signal transformation occurs at the input of the transmission line: $\mathbf{B}^{-1}$.

2) The second signal transformation occurs after the first transformation: **F**.

3) The third signal transformation occurs at the output of the transmission line: $\mathbf{G}^H$.

We define:

$$\mathbf{P}_b=\mathbf{F}\mathbf{B}^{-1}, \quad (34)$$

$$\mathbf{P}_e=\mathbf{G}^H. \quad (35)$$

In other words, the crosstalk can be suppressed by implementing two matrix operations at the transmission line ends. The crosstalk suppression circuit $\mathbf{P}_b$ on the source end is shown in Fig. 7, and the load end $\mathbf{P}_e$ is also the same implementation circuit.

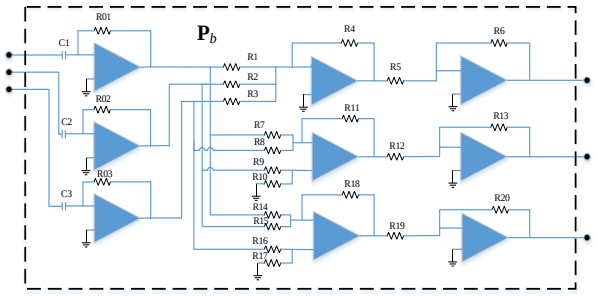

Fig. 7. Crosstalk suppression circuit.

We select operational amplifiers as the components for matrix operation, and negative feedback circuits formed by operational amplifier can meet requirements. Then, simulations are performed before and after crosstalk suppression in PSPICE. Because at high frequencies, $\omega\mathbf{L}>>\mathbf{R}$ and $\omega\mathbf{C}>>\mathbf{G}$, therefore in this part: **R=G=0**.

Due to the unidirectional conductivity of the operational amplifier, NEXT will not exist. Next, we give the FEXT suppression effect under 100MHz sinusoidal signal.

It can be seen from Fig. 8 that suppress crosstalk method proposed in this paper is effective, and its effect partly depends on the accuracy of circuit components.

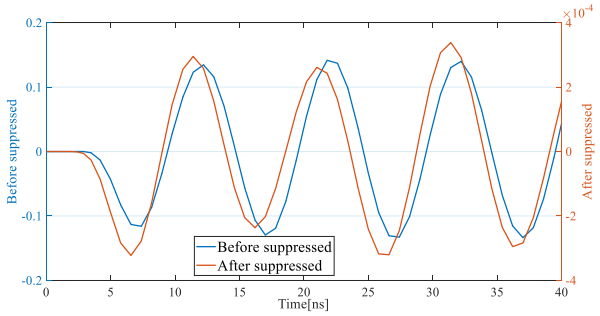

Fig. 8. FEXT suppression effect comparison.

V. CONCLUSION

In this paper, a new algorithm for predicting the p.u.l RLCG parameters of TWP is proposed: beetle swarm optimization. Based on the transmission lines cascade theory, the TWP is divided into several segments, each segment is regarded as a parallel transmission line, and crosstalk is solved and suppressed through the p.u.l parameter.

In this paper, the newly proposed BSO algorithm is compared with the previous BAS and BP algorithms, which proves that BSO has smaller iteration errors and better convergence, so that the accuracy of parameter prediction is higher.

The verification in Section IV is divided into two parts, namely solving and suppressing crosstalk. In the first part, using the MTL frequency domain analysis method to solve crosstalk is given, and three prediction methods are compared with the CST results to prove the improvement of BSO; the second part uses the SVD method to add auxiliary circuit at both ends of the transmission line, which composed of operational amplifiers. Its purpose is to turn the transmission matrix into a unit matrix. Finally, the comparison figure before and after crosstalk suppression is given with the PSPICE software.

ACKNOWLEDGMENT

This work is supported by the National Natural Science Foundation of China under Grant (51475246), the National Natural Science Foundation of Jiangsu Province under Grant (BK20161019), the Aviation Science Foundation under Grant (20172552017), the Key Project of Social Development in Jiangsu Province under Grant (BE2019716), the Open Fund Project of State Key Laboratory of Power Grid Environmental Protection under Grant (GYW51202001558), and the Nanjing International Industrial Technology Research and Development Cooperation Project under Grant (201911021).

REFERENCES

[1] S. Chabane, P. Besnier, and M. Klingler, "A modified enhanced transmission line theory applied to multiconductor transmission lines," *IEEE Trans. Electromagn. Compat.*, vol. 59, no. 2, pp. 518-528, Apr. 2017.

[2] F. Grassi and S. A. Pignari, "Immunity to conducted noise of data transmission along DC power lines involving twisted-wire pairs above ground," *IEEE Trans. Electromagn. Compat.*, vol. 55, no. 1, pp. 195-207, Feb. 2013.

[3] Y. Guo, L. Wang, and C. Liao, "Crosstalk spectrum predictions considering frequency-dependent parameters in electric vehicles," *Applied Computational Electromagnetics Society Journal*, vol. 30, no. 5, pp. 551-557, May 2015.

[4] J. L. Rotgerink, H. Schippers, and F. Leferink, "Low-Frequency analysis of multiconductor transmission lines for crosstalk design rules," *IEEE Trans. Electromagn. Compat.*, vol. 61, no. 5, pp. 1612-1620, Oct. 2017.

[5] G. Spadacini, and S. A. Pignari, "Numerical assessment of radiated susceptibility of twisted-wire pairs with random non-uniform twisting," *IEEE Trans. Electromagn. Compat.*, vol. 55, no. 5, pp. 956-964, Jan. 2013.

[6] G. Spadacini and S. A. Pignari, "Radiated susceptibility of a twisted-wire pair illuminated by a random plane-wave spectrum," *IEICE Trans. Commun.*, vol. E93-B, no. 7, pp. 1781-1787, July 2010.

[7] B. Cannas, A. Fanni, and F. Maradei, "A neural network approach to predict the crosstalk in non-uniform multiconductor transmission lines," *IEEE International Symposium on Circuits and Systems. Proceedings (Cat. No.02CH37353)*, Phoenix-Scottsdale, pp. 573-576, 2002.

[8] F. Dai, G. H. Bao, and D. L. Su, "Crosstalk prediction in non-uniform cable bundles based on neural network," *Proceedings of the 9th International Symposium on Antennas, Propagation and EM Theory*, Guangzhou, pp. 1043-1046, 2010.

[9] S. Sun, G. Liu, J. L. Drewniak, and D. J. Pommerenke, "Hand-assembled cable bundle modeling for crosstalk and common-mode radiation prediction," *IEEE Trans. Electromagn. Compat.*, vol. 49, no. 3, pp. 708-718, Aug. 2007.

[10] O. Olusegun, A. Duffy, and C. Nche, "Parameter for near end crosstalk prediction in twisted pair cables," *2016 IEEE International Symposium on Electromagnetic Compatibility (EMC)*, Ottawa, pp. 485-490, 2016.

[11] D. F. Wiliams, L. A. Hayden, and R. B. Marks, "A complete multimode equivalent-circuit theory for electrical design," *Journal of Research of the National Institute of Standards and Technology*, vol. 102, no. 4, pp. 405-423, Aug. 1997.

[12] T. Ciamulski and W. K. Gwarek, "A study of feeding options aimed at canceling crosstalk in

multiconductor transmission lines," *IEEE MTT-S International Microwave Symposium Digest, (IEEE Cat. No.04CH37535)*, Fort Worth, pp. 1631-1634, 2004.

[13] M. H. Wu, W. J. Chen, J. W. Liang and X. B. Fang, "An improvement method of the increasing mutual capacitance for reducing far-end crosstalk in transmission line," *IEEE Antennas and Propagation Society International Symposium*, Albuquerque, pp. 1227-1230, 2006.

[14] V. Vladimir and R. Ianconescu, "Transmission of the maximum number of signals through a multiconductor transmission line without crosstalk or return loss: Theory and simulation," *IET Microwaves, Antennas & Propagation*, vol. 9, no. 13, pp. 1444-1452, Oct. 2015.

[15] A. Shoory, M. Rubinstein, A. Rubinstein, C. Romero, N. Mora, and F. Rachidi, "Application of the cascaded transmission line theory of Paul and McKnight to the evaluation of NEXT and FEXT in twisted wire pair bundles," *IEEE Trans. Electromagn. Compat.*, vol. 55, no. 4, pp. 648-656, Aug. 2013.

[16] Z. Zhu, Z. Zhang, W. Man, X. Tong, J. Qiu, and F. Li, "A new beetle antennae search algorithm for multi-objective energy management in microgrid," *2018 13th IEEE Conference on Industrial Electronics and Applications (ICIEA)*, Wuhan, pp. 1599-1603, 2018.

[17] C. R. Paul, *Analysis of Multiconductor Transmission Lines*. 2nd ed., New York, USA: Wiley, 1994.

[18] P. Manfredi, D. D. Zutter, and D. V. Ginste, "Analysis of nonuniform transmission lines with an iterative and adaptive perturbation technique," *IEEE Trans. Electromagn. Compat.*, vol. 58, no. 3, pp. 859-867, June 2016.

[19] C. P. Yang, W. Yan, Y. Zhao, Y. Chen, C. M. Zhu, and Z. B. Zhu, "Analysis on RLCG parameter matrix extraction for multi-core twisted cable based on back propagation neural network algorithm," *IEEE Access*, vol. 7, pp. 126315-126322, Aug. 2019.

[20] C. Huang, W. Yan, Y. Zhao, Q. Q. Liu, and J. M. Zhou, "A new method for predicting crosstalk of random cable bundle based on BAS-BP neural network algorithm," *IEEE Access*, vol. 8, pp. 20224-20232, Jan. 2020.

[21] Q. Q. Liu, Y Zhao, W Yan, C Huang, M. Abdul, and Z Meng, "A novel crosstalk estimation method for twist non-uniformity in twisted-wire pairs," *IEEE Access*, vol. 8, pp. 38318-38326, Feb. 2020.

Improvement of Shaped Conductive Backfill Material for Grounding Systems

Run Xiong [1], Qin Yin [1], Wen Yang [2], Yan Liu [1], and Jun Li [1]

[1] PLA Army Engineering University, Nanjing 210007, Jiangsu, China
xiongrun1983@sina.com, yinqin1983@139.com, 76077381@qq.com, 3459990149@qq.com

[2] PLA Army Research Institution, Kunming, Yunnan 650222, China
76077381@qq.com

Abstract ─ In this paper, some improvements have been proposed for low resistance shaped conductive backfill material (SCBM) based on finite-difference time-domain (FDTD) simulations in grounding systems. It is found SCBM can be produced by conjunction of several layers with conductivity decreasing gradually from inner layer to outer layer, and smooth conductivity reduction between layers would lead to a better grounding performance. It is also found cuboid shape is a much more efficient shape than cube and cylinder shapes for SCBM, and holes can be made on the SCBM's main body. It suggested to bury SCBM vertically when ground soil permits, otherwise bury SCBM horizontally and deeper burying depth would result in smaller grounding resistance. Results show it is not needed to connect the SCBMs one by one tightly in series SCBM, and some distances is allowed without dramatically increasing grounding resistance.

Index Terms ─ Finite-difference time-domain (FDTD) method, shaped conductive backfill material (SCBM), transient grounding resistance (TGR).

I. INTRODUCTION

Grounding system plays an important role in lightning protection systems. When lightning strikes, the overvoltage is dependent on the grounding system resistance and a lot of papers have been published on efforts to reduce the system's grounding resistance [1-3].

Low resistance shaped conductive backfill material (SCBM), increases the grounding and soil contact area and thus decreases the grounding system's resistance. SCBM can be widely used in various grounding systems, especially to areas of high soil resistivity, to reduce grounding resistance and ensure long-term stable grounding effect without resulting huge cost rise [4-5].

Besides experimental analyses [6-8], numerical simulations have been widely used in lightning protection grounding systems design [8-11]. The finite-difference time-domain (FDTD) method [12-14], which provides a simple and efficient way of solving Maxwell's equations for a variety of problems, has been usually used to evaluate grounding system performance.

In [15], some optimal programs have been proposed for SCBM to be used in lightning protection systems. In this paper, some additional improvements are proposed for SCBM in the grounding system. Firstly, to simplify the production of the linear or parabolic type varied conductivity SCBM in Section D of Part III in [15], layered SCBM's performance, whose conductivity decreases gradually from the inner layer to the outer layer, is studied. Secondly, shape effect of SCBM on resistance is studied to find out the optimized shape to reduce high conductivity material usage in the SCBM production, and in this paper three typical shapes are involved, which are cube, cylinder and cuboid SCBMs. Thirdly, square and round holes are made on the SCBM main body to further reduce high conductivity material usage, and both field distribution and transient grounding resistance (TGR) are monitored to find out the holes effect on the SCBM performance. Fourthly, the performance of vertically buried SCBM is compared with that of horizontally buried SCBM with the same size to learn the SCBM position's effect on TGR. Lastly, series SCBM's performance is studied, and both field distribution and TGR are monitored to derive some suggestions on the distance between neighboring SCBMs in the series SCBM. Based on these analyses, some improvements are proposed for SCBM in grounding systems.

II. TGR CALCULATION MODEL

To improve SCBM programs of grounding system, the TGR calculation model proposed in [15] is adopt as shown in Fig. 1. It worth to note that the in Fig. 1, CPML stands for Convolutional Perfectly Matched Layer [16], and PEC stands for Perfect Electric Conductor which is used to truncate the CPML. A homogenous ground, whose relative permittivity is $\varepsilon_g=10\varepsilon_0$ and conductivity is $\sigma_g=0.004$ S/m, is adopted.

Submitted On: November 23, 2020
Accepted On: February 19, 2021

https://doi.org/10.47037/2020.ACES.J.360410

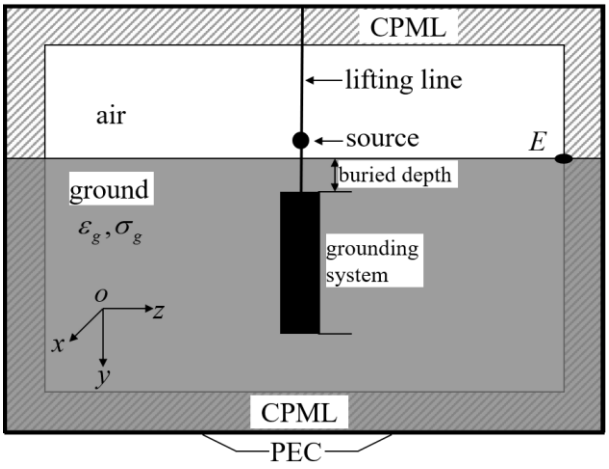

Fig. 1. TGR simulation model.

The lightning restrike current is injected 200 mm above ground through, which is modeled by:

$$\boldsymbol{I}(t) = I_0(e^{-\alpha t} - e^{-\beta t}), \quad (1)$$

where I_0=109405 A, α=22708 s^{-1}, β=1294530 s^{-1}.

The TGR is defined as a ratio of the transient voltage to the transient current:

$$R_t = V_t / I_t. \quad (2)$$

Here I_t is the transient current flowing through the grounding system, which can be defined from the Ampere circuital theorem as shown in [17]:

$$I(t) = [H_z(i_0 - \tfrac{1}{2}, j_0 - \tfrac{1}{2}, k_0) - H_z(i_0 + \tfrac{1}{2}, j_0 - \tfrac{1}{2}, k_0)]\pi\Delta_z / 4 + [H_x(i_0, j_0 - \tfrac{1}{2}, k_0 + \tfrac{1}{2}) - H_x(i_0, j_0 - \tfrac{1}{2}, k_0 - \tfrac{1}{2})]\pi\Delta_x / 4, \quad (3)$$

where (i_0, j_0, k_0) is the point where the lifting line entering ground.

The transient voltage V_t can be obtained from:

$$V_t = \sum_{k=N_l}^{N_A} V_j = -\sum_{k=N_l}^{N_A} E_z(i_0, j_0, k)\Delta_z, \quad (4)$$

where $E_z(i_0, j_0, k)$ is the electric field in the z direction in the air-ground interface plane, N_l and N_A are FDTD mesh indexes of the point (i_0, j_0, k_0) and point "E" in Fig.1 respectively.

All simulation is carried out on a PC with the parameter below:

Pentium IV 2.8GHz CPU per Node,
2.0GBytes Memory per Node,
1000M High-speed Network Interface Card,
1000M Bites Switch.

III. OPTIMIZED PROGRAMS FOR SCBM

In this part, several proposed programs are tested to derive some efficient improvements for SCBM in grounding system.

A. The layered SCBM

As pointed out in Section D of Part III in [14], TGR of SCBM whose conductivity is linear or parabolic type varied, can be as low as the resistance of a totally high conductivity SCBM. However, it is not easy to produce continuous varied conductivity SCBM in practice, thus layered SCBM is proposed. The permittivity in each layer is the same, but the conductivity decreases gradually from the inner layer to the outer layer.

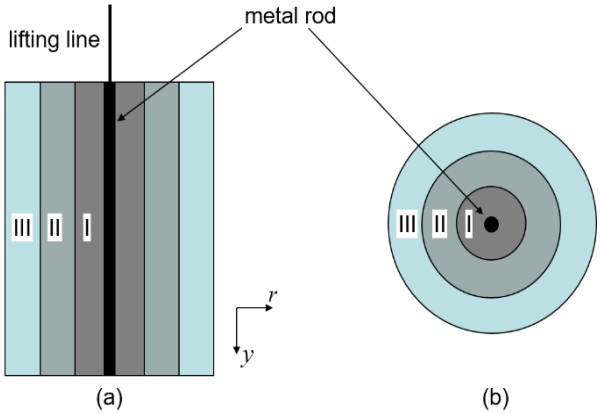

Fig. 2. Layered cylinder SCBM.

In this section, a 2-D cylindrical coordinate area of the proposed TGR calculation area in part IV of [15] is occupied, and the SCBM dimension is the same as that in [15]. The cylinder SCBM is produced into three layers, as shown in Fig. 2.

The cylindrical SCBM is 150 mm in radius and 800 mm in length, and the metal rod radius is 5 mm. Here the main body of SCBM is divided into three layers, and the inner layer (layer I) radius is 45 mm and the outer two layers (layer II and III) are both 50 mm in radius.

Two cases of layered SCBMs are tested here, where conductivity decreases more smoothly in case II than case I, and the conductivity of the two SCBMs decreases from inner layer to the outer layer gradually. The conductivity of the two cases are listed in Table 1, and the relative permittivity in the three layers are all set at ε_s=10.0.

Table 1: Conductivity of the three layered SCBM

	Layer I	Layer II	Layer III
Case I	0.5 S/m	0.1 S/m	0.02 S/m
Case II	0.5 S/m	0.2 S/m	0.08 S/m

The computational grid size is $\Delta=\Delta_r=\Delta_z$=5 mm and the time step is $\Delta t=\Delta/2c$, where c is the speed of light. The simulation is carried out 240000 time steps, which equals to 2 ns, and the TGR is calculated through (2).

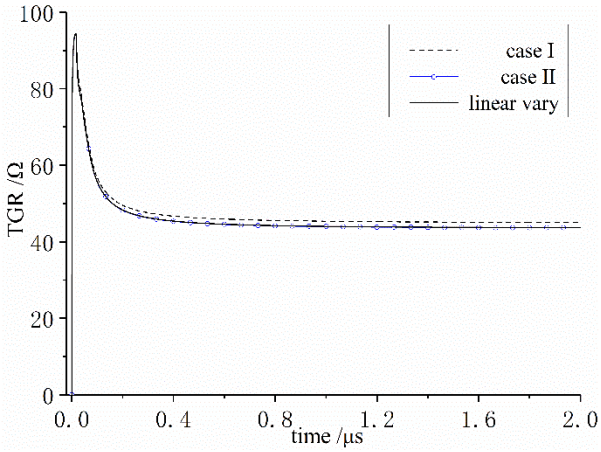

Fig. 3. TGRs of the layered SCBM compared with liner varied conductivity SCBM.

In Fig. 3 is graphed the TGRs of the two cases of layered SCBM, where the TGR of linear varied conductivity SCBM given by (8) of [15] is also presented for comparison. It can be seen that the three SCBMs has similar early performance from 0 to 0.05 μs, while performance varies after 0.05 μs. The steady grounding resistance is 45.06 Ω for case I and 43.70 Ω for case II, compared with 43.66 Ω for linear varied SCBM. It is clear that the layered SCBM of case II performs similarly as the linear varied SCBM. Thus, it can be concluded SCBM can be produced into several layers with conductivity decreasing gradually from inner layer to outer layer, and smooth conductivity reduction between layers would result in a better grounding performance.

B. SCBM shape effect on TGR

SCBM can be made into different shapes, but how SCBM shape will affect the grounding performance have not been studied, thus it is needed to test shape effect on SCBM's TGR. In this section, three typical SCBMs are tested, as shown in Fig. 4. The lengths of the three SCBMs are all 800 mm in this section, and buried vertically with the upper side of the SCBMs 500 mm below the air-ground interface. To

In Fig. 4 (a) is the sectional dimension of the cube SCBM, which is 150 mm in each direction, the sectional area is 2.25×10^4 mm^2. In Fig. 4 (b) is graphed the sectional dimension of cylinder SCBM, whose radius is 85 mm and the sectional area is 2.27×10^4 mm^2. In Fig. 4 (c) is graphed the sectional dimension of the cuboid SCBM, which is 380 mm×60 mm and the sectional area is 2.28×10^4 mm^2. To simulate the problem with less computational error introduced by three dimensional cubic FDTD cell modelling, cube metal rod is occupied here. Cylinder SCBM in Fig. 4 (b) is simulated by conformal grids [12]. It is worthy of noting that the sectional area of the three SCBMs is close to each other, which means similar material will be consumed in the production of the three SCBMs.

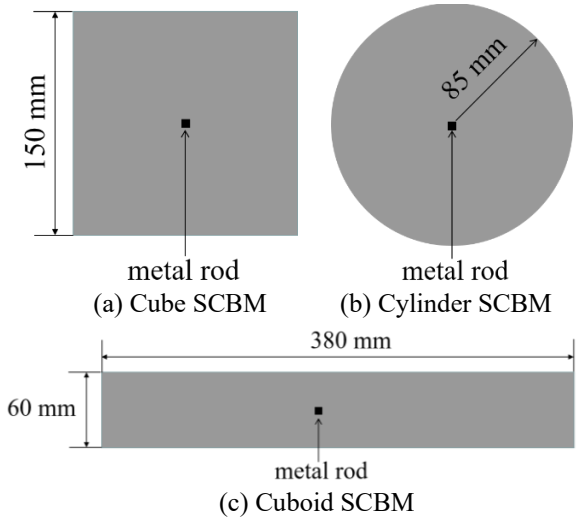

Fig. 4. Typical SCBM shapes tested.

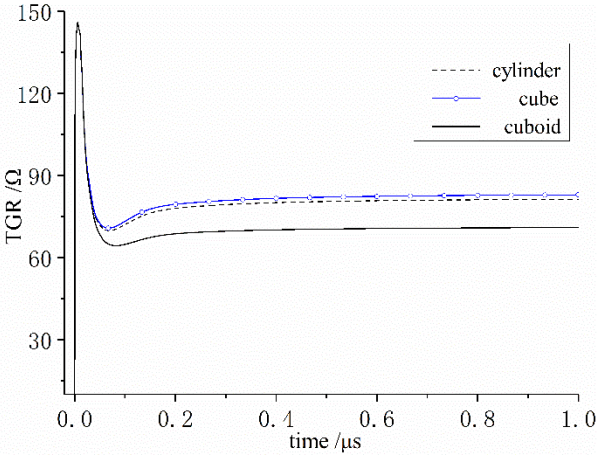

Fig. 5. TGRs of three typical shape SCBM.

In this section and below, three dimensional FDTD simulations are occupied. The computational grid size is $\Delta=\Delta_x=\Delta_y=\Delta_z=5$ mm and the time step is $\Delta t=\Delta/2c$, where c is the speed of light. The simulation is carried out 120000 time steps, which equals to 1 μs, and TGR of SCBMs are calculated through (2). TGR of the three SCBMs in Fig. 4 is simulated and graphed in Fig. 5.

From Fig. 5, it can be seen that the three SCBMs has similar early performance from 0 to 0.05 μs, however varies after 0.05 μs. The steady resistance is 81.31 Ω for cylinder SCBM, 82.91 Ω for cube SCBM, and 70.86 for cuboid SCBM. Thus, it can be concluded cuboid shape is a more efficient shape for SCBM which can result in smaller grounding resistance at similar high conductivity material usage.

C. Holes on SCBM main body

To test effect of holes on the SCBM main body on TGR, two SCBMs with four penetrating square holes on each SCBM are tested, and sectional dimensions are shown in Fig. 6. Vertically cube buried SCBM is adopted in this section, whose size is 150 mm×150 mm×800 mm, and buried 500 mm below ground. The four square holes are located symmetrically on SCBM main body, and the distance between two neighboring holes is 30 mm. The square hole's width is 25 mm and 35 mm for the two SCBMs respectively. It worth to note that the four holes are filled with ordinary soil when buried, and the relative permittivity of ground is ε_r=10.0 and the conductivity is σ_g=0.004 S/m.

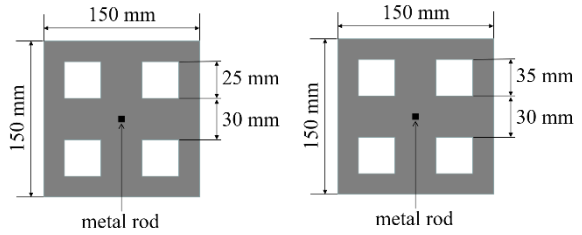

(a) SCBM with 4×25mm holes (b) SCBM with 4×35mm holes

Fig. 6. SCBM with different size holes.

To analyze the holed SCBM's performance, we monitored electric field component distribution firstly, as shown in Fig. 7. It is worthy of noting that the SCBM locates at the center of the two figures, that is $x \in$ (-7.5 mm, 7.5 mm), $z \in$ (-7.5 mm, 7.5 mm). In Fig. 7 is showed the horizontal electric field E_h in *xoz* plane, which is given by:

$$E_h(x,z) = \sqrt{E_x^2(x,z) + E_y^2(x,z)}\,, \tag{5}$$

where $E_x(x, z)$ and $E_z(x, z)$ are the electric field component in *x* and *z* direction in *xoz* plane respectively. Since electric fields located at half space steps in FDTD. It worth to note that $E_x(x, z)$ is get from $\frac{1}{2}(E_x(x+\frac{\Delta_x}{2}, z) + E_x(x-\frac{\Delta_x}{2}, z))$ and $E_z(x, z)$ is get from $\frac{1}{2}(E_z(x, z+\frac{\Delta_z}{2}) + E_z(x, z-\frac{\Delta_z}{2}))$.

It can be seen from Fig. 7 that electric field in the SCBM main body is lower than the surrounding area, and the electric field at the four corners of the cube SCBM is much higher than other places. In the SCBM main body, the electric field increases from the center to the outer edge. It can also be seen that lightning current flows from the SCBM to the surrounding areas and amplitude decreases as the distance from SCBM edge increases. The electric field in the SCBM is much lower than surrounding soil, which demonstrates SCBM performs well to conduct lightning electricity. However, electric field component E_h distributes continuously in the SCBM main body even though there are four holes located, and the holes are not visible in Fig. 7, which means effect of holes on SCBM's current-carrying capacity is limited.

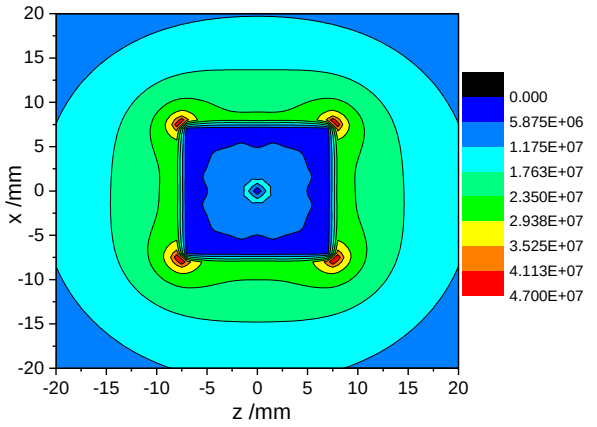

Fig. 7. E_h distribution in *xoz* plane.

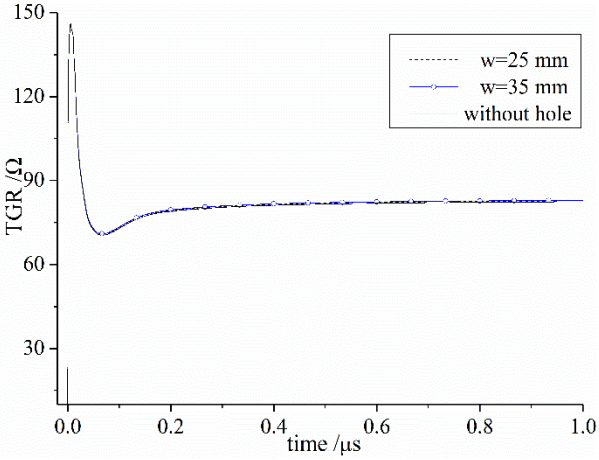

Fig. 8. TGR of SCBMs with different size square holes.

Besides field distribution, we also monitored TGRs of the two SCBMs, as shown in Fig. 8, where the TGR of a same size SCBM without any hole on the main body is also presented as reference. From Fig. 8, it can be seen that TGR is nearly the same for the two SCBMs with holes. The steady resistance for the SCBM shown in Fig. 6 (a) is 82.71 Ω, and 82.93 Ω for the SCBM shown in Fig. 6 (b), compared with 82.40 Ω for a same size SCBM without any hole.

Additionally, we also tested round holes effect on SCBM's TGR. Two size holes are simulated here, as shown in Fig. 9. In Fig. 9 (a) is shown the SCBM where radius of the four holes is 20 mm and the distance between two neighbouring holes is 40 mm; while in Fig. 9 (b) is the SCBM where radius of the four holes is 30 mm and the distance between two neighbouring holes

is 20 mm.

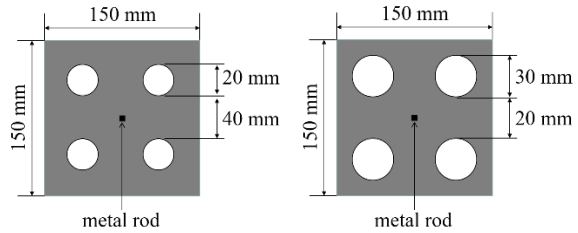

(a) Radius of the 4 holes is 20mm (b) Radius of the 4 holes is 30mm

Fig. 9. SCBM with different size holes.

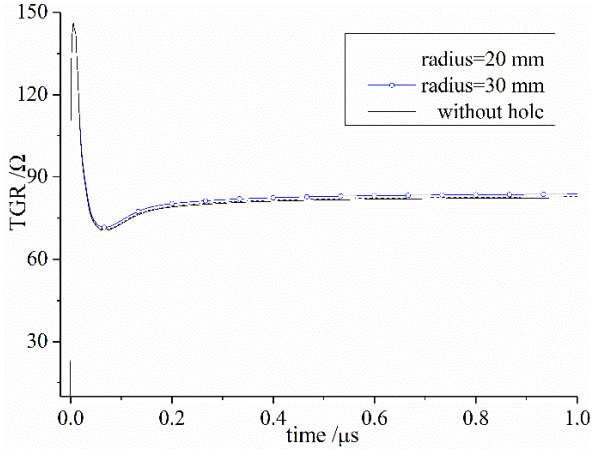

Fig. 10. SCBM with different radius round holes.

Figure 10 graphs TGRs of the two SCBMs shown in Fig. 9, where the TGR of a same size SCBM without any holes on the main body is also presented as reference. It can be seen that there is mild difference between TGRs of the two SCBMs with holes. The steady resistance for the SCBM of Fig. 9 (a) is 82.78 Ω, and 83.70 Ω for the SCBM of Fig. 9 (b), compared with 82.40 Ω for a same size SCBM without any hole. From the analyses in this section, it can be concluded that holes can be made on SCBM main body to reduce high conductivity material usage.

D. Vertically buried versus horizontally buried

At some places it may be costly to dig deep enough to bury SCBM vertically, so it is needed to evaluate the cost and SCBM buried position. To study the SCBM buried position effect, we compared TGRs of a same SCBM buried vertically versus horizontally. The dimension of the SCBM is 380 mm×60 mm×800 mm, and two burying depths are tested. The horizontally buried SCBM is as shown in Fig. 11, where *d* is burying depth of SCBM's upper side below ground. The burying depth is *d*=500 mm and *d*=1300 mm respectively here. The upper side depth of the vertically buried SCBM is 500mm, and the down side depth is 1300 mm. TGRs of the three cases are monitored as shown in Fig. 12.

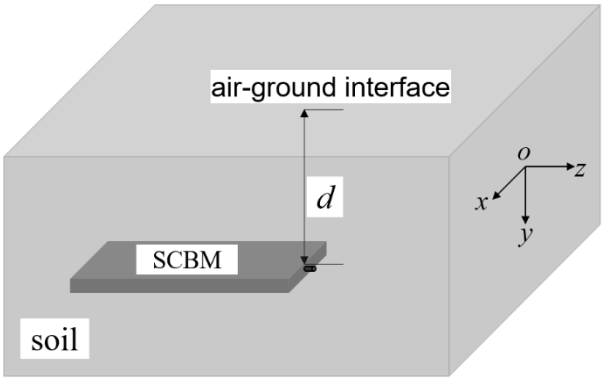

Fig. 11. The horizontally buried SCBM.

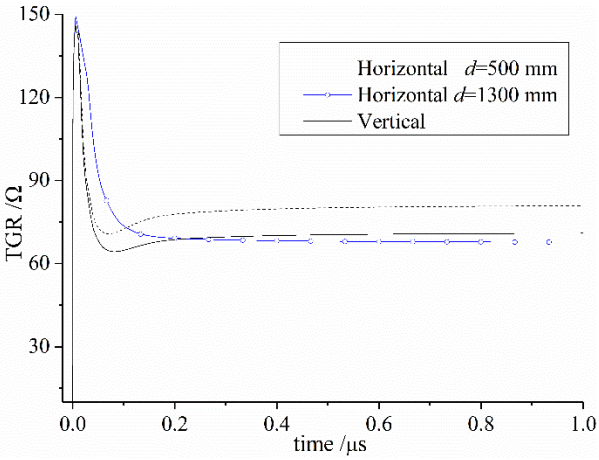

Fig. 12. Resistance of horizontally buried SCBMs.

From Fig. 12, it can be seen that the horizontally buried SCBMs' performance is quite different from the vertically buried one. The steady resistance of the horizontally buried SCBM is 80.89 Ω when *d*=500 mm, and 67.75 Ω when *d*=1300 mm, compared with 70.96 Ω for the vertically buried SCBM. From comparison of horizontally buried SCBM with vertically buried SCBM at the same depth *d*=1300 mm, there is only a 2.21 Ω resistance improvement for horizontal position, but that would result in a quite larger amount of soil excavation in construction. Thus, it suggested to bury SCBM vertically when ground soil permits, otherwise bury SCBM horizontally and greater depth of the horizontally buried SCBM would result in smaller resistance, but the effect of increasing the buried depth on the resistance reduction is limited.

Fig. 13. Series SCBM to be buried.

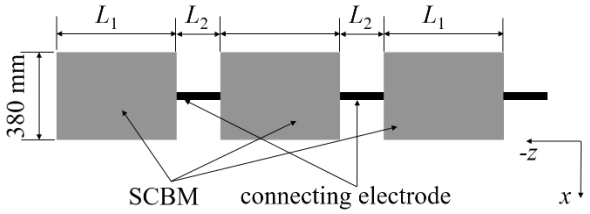

Fig. 14. Dimension of series SCBM.

Table 2: Parameters of 5 Series SCBM

	Case I	Case II	Case III	Case IV	Case V
L_1 (mm)	450	350	475	275	5000
L_2 (mm)	50	150	150	250	0
n (number)	10	10	8	8	1

E. Series SCBM performance

To get a low-level grounding resistance, SCBMs are connected horizontally into series SCBM in practice, as shown in Fig. 13. However, the series SCBM performance has yet been studied. In this section, the metal rod of SCBMs is connected one by one to make a series SCBM and grounding resistance is studied as the SCBM numbers and distance between SCBMs varies. It worth to note that to avoid the grounding system's effect on the accuracy of the simulated TGR as pointed out in [17], the series SCBM are buried in the –z direction, whereas the transient voltage V_t in (4) is integrated in +z direction. The series SCBM is connected to lifting line at x=0 mm, z=0 mm.

The total length of the series SCBM is 5 m, and all the SCBMs are of the same size for each case. The length of each SCBM is L_1 and the distance between two neighbouring SCBMs is L_2, as shown in Fig. 14. In all cases, the SCBMs are 380 mm in width and 60 mm in depth, but length L_1 varies. The SCBMs are connected by metal connecting electrodes with sectional dimension 10 mm×10 mm, and the series SCBM is buried 300 mm below the ground surface.

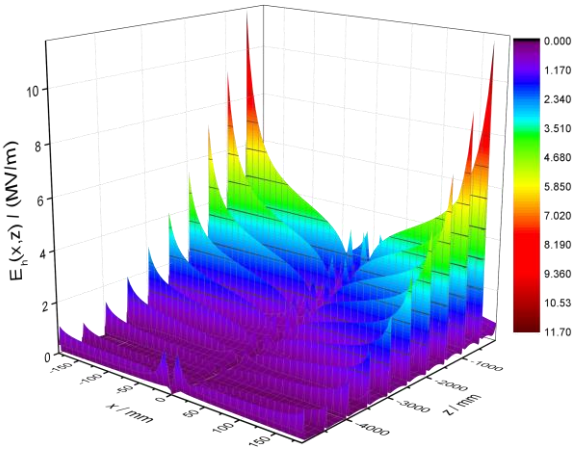

Fig. 15. $E_h(x, z)$ distribution in the series SCBM area.

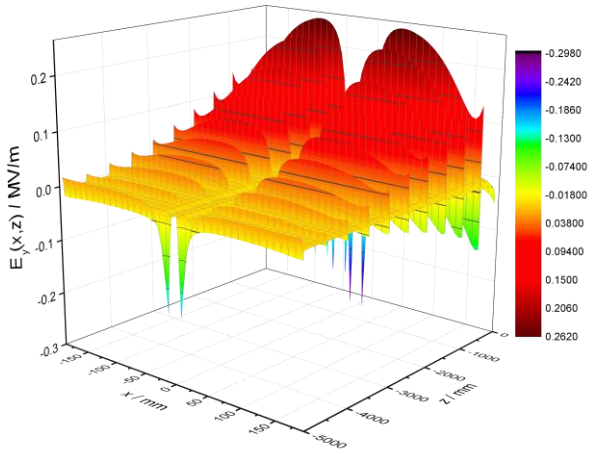

Fig. 16. $E_y(x, z)$ distribution in the series SCBM area.

In this section, 5 cases of series SCBM are tested, as shown in Table 2. There are 10 SCBMs connected for case I and case II, and the length of each SCBM is L_1=450 mm and the distance between two neighbouring SCBMs are all L_2=50 mm for case I, while L_1= 350 mm and L_2=150 mm for case II. The connected SCBMs number is 8 for case III and case IV, and L_1=475 mm and L_2 =150 mm for case III, while L_1=275 mm and L_2=250 mm for case IV. Additionally, the extreme condition case V, where L_2 =0 mm, is also included as for comparison.

To analyse series SCBM performance, we firstly monitored field distribution $E_h(x, z)$ in SCBM plane of case I, which is calculated by (5). In Fig. 14 is graphed $E_h(x, z)$ in the series SCBM area, where $x \in$ (-190 mm, 190 mm), $z \in$ (-5000 mm, 0 mm). And Fig.15 graphs $E_y(x, z)$ in the series SCBM area.

Firstly, it can be seen that the electric field in each SCBM is much lower than that in the space area between SCBMs, which means all the SCBMs play positive role

in flowing lightening current to the ground. Secondly, electric field E_h and E_y amplitude decreases from the lifting line side to the opposite side in the series SCBM length direction. Thirdly, electric field E_h increases from the central part of series SCBM to the outer sides in the width direction. Fourthly, from the comparison of Fig. 15 with Fig. 16, it can be seen that the electric field in Fig. 16 is much larger than that in Fig. 16, which means that horizontal direction is the main direction that lightning current flows. Thus, it is suggested to use cuboid SCBM horizontally buried to allow lightning current flow horizontally in mountain areas, where only a thin low resistivity soil is covered and high resistivity rocks buried below.

Table 3: Steady resistance of 5 Series SCBM

	Case I	**Case II**	**Case III**	**Case IV**	**Case V**
L (mm)	4500	3500	3800	2200	5000
Resistance	20.35 Ω	21.41 Ω	21.18 Ω	22.52 Ω	19.69 Ω

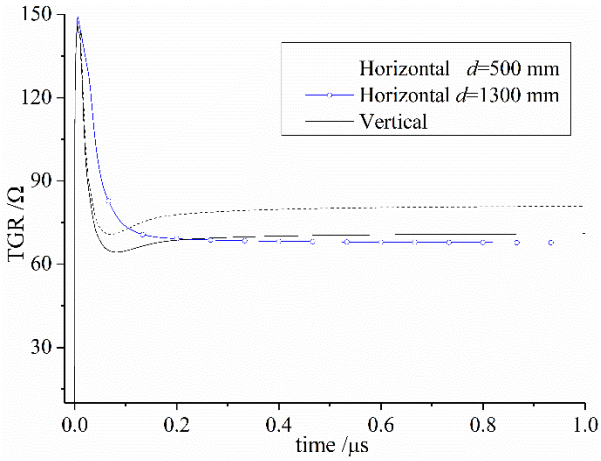

Fig. 17. TGR of 5 cases series SCBM.

From both Fig. 15 and Fig. 16, it can be seen that the electric field component in space areas between SCBMs is very high, which means closely buried two SCBMs will affect each other in flowing lightning current. Further, it can be concluded that the SCBMs have not performed sufficiently to flow lighting current to the ground when there was only 50 mm between the two neighbouring SCBMs.

Additionally, TGRs of the 5 cases series SCBM are also calculated and graphed in Fig. 17. In Table 3 is listed the steady resistance of the 5 cases, where the total SCBMs length given by $L=n\times L_1$ is also compared.

In Fig. 17, case V is used as a reference where the distance between neighbouring SCBMs L_2 is reduced to 0, which means one 5 m long SCBM is involved. From Fig. 17, it is clear that TGRs from 0 to 0.05 μs of the 5 cases are nearly the same, but transient resistance varies after 0.05 μs. The resistance of case I to case IV are both larger than that of case V after 0.05 μs, however the difference is not very significant. From Table 3, it can be seen that more SCBM usage would result in a lower steady resistance. Compared with a 5 m long SCBM used for case V, only 44% SCBM is used for case IV and there is only a 2.83 Ω more steady resistance gained. Thus, it can be concluded that it is not needed to connect the SCBMs one by one tightly in series SCBM, and some distances is allowed without dramatically increase the resistance but can dramatically reduce SCBM usage.

IV. CONCLUSIONS

In this paper, some improvements are proposed based on FDTD simulation for SCBM in grounding systems. Firstly, the SCBM can be made into several layers with conductivity decreasing gradually from inner layer to outer layer, and smooth conductivity reduction between neighbouring layers would lead to a better grounding performance. Secondly, SCBM shape has significant effect on its grounding resistance and cuboid shape is a more efficient shape for SCBM which can result in smaller grounding resistance at similar high conductivity material usage. Thirdly, holes effect on SCBM's performance is studied, and it is found both square and round holes can be made on the SCBM main body when producing the SCBM, which will affect the SCBM performance slightly. Fourthly, from comparison of SCBM buried position effect on TGR, it suggested to bury SCBM vertically when ground soil permits, otherwise bury SCBM horizontally and greater depth of the horizontal buried SCBM would result in smaller resistance. Lastly, series SCBM performance is analysed and results show it is not needed to connect the SCBMs one by one tightly in series SCBM, and some distance is allowed without dramatically increasing grounding resistance.

REFERENCES

[1] M. E. M. Rizk, M. Lehtonen, Y. Baba, S. Abulanwar, "Performance of large-scale grounding systems in thermal power plants against lightning strikes to nearby transmission towers," *IEEE Trans. on Elecgtromagn. Compt.*, vol. 61, no. 2, pp. 400-408, 2019.

[2] J. He, G. Yu, J. Yuan, R. Zeng, B. Zhang, J. Zou, and Z. Guan, "Decreasing grounding resistance of substation by deep-ground-well method," *IEEE Trans. on Power Del.*, vol. 20, no. 2, pp. 738-794, 2005.

[3] A. M. R. Martins, S. J. P. S. Mariano, M. R. A. Calado, and J. A. M. Felippe de Souza, "The sinusoidal ground electrode: Theory and case study results," *Applied Computational Electromagnetics*

Society Journal, vol. 31, no. 3, pp. 261-269, 2016.

[4] W. Zhou, G. Wu, X. Cao, and S. Li, "Research on effects between grounding module and grounding resistance," *Transmission and Distribution Conf. and Exposition*, T&D. *IEEE/PES*, pp. 1-4, 2008.

[5] Y.-Y. Chung, "Low-resistance carbon grounding module and method for manufacturing the same," *U.S. Patent, 20120293300 A1*, Nov. 2012.

[6] S. Visacro and G. Rosado, "Response of grounding electrodes to impulsive currents: An experimental evaluation," *IEEE Trans on Electromagn. Compat.*, vol. 51, no. 1, pp. 161-164, 2009.

[7] S. Sekioka, T. Sonoda, and A. Ametani, "Experimental study of current-dependent grounding resistance of rod electrode," *IEEE Trans. on Power Del.*, vol. 20, no. 2, pp. 1569-1576, 2005.

[8] H. Wan, X. Wang, Y. Chen, X. Pan, and X. Lu, "An extension of Cooray-Rubinstein formula on the calculation of horizontal electric field from inclined lightning channel," *Applied Computational Electromagnetics Society Journal*, vol. 33, no. 5, pp. 537-545, 2018.

[9] M. O. Goni, E. Kaneko and A. Ametani, "Simulation of lightning return stroke currents and its effect to nearby overhead conductor," *Applied Computational Electromagnetics Society Journal*, vol. 28, no. 1, pp. 469-477, 2009.

[10] M. Tsumura, Y. Baba, N. Nagaoka, and A. Ametani, "FDTD simulation of a horizontal grounding electrode and modeling of its equivalent circuit," *IEEE Trans Electromagn. Compat.*, vol. 48, no. 4, pp. 817-825, 2006.

[11] B. Li, Y. Du, and M. Chen, "An FDTD thin-wire model for lossy wire structures with noncircular cross section," *IEEE Trans. on Power Del.*, vol. 33, no. 6, pp. 3055-3064, 2018.

[12] A. Taflove and S. C. Hagness, *Computational Electrodynamics: The Finite-Difference Time-Domain Method*. Artech House, 3rd ed., 2005.

[13] X.-K. Wei, W. Shao, X. Ding, and B.-Z. Wang, "Efficient sub-gridded FDTD for three-dimensional time-reversed electromagnetic field shaping," *Applied Computational Electromagnetics Society Journal*, vol. 33, no. 8, pp. 828-836, 2018.

[14] Z. Sun, L. Shi, Y. Zhou, B. Yang, and W. Jiang, "FDTD evaluation of LEMP considering the lossy dispersive ground," *Applied Computational Electromagnetics Society Journal*, vol. 33, no. 1, pp. 7-14, 2018.

[15] R. Xiong, B. Chen, B.-H. Zhou, and C. Gao, "Optimized programs for shaped conductive backfill material of grounding systems based on the FDTD simulations," *IEEE Trans. on Power Del.*, vol. 29, no. 4, pp. 1744-1751, 2014.

[16] J. A. Roden and S. D. Gedney, "Convolution PML (CPML): An efficient FDTD implementation of the CFS-PML for arbitrary media," *Microw. Opt. Technol. Lett.*, vol. 27, no. 5, pp. 334-339, 2000.

[17] R. Xiong, B. Chen, C. Gao, Y. Yi, and W. Yang, "FDTD calculation model for the transient analyses of grounding systems," *IEEE Trans. on Electromagn. Compat.*, vol. 56, no. 5, pp. 1155-1162, 2014.

Research on the Influence of Train Speed Change on the EMI of Pantograph-Catenary Arc to Main Navigation Stations

Yutao Tang, Feng Zhu, and Yingying Chen

School of Electrical Engineering
Southwest Jiaotong University, Chengdu, 610031, China
tangyutao@my.swjtu.edu.cn, zhufeng@swjtu.edu.cn, 454621625@qq.com

Abstract — The electromagnetic interference (EMI) of the pantograph-catenary arc (PCA) to the main navigation stations will be affected when the speed of the high-speed train is changed. In order to study the influence of the speed change, we measured and analyzed the electric field intensity of the PCA generated at common and neutral section of power supply line at different train speeds. The frequency range in this study is the frequency of the main navigation stations (108 ~ 336 MHz). Both theoretical and experimental results show that PCA radiation increases with the increase of train speed. Besides, we calculated the maximum train speed without interfering the navigation signal. This work is useful for estimating EMI of the PCA at different train speeds and mitigating the interference to the navigation station near the high-speed railway by proposing corresponding speed limits.

Index Terms — Airport navigation stations, electromagnetic interference, pantograph-catenary arc, speed of high-speed train.

I. INTRODUCTION

Nowadays, it is inevitable for the high-speed train to enter the airport electromagnetic (EM) environmental protection zone to facilitate the transfer of passengers [1]. Therefore, it is necessary to evaluate whether the pantograph-catenary arc (PCA) will interfere with the airport navigation station [2]. However, the influence of the train speed on the EM radiation of the PCA has not been taken into account in the existing evaluation process of potential EM interference (EMI) on the airport navigation stations [3].

Some researchers used the arc simulation model or experimental systems to study the effect of train speed on voltage, current, power, and shape of the PCA [4-6]. In Ref. [7], researchers studied the relationship between train speed and the PCA. However, their data came from the simulation device in the reverberation chamber, which is somewhat different from the actual measurement results of the real train. Our team has done many practical measurements of the PCA and assessments of the EM environment at airports [8-10]. But the impact of the speed change on PCA radiation was not considered in previous studies.

As an extension of previous works, firstly, the characteristics of the PCA generated at two typical positions of the power supply line–common and neutral sections are analyzed. Secondly, taking one high-speed railway as the test object, the electric field intensity of the PCA is measured at different train speeds. Thirdly, the linear regression method is used to process and analyze the measurement data. Then, the amplitude-frequency characteristic curves of the PCA at different speeds are fitted. It should be noted that the frequency ranges are the frequency of main airport navigation stations: Omnidirectional Beacon Station (OBS) (108 ~ 117.975 MHz), Very-High-Frequency Communication System (VHFCS) (118 ~ 136.975 MHz), and Glide Beacon Station (GBS) (328.6 ~ 335.4 MHz). Finally, the maximum train speed that can guarantee the airport navigation signals to be normal is calculated. The results of this paper can provide the basis for perfecting the existing assessment of the airport EM environment.

II. ANALYSIS OF THE EFFECT OF TRAIN SPEED ON THE PCA

A. Characteristics of the PCA at the common sections

The high-speed train gets electricity power by connecting its pantographs to the power supply line. The reason for generating the PCA at the common sections is that there are some fixed hard-points on the power supply line. When the train passes through the hard-points, the pantograph and the line will be separated for a short time. Besides, the diameter and the convective power (P_k) of the PCA will change with the train speed. Moreover, P_k includes the convective power generated by the transverse arc blowing (P_{kT}) and by the longitudinal arc blowing (P_{kL}) [11]. The distance between the pantograph and the power supply line (r_{com}) is short. Thus, only P_{kT} exists because the PCA is almost vertical as shown in Fig. 1.

P_{kT} of the PCA can be obtained by [12]:

Submitted On: October 4, 2020
Accepted On: February 21, 2021

https://doi.org/10.47037/2020.ACES.J.360411

$$P_{kT}' = 0.1464d(v+36)^{1.5}, \quad (1)$$

where P_{kT}' is P_{kT} per unit length of the PCA, v is the train speed, which unit is km/h.

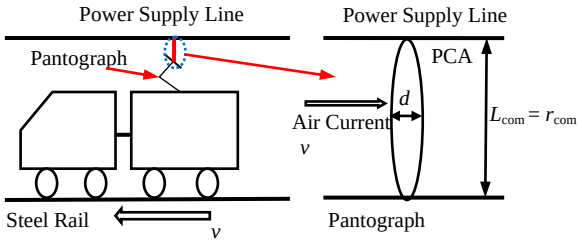

Fig. 1. Diagram of the PCA generated at the common section.

The diameter of the arc (d) is reduced by the transverse airflow and d can be calculated by [13, 14]:

$$d = 1.5369\sqrt{\frac{I/\sqrt{2}}{v+36}}, \quad (2)$$

where I is the maximum value of the PCA current.

P_{kT}' can be calculated by Eq. (1) and Eq. (2):

$$P_{kT}' = 0.1892\sqrt{I}(v+36). \quad (3)$$

The length of the PCA at the common section (L_{com}) is about 10 mm, which is the same as r_{com}. The convective power of the PCA at common sections ($P_{k(com)}$) can be obtained by Eq. (3):

$$P_{k(com)} = P_{kT} = P_{kT}' \cdot L_{com} = 1.892\sqrt{I}(v+36), \quad (4)$$

where $P_{k(com)}$ and radiation power ($P_{s(com)}$) of the PCA account for approximately 80% and 20% of the total dissipative power ($P_{loss(com)}$), respectively. So $P_{loss(com)}$ and $P_{s(com)}$ of the PCA at the common sections are:

$$P_{loss(com)} = \frac{P_{k(com)}}{80\%}, \quad (5)$$

and

$$P_{s(com)} = 20\%P_{loss(com)} = 0.473\sqrt{I}(v+36). \quad (6)$$

B. Characteristics of the PCA at the neutral sections

The reason for generating the PCA at the neutral sections is that the pantograph need to be separated from the original power supply line and enter into the neutral line to realize the voltage phase conversion. The distance between the pantograph and the power supply line (r_{neu}) is long. Thus, both P_{kT} and P_{kL} exist because the PCA has an angle with the horizontal plane as shown in Fig. 2. At this time, the length of PCA will be elongated because of the multiple external forces, and its stress diagram is shown in Fig. 3. Where F_{wind} is the wind load force; F_{float} is the thermal buoyancy force; F_m is the magnetic force (the direction is related to the direction of magnetic field).

If the PCA keeps uniform motion in a short time and the mass of it is negligible at high temperature.

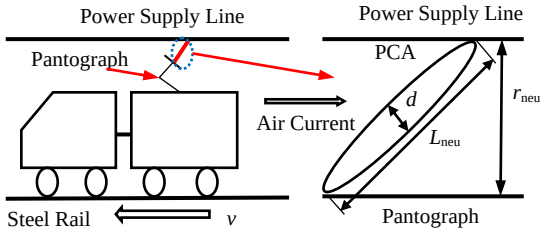

Fig. 2. Diagram of the PCA generated at the neutral section.

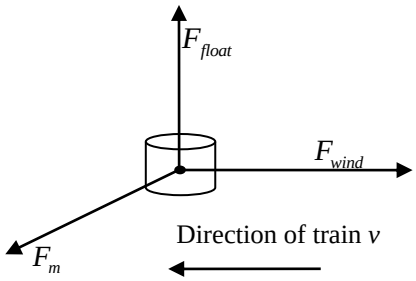

Fig. 3. Force diagram of the PCA generated at the neutral section.

The resultant force on the PCA is:

$$\boldsymbol{F}_{wind} + \boldsymbol{F}_{float} + \boldsymbol{F}_m = 0. \quad (7)$$

If r_{neu} is 15 mm, the direction of the initial PCA is vertical and the initial length is equal to r_{neu}. The diagram of the length of the PCA at the neutral section (L_{neu}) variation with external force can be obtained by simulation calculation, as shown in Fig. 4.

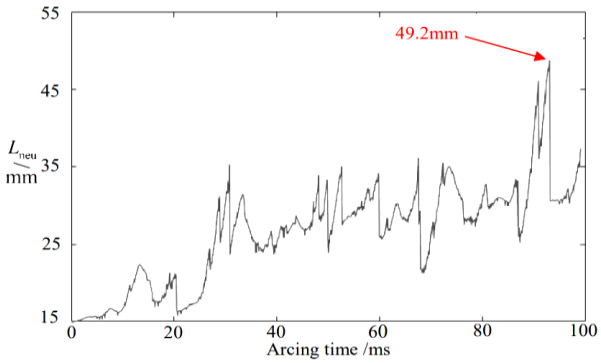

Fig. 4. Diagram of the L_{neu} change caused by the external force.

The simulation results show that the PCA increases with the arcing time until it reaches the critical length

and extinguished. The maximum of L_{neu} is about 49.2 mm. Therefore, the L_{neu} is about 3.28 times of the r_{neu}.

Based on the simulation and measurement data from [15], r_{neu} can be fitted by:

$$r_{neu} = 4.571\times10^{-5}v^2+0.238v-1.411. \quad (8)$$

So,

$$L_{neu} = 3.28r_{neu} = 1.5\times10^{-4}v^2+0.78v-4.628. \quad (9)$$

P_{kL} of the PCA at the neutral section is [16]

$$P_{kL}' = 0.2182d^2v\int_{T_0}^{T_C} CdT, \quad (10)$$

where P_{kL}' is P_{kL} per unit length of the PCA, which is produced by air heating from temperature T_0 to the average temperature of the arc T_C. T_0 and T_C are 4000 K and 9500, respectively. C is the heat capacity coefficient of air and C is [17]:

$$C \approx \frac{0.41}{T}. \quad (11)$$

P_{kL}' can be derived by Eq. (2) and Eqs. (9) ~ (11):

$$P_{kL}' = 0.13\sqrt{I}\,\frac{v}{v+36}. \quad (12)$$

The convective power of the PCA at neutral sections ($P_{k(neu)}$) can be obtained by Eq. (3) and Eq. (12):

$$P_{k(neu)} = \sqrt{I}[0.1892(v+36)+0.13\frac{v}{v+36}]\cdot(1.5\times10^{-4}v^2+0.78v-4.628). \quad (13)$$

It is similar to the above, $P_{loss(neu)}$ and $P_{s(neu)}$ of the PCA at neutral sections are:

$$P_{loss(neu)} = \frac{P_{k(neu)}}{80\%}, \quad (14)$$

and

$$P_{s(neu)} = 0.25\sqrt{I}[0.1892(v+36)+0.13\frac{v}{v+36}]\cdot(1.5\times10^{-4}v^2+0.78v-4.628). \quad (15)$$

C. The *E* values of the PCA at the common/neutral sections

The values of E at different distances from the PCA are unequal. According to Eq. (6) and Eq. (15), E at 10 m away from the PCA at the common or neutral sections ($E_{10(com/neu)}$) can be derived by:

$$E_{10(com/neu)} = \sqrt{\frac{P_{s(com/neu)}}{4\pi\cdot10^2}\cdot120\pi}. \quad (16)$$

The unit of $E_{10(com/neu)}$ is V/m, which can be converted to dBμV/m by:

$$E_{10(com/neu)} = 20\log_{10}(\sqrt{0.3P_{s(com/neu)}})+120. \quad (17)$$

According to the above analysis, the train speed affects the electric field intensity of the PCA by affecting the radiation power of it. Besides, the faster the train speed, the stronger the electric field of the PCA.

III. PRACTICAL MEASUREMENTS

One high-speed railway (the maximum speed is 250 km/h) in the Sichuan Province of China is taken as the measurement object in this paper. This railway is divided into two parallel tracks for round trips. The PCA usually occurs at the common and neutral sections of the power supply line. For the former, the measurement distance is the linear distance from the antenna to the railroad, and for the latter, it is the distance between the antenna and the neutral sections. Figure 5 shows the scene of the practical measurement (a) and the specific layout (b).

The linear distances from the antenna to the two parallel tracks are 41 m and 52 m. Besides, the distances from the antenna to the neutral sections are 79 m and 83 m, respectively. The height of the antenna is 2 m.

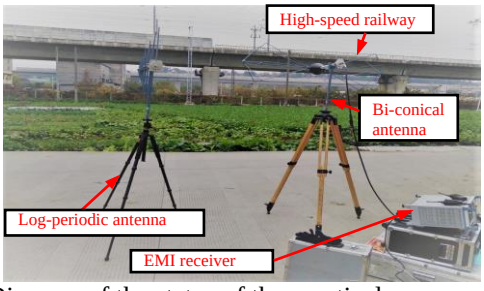

(a) Diagram of the status of the practical measurement

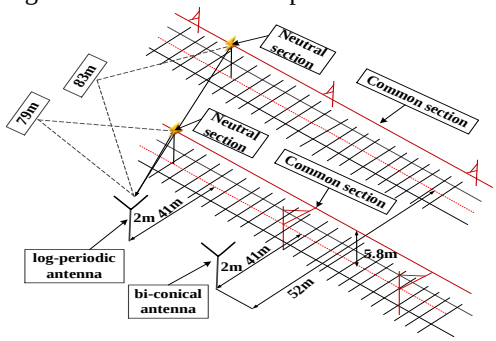

(b) Layout diagram of the measurement

Fig. 5. The situation of the practical measurement.

According to the standards [4, 18], the polarization modes of antennas are horizontal Bi-conical for OBS, perpendicular Bi-conical for VHFCS, and horizontal Log-periodic for GBS. Besides, the resolution bandwidth is 120 KHz and the measurement time is 50 ms. In this paper, the following typical frequency points of the airport navigation stations are selected:

1) 108 MHz, 109.7 MHz, 110 MHz, and 115 MHz in the frequency range of OBS.

2) 119 MHz, 126.48 MHz, 128 MHz, and 135 MHz

in the frequency range of VHFCS.

3) 329.3 MHz, 330.5 MHz, and 332 MHz in the frequency range of GBS.

The maximum value of E is used to analyze the most serious radiation. For comparison purposes, the results are converted to values at 10 m equivalent distance by:

$$E_{10}=E_D+n\times 20\log_{10}(D/10), \quad (18)$$

where E_{10} and E_D are E at the distance of 10 m and D m from the PCA; n is the coefficient related to frequency. When the frequencies are 108 MHz and 109.7 MHz, n is 1.2, and the others are 1. Due to the large amount of measurement data, this paper does not list the complete data. Table 1 lists the data obtained after the abnormal measurement data were excluded by *Grubbs* method [19] and replaced by retest.

Table 1: Part of testing data (v = 250 km/h)

Frequency (MHz)	E (dBμV/m)		Distance (m)		E_{10} (dBμV/m)	
	Common Section	Neutral Section	Common Section	Neutral Section	Common Section	Neutral Section
108	40.78	52.07	41	79	55.49	73.62
109.7	38.2	51.45	52	83	55.38	73.51
110	43.11	55.54	41	79	55.37	73.49
115	40.75	54.80	52	83	55.07	73.18
119	40.53	54.99	52	79	54.85	72.94
126.48	42.2	54.14	41	83	54.46	72.52
128	42.12	54.48	41	79	54.38	72.43
135	39.7	53.68	52	83	54.02	72.06
329.3	35.93	47.49	41	83	48.19	65.87
330.5	33.84	47.89	52	79	48.16	65.84
332	35.88	47.86	41	79	48.14	65.81

IV. PROCESSING AND ANALYSIS OF MEASUREMENT DATA

A. Amplitude-frequency curves of E of the PCA

To find out the relationship between frequency (f) and E_{10}, the correlation between the two variables is determined by [19]:

$$r=\frac{\sum_{i=1}^{N}[\log_{10}(f_i)\times E_{10i}]-N\times\overline{\log_{10}(f)}\times\overline{E_{10}}}{\sqrt{(\sum_{i=1}^{N}[\log_{10}(f_i)]^2-N\times\overline{\log_{10}(f)}^2)\times(\sum_{i=1}^{N}{E_{10i}}^2-N\times\overline{E_{10}}^2)}}, \quad (19)$$

where i is the ordinal number of the samples; N is the total number of the samples; r is the correlation coefficient between f and E_{10}. The parameters marked with a hat denote the mean. N=11 and $r\approx$-0.99 are calculated by Table 1 and Eq. (19). The negative correlation between f and E_{10} is very strong because of $r\in$[-1, -0.75]. Therefore, the two variables satisfy the linear correlation. The linear regression equation between f and E_{10} can be expressed as:

$$E_{10}=a\log_{10}(f)+b, \quad (20)$$

where a is the regression coefficient, and b is the intercept. They are calculated by:

$$\begin{cases} a=\dfrac{\sum_{i=1}^{N}[\log_{10}(f_i)\times E_{10i}]-N\times\overline{\log_{10}(f)}\times\overline{E_{10}}}{\sum_{i=1}^{N}[\log_{10}(f_i)]^2-N\times\overline{\log_{10}(f)}^2} \\ b=\overline{E_{10}}-a\times\overline{\log_{10}(f)} \end{cases}. \quad (21)$$

For OBS, VHFCS, and GBS (108 ~ 336 MHz), when the train passes through the common section at a speed of roughly 250 km/h, $a\approx$ -15.08 and $b\approx$ 86.15 can be calculated by Eq. (21). Thus, the relationship between f and E_{10} is derived by:

$$E_{10}=-15.08\log_{10}(f)+86.15. \quad (22)$$

Similarly, the curves of f and E_{10} at different speeds can be obtained, and the relevant parameters are shown in Table 2.

Table 2: The parameters of relation curves

Frequency (MHz)	Site	Speed (km/h)	a	b
108 ~ 336 (OBS, VHFCS, and GBS)	Common Section	80	-12.59	73.19
		110	-13.59	76.39
		130	-14.05	78.46
		175	-14.78	82.15
		250	-15.08	86.15
	Neutral Section	110	-15.05	97.44
		130	-15.15	98.44
		180	-15.32	100.54
		200	-15.50	102.74
		250	-16.00	106.15

B. EMI limit of navigation signals

This high-speed train will cross the extension line of an airport runway. The locations and distances are shown in Fig. 6, where X is the intersection of the railway and extension line of airport runway; h is the altitude of the aircraft from X; d_{s1}, d_{s2}, and d_{s3} are the distances from OBS, VHFCS, and GBS to the airplane.

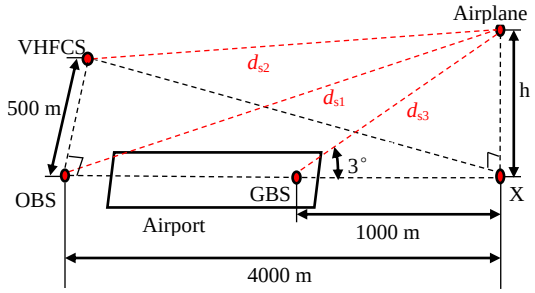

Fig. 6. The location and distance of the navigation equipment, aircraft, and intersection.

The signal strength (E_s) of the navigation stations is specified by [20]:

$$E_s=134.77+10\log_{10}P+G-20\log_{10}d_s, \quad (23)$$

where P and G are the transmission power and the antenna gain of the navigational equipment; d_s is the distance from the navigational equipment to the aircraft. The relevant parameters of the navigational equipment in this paper are shown in Table 3, where R is the margin to ensure normal navigation signals. At the same frequency, the signal strength (E_s) of the navigational stations should be at least R dB more than the E value of EMI, namely, $E_s - E \geq R$.

Table 3: Relevant parameters of navigation equipment

Name	P (W)	G (dB)	d_s (m)	R(dB)
OBS	50.0	2	d_{s1}= 4000.3	20
VHFCS	20	5	d_{s2}=1001.4	
GBS	9.5	14.3	d_{s3}=4031.5	

According to Eq. (18), Eq. (23), and Table 3, the maximum limits of EMI at the distance of 10 m ($E_{10(\text{Limit})}$) can be calculated by:

$$E_{10(\text{Limit})} = 94.77 + 10\log_{10} P + G + 20\log_{10}\frac{d_n}{d_s}, \quad (24)$$

where d_n is the distance from the PCA to the airplane.

Based on Fig. 6, Table 3, and Eq. (24), $E_{10(\text{Limit})}$ of OBS, VHFCS, and GBS are 71.93 dBμV/m, 70.88 dBμV/m, and 89.05 dBμV/m, respectively.

According to the above results, the influences of the train speed on E_{10} of the PCA in the frequency range of OBS, VHFCS, and GBS are shown in Fig. 7 and Fig. 8.

As shown in Fig. 7 and Fig. 8, E_{10} of the PCA at the neutral sections is approximately 18 dB higher than that at the common sections. Besides, E_{10} does not exceed $E_{10(\text{Limit})}$ when the train passes through the common sections. However, for neutral sections, E_{10} in the frequency range of OBS and VHFCS will higher than $E_{10(\text{Limit})}$ if the train exceeds a certain speed. Therefore, the X point in Fig. 6 is a sensitive position for OBS and VHFCS.

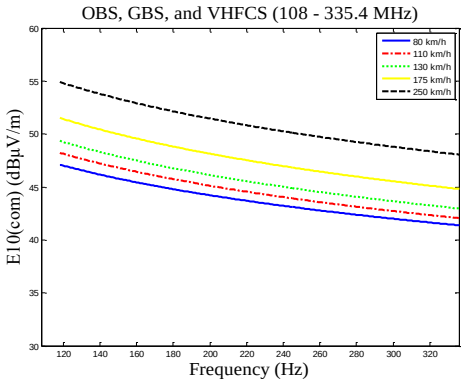

Fig. 7. Diagram of the relationship between the speed and E_{10} at the common sections.

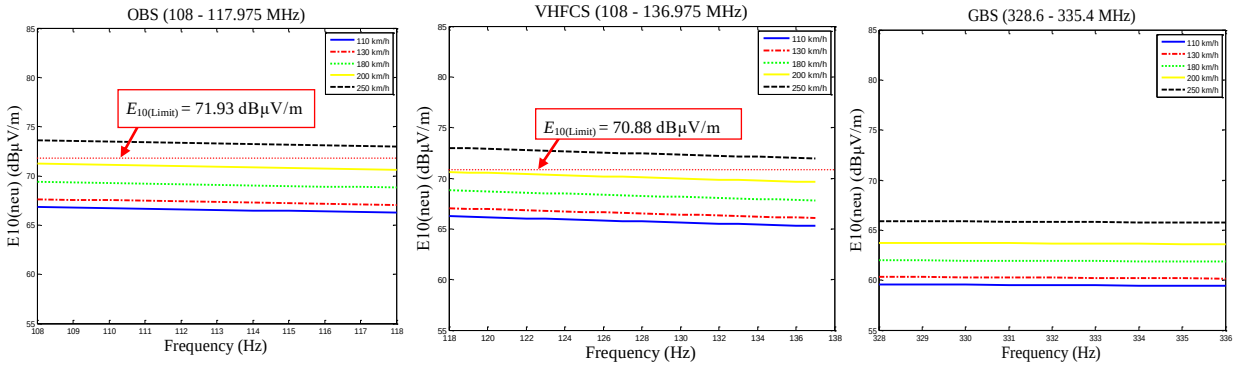

Fig. 8. Diagram of the relationship between the speed and E_{10} at the neutral sections.

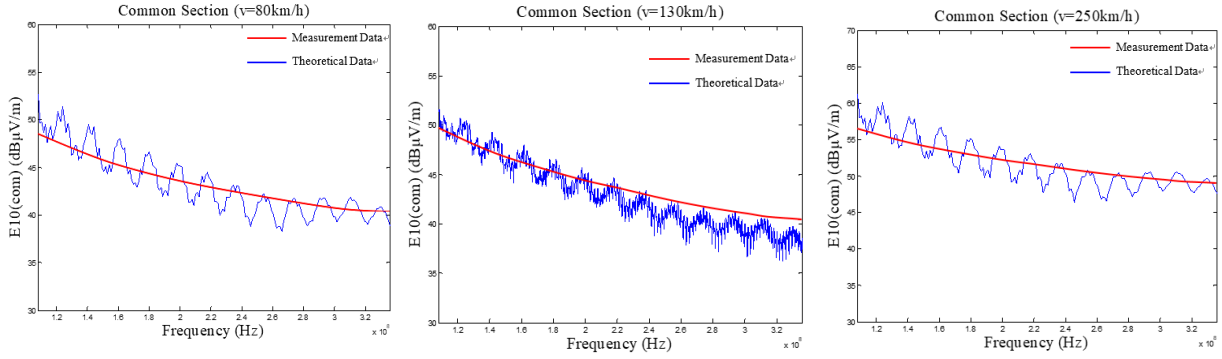

Fig. 9. Comparison of E_{10} of measurement and theoretical results at the common sections.

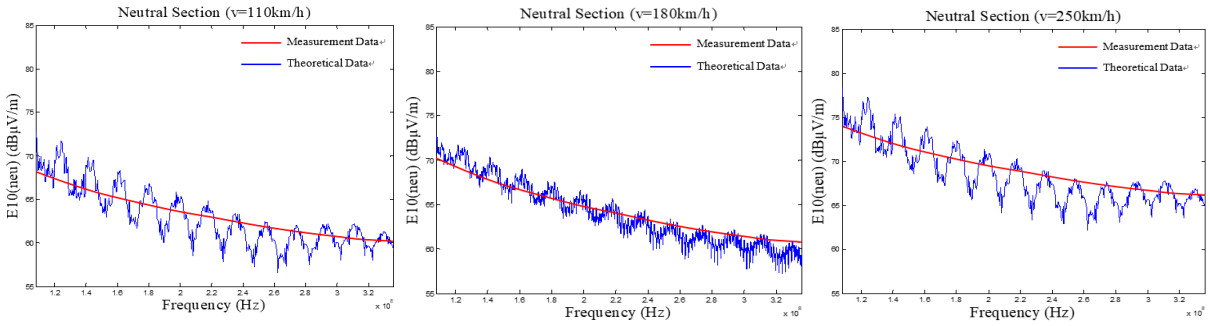

Fig. 10. Comparison of E_{10} of measurement and theoretical results at the neutral sections.

V. CALCULATION OF THE LIMITS OF TRAIN SPEED

The $E_{10(com)}$ values of the train passing through the common sections at a speed of 80 km/h, 130 km/h, and 250 km/h can be calculated by using Eq. (6) and Eq. (17). Its amplitude-frequency relation at 108 ~ 336 MHz can be obtained by Fast Fourier Transform (FFT). The results compared with the measurement data of Fig. 7 are shown in Fig. 9. Similarly, $E_{10(neu)}$ of the train passing through the neutral sections at a speed of 110 km/h, 180 km/h, and 250 km/h are shown in Fig. 10. The average errors of E_{10} are shown in Table 4, which the error is within 10%. It is reasonable because of the error of practical measurements.

Table 4: The E_{10} Error between measurement and theoretical data

Frequency (MHz)	Site	Speed (km/h)	Average Error
108 ~ 336 (OBS, VHFCS, and GBS)	Common Section	80	6.52%
		130	6.96%
		250	4.84%
	Neutral Section	110	8.37%
		180	7.87%
		250	6.65%

As can be seen from the theoretical analysis, the radiated power of the PCA increases with the train speed, which is the main reason for E of the PCA increases with the speed. The maximum train speeds without affecting the signals of the OBS and VHFCS are calculated by Eq. (6), Eq. (15), and Eq. (17). As shown in Fig. 11, E_{10} in the frequency ranges of OBS and VHFCS exceed $E_{10(Limit)}$ (71.93 dBμV/m and 70.88 dBμV/m) when the train speed beyond 225 km/h and 215 km/h, respectively.

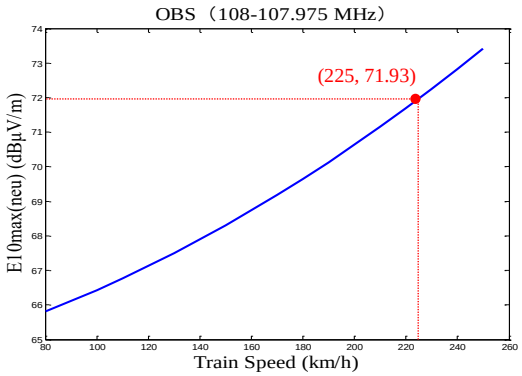

(a) In the frequency range of OBS

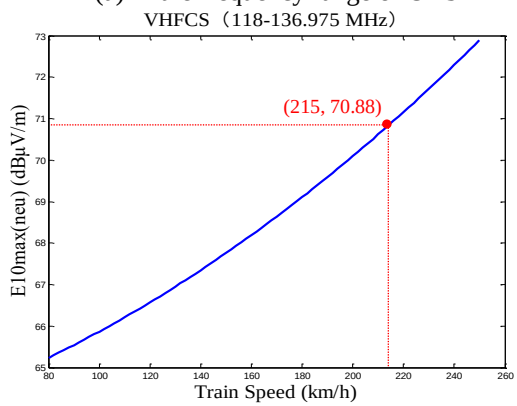

(b) In the frequency range of VHFCS

Fig. 11. The curve of the relationship between v and E_{10} maximum at the neutral sections.

VI. CONCLUSION

The influence of the train speed on the electric field intensity (E) of the PCA in the frequency ranges of OBS, VHFCS, and GBS is studied. The conclusions are as follows:

1) If both the speed and the frequency are the same, E at the neutral sections is nearly 18 dB higher than that

at the common sections. Namely, the PCA at the common sections tends to cause less interference.

2) The *E* values will increase with the train speed at the same frequency range, but it will decrease at higher frequencies. In other words, high-frequency navigation stations (like GBS) are immune to the EMI generated by the PCA.

3) In order to avoid the interference of the PCA on the navigation stations, the neutral sections should not be designed in sensitive positions (like X in Fig. 6) in railway design. If it is inevitable, the train should slow down (not exceeding 215 km/h) when it passes through the sensitive positions.

4) The main reason that the train speed affects *E* is that the speed can cause the change of the PCA length and further impact the radiation power of the PCA.

To sum up, the speed of high-speed trains can affect the EM radiation of the PCA. Defining appropriate speed limits can alleviate the EMI caused by the PCA to the nearby navigation stations.

ACKNOWLEDGMENT

The authors would like to thank the editors and anonymous reviewers for their insightful comments and thank Ling Zhang for the help in English grammar. This paper is supported by the National Key R&D Program of China (No. 2018YFC0809500).

REFERENCES

[1] X. Li, F. Zhu, H. Lu, R. Qiu, and Y. Tang, "Longitudinal propagation characteristic of pantograph arcing electromagnetic emission with high-speed train passing the articulated neutral section," *IEEE Trans. Electromagn. Compat.*, vol. 61, no. 2, pp. 319-326, June 2018.

[2] H. Lu, F. Zhu, Q. Liu, X. Li, Y. Tang, and R. Qiu, "Suppression of cable overvoltage in a high-speed electric multiple units system," *IEEE Trans. Electromagn. Compat.*, vol. 61, no. 2, pp. 361-371, June 2018.

[3] *Electromagnetic Environment Requirements for Aeronautical Radio Navigation Stations*, GB/T 6364, 2013 (in Chinese).

[4] W. Wei, T. Zhang, G. Gao, and G. Wu, "Influences of pantograph-catenary arc on electrical characteristics of a traction drive system," *High Voltage Eng*., vol. 44, no. 5, pp. 1589-1597, May 2018. (In Chinese).

[5] A. Dong, G. Wu, G. Gao, L. Zhou, and W. Wang, "Simulation system of pantograph arcing," *Electric Power Equipment-Switching Technology 2011 1st Int. Conf. on. IEEE*, pp. 637-641, Oct. 2011.

[6] Y. Wang, Z. Liu, X, Mu, K. Huang, and H. Wang, "An extended Habedank's equation-based EMTP model of pantograph arcing considering pantograph-catenary interactions and train speeds," *IEEE Trans. on Power Del*., vol. 31, no. 3, pp. 1186-1194, Jan. 2016.

[7] E. Karadimou and R. Armstrong, "Test of rolling stock electromagnetic compatibility for cross-domain interoperability," *IET Intelligent Transport Systems*, vol. 10, no. 1, pp. 10-16, Feb. 2016.

[8] F. Zhu, Y. Tang, and C. Gao, "Mechanism and suppression of electromagnetic interference of pantograph-catenary arc to speed sensor of CRH380BL electric multiple unit," *China Railway Science*, vol. 37, no. 6, pp. 69-74, Nov. 2016. (In Chinese).

[9] Y. Tang and F. Zhu, "Measurement and suppression of electromagnetic interference to speed sensor of CRH380BL electric multiple unit," *2017 International Applied Computational Electromagnetics Society Symposium*, Sept. 2017.

[10] Y. Tang, F. Zhu, H. Lu, and X. Li, "Analysis and suppression of EMI for traction control unit speed sensors of CRH380BL electric multiple unit," *Applied Computational Electromagnetics Society Journal*, vol. 33, no. 5, pp. 553-560, May 2018.

[11] X. Chen, B, Cao, Y. Liu, G. Gao, and G. Wu, "Dynamic model of pantograph-catenary arc of train in high speed airflow field," *High Voltage Eng*., vol. 24, no. 11, pp. 3593-3600, Nov. 2016. (In Chinese).

[12] X. Yan, W. Chen, and Z. Li, "Simulation for self-extinction behavior of secondary arc in transmission lines," *High Voltage Eng*., vol. 38, no. 9, pp. 2150-2156, 2012. (In Chinese).

[13] Y. Liu, G. Chang, and H. Huang, "Mayr's equation-based model for pantograph arc of high-speed railway traction system," *IEEE Trans. on Power Del*., vol. 25, no. 3, pp. 2025-2027, Aug. 2010.

[14] H. Zhou, Z. Liu, Y, Cheng, and K. Huang, "Extended black-box model of pantograph arcing considering varying pantograph detachment distance," *2017 IEEE Transportation Electrification Conference and Expo, Asia-Pacific (ITEC Asia-Pacific)*, Harbin, pp. 1-6, 2017.

[15] Y. Wu, "Research on dynamic performance and active control strategy of high speed pantograph-catenary systems," *Ph.D. dissertation, Dept. Elect. Eng., Beijing Jiaotong Univ*., Beijing, China, 2011. (In Chinese).

[16] S. Midya, D. Bormann, T. Schutte, and R. Thottappillil, "Pantograph arcing in electrified railways—Mechanism and influence of various parameters—Part II: With AC traction power supply," *IEEE Trans. on Power Del*., vol. 24, no. 4, pp. 1940-1950, Sep. 2009.

[17] S. Li, X. Jin, and H. Bi, "Numerical calculation on very fast transient overvoltage of UHV gas insulated substation by variable gap arc model,"

High Voltage Eng., vol. 41, no. 4, pp. 1306-1312, 2015. (In Chinese).

[18] *Railway Applications-Electromagnetic Compatibility-Part 2: Emission of the Whole Railway System to the Outside World*, IEC Standard 62236-2, 2018.

[19] C. Zhang, X. Cai, and Z. Jiang, "Characteristics and measurement of interference sources in electrified railway," *Journal of Beijing Jiaotong Univ*., no. 2, pp. 13-29, July 1980. (In Chinese).

[20] J. Gou, F. Zhu, J. Zou, J. Ye, H. Li, and Y. Wang, "Research on EMI of instrument landing system on aircraft caused by pantograph arc," *Journal of the China Railway Society*, vol. 40, no. 7, pp. 61-66, July 2018. (In Chinese).

Yutao Tang was born in Sichuan Province, China, in 1991. She received the B.S. degree in Automation from Southwest Science and Technology University, Mianyang, China, in 2013, and is currently working toward the Ph.D. degree in Electrical Engineering at Southwest Jiaotong University, Chengdu, China.

Her research interests include electromagnetic environment test and evaluation, and electromagnetic compatibility analysis and design.

Feng Zhu was born in Anhui Province, China, in 1963. He received a B.S. degree in Physics from Huaibei Normal University, Huaibei, China, in 1984, an M.S. degree in Physics from Sichuan University, Chengdu, China, in 1987, and the Ph.D. degree in Electromagnetic Theory and Microwave Techniques from Southwest Jiaotong University, Chengdu, in 1997.

He is currently a Professor in the Department of Electrical Engineering, Southwest Jiaotong University. His research interests include electromagnetic environment test and evaluation, electromagnetic compatibility, and numerical electromagnetic methods.

Yingying Chen was born in Shanxi Province, China, in 1996. She received a B.S. degree in Electrical Engineering and Automation from Taiyuan University of Science and Technology in China, in 2018. She is currently pursuing a master's degree in Electrical Engineering at Southwest Jiaotong University, Chengdu, China.

Her research interests include electromagnetic environment testing and evaluation, as well as electromagnetic compatibility analysis and design.

A MIMO Antenna with Enhanced Gain using Metasurface

Lan Ngoc Nguyen

Faculty of Electronics and Telecommunications, Saigon University, Vietnam
nnlan@moet.edu.vn

Abstract ─ This paper proposes a new metasurface to improve gain for dipole antenna. The antenna includes two sets of two elements (1 x 2), the integrated J shaped baluns, five metasurface cells (each metasurface cell consists of 5 periodic metallic plates printed on a thin low-cost FR4 substrate) for four antenna elements and the antenna is supplied by two T-junction power dividers. The metasurface is designed to operate as reflection surface. The antenna is designed based on RT5880 and witnesses an overall size of 140 x 37 x 35.075 mm^3 (2.7λ x 0.71λ x 0.67λ at 5.8 GHz), an isolation of approximately 28 dB, a peak gain of 9.5 dBi, and a radiation efficiency of 84%.

Index Terms ─ Dipole array, gain enhancement, metasurface, MIMO antenna.

I. INTRODUCTION

Metasurfaces are 2-D artificial material surfaces (MTSs) consisting of periodic arrangements of small inclusions in a dielectric host medium [1]. As its definition, MTSs are two-dimensional periodic structures and they are very thin compared to wavelength. Based on these features, MTSs can be divided into two categories, that are metafilm and metascreen. Recently, MTSs are a significant topic that are getting much attention of researchers thanks to highlight features such as less-lossy (due to having less physical space than 3D metamaterial structures), light-weight, easy fabrication, flexible [2]. Thanks to all above characteristics, there are wide ranges in applications of MTSs, for example: controllable smart surface [3], miniaturized cavity resonators [4], waveguide [5], biomedical devices [6] and so on [7], [8].

Besides, along with the development of modern wireless communication systems such as 5G, wireless local area network (WLAN), Global Positioning System (GPS), and so on, the demand for antennas with compact size, high gain and isolation, low cost has increased. A lot of antennas with different solutions to improve parameters have been reported, for example: artificial magnetic conductor (AMC) [9], defected ground structure (DGS) [10], epsilon negative transmission line (ENG-TL) [11], meander line [12]. In [9], the authors proposed an antenna for WLAN applications. Although the antenna achieves a high isolation (22 dB), gain is not good (7.3 dBi). Similarly, a magneto-electric dipole antenna with defected ground structure is presented in [10]. The antenna has a large bandwidth percentage (86.9%), but gain is only 7.2 dBi. This also appears with the proposed antennas in [11] and [12]. Moreover, antenna in [12] is a MIMO antenna, not only gain value is low (5.43 dBi), but also there is a low isolation (13 dB).

For the above reasons, a MIMO antenna dipole antenna with enhanced gain is presented in this paper. To enhance gain for antenna, metasurfaces are utilized and they are placed under each element. Here, metasurface acts as a reflective surface and its operating principle is based on Huygens–Fresnel principle. Each metasurface plate is a lattice including 5 metallic plates. In addition, to reduce cost, while the power dividers and elements are implemented on RT5880 (h = 1.575 mm, ε_r = 2.2, and tanδ = 0.0009), metasurfaces are realized on FR4 (h = 1.6 mm, ε_r = 4.4, and tanδ = 0.02). The antenna is designed for WLAN applications. At the 5.8 GHz, a peak gain value of 9.5 dBi and a high isolation of 28 dB are obtained. Furthermore, the antenna achieves a high efficiency of 84% at the resonant frequency. The measured results are compared to the simulated ones to verify the performance of the proposed antenna.

II. ANTENNA DESIGN

A. Metasurface structure

The unit-cell model of the metasurface structure is shown in Fig. 1 (a). The metallic plate is printed on the top side of FR4 substrate while the opposite side is ground plane. Initially, this model is constructed based on electric-LC resonator in [13]. By the modification in the shape of structure, the paper got a new structure as shown in Fig. 1 (a) while the reflection phase of the proposed structure is displayed in Fig. 1 (b). The configuration of metasurface includes a square at center and four squares at four corners.

The proposed structure yielded at the resonant frequency of 5.8 GHz. From Fig. 1 (b), we can see that the bandwidth of the proposed metasurface is 5.5 – 6.5 GHz for a fluctuation of reflection phase from -90° to +90° [14]. In which, the reflection phase is 0 degree at

Submitted On: December 27, 2020
Accepted On: February 23, 2021

https://doi.org/10.47037/2020.ACES.J.360412

5.9 GHz. It is clear that the proposed structure has a large bandwidth and it is enough to satisfy for operating range of frequency of antenna.

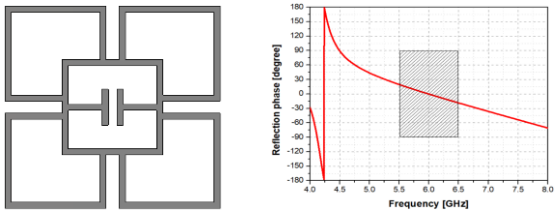

(a) (b)

Fig. 1. The metasurface structure: (a) the model of the unit-cell, and (b) reflection phase.

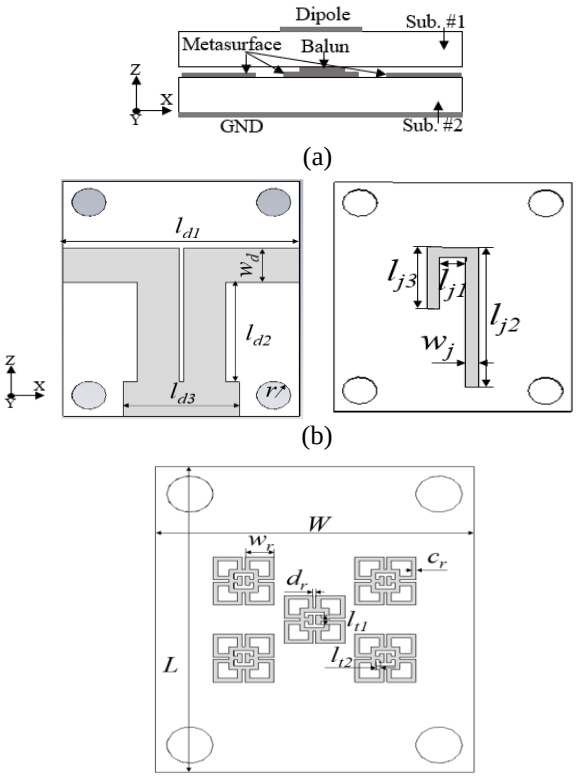

(a) (b) (c)

Fig. 2. The geometry of an antenna element: (a) cross-sectional view; (b) dipole and balun; (c) metasurface.

B. Geometry of the antenna

Firstly, Fig. 2 shows the geometry of an antenna element. It includes a dipole, a J shaped balun, a metasurface and ground plane. The dipole is printed on the upper side while J-shaped balun is placed on the bottom side of substrate-1. Similarly, there are metasurfaces at center of the top side and the opposite side is ground plane for substrate-2. Here, the kind of utilized dipole is half-wavelength at frequency of 5.8 GHz and it is realized on RT5880 (ε_r = 2.2, tanδ = 0.0009, and thickness of h = 1.575 mm). Meanwhile, metasurface is a lattice including 5 unit-cells, which is implemented on low-cost FR4 substrate (ε_r = 4.4, tanδ = 0.02, and thickness of h = 1.6 mm). In addition, four holes are created for using plastic piles to keep two substrates. Table 1 shows some parameters of an element.

In addition, an indispensable component in antenna array is power dividers. To achieve low profile and easy fabrication, T-junction power dividers is used and they are printed on RT5880 substrate. Fig. 3 (a) illustrates the model of power divider and its principle is presented in [15]. Because this is the equal power divider, in theory, S_{21} and S_{31} are -3dB. However, due to effect of mutual coupling and other reasons, S21 and S31 values are -3.3 dB at 5.8 GHz for simulation as shown in Fig. 3 (b). Table 2 shows some parameters of power divider. While the dimension of single antenna (1 x 2 elements) is 70 x 37 x 35.075 mm^3, the size of MIMO antenna is 140 x 37 x 35.075 mm^3 (MIMO antenna consists two set of two elements (1 x 2)).

Table1: Some parameters of an element

W	L	l_{d1}	w_d	l_{d2}	l_{d3}	r	l_{t1}
27.5	33.5	27.5	4.9	14.2	13.5	2	1
l_{j1}	l_{j2}	l_{j3}	w_j	w_r	c_r	d_r	l_{t2}
3	20.55	9	1.45	2.5	0.4	0.25	0.725

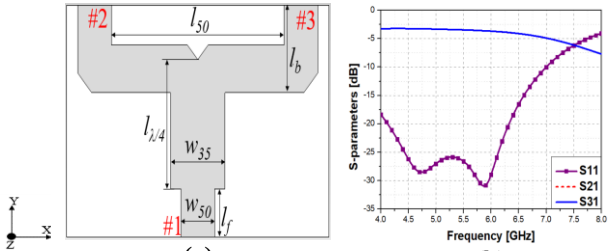

(a) (b)

Fig. 3. The model of power divider (a) and its S-parameters (b).

Table 2: Some parameters of power divider

l_{50}	l_b	w_{50}	l_f	$l_{\lambda/4}$	w_{35}
25	9.5	4.9	5.7	14.9	8

III. RESULTS AND DISCUSSION

As mentioned above, the goal of using metasurface in this paper is to enhance gain for antenna. In this case, metasurface acts as a reflection surface. For a better understanding, the paper simulates in two cases with and without metasurface and these simulated results are shown in Fig. 4.

Observe Fig. 4, we can see that the presence of metasurface is remarkably improved gain for antenna. To make it more specific, gain values are 8 dBi and 9.5

dBi at 5.8 GHz without and with metasurface, respectively. This gain enhancement is based on Huygens-Fresnel principle. We know that the Huygens-Fresnel principle said that each point on a primary wavefront can be considered to be a new source of a secondary spherical wave and it can be propagated according to a certain direction [16]. Therefore, in this case, when a plane wave comes on the metasurface, the total reflected energy flow from metasurface is the sum of reflection from all unit cells. If the phase of the total energy is same the phase of the excited wave in antenna, gain of antenna is enhanced. Switch to Fig. 4 (b), although the isolation of antennas is not improved at the frequency of 5.8 GHz, it is still better in the frequency range of 4.5 – 7.0 GHz (deeper). This shows that using metasurface not only enhances gain, but also improves isolation for antenna. To illustrate in more detail about gain enhancement for antenna, the paper demonstrates the difference in E- and H-fields between with and without metasurface. From Fig. 5, we can see that for the H-field, the maximum intensity value of antenna with metasurface (58.3 A/m) is greater than the one of antenna without metasurface (52.1 A/m). In contrast, for E-field, the maximum intensity value of antenna without metasurface is greater than the one with metasurface. This can be explained as follows. The radiation intensity is given by [16]:

$$U = \frac{1}{2} Re(E \times H^*) r^2, \quad (1)$$

with r is the distance.

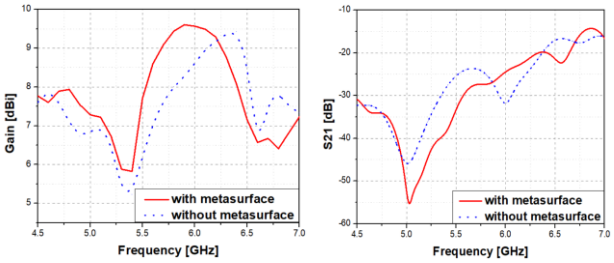

(a) (b)

Fig. 4. Gain values versus the frequency with and without metasurface.

In addition, the directivity is calculated:

$$D = \frac{U}{U_0}, \quad (2)$$

with U_0 is radiation intensity of isotropic source.

Then, gain of antenna can be expressed as:

$$G = eD = \frac{e\left[\frac{1}{2} Re(E \times H^*) r^2\right]}{U_0}, \quad (3)$$

in which e is the radiation efficiency of antenna. Therefore, although the maximum intensity value of antenna with metasurface is smaller than the one of antenna without metasurface in E-field, gain of antenna with metasurface is better than without metasurface. This is because the radiation intensity of antenna (H-field) with metasurface (U) is much greater than the one of antenna without metasurface. As a result, the product of E- and H-field with metasurface is still greater than the one of E- and H-filed without metasurface.

Figure 6 illustrates simulated gain for the different lengths of metasurface substrate (L in Table 1) and the various sizes of unit cell (w_r in Table 1).

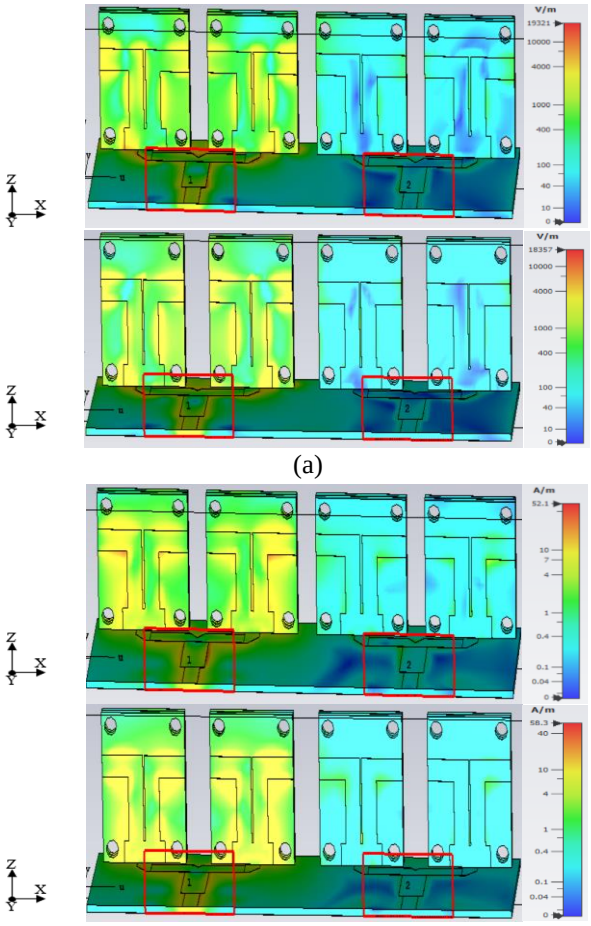

(a) (b)

Fig. 5. The intensity of E-field (a) and H-field (b): without metasurface (up) and with metasurface (down) when the first element is excited.

From Fig. 6 (a), we can see that at the frequency of 5.8 GHz, gain of antenna increases with increasing the length of metasurface (L) substrate while the isolation is guaranteed under -25 dB in three cases. Meanwhile, the isolation of antenna is improved better (compared to the change of the metasurface length (L)) with the different sizes of unit cell (w_r) (Fig. 6 (b)). In contrast, gain of antenna with the various lengths of substrate is better than the one of various dimensions of unit cell. For the reflection coefficient, there is no significant difference and the resonant frequency is ensured in all above cases. This shows that while the changes of w_r improve the

isolation, the changes of L enhance gain for antenna. By combining the changes of both above parameters, the paper achieves an improvement for both gain and isolation. Finally, the optimized dimensions of L and w_r are 33.5 and 2.5 mm, respectively.

To verify the performance of the proposed antenna, the prototypes of MIMO antenna are fabricated and shown in Fig. 7. The size of an element is 33.5 x 27.5 x 3.175 mm^3 while the dimensions of single antenna and MIMO antenna are 70 x 37 x 35.075 mm^3 and 140 x 37 x 35.075 mm^3, respectively. Moreover, the elements including dipole antennas, baluns, power dividers are based on RT5880 (h = 1.575 mm, ε_r = 2.2, and tanδ = 0.0009) while metasurface is implemented on FR4 (h = 1.6 mm, ε_r = 2.2, and tanδ = 0.0009). The measurement of antenna is implemented at Laboratory of Monolithic Microwave Integrated Circuit (MMIC) & Applications for Embedded Systems – International University, VNU HoChiMinh City, Vietnam. The computed and measured results consisting of the reflection coefficient, pattern and directivity of the proposed antenna are compared together and shown in Fig. 8 and Fig. 9. Observe Fig. 8, we can see that there is a better impedance matching in simulated result at resonant frequency. However, the measured and simulated results are quite similar. In addition, the working frequency range (from 5.74 GHz to 5.99 GHz) is still ensured under -10 dB and the mutual coupling is -28 dB (for both simulation and measurement).

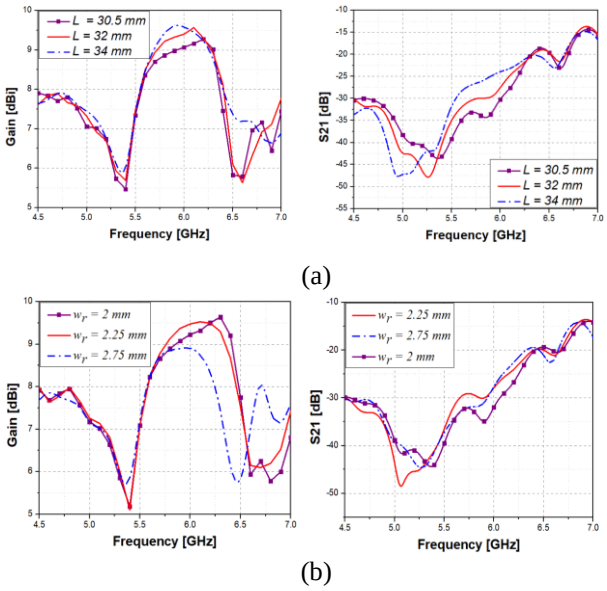

Fig. 6. Simulated gain versus the different lengths of metasurface substrate (a), and various sizes of unit cell (b).

Switch to Fig. 9, we can see that there is a difference between simulated and measured results in xz and yz planes. Here, the directivity of the MIMO antenna for simulation is 10.16 dBi while this value for measurement is 8.8 dBi at 5.8 GHz. This tolerance can be caused from attenuation of FR4. However, the shapes of planes are quite similar. In addition, as mentioned above, using metasurface enhances gain for antenna by combining all reflection flows from all unit cells that they are the same phase. Then, the phase of the total flow from reflection can be shifted compared to normal case (0^o). As a result, there is a slight shift in the main lobe of antenna as in Fig. 9. In addition, there is a difference between simulation and measurement results in xz and yz planes of antenna. This error can be contributed from mistakes in the fabrication progress. Moreover, the test environment is not ideal and this leads the tolerance in antenna measurement. However, these results are acceptable. Moreover, the efficiency of antenna achieves over 84%.

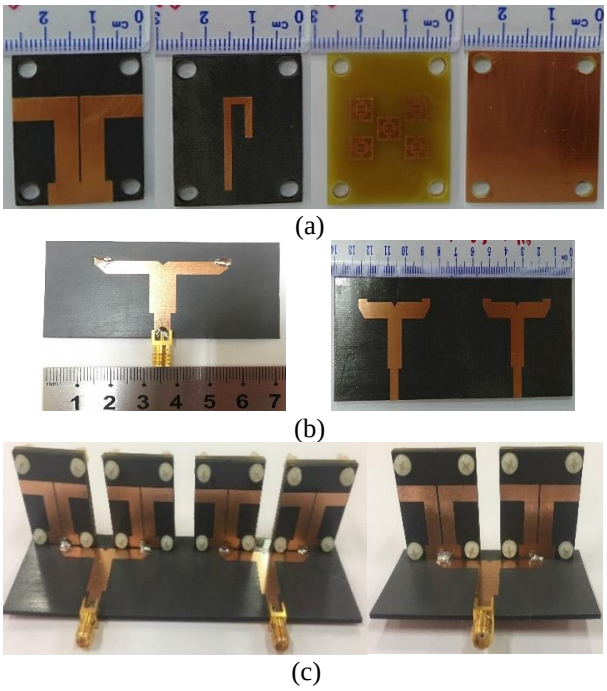

Fig. 7. The prototypes of the proposed antenna: (a) dipole, balun, metasurface and ground; (b) power dividers; (c) single array and MIMO antenna.

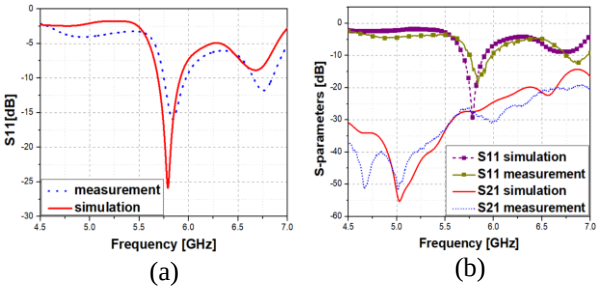

Fig. 8. The measurement results of the reflection coefficient: (a) single array; (b) MIMO antenna.

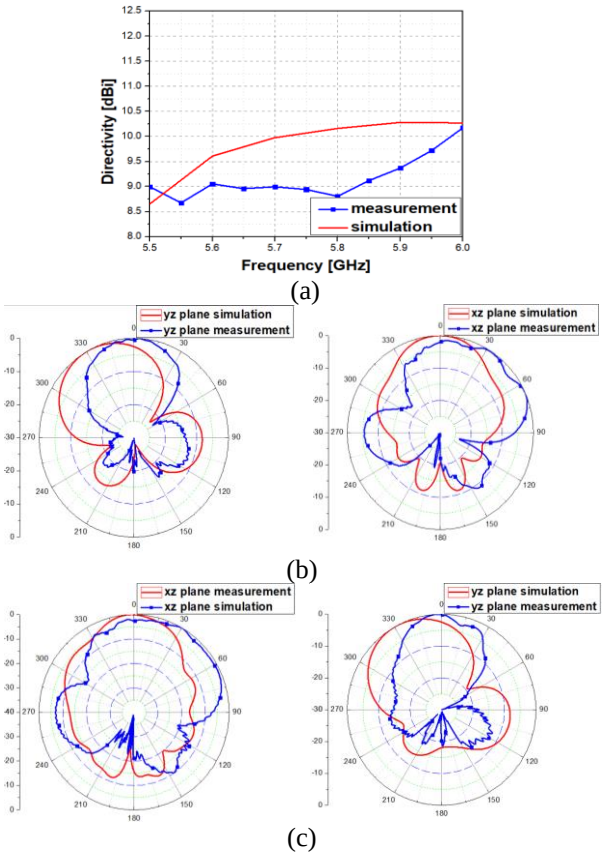

Fig. 9. The measured results of pattern and directivity of the proposed antenna: (a) directivity, (b) xz and yz planes of single array; (c) xz and yz planes of MIMO antenna.

Figure 10 illustrates the enveloped correlation coefficient (ECC) of the MIMO antenna. Here, ECC is calculated by using formula in [17]:

$$\rho_e = \frac{|S_{11}^* S_{12} + S_{21}^* S_{22}|^2}{(1-|S_{11}|^2-|S_{21}|^2)(1-|S_{22}|^2-|S_{12}|^2)}. \quad (4)$$

It is clear that the ECC of the proposed antenna is less than 0.0025 in a wide frequency range from 5 GHz to 6 GHz. This shows that the proposed antenna is enough to respond for MIMO applications.

Table 3 shows a performance comparison among the proposed antenna and recent MIMO antennas. It should be noted that the proposed antenna concentrates gain enhancement. In addition, it is difficult to find MIMO arrays in papers. Currently, MIMO antennas in papers are mostly MIMO single antenna (it means that MIMO antenna has n ports in which each port is an element) while the proposed antenna is two elements in each port. As a result, the size of the proposed antenna is larger and this is natural. Observing Table 3, we can see that antenna in [18] has a large bandwidth percentage (29.6%) and a high efficiency (85%); however, the isolation between elements is low (15dB). Similarly, an dual band and dual polarization log-periodic dipole array is proposed for MIMO WLAN applications [19]. Although this antenna achieves a wide impedance bandwidth (10% and 24%) and a low mutual coupling (-20 dB), gain of antenna is only 6 dBi. In addition, this MIMO antenna includes 12 elements (6 elements for horizontal polarization and 6 elements for vertical polarization) and a high complexity. Meanwhile, there is a narrow bandwidth of the proposed antennas in [19] and [20] although the isolations are high (20 and 40 dB). Moreover, gain of the antenna in [21] is not good (4 dB).

Table 3: The comparison among the proposed antenna and recent MIMO antennas

References	[18]	[20]	[21]	[19]	[22]	**My work**
Frequency [GHz]	2.6	2.45	2.4	2.4/5.5	2.55	5.8
Bandwidth [%]	29.6	2.5	2.2	10/24	56	4.3
Isolation [dB]	15	20	40	20	10	28
Efficiency [%]	85	x	x	x	<90	84
Gain [dBi]	x	x	4	6	4	9.5
Size (λ)	0.69 x 0.69 x 0.014	0.82 x 0.65 x 0.013	0.96 x 0.96 x 0.18	1.2 x 1.2 x 0.48	0.85 x 0.85 x 0.21	2.7 x 0.71 x 0.67

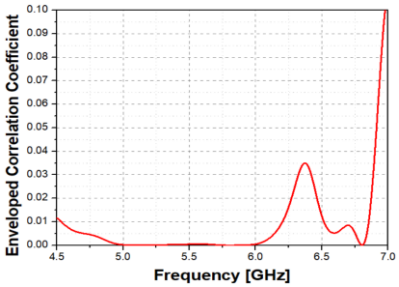

Fig. 10. The enveloped correlation coefficient of the proposed MIMO antenna.

IV. CONCLUSION

A MIMO dipole antenna with enhanced gain by using metasurface is proposed in this paper. The antenna array consists of two sets of two elements (1 x 2) dipole antenna with an overall dimension of 140 x 37 x 35.075 mm^3. While the elements, baluns and power dividers are fabricated on RT5880 substrate, metasurface is printed on FR4 substrate. The antenna is yielded at 5.8 GHz and witnesses a measured $|S_{11}|$ < -10 dB bandwidth of 5.74-5.99 GHz (4.3%). In addition, the proposed antenna resulted in a pick gain 9.5 dBi (at 5.8 GHz), a radiation efficiency of 84% and a high isolation of approximately 30 dB. With the above achieved results along with

advantages such as low profile and, low cost and easy fabrication, the proposed antenna is a good candidate for utilizing in wireless communication systems.

ACKNOWLEDGEMENT

This paper is carried out in the framework of the project titled Design of dipole antenna with high gain using reflective surface under the Grant number TĐ2020-18. The author would like to thank the Saigon University, Vietnam for their financial support.

REFERENCES

[1] M. Faenzi, G. Minatti, D. González-Ovejero, F. Caminita, E. Martini, C. Della Giovampaola, and S. Maci, "Metasurface antennas: New models, applications and realizations," *Scientific Reports*, vol. 9, no. 1, pp. 1-14, 2019.

[2] C. L. Holloway, E. F. Kuester, J. A. Gordon, J. O'Hara, J. Booth, and D. R. Smith, "An overview of the theory and applications of metasurfaces: The two-dimensional equivalents of metamaterials," *IEEE Antennas and Propagation Magazine*, vol. 54, no. 2, pp. 10-35, 2012.

[3] Q. Ma, G. D. Bai, H. B. Jing, C. Yang, L. Li, and T. J. Cui, "Smart metasurface with self-adaptively reprogrammable functions," *Light: Science and Applications*, vol. 8, no. 1, pp. 1-12, 2019.

[4] M. Caiazzo, S. Maci, and N. Engheta, "A metamaterial surface for compact cavity resonators," *IEEE Antennas and Wireless Propagation Letters*, vol. 3, no. 1, pp. 261-264, 2004.

[5] Z. Li, M.-H. Kim, C. Wang, Z. Han, S. Shrestha, A. C. Overvig, M. Lu, A. Stein, A. M. Agarwal, M. Lončar, and N. Yu, "Controlling propagation and coupling of waveguide modes using phase-gradient metasurfaces," *Nature Nanotechnology*, vol. 12, no. 7, pp. 675-683, 2017.

[6] L. La Spada, "Metasurfaces for advanced sensing and diagnostics," *MDPI-Sensors (Switzerland)*, vol. 19, no. 2, p. 355, 2019.

[7] J. Guo, T. Wang, H. Zhao, X. Wang, S. Feng, P. Han, W. Sun, J. Ye, G. Situ, H.-T. Chen, and Y. Zhang, "Reconfigurable terahertz metasurface pure phase holograms," *Advanced Optical Materials*, vol. 7, no. 10, pp. 1-7, 2019.

[8] J. A. Gordon, C. L. Holloway, J. Booth, S. Kim, Y. Wang, J. Baker-Jarvis, and D. R. Novotny, "Fluid interactions with metafilms/metasurfaces for tuning, sensing, and microwave-assisted chemical processes," *Physical Review B - Condensed Matter and Materials Physics*, vol. 83, no. 20, pp. 1-5, 2011.

[9] H. Zhai, K. Zhang, S. Yang, and D. Feng, "A low-profile dual-band dual-polarized antenna with an AMC surface for WLAN applications," *IEEE Antennas and Wireless Propagation Letters*, vol. 16, no. 61501341, pp. 2692-2695, 2017.

[10] J. Zeng and K. M. Luk, "A simple wideband magnetoelectric dipole antenna with a defected ground structure," *IEEE Antennas and Wireless Propagation Letters*, vol. 17, no. 8, pp. 1497-1500, 2018.

[11] E. Kantola, J. Penttinen, S. Ranta, and M. Guina, "Metamaterial based circularly polarized antenna employing ENG-TL with enhanced bandwidth for WLAN applications," *Electronics Letters*, vol. 54, no. 20, pp. 1152-1154, 2018.

[12] S. Chouhan, D. K. Panda, M. Gupta, and S. Singhal, "Meander line MIMO antenna for 5.8 GHz WLAN application," *International Journal of RF and Microwave Computer-Aided Engineering*, vol. 28, no. 4, e21222, 2018.

[13] W. Withayachumnankul, C. Fumeaux, and D. Abbott, "Compact electric-LC resonators for metamaterials," *Optics Express*, vol. 18, no. 25, pp. 25912-25921, 2010.

[14] T. N. Hien Doan, S. X. Ta, K. Van Nguyen, K. K. Nguyen, and C. Dao-Ngoc, "Low-profile, dual-band, unidirectional RFID tag antenna using metasurface," *Progress In Electromagnetics Research C*, vol. 93, no. May, pp. 131-141, 2019.

[15] D. M. Pozar, *Microwave Engineering*. Third ed., John Wiley & Sons, Inc., 2005.

[16] C. A. Balanis, *Antenna Theory: Analysis and Design*, Third Ed., John Wiley & Sons, 2005.

[17] S. Blanch, J. Romeu, and I. Corbella, "Exact representation of antenna system diversity performance from input parameter description," *Electronics Letters*, vol. 39, no. 9, pp. 705-707, 2003.

[18] Y. Zhang and P. Wang, "Single ring two-port MIMO antenna for LTE applications," *Electronics Letters*, vol. 52, no. 12, pp. 998-1000, 2016.

[19] J. J. Liang, J. S. Hong, J. B. Zhao, and W. Wu, "Dual-band dual-polarized compact log-periodic dipole array for MIMO WLAN applications," *IEEE Antennas and Wireless Propagation Letters*, vol. 14, no. c, pp. 751-754, 2015.

[20] H. Arun, A. K. Sarma, M. Kanagasabai, S. Velan, C. Raviteja, and M. G. N. Alsath, "Deployment of modified serpentine structure for mutual coupling reduction in MIMO antennas," *IEEE Antennas and Wireless Propagation Letters*, vol. 13, pp. 277-280, 2014.

[21] G. Zhai, Z. N. Chen, and X. Qing, "Enhanced isolation of a closely spaced four-element MIMO antenna system using metamaterial mushroom," *IEEE Transactions on Antennas and Propagation*, vol. 63, no. 8, pp. 3362-3370, 2015.

[22] E. Fritz-Andrade, R. Gómez-Villanueva, J. A. Tirado-Méndez, L. A. Vasquez-Toledo, A. Rangel-Merino, and H. Jardón-Aguilar, "Broadband four elements pifa array for access-point mimo systems,"

Progress in Electromagnetics Research C, vol. 106, pp. 163-176, 2020.

Lan Ngoc Nguyen received Ph.D. degree from School of Electronics and Telecommunications, Hanoi University of Science and Technology in 2019. Currently, she is a Lecturer at Faculty of Electronics and Telecommunications, Saigon University, Vietnam. Her research interests are microstrip antenna, mutual coupling, MIMO antennas, array antennas, reconfigurable antennas, polarization antennas, metamaterial, metasurface. ORCID: https://orcid.org/0000-0001-8506-9979

MIMO Antenna Based on Metamaterial Frequency Selective Surface

Shengyuan Luo [1], Yingsong Li [1,2], Chow-Yen-Desmond Sim [3], Yinfeng Xia [1,*], and Xiaoguang Liu [4]

[1] College of Information and Communications Engineering, Harbin Engineering University, Harbin 150001, China
*xiayinfeng@hrbeu.edu.cn

[2] Key Laboratory of Microwave Remote Sensing, National Space Science Center, CAS, Beijing 100190, China

[3] Department of Electrical Engineering, Feng Chia University, Taichung 40724, Taiwan

[4] Electrical and Computer Engineering, University of California, Davis, California 95616, USA

Abstract ─ In this paper, a metamaterial-based novel antenna-mutual-coupling reduction structure is proposed and demonstrated. The structure consists of a three-layer metamaterial frequency selective surface (MFSS) superstrate with split-ring resonators and metal grids. The MFSS means metamaterial frequency selective surface that has the metamaterial performance along the substrate and the frequency selective characteristic on the normal direction of the antenna array simultaneously. A 1×2 MIMO antenna that has a short edge-to-edge distance ($0.037\lambda_0$) is designed as an illustration to demonstrate the validity of the meta-surface for mutual. When loaded with the proposed MFSS, the mutual coupling between the antenna elements is significantly reduced and the gain of the antenna array is improved by 2.5 dBi.

Index Terms ─ Frequency selective surface, gain, MIMO antenna array, mutual decoupling.

I. INTRODUCTION

Multiple-input multiple-output (MIMO) technology plays an important role in wireless communication because it has the potential to increase the throughput and capacity of the system [1-3]. Compared with traditional MIMO technology, massive MIMO has the advantages of serving more user terminals and possessing higher energy efficiency and capacity [4-6]. In a massive MIMO communication system, the antenna array usually consists of tens or even hundreds of array elements that are evenly devised with a special contour [4, 5]. For mobile terminal or portable base station that has limited physical space, as the distance between antenna array elements reaches only a fraction of the wavelength, high mutual coupling between them is inevitable.

Recently, many mutual decoupling techniques have been studied [7-19]. Among them, the introduction of decoupling network/structure such as directional couplers, transmission lines with indirect coupling mechanism, inverted T-slot on ground, and coupled resonators have been reported in [7-9]. As the EBG can exhibit band-gap characteristic to reject the surface wave with high impedance [10], electromagnetic band gap (EBG) and fractal uniplanar compact electromagnetic bandgap (UC-EBG) structure with cross slots, and using periodic mushroom EBG structures have also been investigated to improve the isolation between array elements [10-14]. The defected ground structure (DGS) is also a mature technology for isolation enhancement [15-17]. However, etching a series of periodic DGSs on the metal ground will damage the integrity of the ground plane, which leads to leakage waves and deteriorated radiation patterns of the MIMO antenna array.

In the past decades, metamaterials have received much attention due to its unique characteristics such as negative permittivity, permeability, and reflective index [18-22]. In [18-21], antenna arrays integrated with metamaterial substrate have shown significant size reduction and lower mutual coupling due to the high impedance property of metamaterial. Metamaterial structures can also be suspended above the MIMO antenna to obtain mutual coupling reduction. Even though the suspended metamaterial can significantly enhance the isolation of the MIMO antenna, its matching performance is not ideal as the antennas are no longer matched to free-space medium. Therefore, it is worthy to further study other unique technique that can be integrated with the previous designed MIMO antennas, which can achieve good impedance matching, while still maintaining desirable mutual decoupling performance. Interestingly, in practical engineering applications, the frequency selective surface (FSS) technique is mostly used to reduce radar cross-sectional, realize beam multiplexing and applied as a large bandwidth absorbing

Submitted On: January 15, 2021
Accepted On: March 17, 2021

https://doi.org/10.47037/2020.ACES.J.360413

material [23-28], but it is rarely applied to achieve mutual decoupling of array antennas. In recently, an array-antenna decoupling surface has been proposed, but, the mutual decoupling principle is different with the principle in our paper. Partially diffracted waves from the antenna decoupling surface can be controlled to cancel the unwanted coupled waves for the antenna array by using the array-antenna decoupling surface. There are also some meta-surfaces have been proposed in [30, 31], but the impedance of the meta-surfaces in these two papers cannot match well with the antenna array.

In this paper, the technique of integrating the FSS with metamaterial is proposed, in which a single cell (three layers) MFSS structure operating at 5.5 GHz is initially investigated. To further identify its mutual decoupling ability, it is transformed into a metamaterial superstrate (MS) (with 4×6 cells) that is suspended above a conventional 1×2 patch array. Compared with existing mutual decoupling techniques applied to MIMO antenna, this work has the following technical merits:

1. A novel suspended MFSS superstrate is proposed for mutual coupling reduction in MIMO antenna
2. As the suspended MS is composed of a layer of metal grids sandwiched by two layers of split ring resonators (SRRs), it contains the properties of both metamaterial and FSS simultaneously
3. Due to the effects of the FSS, the MFSS can also aid in improving the gain of the antenna array.
4. Because the edge-to-edge distance between two designated antenna array elements in this work can be extremely small ($0.037\lambda_0$), it can therefore be transformed into a low mutual coupling massive MIMO antenna.
5. Compared with the meta-surface in [30] and [31], the MFSS proposed in our paper has a merit that the impedance of this MFSS can match well with the original antenna array, so that it does not need any other options improve the impedance matching between the MFSS and original antenna array due to the frequency selective surface characteristic of the proposed meta-surface.

II. DESIGN OF THE PROPOSED ANTENNA ARRAY

A. Single cell MFSS design

Because the MFSS structure possesses the properties of metamaterial and FSS simultaneously, it is instructive to analyze the MFSS unit cell (Fig. 1) to understand its operating principles. The MFSS unit cell is composed of two stacked square FR4 substrates, each 1.6-mm thick with relative permittivity of 4.4 and loss tangent of 0.02. The substrate is 6 mm•6 mm in size. A 6 mm•6 mm square-ring metal grid with width t=0.1 mm is sandwiched between two identical modified SRRs whose split gap g=0.5 mm and size length a1=5.6 mm. As shown in Fig. 1, propagation characteristics are first studied along the x-direction. The boundary conditions are set to be perfect magnetic conductors (PMC) and perfect electric conductors (PEC), which used default isotropic homogeneous slab model and leaner polarization, and the default number of modes is 1. The polarization of the incident wave in the waveguide model is the E-field in z polarization with the H-field in y polarization, meanwhile the incident wave of the metamaterial frequency selective surface (MFSS) is TEM mode.

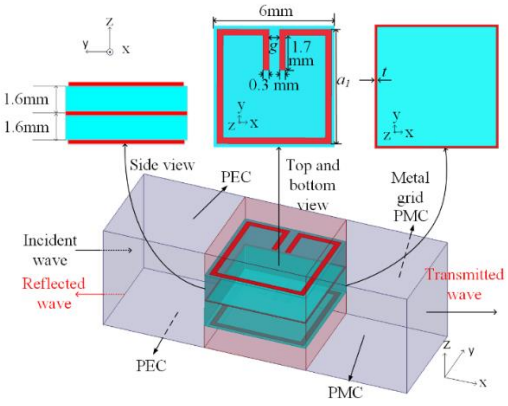

Fig. 1. The geometry and dimensions of the proposed single cell (three-layer) MFSS structure. Top and bottom layers are split ring resonator (SRR) and the middle layer is a metal grid. a1=5.6 mm, g=0.5 mm, t=0.1 mm.

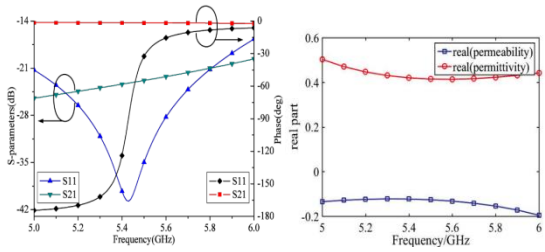

(a) (b)

Fig. 2. (a) Simulated amplitude $|S_{11}|$and $|S_{21}|$ and phase of S_{11} and S_{21}. (b) Extracted permittivity and permeability with respect to frequency.

Figure 2 (a) shows the simulated S-parameters of the structure and Fig. 2 (b) shows the correspondingly extracted permeability and permittivity [32]. From Fig. 2 (a), it can be seen that the phase of S11 changes drastically between 5.2 GHz and 5.7 GHz, while the phase of the S21 remains almost constant at 0. In the frequency range of 5.2–5.7 GHz, the isolation and return loss are better than 21 dB and 23 dB, respectively. This means that the proposed MFSS unit cell can be expanded and applied as a mutual decoupling device for an antenna array. According to the metamaterial theories, the

resonant frequency and the negative permeability frequency region is determined by the physical size and the gap dimension of the SRRs.

Because the proposed MFSS unit cell shows negative permeability in the 5–6 GHz bands, it is vital to study its transmission characteristics along the z-direction with respect to its physical dimensions (a1, g and t). The simulation setup is shown in Fig. 3 (a). As is shown in Fig. 3 (b), the resonant frequency can be linearly decreased from 5.83 GHz to 5.2 GHz by increasing a1 from 5.5 mm to 5.7 mm. At a1=5.6 mm, a resonant frequency of 5.52 GHz is achieved. Correspondingly, the S21 is approximately 1.2 dB [Fig. 3 (c)].

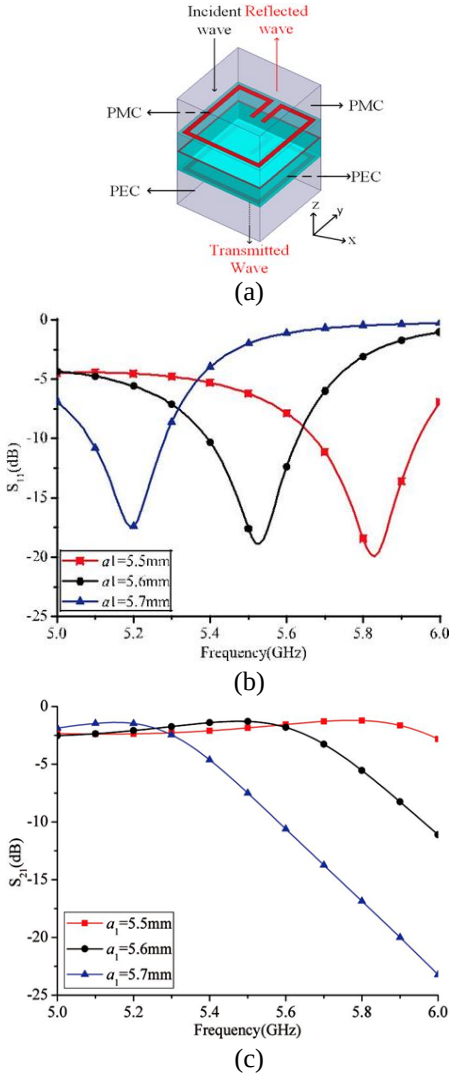

Fig. 3. Simulation setup for incident wave along the z-direction.

Figure 4 (a) and Fig. 4 (b) show the simulated S11 when parameters g and t are tuned, respectively. Here, an increasing g from 0.5 mm to 2.5 mm will linearly shift the resonant frequency from 5.52 GHz to 5.97 GHz. Comparing the two cases where t=0 mm, i.e., no metal grids, and t=0.1 mm, we can see that the resonant frequencies are similar. However, it is worth mentioning that the resonant frequency of S11 for t=0 mm will be vanished when the position of the wave ports is the same as in Fig. 1. From the above results, a1=5.6 mm, g=0.5 mm and t=0.1 mm is selected as the optimized parameters. The equivalent circuits of the MFSS units proposed in this paper has been given in Fig. 5. Due to the effective permeability and the permittivity of the metamaterial ware retrieved from the waveguide model, where the incident waves are transmitted on the side direction, therefore, the equivalent circuit given in this paper is correspond to the side excitation. The SRRs on upper and lower planes of this structure can produce an inductance (L1) and capacitance (C1), which will result in a band-stop region that has a negative permeability and positive permittivity along the substrate of the MIMO antenna, while the inductance (L2) in grid and the capacitance (C1) can form another resonant that results in a band-pass region on the normal direction of the MIMO antenna. Compared with the existing technology of mutual decoupling of the antenna array by using the meta-surface, the meta-surface proposed in this paper does not need any other options to improve the impedance matching between the antenna array and meta-surface. So, if we want to expend this structure into another antenna array, we can apply it directly.

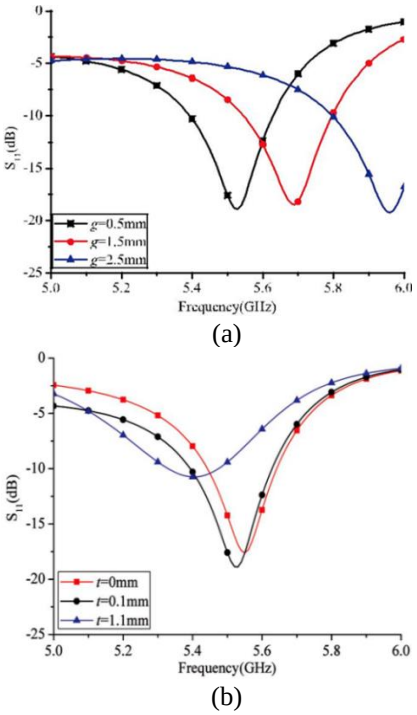

Fig. 4. Simulation setup for incident wave along the z-direction.

According to the simulated results in Fig. 2 (b) and Fig. 3 (b), it can be found that the MFSS means metamaterial frequency selective surface, and this structure owns the metamaterial property along the substrate of the MIMO antenna, meanwhile it has a frequency selective characteristic that can be found from the Fig. 3 (b), which performs a band-pass characteristic along the normal direction of the MIMO antenna. Therefore, the MFSS has another metamaterial characteristic comparing with the normal FSS structure.

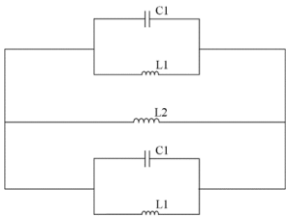

Fig. 5. Equivalent circuit of the MFSS units.

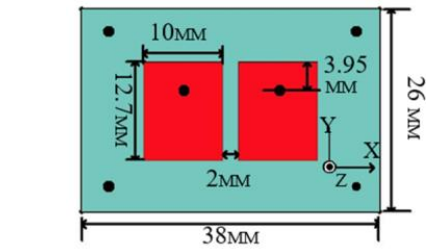

(a)

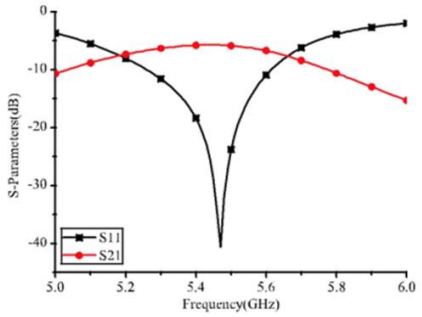

(b)

Fig. 6. (a) The geometry and dimensions, and (b) the simulated S-parameters of the proposed reference 1×2 MIMO array.

B. Design of reference 1×2 MIMO antenna array

To validate the mutual coupling reduction performance of the proposed structure, a reference antenna array is first presented Fig. 6 (a). The reference antenna array consists of two identical microstrip antenna elements on a 1.6-mm thick FR4 substrate. The antenna elements are 12.7×10 mm in size and are separated by an edge-to-edge distance of 2 mm. Both array elements are centrally fed by a 50-coaxial probe. Figure 6 (b) shows the simulated S-parameters between the two feedings of the reference antenna. Although a desirable resonant frequency of 5.48 GHz and a 10-dB impedance bandwidth of 6.25% (5.27-5.61 GHz) are achieved, undesirable coupling of 5.71 dB is observed between the antenna elements due to the tight spacing between them.

C. Design of MIMO antenna array with suspended MFSS

To reduce the mutual coupling between the antenna elements, the proposed MFSS structures are placed as a superstrate 5-mm above the reference antennas. As shown in Fig. 7 (a), the MFSS superstrate is composed of 6×4 MFSS unit cells that collectively cover the reference antennas. The center metal grid of each cell is connected to those of the adjacent cells.

To understand the principle of the MIMO Antenna array with the suspended MFSS, the radiation model is shown in Fig. 7 (b). According to the space electromagnetic wave propagation theory, the plane electromagnetic wave can be expressed as: $\boldsymbol{A}(x)=\boldsymbol{A}_0 e^{i(kx-\omega t)}$.

When a superstrate comprised of the proposed MFSS is placed above the reference MIMO antenna, a negative permeability frequency band region can be achieved, while its corresponding permittivity is positive in this band. Therefore, the wave number in A_0e^{jkx} can be expressed as:

$$k = k_0 \cdot \sqrt{-|u_r| \cdot |\varepsilon_r|} = jk_0 \cdot \sqrt{|u_r| \cdot |\varepsilon_r|}, \qquad (1)$$

where k is purely imaginary in the negative permeability frequency band. As such, the electromagnetic (EM) wave propagation is not allowed.

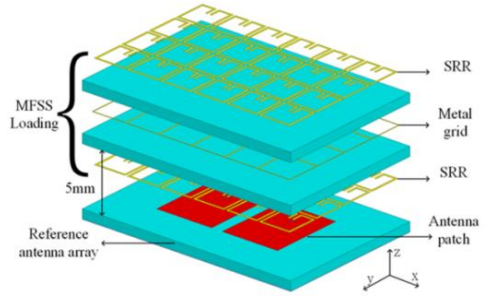

(a)

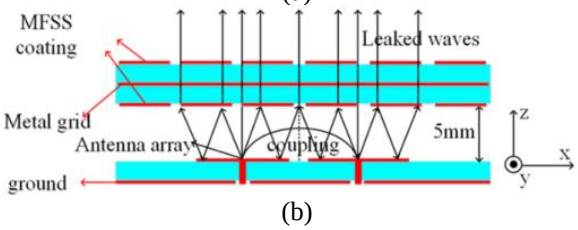

(b)

Fig. 7. (a) 3D Illustration and (b) side view of the MFSS loaded 1×2 MIMO array.

To better understand the mutual decoupling mechanism of the MFSS loading, the simulated surface

current distribution without and with MFSS loading are presented in Fig. 8 (a) and Fig. 8 (b), respectively. Without the MFSS loading, one can be seen that a strong induction current appears on the right antenna patch when the left antenna patch was fed by an excitation source. In contrast, with MFSS loading, the induction current on the right antenna patch is very weak. Thus, it is obvious that the suspended MS can effectively reduce the mutual coupling between antenna array elements. Therefore, the surface current distributions of the antenna array with and without the MFSS can fully illustrate the mutual decupling principle of the antenna array with the MFSS.

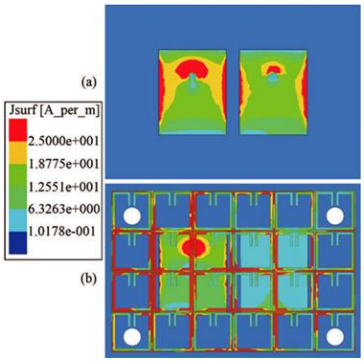

Fig. 8. Surface current distribution of the proposed MIMO antenna array (a) without MFSS loading and (b) with MFSS loading.

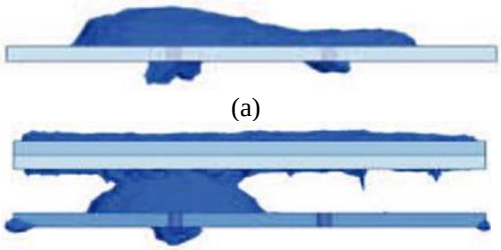

Fig. 9. Simulated electric field distributions in the XOZ-plane for (a) without and (b) with the MFSS loading.

For the FSS, the properties change corresponding to the different distance between antenna array and MFSS. According to the simulation results, when the distance between the antenna array and the MFSS is less than 5 mm, the electromagnetic wave radiated to the MFSS cannot be regarded as a plane wave, which will result in multipath interference in the space between antenna array and MFSS. When the distance between antenna array and MFSS is longer than 5 mm, the negative permeability space of the MFSS cannot cover the antenna array. The decoupling performance is best when the distance between the antenna array and MFSS are suitably selected. Yet, from the simulated surface current distribution of the proposed MIMO antenna array in Fig. 8, it can be observed the right antenna still exists induced current.

To further explain the above phenomena, the electric field distributions of the proposed MIMO antenna without and with MFSS loading are also shown in Fig. 9 (a) and Fig. 9 (b), respectively. As shown in Fig. 9 (a), without MFSS loading, a large amount of electric field is coupled to the right patch antenna. In contrast, Fig. 9 (b) shows that the electric field is directed toward the broadside direction of the radiating antenna in the presence of MFSS loading.

III. MEASURED PERFORMANCE OF PROPOSED MIMO ANTENNA ARRAY WITH MFSS LOADING

The proposed MIMO antenna array with MFSS loading is fabricated and measured in an anechoic chamber. A photograph of the fabricated device is given in Fig. 10 (a). The measured and simulated S-parameters of the fabricated prototype (with and without MFSS loading) are shown in Fig. 10 (b). With MFSS loading, a measured 10-dB reflection bandwidth of 5.13% (5.32–5.6 GHz) is achieved at a center frequency of 5.46 GHz. The measured S21 is better than 12 dB. Comparing with Fig. 6, we can see that the isolation between the two patch antennas can be enhanced by as much as 20 dB without disturbing the impedance bandwidth. The measurement and simulation generally agree well with each other. The slight difference between the measured and simulated results can be attributed to fabrication tolerances.

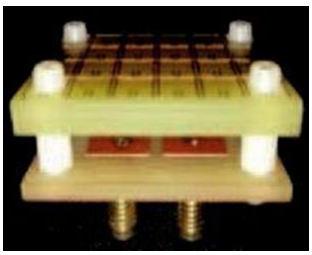

(a)

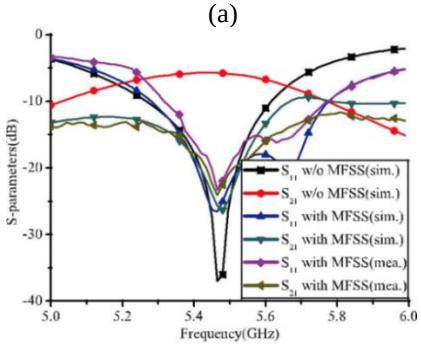

(b)

Fig. 10. (a) The photograph of the fabricated device, and (b) the measured and simulated S-parameters of the fabricated prototype.

Figure 11 shows the influence of various distance between MIMO antenna and MFSS. It can be found that when the distance between MIMO antenna and MFSS is 5 mm, the mutual coupling between antenna array elements is the lowest.

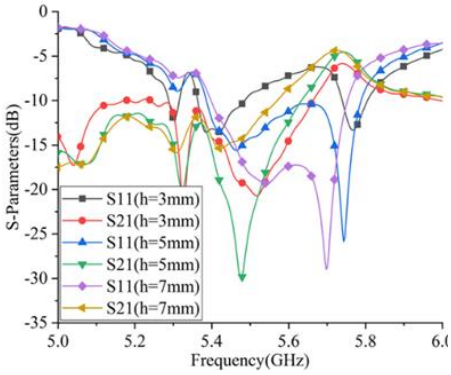

Fig. 11. Simulated S-parameters with influence of various distance h.

Figure 12 shows the measured radiation pattern of the array with MFSS loading. The MFSS loading introduces little perturbation to the radiation characteristics of the antenna array. The measured peak gain with MFSS loading is 7.5 dBi, which represents a 2.5-dBi improvement over the reference array. This is because the MFSS superstrate has aided in concentrating more energy into the band-pass frequency band. The measured radiation efficiency of the proposed antenna array with MFSS loading varies between 67.03% and 74.17% in the 5.35~5.60 GHz range. The calculated peak envelop correlation coefficient (ECC) in the operating band is less than 0.011.

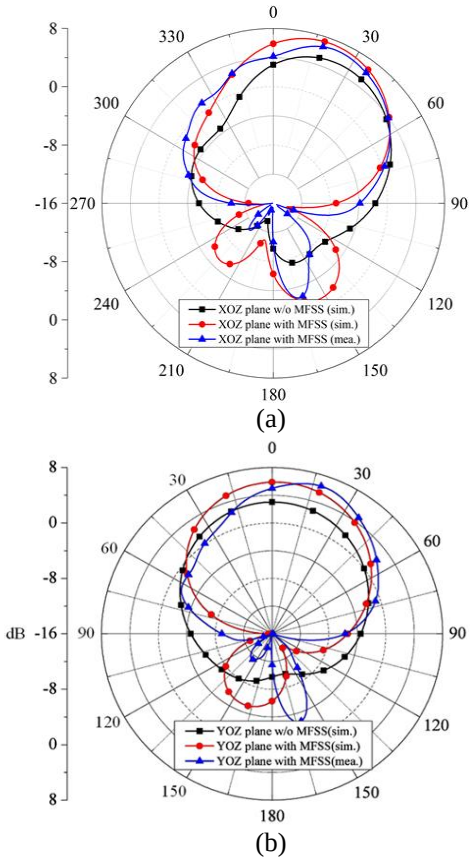

Fig. 12. The simulated and measured radiation patterns of the proposed MIMO antenna array with and without MFSS loading at 5.5 GHz. (a) XOZ plane and (b) YOZ plane.

Table 1: Comparison with the state-of-the-art

Ref.	10-dB BW	Effective Size (c)	Gain/Iso. Enhancement (dB)	Peak ECC/Gain	Eff.
[7]	9.5%	$1.0_{7.5}\times1.0_{7.5}$	0.33/33	NA/6.55	NA
[10]	2.5%	$0.83_{5.0}\times0.5_{5.0}$	NA/16	NA/NA	NA
[11]	1.9%	$1.92_{5.82}\times0.96_{5.82}$	NA/9	NA/NA	NA
[16]	1.9%	$1.48_{5.3}\times0.86_{5.3}$	0.25/12	NA/NA	NA
[19]	1%	$0.81_{3.475}\times0.35_{3.475}$	NA/11	NA/4.37	NA
This work	2.7%	$0.69_{5.5}\times0.47_{5.5}$	2.5/20	0.011/7.5	74.17

*Ref.= Reference, Iso = Isolation, Eff. = Efficiency, BW = Bandwidth.

The performance of the antenna is compared with the state-of-the-art in Table 1. The proposed mutual-coupling-reduction scheme shows smaller physical size, higher gain, and efficiency.

IV. CONCLUSION

A high isolation and gain enhancement MIMO antenna by using the MFSS loading is successfully investigated. The performance of the MIMO antenna with different dimensions is discussed, optimized and fabricated. From the simulated and measured results, it can be shown that the MFSS has exhibited good metamaterial property and frequency selective characteristic, and the isolation and peak gain of the MIMO antenna are improved by 20 dB and 2.5 dBi with an edge-to-edge distance of only 2 mm. In the future, the embedded decoupling techniques and the other metamaterials can be used for realizing the low coupling

design [33-35]. Also, the MIMO antenna can be used for beamforming using the adaptive techniques [36-39].

ACKNOWLEDGMENT

The authors would like to thank the AnHui Province Key Laboratory of Simulation and Design for Electronic Information System and Shenzhen Sunyield Technologies Co., LTD for help with the measurement. This work was supported in part by the National Key Research and Development Program of China under Grant 2016YFE0111100, the Fundamental Research Funds for the Central Universities 3072020CFT0802, the Key Research and Development Program of Heilongjiang under Grant GX17A016.

REFERENCES

[1] M. Jensen and J. Wallace, "A review of antennas and propagation for MIMO wireless communications," *IEEE Transactions on Antennas and Propagation*, vol. 52, no. 11, pp. 2810-2824, 2004.

[2] Y. Li, W. Li, and W. Yu, "A multi-band/UWB MIMO/diversity antenna with an enhanced isolation using radial stub loaded resonator," *Applied Computational Electromagnetics Society Journal*, vol. 28, no. 1, pp. 8-20, 2013.

[3] L. Kang, H. Li, X. Wang, and X. Shi, "Compact offset microstrip-fed MIMO antenna for band-notched UWB applications," *IEEE Antennas and Wireless Propagation Letter*, vol. 14, pp. 1754-1757, 2015.

[4] E. Larsson, O. Edfors, F. Tufvesson, and T. Marzetta, "Massive MIMO for next generation wireless systems," *IEEE Communications Magazine*, vol. 52, no. 2, pp. 186-195, 2014.

[5] L. Lu, G. Li, A. L. Swindlehurst, A. Ashikhmin, and R. Zhang, "An overview of massive MIMO: Benefits and challenges," *IEEE Journal of Selected Topics in Signal Processing*, vol. 8, no. 5, pp. 742-758, 2014.

[6] M. Wang, Y. Li, H. Zou, M. Peng, and G. Yang, "Compact MIMO antenna for 5G portable device using simple neutralization line structures," *2018 IEEE International Symposium on Antennas and Propagation & USNC/URSI National Radio Science Meeting*, pp. 37-38, Boston, MA, USA, July 2018.

[7] R. Xia, S. Qu, P. Li, Q. Jiang, and Z. Nie, "An efficient decoupling feeding network for microstrip antenna array," *IEEE Antennas and Wireless Propagation Letters*, vol. 14, pp. 871-874, 2015.

[8] J. Deng, J. Li, L. Zhao, and L. Guo, "A dual-band inverted-F MIMO antenna with enhanced isolation for WLAN applications," *IEEE Antennas and Wireless Propagation Letters*, vol. 16, pp. 2270-2273, 2017.

[9] L. Zhao and K. L. Wu, "A dual-band coupled resonator decoupling network for two coupled antennas," *IEEE Transactions on Antennas and Propagation*, vol. 63, no. 7, pp. 2843-2850, 2015.

[10] X. Yang, Y. Liu, Y. Xu, and S. Gong, "Isolation enhancement in patch antenna array with fractal UC-EBG structure and cross slot," *IEEE Antennas and Wireless Propagation Letters*, vol. 16, pp. 2175-2178, 2017.

[11] F. Yang andY. Rahmat-Samii, "Microstrip antennas integrated with electromagnetic band-gap (EBG) structures: A low mutual coupling design for array applications," *IEEE Transactions on Antennas and Propagation*, vol. 51, no. 10, pp. 2936-2946, 2003.

[12] T. Jiang, T. Jiao, and Y. Li, "Array mutual coupling reduction using L-loading E-shaped electromagnetic band gap structures," *International Journal of Antennas and Propagation*, vol. 2016, Article ID: 6731014, 2016.

[13] T. Jiang, T. Jiao, and Y. Li, "A low mutual coupling MIMO antenna using periodic multi-layered electromagnetic band gap structures," *Applied Computational Electromagnetics Society Journal*, vol. 33, no. 3, pp. 305-311, 2018.

[14] Y. Fan, J. Huang, T. Chang, and X. Liu, "A miniaturized four-element MIMO antenna with EBG for implantable medical devices," *IEEE Journal of Electromagnetics, RF and Microwaves in Medicine and Biology*, vol. 2, no. 4, pp. 226-233, 2018.

[15] D. Hou, S. Xiao, B. Wang, L. Jiang, J. Wang, and W. Hong, "Elimination of scan blindness with compact defected ground structures in microstrip phased array," *IET Microwaves, Antennas & Propagation*, vol. 3, no. 2, pp. 269-275, 2009.

[16] F. Zhu, J. Xu, and Q. Xu, "Reduction of mutual coupling between closely-packed antenna elements using defected ground structure," *Electronics Letters*, vol. 45, no. 12, pp. 601-602, 2009.

[17] K. Wei, J. Li, L. Wang, Z. Xing, and R. Xu, "Mutual coupling reduction by novel fractal defected ground structure bandgap filter," *IEEE Transactions on Antennas and Propagation*, vol. 64, no. 10, pp. 4328-4335, 2016.

[18] R. Hafezifard, M. Naser-Moghadasi, J. Mohassel, and R. Sadeghzadeh, "Mutual coupling reduction for two closely spaced meander line antennas using metamaterial substrate," *IEEE Antennas and Wireless Propagation Letters*, vol. 15, pp. 40-43, 2016.

[19] Z. Qamar, U. Naeem, S. Khan, and M. Chongcheawchamnan, "Shafique MF mutual coupling reduction for high-performance densely packed patch antenna arrays on finite substrate," *IEEE Transactions on Antennas and Propagation*, vol. 64, no. 5, pp. 1653-1660, 2016.

[20] K. Yu, Y. Li, and X. Liu, "Mutual coupling reduction of a MIMO antenna array using 3-D novel

meta-material structures," *Applied Computational Electromagnetics Society Journal*, vol. 33, no. 7, pp. 758-763, 2018.

[21] M. Farahani, J. Pourahmadazar, M. Akbari, M. Nedil, A. Sebak, and T. Denidni, "Mutual coupling reduction in millimeter-wave MIMO antenna array using a metamaterial polarization-rotator wall," *IEEE Antennas and Wireless Propagation Letters*, vol. 16, pp. 2324-2327, 2017.

[22] D. Binion, P. Werner, D. Werner, E. Lier, and T. Hand, "Metamaterial enhanced antenna systems: A review," *2018 International Applied Computational Electromagnetics Society Symposium (ACES)*, Denver, CO, USA, Mar. 2018.

[23] Y. Liu, Y. Hao, H. Wang, K. Li, and S. Gong, "Low RCS microstrip patch antenna using frequency-selective surface and microstrip resonator," *IEEE Antennas and Wireless Propagation Letters*, vol. 14, pp. 1290-1293, 2015.

[24] M. Pazokian, N. Komjani, and M. Karimipour, "Broadband RCS reduction of microstrip antenna using coding frequency selective surface," *IEEE Antennas and Wireless Propagation Letters*, vol. 17, no. 8, pp. 1382-1385, 2018.

[25] R. Dickie, S. Christie, R. Cahill, P. Baine, V. Fusco, K. Parow-Souchon, M. Henry, P. G. Huggard, R. S. Donnan, O. Sushko, R. Dubrovka, C. G. Parini, and V. Kangas, "Low-pass FSS for 50–230 GHz quasi-optical demultiplexing for the metop second-generation microwave sounder instrument," *IEEE Transactions on Antennas and Propagation*, vol. 65, no. 10, pp. 5312-5321, 2017.

[26] R. Dickie, R, Cahill, H. Gamble, V. Fusco, A. Schuchinsky, and N. Grant, "Spatial demultiplexing in the submillimeter wave band using multilayer free-standing frequency selective surfaces," *IEEE Transactions on Antennas and Propagation*, vol. 53, no. 6, pp. 1904-1911, 2005.

[27] D. Xie, X. Liu, H. Guo, X. Yang, C. Liu, and L. Zhu. "A wideband absorber with a multiresonant gridded-square FSS for antenna RCS reduction," *IEEE Antennas and Wireless Propagation Letters*, vol. 16, pp. 629-632, 2017.

[28] M. Li, S. Xiao, Y. Bai, and B. Wang, "An ultrathin and broadband radar absorber using resistive FSS," *IEEE Antennas and Wireless Propagation Letters*, vol. 11, pp. 748-751, 2012.

[29] K. Wu, C. Wei, X. Mei, and Z. Zhang, "Array-antenna decoupling surface," *IEEE Transactions on Antennas and Propagation*, vol. 64, no. 12, pp. 6728-6738, 2017.

[30] J. Guo, F. Liu, L. Zhao, G. Huang, and Y. Li, "Meta-surface antenna array decoupling designs for two linear polarized antennas coupled in H-plane and E-plane," *IEEE Access*, vol. 7, pp. 100442-100452, 2019.

[31] F. Liu, J. Guo, L. Zhao, X. Shen, and Y. Yin, "A meta-surface decoupling method for two linear polarized antenna array in sub-6 GHz base station applications," *IEEE Access*, vol. 7, pp. 2759-2768, 2019.

[32] D. Smith and S. Schultz, "Determination of effective permittivity and permeability of metamaterial from reflection and transmission coefficients," *Physical Review B*, vol. 65, pp. 195104.1-195104.5, 2002.

[33] F. Liu, J. Guo, L. Zhao, G. L. Huang, Y. Li, and Y. Yin, "Ceramic superstrate-based decoupling method for two closely packed antennas with cross-polarization suppression," *IEEE Transactions on Antennas and Propagation*, vol. 69, no. 3, pp. 1751-1756, 2021.

[34] J. Jiang, Y. Xia, and Y. Li, "High isolated X-band MIMO array using novel wheel-like metamaterial decoupling structure," *Applied Computational Electromagnetics Society Journal*, vol. 34, no. 12, pp. 1829-1836, 2019.

[35] J. Jiang, Y. Li, L. Zhao, and X. Liu, "Wideband MIMO Directional antenna array with single-layered meta-material decoupling structure for X-band application," *Applied Computational Electromagnetics Society Journal*, vol. 35, no. 5, 2020.

[36] X. Huang, Y. Li, Y. Zakharow, and B. Chen, "Affine projection Lorentzian algorithm for vehicle hands-free echo cancellation," *IEEE Transactions on Vehicular Technology*, 10.1109/TVT.2021. 3061126, 2021.

[37] T. Liang, Y. Li, W. Xue, Y. Li, and T. Jiang, "Performance and analysis of recursive constrained least Lncosh algorithm under impulsive noises," *IEEE Transactions on Circuits and Systems II: Express Briefs*, 10.1109/TCSII.2020.3037877, 2021.

[38] W. Shi, Y. Li, and Y. Wang, "Noise-free maximum correntropy criterion algorithm in non-gaussian environment," *IEEE Transactions on Circuits and Systems II: Express Briefs*, vol. 67, no. 10, pp. 2224-2228, Oct. 2020.

[39] Y. Li, Z. Jiang, W. Shi, X. Han, and B. D. Chen, "Blocked maximum correntropy criterion algorithm for cluster-sparse system identification," *IEEE Transactions on Circuits and Systems II: Express Briefs*, vol. 66, no. 11, pp. 1915-1919, 2019.

Design of Dual Band Meta-Material Resonator Sensor for Material Characterization

Sucitra R. Harry, Zahriladha Zakaria*, Maizatul Alice M. Said, Rammah Alahnomi, and M. Harris Misran

Microwave Research Group, Centre for Telecommunication Research and Innovation (CeTRI)
Faculty of Electronics and Computer Engineering, Universiti Teknikal Malaysia Melaka (UTeM) Malaysia
*zahriladha@utem.edu.my

Abstract ─ This paper describes the design and implementation of the dual band metamaterial resonator for sensing applications by employing perturbation theory in which the dielectric properties of resonator affect Q-factor and resonance frequency. The designed sensor operates at two resonance frequency 3.20 GHz and 4.18 GHz in the range of 1 GHz to 5.5 GHz for testing solid materials. The Computer Simulation Technology (CST) software is used to design and model this sensor and it was analyzed by using vector network analyzer (VNA) for testing measurement. This study uses empirical equation from the tested materials with well-known permittivity to estimate the permittivity of other materials with unknown permittivity. The proposed sensor has achieved a narrow band with high Q-factor value of 642 and 521 at the operating frequencies of 3.16 GHz and 4.18 GHz respectively. These findings are compared with findings of previous study and the proposed sensor has achieved a high sensitivity and accuracy of 80% compare to others. This is proof that this senor could be used to characterize materials and sensing applications.

Index Terms ─ Dual band, dielectric material characterization, high Q-factor, microwave resonator sensor, solid sample.

I. INTRODUCTION

Microwave sensor for detecting material characterization is the most popular sensor for food industry, quality control, biomedical and industrial application[1]–[3]. Health and safety controls in food products are important to ensure the health and wellbeing of customers which the presence of certain ingredients can affect consumers and cause certain diseases, such as allergies, poisoning and cancer[3]. Due to the reasons above, it is necessary to ensure the quality and safety of the product (e.g., beverages and cooking oils) before marketing them to customers [3]. There are two types of resonant microwave methods for characterizing materials, there are resonant methods and non-resonant methods. Non-resonant method are often used over a frequency range for the electromagnetic properties while resonant method are typically used to correctly understand single frequency or several distinct frequencies of dielectric properties [4].

Microwave resonant technique is one of the potential techniques that is used for highly accurate measurement of dielectric material characterization at single or discrete frequency. The old method states that material characterization has been realized by using conventional waveguide, dielectric and coaxial resonators that have high sensitivity and accuracy [5]. However, the conventional resonator sensor is typically huge, expensive to manufacture and requires a large amount for the detection of the sample of material under test (MUT) [5]–[8]. Thus, planar resonant techniques are among the most common techniques in recent years due to their advantages of compact size, low cost and ease of manufacture [9]–[12]. Moreover, this technique leads to low sensitivity and Q-factor values which restrict the range of material characterization.

The present study was used to find the weaknesses of the previous study through a new microwave sensor that has compatibility, low cost, simple design, easy handling, higher Q-factor, higher accuracy and sensitivity. Therefore, permittivity is a critical function of properties that determine electrical nature of the material. The resonant frequency will be decreasingly shifted to the left from small to large value of permittivity [13], [14].

II. DESIGN METHODOLOGY

A. Structure design

There are two types of designs called design A and design B, which have been successfully investigated and analyzed by the researcher. This microwave resonator sensor is using Roger 5880 with 0.787 thickness, dielectric constant 2.2 and tangent loss 0.0009 as the substrate with dimension 35mm x 25mm which is compact in size. The operating frequency is 3.16 GHz and 4.81 GHz (Design A) and 3.20 GHz and 4.78 GHz (Design B), which is

Submitted On: September 3, 2020
Accepted On: February 14, 2021
https://doi.org/10.47037/2020.ACES.J.360414

from the range 1 GHz to 5.5 GHz.

Before the microwave resonator is designed in the computer simulation technology (CST) software, there are mathematical analysis for the parameter of designation. The frequency of resonance can be determined through the compatible folded arm loading by the length and width of the patch. Thus, length is the parameter that regulates resonant frequency. The length of the of the resonator is half of the wavelength can be expressed in Equation (1) [12]:

$$l = \frac{c}{2\pi\sqrt{\varepsilon_{eff}}} x \frac{1}{f_o}, \quad (1)$$

Whereas the resonant frequency and the effective permittivity that can be calculated in Equation (2) and Equation (3) respectively [15]:

$$f_o = \frac{c}{2\pi r\sqrt{\varepsilon_{eff}}}, \quad (2)$$

$$\varepsilon_{eff} = \frac{\varepsilon_r + 1}{2} + \frac{\varepsilon_r - 1}{2}\left[\frac{1}{1+12\frac{h}{w}}\right]. \quad (3)$$

B. Simulation process

This study used Computer Simulation Technology (CST) to design the sensor. The design of the propose sensor based on the operating frequency, parameter specifications, and the transmission coefficients of the sensor. Parameter value of design sensor as shown in Table 1. When the metamaterial patch size is large, the frequency will be low, then vice versa. Designation on CST design A and design B, as illustrated by Fig. 1 below.

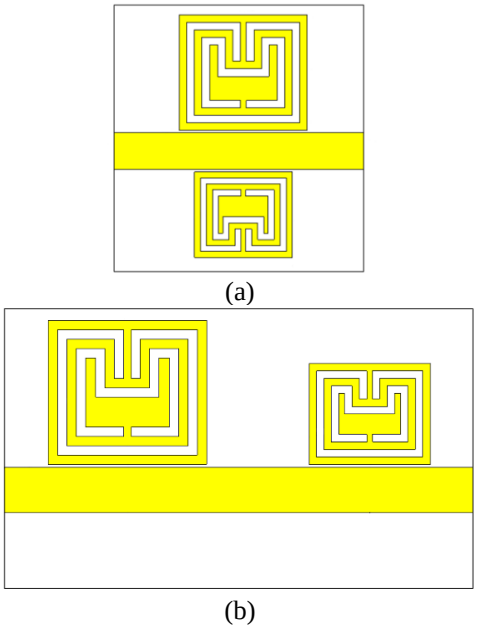

Fig. 1. Designation on CST: (a) design A and (b) design B.

Table 1: Parameter value of design sensor

Substrate	Operating Frequency
Roger 5880	3.16GHz and 4.81GHz (Design A)
	3.20GHz and 4.78GHz (Design B)

Parameter	Design Value	Parameter	Design Value
hs	0.787mm	w	0.5mm
εr	2.2	wk	0.4mm
t	0.0175mm	Cg	0.15mm
Ls	35mm	Dt	17mm
Ws	25mm	g	0.4mm
Lf	35mm	gk	0.3mm
Wf	2.433mm	s	3.4mm
Wr	7.7mm	s2	2.7mm
Lr	8.5mm	la	2.1mm
W2	5.7mm	lb	1.1mm
L2	6.5mm		

In the simulation process, the material under test (MUT) is located at the maximum concentration region of electric field which in red color. Location of MUT at maximum concentration of e-field, as illustrated by Fig. 2 below.

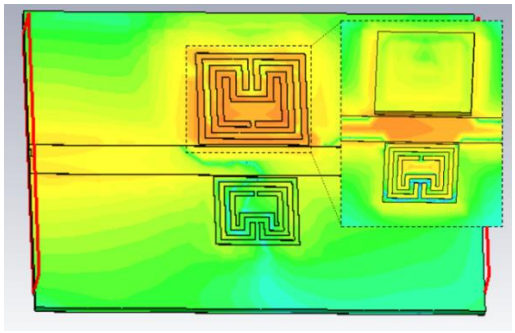

Fig. 2. Location of MUT at maximum concentration of e-field.

C. Measurement process

The microwave resonator sensor is measured by using vector network analyzer (VNA) which analyzed the insertion loss, S21 (dB) of the microwave resonator sensor in the range of frequency 1 GHz to 5.5 GHz. The VNA is connected to the sensor using the two probes station through 50Ω SMA-Connector port of the sensor. The MUT is placed at the top copper of metamaterial patch without touching the feedline in order to avoid other resonant frequency. The dimension for the big MUT is 8.5 mm x 7.7 mm and for the small MUT is 6.5 mm x 5.7 mm. Measurement setup using VNA, as illustrated by Fig. 3 below.

III. RESULTS AND DISCUSSION

A. Q-factor analysis

The resonant frequency shifting determined the accuracy of the microwave resonator sensor. Design A,

resonance frequency for unloaded condition is 3.21 GHz for low frequency and 4.66 GHz for high frequency. However, design B's resonance frequency for unloaded condition is 3.19 GHz for low frequency and 4.69 GHz for high frequency due to coupling loss of gap between feedlines and square patch structure for both designs are 0.15 mm. Therefore, distance between two frequency of design B which is 17 mm also affect resonant frequency shifting of microwave resonator sensor. Low loss occurred when smaller gap between feedline and structure of patch which affect fringing field of perturbation of resonator structure.

Coupling phenomenon between the resonators is also known as mutual coupling which when two patches are coupled through all media such as substrate and air when they are place closed to each other. Comparison result simulation and measurements of design A and design B, as illustrated by Fig. 4 below.

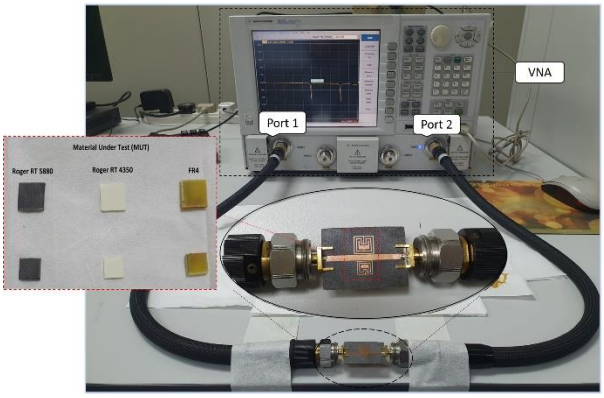

Fig. 3. Measurement setup using VNA.

Design A achieves high quality factor value 350 and 329 for low and high frequency respectively without material under test (MUT). On the other hand, design B achieves high quality factor for low and high frequency are 290 and 278 respectively. Q-factor can be calculated by[16]:

$$Q = \frac{2 f_o}{\Delta f}, \tag{4}$$

where f_o is the resonant frequency and Δf of the resonant peak at -3db. Comparison simulation vs measurement result of low and high frequency (design A & B) as shown in Table 2, Table 3, Table 4 and Table 5.

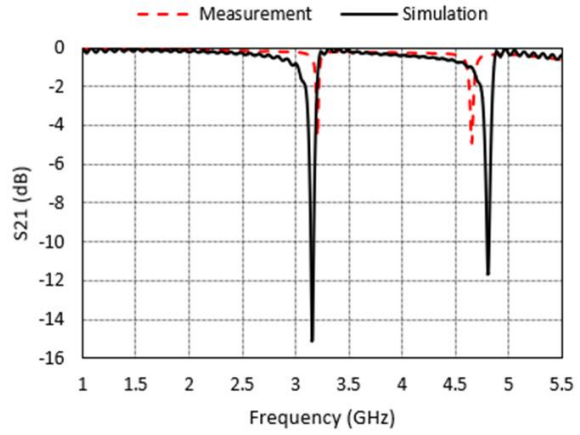

(a)

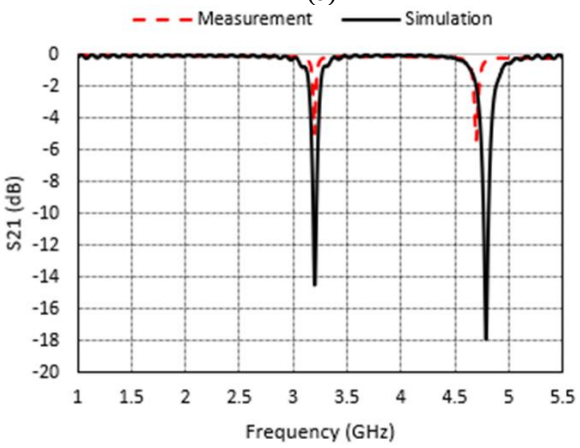

(b)

Fig. 4. Comparison result simulation and measurements of: (a) design A and (b) design B.

Table 2: Comparison simulation vs measurement result of low frequency (design A)

MUT	Simulation						Measurement					
	Q-Factor	S21	BW	f (GHz)	Δf	Error %	Q-Factor	S21	BW	f (GHz)	Δf	Error %
Air	75	-16.959	0.0842	3.16	0	0	350	-4.565	0.0183	3.21	0	0
Roger 5880	70	-16.481	0.0799	2.81	0.35	11.1	642	-3.375	0.0095	3.05	0.16	5
Roger 4350	51	-17.837	0.1009	2.58	0.58	18.3	-	-2.913	-	2.95	0.26	8.1
Fr4	43	-9.227	0.1088	2.34	0.82	26	-	-1.107	-	2.70	0.51	15.9

Table 3: Comparison simulation vs measurement result of high frequency (design A)

MUT	Simulation						Measurement					
	Q-Factor	S21	BW	f (GHz)	Δf	Error %	Q-Factor	S21	BW	f (GHz)	Δf	Error %
Air	113	-13.015	0.0847	4.81	0	0	329	-4.910	0.0283	4.66	0	0
Roger 5880	108	-12.976	0.0786	4.23	0.58	12.1	521	-3.500	0.0168	4.38	0.28	6
Roger 4350	73	-13.771	0.1050	3.83	0.98	20.4	-	-2.832	-	4.35	0.31	6.7
Fr4	64	-6.882	0.1086	3.49	1.32	27.4	-	-0.942	-	3.74	0.92	19.7

Table 4: Comparison simulation vs measurement result of low frequency (design B)

MUT	Simulation						Measurement					
	Q-Factor	S21	BW	f (GHz)	Δf	Error %	Q-Factor	S21	BW	f (GHz)	Δf	Error %
Air	71	-14.496	0.0897	3.20	0	0	290	-5.022	0.0220	3.19	0	0
Roger 5880	107	-13.657	0.0543	2.91	0.29	9.1	474	-3.604	0.0129	3.06	0.13	4.1
Roger 4350	113	-11.503	0.0487	2.74	0.46	14.4	-	-3.003	-	2.92	0.27	8.5
Fr4	121	-4.330	0.0412	2.49	0.71	22.2	-	-1.228	-	2.69	0.5	15.7

Table 5: Comparison simulation vs measurement result of high frequency (design B)

MUT	Simulation						Measurement					
	Q-Factor	S21	BW	f (GHz)	Δf	Error %	Q-Factor	S21	BW	f (GHz)	Δf	Error %
Air	69	-17.911	0.1397	4.78	0	0	278	-5.429	0.0336	4.69	0	0
Roger 5880	102	-14.231	0.0839	4.29	0.49	10.3	380	-4.185	0.0233	4.44	0.25	5.3
Roger 4350	108	-11.302	0.0741	3.99	0.79	16.5	-	-3.346	0.0149	4.40	0.29	6.2
Fr4	137	-4.272	0.0532	3.65	1.13	23.6	-	-1.133	-	3.91	0.78	16.6

B. Analysis dielectric constant and tangent loss analysis

The frequency shift depends on the interference of signal between the maximum concentration of electric fields with the permittivity of the MUT. The measured value of the permittivity value for the MUT have been obtained by using the second order polynomial fitting technique. The difference between reference and the measurement permittivity was analyzed based on percentage error trend line. For design A, the percentage error for permittivity of the samples <12.7% and <26.4% for low frequency and high frequency. For design B, the percentage error for low and high frequency are <5% and <25% respectively.

Loss tangent is the frequency dependent that creates a loss that is proportional to the frequency.

It has higher impact on the peak amplitude S21 when the tangent loss value is smaller. Thus, it makes the S21 parameter narrower when the tangent loss value is smallest. Q-factor of insertion loss is reduced because of the radiation loss that may occur in input and output port network due to the weak connectivity of port couplings and losses occur during fabrication process. Percentage error of losses occur can be calculated in Equation 5:

Comparison permittivity value of reference vs measurement as shown in Table 6. Comparison tangent loss value of reference vs measurement as shown in Table 7. Comparison with previous researcher's sensor as shown in Table 8.

Table 6: Comparison permittivity value of reference vs measurement

MUT	Ref. εr	Measured Permittivity, εr							
		f=3.21 GHz	% Error	f=4.66 GHz	% Error	f=3.19 GHz	% Error	f=4.69 GHz	% Error
Air	1	0.93	7	0.96	4	0.96	4	0.95	5
Roger 5880	2.2	2.48	12.7	2.78	26.4	2.30	4.5	2.75	25
Roger 4350	3.48	3.24	6.9	2.94	15.5	3.40	2.3	2.97	14.7
Fr4	4.4	4.43	0.7	4.41	0.2	4.42	0.5	4.42	0.5

Table 7: Comparison tangent loss value of reference vs measurement

MUT	Ref. Tan δ	Measured Tan δ							
		f=3.21 GHz	% Error	f=4.66 GHz	% Error	f=3.19 GHz	% Error	f=4.69 GHz	% Error
Air	0	0	0	0	0	0	0	0	0
Roger 5880	0.0009	0.000893	0.78	0.000883	1.89	0.000894	0.67	0.000887	1.44
Roger 4350	0.004	0.00399	0.25	0.00398	0.5	0.00398	0.5	0.00399	0.25
Fr4	0.02	0.0199	0.5	0.0199	0.5	0.0199	0.5	0.0199	0.5

Table 8: Comparison with previous researcher's sensor

Ref.	MUT	f (GHz)	Q-Factor	S21 (dB)	E-field	% Accuracy
[16]	Solid	2.50	74	-23.50	Medium	66.2
[17]	Liquid	2.10	130	-13.00	Low	75.8**8**
[18]	Liquid	2.40	-	-35.00	Medium	-
[19]	Solid and Liquid	1.84	49	-2.00	Medium	65.7
[20]	Aqueous Solution	20.00	9.6	-17.77	High	58.5
[21]	Liquid	2.44	146.67	-5.52	Low	78.5
Dual band sensor	Solid	3.16 and 4.18	642 and 521	-3.75 and -3.50	High	>80

IV. CONCLUSION

This paper presented as dual band sensor which proof it can be used to detect the properties of the solid material. Thus, high accuracy and sensitivity sensor works on 3.16GHz and 4.18GHz. This sensor produces a high Q-factor value which are 642 and 541 compared to previous research. A mathematical model is developed for the determination of the dielectric constant and the loss tangent of the MUT. The polynomial curve fitting also applied to determine the dielectric properties of the material. Percentage error for permittivity of measurement

and tangent loss is below 10%. Therefore, percentage of accuracy for this sensor is more than 80% which make the sensor suitable to be apply in further reference.

V. FUTURE WORKS

For further improvement, the sensor can be enhanced by having a portable device to classify the material properties without using the Vector Network Analyzer (VNA) for future suggestions. Thus, it makes the sensor compact in sizes with low cost frequency and can classify the material properties automatically. Then, the sensor also can be enhanced by using algorithms and a Graphical User Interface (GUI) which can read the material characterization of the tested materials. The use of the sensor in the future might be further expanded by measuring the human body's cell tissues, which also involved in dielectric measurement. Thus, this sensor has the high sensitivity which could be used to detect a little change in dielectric properties of the material being tested. The sensor also can be improving by using Internet of Things which allow the user to monitor the material characterization of the tested material.

ACKNOWLEDGMENT

The author gratefully acknowledges the Centre for Research & Innovation Management (CRIM) UTeM, Universiti Teknikal Malaysia Melaka (UTeM) and Ministry of Higher Education (MOHE), Malaysia for funding this work under RACER/2019/FKEKK-CETRI/ F00406.

REFERENCES

[1] S. N. Jha, "Measurement techniques and application of electrical properties for nondestructive quality evaluation of foods-A review," *J. Food Sci. Technol.*, vol. 48, no. 4, pp. 387-411, 2011.

[2] R. A. Alahnomi, Z. Zakaria, E. Ruslan, S. R. A. Rashid, A. Azuan, and M. Bahar, "High - Q sensor based on symmetrical split ring resonator with spurlines for solids material detection," no. c, 2017.

[3] J. Tang, "Unlocking potentials of microwaves for food safety and quality," *J. Food Sci.*, vol. 80, no. 8, pp. E1776-E1793, 2015.

[4] P. M. Narayanan, "Microstrip transmission line method for broadband permittivity measurement of dielectric substrates," *IEEE Trans. Microw. Theory Tech.*, vol. 62, no. 11, pp. 2784-2790, 2014.

[5] U. Schwerthoeffer, R. Weigel, and D. Kissinger, "Microwave sensor for precise permittivity characterization of liquids used for aqueous glucose detection in medical applications," *Microw. Conf.*, vol. 1, no. 4, pp. 1-2, 2014.

[6] K. Shibata and M. Kobayashi, "Measurement of dielectric properties for thick ceramic film on an substrate at microwave frequencies by applying the mode-matchig method," *2016 IEEE MTT-S Int. Conf. Numer. Electromagn. Multiphysics Model. Optim. NEMO 2016*, pp. 1-4, 2016.

[7] A. A. Mohd Bahar, Z. Zakaria, M. K. Md. Arshad, A. A. M. Isa, Y. Dasril, and R. A. Alahnomi, "Real time microwave biochemical sensor based on circular SIW approach for aqueous dielectric detection," *Sci. Rep.*, vol. 9, no. 1, pp. 1-12, 2019.

[8] A. Azuan, M. Bahar, Z. Zakaria, S. Rosmaniza, A. Rashid, and A. A. Isa, "Microstrip planar resonator sensors for accurate dielectric measurement of microfluidic solutions," pp. 416-421, 2016.

[9] M. A. H. Ansari, A. K. Jha, and M. J. Akhtar, "Design and application of the CSRR-based planar sensor for noninvasive measurement of complex permittivity," *IEEE Sens. J.*, vol. 15, no. 12, pp. 7181-7189, 2015.

[10] R. A. Alahnomi, Z. Zakaria, E. Ruslan, and A. A. M. Isa, "Optimization analysis of microwave ring resonator for bio-sensing application," *Int. J. Appl. Eng. Res.*, vol. 10, no. 7, 2015.

[11] R. A. Alahnomi, Z. Zakaria, E. Ruslan, S. R. Ab Rashid, A. A. Mohd Bahar, and A. Shaaban, "Microwave bio-sensor based on symmetrical split ring resonator with spurline filters for therapeutic goods detection," *PLoS One*, vol. 12, no. 9, 2017.

[12] S. Farsinezhad, K. Shankar, M. Daneshmand, and S. Member, "Assisted planar microwave resonator," *IEEE Microw. Wirel. Components Lett.*, vol. 25, no. 9, pp. 621-623, 2015.

[13] A. Iqbal, A. Smida, O. A. Saraereh, Q. H. Alsafasfeh, N. K. Mallat, and B. M. Lee, "Cylindrical dielectric resonator antenna-based sensors for liquid chemical detection," *Sensors (Switzerland)*, vol. 19, no. 5, pp. 2-10, 2019.

[14] J. Yeo and J. I. Lee, "Slot-loaded microstrip patch sensor antenna for high-sensitivity permittivity characterization," *Electron.*, vol. 8, no. 5, 2019, doi: 10.3390/electronics8050502.

[15] K. Chang and L.-H. Hsieh, "Microwave ring circuits and related structures," *Microw. Ring Circuits Relat. Struct.*, 2005, doi: 10.1002/0471721298.

[16] M. A. H. Ansari, A. K. Jha, S. Member, M. J. Akhtar, and S. Member, "Design and application of the CSRR based planar sensor for non-invasive measurement of complex permittivity," no. c, 2015, doi: 10.1109/JSEN.2015.2469683.

[17] W. Withayachumnankul, K. Jaruwongrungsee, A. Tuantranont, C. Fumeaux, and D. Abbott, "Sensors and actuators: A physical metamaterial-based microfluidic sensor for dielectric characterization," *Sensors Actuators A. Phys.*, vol. 189, pp. 233-237, 2013.

[18] M. D. Characterization, A. Ebrahimi, S. Member, and W. Withayachumnankul, "High-sensitivity metamaterial-inspired sensor for," vol. 14, no. 5, pp. 1345-1351, 2014.

[19] G. Galindo-Romera, F. J. Herraiz-Martínez, M. Gil, J. Juan, and D. Segovia-vargas, "Submersible printed split-ring resonator-based sensor for thin-film detection and permittivity characterization," no. c, 2016.

[20] T. Chretiennot, D. Dubuc, and K. Grenier, "A microwave and microfluidic planar resonator for efficient and accurate complex permittivity characterization of aqueous solutions," *IEEE Trans. Microw. Theory Tech.*, vol. 61, no. 2, pp. 972-978, 2013.

[21] A. Kulkarni, "Material characterization using ring resonator," *Int. J. Innov. Res. Comput. Commun. Eng.*, vol. 3, no. 10, pp. 10131-10138, 2015.

Miniature Dual Band Button Antenna Using Cylindrical Dielectric Resonator Antenna for On/Off Body Communication Devices

Mohammed K. Banafaa [1], Mohmed H. Jamaluddin [1], Samsul H. Dahlan [2], and Ayman A. Althuwayb [3]

[1] Department of Communication Engineering
Universiti Teknologi Malaysia UTM, Johor Bahru, 81310, Malaysia
eng.banafaa@gmail.com, haizal@fke.utm.my

[2] Department of Electrical and Electronic Engineering
Universiti Tun Hussein Malaysia, Batu Pahat, Johor 86400, Malaysia
samsulh@uthm.edu.my

Abstract ─ This paper presents miniature dual-band cylindrical dielectric resonator antenna (CDRA) based on button antenna for wireless body area network (WBAN) applications. A button antenna is designed by stacking two CDRAs (low and high permittivity) fed by coaxial probe through the ground plane and penetrates the bottom CDRA. The prime contributions of using DRAs are to enhance the performance and to provide a compact size of antenna. However, the coaxial probe realizes two radiation patterns, monopole and broadside patterns. A comprehensive validation using CST microwave studio is carried out to determine the characteristics of the proposed button antenna. In addition, to ensure that the results are acceptable to the practitioner in this field, a prototype was fabricated and tested. The superiority of the proposed antenna is confirmed by possessing 39% more compact size compared to previously reported studies, efficiency of more than 63% and bandwidth of 4.9% and 6.6% for lower and upper band, respectively. This proposed design is a promising candidate to benefit on/off body communication devices operating at 2.4 and 5.6 GHz.

Index Terms ─ Button antenna, dual-band dielectric resonator antenna, on/off body communications, wearable antenna, wireless body area network (WBAN).

I. INTRODUCTION

In the latest years, it is remarkable that the wireless technologies have been grown-up rapidly and making an extensive change in electronic devices that are able to be inserted in pockets or worn such as smart glasses, wearable sensor systems, wireless medical systems [1], and smart watches. Practically and during the last decade, wearable devices have been awarded a wide consideration in a lot of operating bands such as ultra-wideband (UWB), wireless local area network (WLAN) and wireless body area network (WBAN) [2]. With the rapid and ongoing development of wearable devices, the need to design a wearable antenna with low cost, lightweight, maintenance-free and installation capability for on/off body communication is required for all modern wearable applications.

WBAN is classified into: in-body mode, on-body mode, and off-body mode [3]. In-body mode is the mode where the antennas are inserted inside the body. It needs to take into account the effects of the human body tissue. In on-body mode, the antenna is able to share data with other antennas placed on other locations on the body surface. Thus, this mode needs omnidirectional radiation pattern alongside the surface of the body [4]. However, off-body mode indicates that the antenna can communicate with stations far away from the body. Thus, it requires broadside radiation pattern [5]. In many researches of same area, wearable antennas were developed to be either flexible using textile material [2, 6-8], or robust material [9-12]. Typically for both types, the radiation element is made up of conductive material such as copper.

A number of studies concentrate on the shapes of antenna and how to obtain miniature size antenna. Authors in [13, 14] achieved a compact size for on/off body communication devices, but the antenna's performance suffered from high conductive losses which negatively influenced the efficiency. However, authors in [2, 15] studied the stability and characteristics of the materials and their effects on the performance of antenna. Both of these studies had achieved a good antenna performance suitable for body centric applications. In contrast, achieving acceptable antenna's performance while keeping the size compact is a major challenge faced nowadays.

Submitted On: September 26, 2020
Accepted On: March 14, 2021

https://doi.org/10.47037/2020.ACES.J.360415

Button antennas have clearly several advantages over entirely textile antennas such as being easily attached on clothes or being embedded into a system [16]. In fact, button antennas are rigid in many cases and might significantly and directly impact the antenna's performance stability [17, 18].

From the above discussion, a miniature dual-band circular dielectric resonator antenna (CDRA) based on button antenna that is expected to benefit on/off body communication devices is proposed in this paper. Despite the numerous works carried out on the same subject, no previous work has thoroughly investigated using DRA as a radiation element in the same area. DRA is chosen due to the practical advantages such as a high radiation efficiency, low dielectric loss, and bandwidth [19] which can easily be controlled by using different design techniques[20, 21]. Since there is an experimental validation, this work will pave the way to integrate this work in real life application such as healthcare monitoring system.

The proposed button antenna is designed for frequencies 2.4 GHz for on body communication and 5.6 GHz for off body communication. The frequency 5.6 GHz is confirmed by the UNII (Unlicensed National Information Infrastructure) band. The UNII worldwide is used for both indoor and outdoor and it is exposed to dynamic frequency selection. The 5.6 GHz band has higher bandwidth and power and mostly used by wireless distribution systems [22]. The characteristics of the proposed button antenna are simulated and optimized using CST microwave studio. Section II introduces the geometry, elaborates the method and provides optimization of the proposed button antenna. Section III discusses the simulation and the measurement results including the comparison to previously reported works. Finally, conclusion and suggestions are provided in Section IV.

II. ANTENNA DESIGN

This section elaborates the geometry of the proposed dual-band CDRA based on button antenna for on/off-body communications. The strategy of achieving dual-band on and off radiation pattern of the proposed antenna is obtained by **a** proper modification of CDRA's size. Moreover, the resonance frequency can be adjusted by optimizing the position and length of the probe. The enhancement of this work is also demonstrated in order to improve the performances of antenna.

A. Antenna geometry

The initial structure of the proposed CDRA based on button antenna is illustrated in Fig. 1. The radiation element is a button-shaped that is made of dielectric material (ceramic) as shown in perspective view in Fig. 1 (a). The proposed antenna is fed from the bottom side by a coaxial probe, where the probe penetrates the CDRA with a height of h_p = 3 mm and is located at X = 7.8 mm from the center of the CDRA as it is shown in Fig. 1 (b). The CDRA has a radius of r = 12 mm, height of h = 9 mm, dielectric loss tangent of tanδ = 0.009 and relative permittivity $\boldsymbol{\varepsilon_d}$ = 30. The CDRA is placed on top of a Rogers RT5880 substrate that has the same radius as CDRA with relative permittivity of $\boldsymbol{\varepsilon_s}$= 2.2, dielectric loss tangent of tanδ = 0.0009, and substrate thickness of h_s = 0.254 mm.

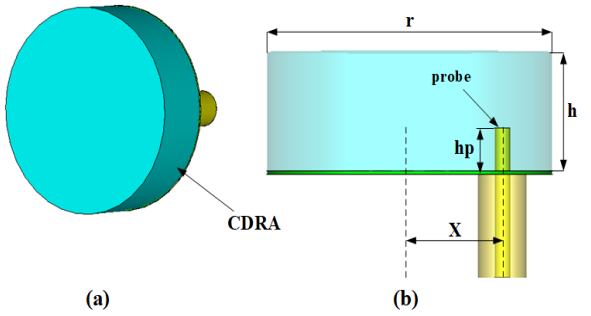

Fig. 1. Geometry of the proposed button antenna: (a) front perspective view and (b) side view.

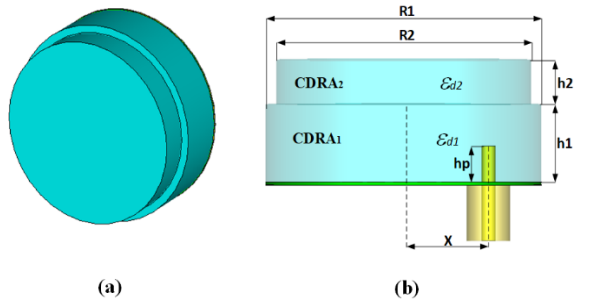

Fig. 2. Geometry of the optimized button antenna: (a) front perspective view and (b) side view.

B. Design methodology

The design has two main objectives. The first one is to obtain a very compact size dual-band CDRA based on button antenna operates in the 2.4 GHz and 5.6 GHz bands for on and off body communications respectively. The second objective is to achieve better performance of the antenna in order to maintain the specifications of on/off body communication devices.

One of the interesting features of CDRA is the size of the CDRA that is inversely proportional to the relative permittivity ($\boldsymbol{\varepsilon_d}$). Therefore, a high dielectric constant can be chosen in order to reduce the size of the DRA [23]. The theoretical resonant frequency (f_r) of the CDRA can be found from the equation (1) [24]:

$$f_r = \frac{c}{2\pi r}\left(\frac{1.6+0.513x+1.392x^2-0.575x^3+0.088x^4}{\varepsilon_d^{0.42}}\right), \quad (1)$$

where $x = R/2h$, c is the free space speed of light, r, $\boldsymbol{\varepsilon_d}$, and h are the radius, relative permittivity, and height of

the CDRA, respectively.

The resonance frequency of the CDRA can be modified by adjusting the position and length of the probe. Moreover, a dual-band omnidirectional and broadside radiation patterns can be achieved by proper modification of CDRA's size. The main advantage related to penetrating the CDRA by a probe is that, a high coupling is delivered to the DR resulting in high radiation efficiency [23]. In contrast, the main drawback associated high dielectric constant of DRA is that the bandwidth is reduced as relative permittivity is increased. In this case optimization should take place.

One of the common techniques used to enhance the bandwidth is stacked DRA. The idea of stacked DRA is to place a DRA of low permittivity on a DRA of high permittivity [25, 26] as depicted in Fig. 2. The dimensions of $CDRA_1$ are $R_1 \times h_1 = 13 \times 7$ mm^2 with permittivity of $\boldsymbol{\varepsilon_{d1}} = 30$, where the dimensions of $CDRA_2$ are $R_2 \times h_2 = 12 \times 4$ mm^2 with permittivity of $\boldsymbol{\varepsilon_{d2}} = 10$. The height and the position (from the center of CDRA) of the probe are $h_p = 3.246$ mm and X = 8 mm, respectively.

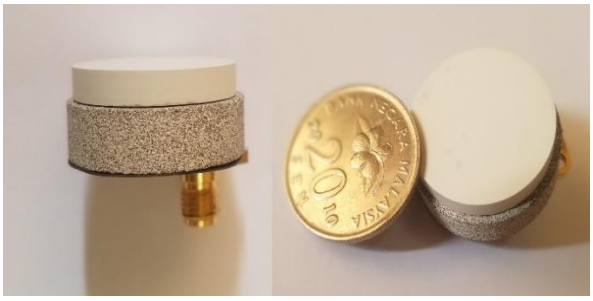

Fig. 3. Shows the fabricated prototype of button antenna, front side view (left) and side view(right).

III. RESULTS

A prototype was fabricated as illustrated in Fig. 3 to verify the proposed button antenna. For this wok, E5071C series network analyzer (NA) is used to test the reflection coefficients while anechoic chamber room used to measure the radiation pattern of the proposed button antenna.

A. Reflection coefficient and bandwidth

The characteristics of the antenna depend on the return loss which describes the matching impedance of the antenna and the amount of power coupled to the antenna around the resonance frequencies. Figure 4 shows the simulated reflection coefficient before and after optimization. Both of the designs achieve dual-band around the resonance frequencies 2.4 GHz and 5.6 GHz. Before optimization, the bandwidth for lower and upper band was 2.1% and 3.7%, respectively. After optimization, bandwidth is increased to 2.7% and 5.2% for lower and upper band, respectively.

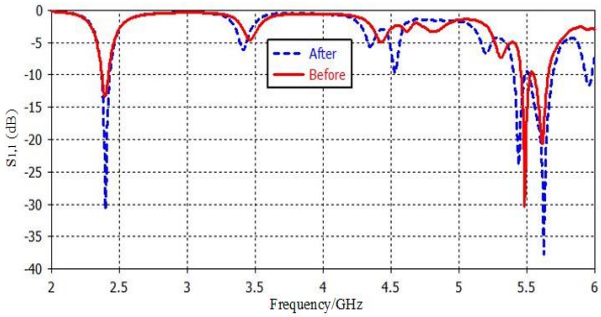

Fig. 4. Simulated reflection coefficient of the proposed button antenna before and after optimization.

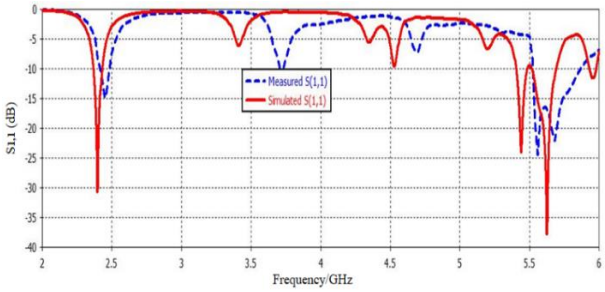

Fig. 5. Measured and simulated S-parameter of the proposed button antenna.

Figure 5 illustrates the measured and simulated return loss of the proposed button antenna. The result ensures that the proposed antenna functions in the dual-band at 2.4 GHz and 5.6 GHz. The result less than -10dB shows that the measured results agree with the simulated ones with wider bandwidth of 4.9% (2.38-2.5GHz) and 6.6% (5.52-5.9GHz) for the lower and upper band, respectively. There is a slightly deviation of the resonance frequency at lower band due to inaccuracy fabrication of CDRA.

B. E-field distributions

To understand the behavior of the proposed antenna, the simulated E-field distributions of operation mode at the resonance frequencies 2.4, 5.6 GHz are shown in Fig. 7. A 50Ω coaxial probe is used to excite CDRA. It has been obtained that the coaxial probe excites fundamental $HEM_{11\delta}$ (Hybrid electromagnetic) mode in the CDRA at both resonance frequencies.

C. Radiation pattern

Figure 6 illustrates the measured and simulated normalized co-polar radiation patterns in E-plane and H-plane of the proposed button antenna at 2.4GHz and 5.6GHz. It can be noticed that, the measured result verifies that the proposed button antenna has omnidirectional radiation pattern at 2.4GHz, which is expected to serve on body communications.

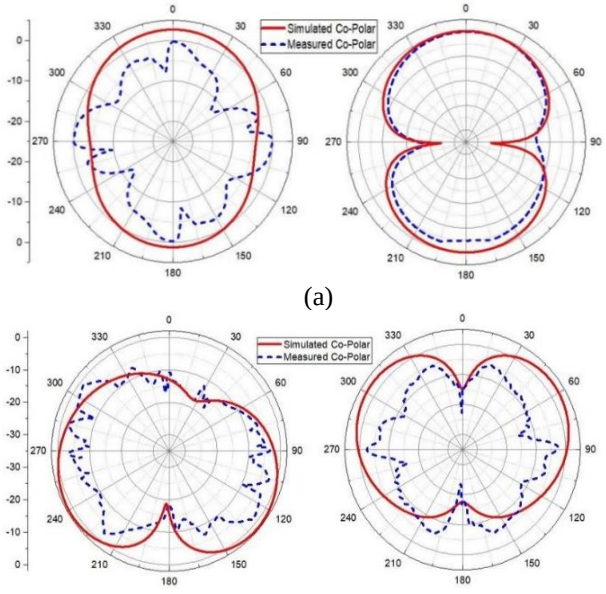

Fig. 6. Simulated and measured radiation patterns in E-plane (left) and H-plane (right) of the proposed button antenna at (a) 2.4 GHz and (b) 5.6 GHz.

Moreover, broadside radiation pattern is obtained at 5.6GHz, which is well-suited for off body communications. Table 1 elaborates the summary of the proposed button antenna performance. The simulated peak gains are a 1.8 and 2.78 dBi at the lower and upper bands, respectively. This is due to the small ground plane. A very good simulated efficiency of 81.5% is obtained at the lower band while due to the high relative permittivity an efficiency of 64% is obtained at the upper band, which is more acceptable than the conventional dual-band antenna compares to [15]. The equivalent figures are not provided here for conciseness.

D. Comparison with previous work

Table 2 shows the comparison between this work and the previous works. It can be remarked that the proposed button antenna has realized the smallest size more than 39% reduction compared to references. Moreover, this work has materialized both omni/broadside radiation patterns applicable for both on/off body communication applications with better performance.

Table 1: Summary of the proposed button antenna performance

Parameters	Lower Band	Upper Band
Frequency	2.4	5.6
BW Sim. (GHz)	2.7	5.2
BW Meas. (GHz)	4.9	6.6
Gain Sim. (dBi)	1.8	2.78
Eff. Sim. (%)	81.5	64

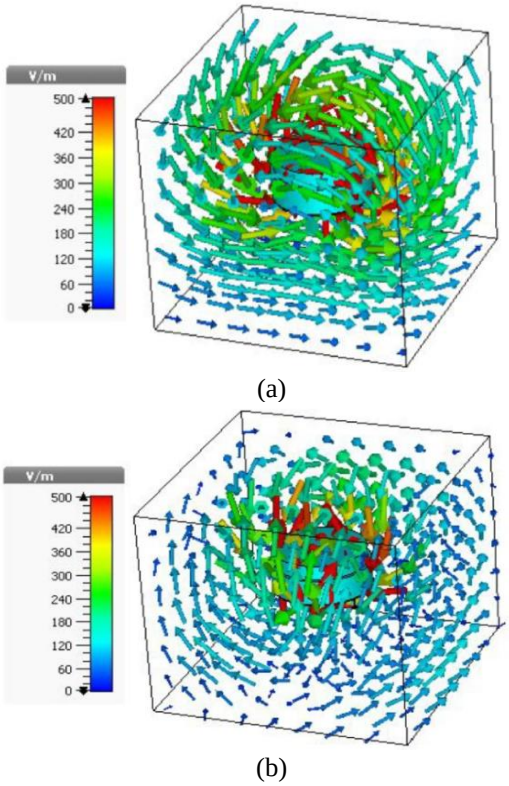

Fig. 7. Simulated E-field distributions at (a) 2.4 GHz and (b) 5.6 GHz.

Table 2: Comparison between the proposed button antenna and previously reported designs

Ref.	Freq. (GHz)	Pattern	Efficiency (%)	Volume (mm^3)
[2]	2.45 5.5	Monopole Patch	90 84	12568
[15]	2.45 5.8	Monopole Patch	46.3 69.3	9965
[27]	2.45 5.8	Monopole Patch	NA	18775
[28]	2.4 5	Monopole Monopole	NA	38520
This work	2.4 5.6	Monopole Patch	81.4 64	5840

IV. CONCLUSION

Based on the findings of this work, it can be concluded that, a new compact dual band CDRA based on button antenna for WBAN 2.4 GHz and 5.6 GHz applications has been proposed, simulated, fabricated and tested. The optimization and feeding technique of the proposed antenna is clarified and elaborated to achieve the objectives of this work. Besides that, the proposed work has notable several features, namely a

very compact size of more than 39% reduction compared to references, bandwidth and efficiency improvement and achieve omni/broadside radiation patterns appropriate to be used for on/off body communication devices.

This work is based on stacked CDRA antenna in which two CDRAs placed on each other with different permittivity. It is suggested to use materials of higher dielectric constants for this kind of applications where the performance of the antenna will be improved, and the size will be smaller. Moreover, the cost of diversity verified by DRAs is the increased complication related to fabricating DRAs, compared to conventional technology. However, as more researches are carried out on DRAs and new fabrication methods are implemented, most of the fabrication issues will be solved.

ACKNOWLEDGMENT

The authors would like to thank the Ministry of Education (MoE) and Universiti Teknologi Malaysia (UTM) for sponsoring this work under Vot 05G20 (TDR Grant) and 4J415 (HiCoE Grant).

REFERENCES

[1] J. E. Gaxiola-Sosa and K. Entesari, "Design and implementation of a wireless medical system prototype for implantable applications," *Analog Integrated Circuits and Signal Processing*, vol. 82, no. 1, pp. 99-111, Jan. 1, 2015.

[2] H. Xiaomu, S. Yan, and G. A. Vandenbosch, "Wearable button antenna for dual-band WLAN applications with combined on and off-body radiation patterns," *IEEE Transactions on Antennas and Propagation*, vol. 65, no. 3, pp. 1384-1387, 2017.

[3] X. Tong, C. Liu, X. Liu, H. Guo, and X. Yang, "Switchable on-/off-body antenna for 2.45 GHz WBAN applications," *IEEE Transactions on Antennas and Propagation*, vol. 66, no. 2, pp. 967-971, 2018.

[4] T. Alves, B. Poussot, and J.-M. Laheurte, "Analytical propagation modeling of BAN channels based on the creeping-wave theory," *IEEE Transactions on Antennas and Propagation*, vol. 59, no. 4, pp. 1269-1274, 2010.

[5] P. Vasina and J. Lacik, "Circularly polarized rectangular ring-slot antenna with chamfered corners for off-body communication at 5.8 GHz ISM band," *Radioengineering*, vol. 26, no. 1, pp. 85-90, 2017.

[6] M. A. Osman, M. Rahim, N. Samsuri, M. Elbasheer, and M. Ali, "UWB wearable textile antenna," *Jurnal Teknologi*, vol. 58, pp. 39-44, 2012.

[7] K.-S. Chin, C.-S. Wu, C.-L. Shen, and K.-C. Tsai, "Designs of textile antenna arrays for smart clothing applications," *Autex Research Journal*, vol. 1, no. ahead-of-print, 2018.

[8] A. Alemaryeen and S. Noghanian, "AMC integrated textile monopole antenna for wearable applications," *Applied Computational Electromagnetics Society Journal*, vol. 31, no. 6, pp. 612-618, 2016.

[9] B. Mandal and S. K. Parui, "A miniaturized wearable button antenna for Wi-Fi and Wi-Max application using transparent acrylic sheet as substrate," *Microwave and Optical Technology Letters*, vol. 57, no. 1, pp. 45-49, 2015.

[10] M. Palandoken, "Compact bioimplantable MICS and ISM band antenna design for wireless biotelemetry applications," *Radioengineering*, vol. 26, no. 4, pp. 917-923, 2017.

[11] S. Doddipalli, A. Kothari, and P. Peshwe, "A low profile ultrawide band monopole antenna for wearable applications," *International Journal of Antennas and Propagation*, vol. 2017, 2017.

[12] P. V. Naidu and A. Malhotra, "A small ACS-fed tri-band antenna employing C and L shaped radiating branches for LTE/WLAN/WiMAX/ITU wireless communication applications," *Analog Integrated Circuits and Signal Processing*, vol. 85, no. 3, pp. 489-496, Dec. 1, 2015.

[13] R. Sreelakshmy and G. Vairavel, "Novel cuff button antenna for dual-band applications," *ICT Express*, 2018.

[14] Z.-G. Liu and Y.-X. Guo, "Compact low-profile dual band metamaterial antenna for body centric communications," *IEEE Antennas and Wireless Propagation Letters*, vol. 14, pp. 863-866, 2014.

[15] X. Y. Zhang, H. Wong, T. Mo, and Y. F. Cao, "Dual-band dual-mode button antenna for on-body and off-body communications," *IEEE Transactions on Biomedical Circuits and Systems*, vol. 11, no. 4, pp. 933-941, 2017.

[16] B. Sanz-Izquierdo, F. Huang, and J. C. Batchelor, "Small size wearable button antenna," in *Antennas and Propagation, 2006. EuCAP 2006. First European Conference on*, *IEEE*, pp. 1-4, 2006.

[17] B. Sanz-Izquierdo, F. Huang, and J. C. Batchelor, "Covert dual-band wearable button antenna," *Electronics Letters*, vol. 42, no. 12, pp. 668-670, 2006.

[18] B. Sanz-Izquierdo, J. Miller, J. C. Batchelor, and M. Sobhy, "Dual-band wearable metallic button antennas and transmission in body area networks," *IET Microwaves, Antennas & Propagation*, vol. 4, no. 2, pp. 182-190, 2010.

[19] S. Danesh, M. Kamarudin, T. Rahman, M. Abedian, M. Jamaluddin, and M. Khalily, "AC-shaped dielectric resonator antenna with frequency reconfigurable for ISM and LTE band applications," *Microwave and Optical Technology Letters*, vol. 59, no. 1, pp. 134-138, 2017.

[20] N. Rais, P. J. Soh, F. Malek, S. Ahmad, N. Hashim, and P. Hall, "A review of wearable antenna," in *Antennas & Propagation Conference, 2009. LAPC 2009. Loughborough, IEEE*, pp. 225-228, 2009.
[21] K. M. Luk, "Dielectric resonator antennas," *Research Studies Pr.*, 2003.
[22] S. Ashok Kumar and T. Shanmuganantham, "Analysis and design of implantable Z-monopole antennas at 2.45 Ghz ISM band for biomedical applications," *Microwave and Optical Technology Letters*, vol. 57, no. 2, pp. 468-473, 2015.
[23] S. Keyrouz and D. Caratelli, "Dielectric resonator antennas: Basic concepts, design guidelines, and recent developments at millimeter-wave frequencies," *International Journal of Antennas and Propagation*, vol. 2016, 2016.
[24] H.-M. Chen, Y.-K. Wang, Y.-F. Lin, S.-C. Lin, and S.-C. Pan, "A compact dual-band dielectric resonator antenna using a parasitic slot," *IEEE Antennas and Wireless Propagation Letters*, vol. 8, pp. 173-176, 2009.
[25] Y. Pan and S. Zheng, "A low-profile stacked dielectric resonator antenna with high-gain and wide bandwidth," *IEEE Antennas and Wireless Propagation Letters*, vol. 15, pp. 68-71, 2015.
[26] W.-J. Sun, W.-W. Yang, P. Chu, and J.-X. Chen, "Design of a wideband circularly polarized stacked dielectric resonator antenna," *IEEE Transactions on Antennas and Propagation*, vol. 67, no. 1, pp. 591-595, 2018.
[27] X.-Q. Zhu, Y.-X. Guo, and W. Wu, "A novel dual-band antenna for wireless communication applications," *IEEE Antennas and Wireless Propagation Letters*, vol. 15, pp. 516-519, 2016.
[28] B. Sanz-Izquierdo, J. C. Batchelor, and M. Sobhy, "Button antenna on textiles for wireless local area network on body applications," *IET Microwaves, Antennas & Propagation*, vol. 4, no. 11, pp. 1980-1987, 2010.

Mohammed Banafaa was born in Yemen. In 2017, he received B.Eng. (Hons.) in Electronic and Communication from University of Aden. in 2019, he received M.Eng. (Hons.) in Telecom from Universiti Technologi Malaysia. He is a member of IEEE. His research interests include dielectric resonator antenna, wireless propagation, wireless communication, 5G technology and Mobile edge computing (MEC). He currently works as Telecom Engineer at Etisalat Telecommunication company in UAE since June 2020.

Mohd Haizal Jamaluddin received the bachelor's and master's degrees in Electrical Engineering from Universiti Teknologi Malaysia, Malaysia, in 2003 and 2006, respectively, and the Ph.D. degree in Signal Processing and Telecommunications from the Université de Rennes 1, France, in 2009, with a focus on microwave communication systems and specific antennas such as dielectric resonator and reflect array and dielectric dome antennas. He joined the Department of Electronic Engineering, Faculty of Electrical Engineering, Universiti Teknologi Malaysia, as a Tutor in 2003. He is currently an Associate Professor with the Wireless Communication Centre, Universiti Teknologi Malaysia (UTM). He was a Senior Lecturer at Wireless Communication Centre (WCC), Universiti Teknologi Malaysia (UTM) until December 2017. He has published more than 100 ISI/Scopus papers in reputed indexed journals and more than 60 conference proceedings.

Samsul Haimi DAHLAN received the degree in Electrical Engineering from the Universiti Kebangsaan Malaysia in 1999, Masters degree in Electrical and Electronic Engineering from the Universiti Teknologi Malaysia in 2005, and the Ph.D degree in Signal Processing and Telecommunications from the Universite de Rennes I, France in 2012. He is currently an Associate Professor with the Faculty of Electrical and Electronic Engineering, Universiti Tun Hussein Onn Malaysia, and holds the position as the head of Research Center for Applied Electromagnetic (EMCENTER) since 2015. He is one of the ALUMNI for the Leaders in Innovation Fellowship program with the Royal Academy of Engineering, UK and holds several intellectual property rights on several innovative products. He has authored and co-authored more than 30 ISI/Scopus journals and over 30 conference papers. His research interests include optical microwave generator, focusing system (dielectric lens and transmit array's synthesis), advance antenna design, material characterization techniques, and computational electromagnetic.

Ayman Althuwayb received the B.Sc. degree (Hons.) in Electrical Engineering (Electronics and Communications) from Jouf University, Saudi Arabia, in 2011, the M.Sc. degree in Electrical Engineering from California State University, Fullerton, CA, USA, in 2015, and the Ph.D. degree in Electrical Engineering from

Southern Methodist University, Dallas, TX, USA, in 2018. He is currently an Assistant Professor with the Department of Electrical Engineering at Jouf University, Kingdom of Saudi Arabia. His current research interests include antenna design and propagation, microwaves and millimeter-waves, wireless power transfer, ultra-wideband and multiband antennas, filters and others.